A study of electrostatic nuclear fusion devices as a low pressure hollow cathode discharge

Author:

Nicholas RANSON

Supervisors:

A/Prof. Joseph KHACHAN
Dr. Nicolas CLAIRE

Co-supervisors:

Prof. Iver CAIRNS
Prof. Alexandre ESCARGUEL

A thesis submitted in fulfilment of the requirements
for the degree of Doctor of Philosophy

in the

Department of Plasma Physics and Nuclear Fusion, School of Physics

et dans le laboratoire de

Physique des Interactions Ioniques et Molèculaires, CNRS

June 2023

Declaration of Authorship

I, Nicholas RANSON, declare that this thesis titled, *A study of electrostatic nuclear fusion devices as a low pressure hollow cathode discharge* and the work presented in it are my own. I confirm that:

- This work was done wholly or mainly while in candidature for a research degree at these Universities.

- Where any part of this thesis has previously been submitted for a degree or any other qualification at these Universities or any other institution, this has been clearly stated.

- Where I have consulted the published work of others, this is always clearly attributed.

- Where I have quoted from the work of others, the source is always given. With the exception of such quotations, this thesis is entirely my own work.

- I have acknowledged all main sources of help.

- Where the thesis is based on work done by myself jointly with others, I have made clear exactly what was done by others and what I have contributed myself.

- Sections of Chapter 2 of this thesis are published as:

  "Measurements and modeling of ion divergence from a gridded inertial electrostatic confinement device using laser induced fluorescence" *Physics of Plasmas*, **27**, 103501, (2020), https://doi.org/10.1063/5.0002916

  I analysed the data, performed the computational analysis, and co-wrote the drafts of the manuscript. The experiments were designed and performed by the remaining authors.

- Sections of Chapter 4 are published as:

  "Langmuir probe measurements of the secondary electron population across the cathodic pre-sheath of a DC argon discharge" *Physics of Plasmas*, **30**, 043502 (2023), https://doi.org/10.1063/5.0130291

  I designed and performed experiments, analysed the data, developed the Bayesian analysis routine, wrote drafts of and edited the manuscript, and responded to referee comments.

Signed: _____   Date: _____

_____

As supervisor for the candidature upon which this thesis is based, I, Joe Khachan, can confirm that the authorship attribution statements above are correct.

Signed: _____   Date: _____

"Anything sufficiently weird must be fishy."

Lui Cixin, *The Three Body Problem*

THE UNIVERSITY OF SYDNEY

and

AIX-MARSEILLE UNIVERSITÉ

Abstract

Faculty of Science, School of Physics
CNRS, PIIM

Doctor of Philosophy

A study of electrostatic nuclear fusion devices as a low pressure hollow cathode discharge

by Nicholas RANSON

Discharge operated inertial electrostatic confinement (IEC) is a method of achieving nuclear fusion using a simple discharge system. For many years it has been proposed that a spherically gridded cathode placed at the centre of a low pressure DC discharge will converge ions into a fusion core of high energy and density. The high transparency of the cathode grid allows ions to oscillate within the core so that they are confined there, forming a virtual anode of positive space charge. In recent years, however, evidence has been building that the exact opposite occurs; ions seem to start at a high density and low energy at the cathode centre and subsequently diverge outwards under acceleration by a virtual anode. A high rate of internal ionisation and diverging beams of charged particles are instead reminiscent of the hollow cathode effect. In this thesis we undertake an experimental, computational, and analytical study to prove that discharge IEC devices in fact operate as a hybrid form of abnormal hollow cathode discharge.

A hybrid IEC/hollow cathode consisting of two co-axial rings is analysed using the laser-induced fluorescence (LIF) diagnostic technique. A higher density of diverging ions is observed compared to converging ions. This behaviour was replicated by considering the acceleration of ions from a virtual anode at the cathode centre as determined by a computational model of the cathode sheath. The two-ring discharge is argued to be consistent with a hollow cathode discharge but did not exhibit some aspects of the hollow cathode effect expected to contribute to forming the virtual anode. An LIF analysis of a cylindrical hollow cathode with solid walls in low pressure IEC discharge conditions was undertaken to clarify the link between each discharge type. Although failing to observe ion divergence, the fluorescence signal indicated an increase in ion density approaching the cathode while most pre-sheath theory predicts the opposite. This seemingly anomalous density phenomenon had been previously observed in the literature and

has important consequences for LIF analysis, but no explanation for it has been given. It is proposed that spatially inhomogeneous secondary electron populations present in the cathode pre-sheath could result in the heightened creation of the ArII 3d$'$ ^{2}G$_{9/2}$ metastable ions that are observed by the LIF diagnostic. The thesis then turns to validating this hypothesis as it may have consequences for the analysis of the two-ring experiment.

An attempt is then made to observe the spatial distribution of secondary electron populations across a cathodic pre-sheath using a Langmuir probe analysis. A Bayesian estimation routine is developed to better clarify experimental uncertainties when measuring multiple electron populations with a single probe. Using this method, a drifting Maxwellian electron population is detected that thermalises with distance travelled through the plasma, along with an ion and bulk electron population. The drifting Maxwellian population is argued to arise by secondary electron emission. These discharge parameters are used in turn to solve a collisional rate equation of the ArII 3d$'$ ^{2}G$_{9/2}$ population across a cathodic pre-sheath. It is shown that energetic secondary electron populations can lead to an increasing metastable ion density approaching a cathode while the ground state population behaves as expected. This suggests that the common practice of using the fluorescence signal of metastable ions as a representative of its ground state distribution is not valid in the presence of spatially inhomogeneous electron populations. This effect is argued to be insufficient to discount the dominant discharge mode of the two-ring cathode as being that of a hollow cathode. As a result of these arguments, it is suggested that discharge IEC fusion systems should be reclassified as 'electrostatic' fusion devices where confinement is excluded.

AIX-MARSEILLE UNIVERSITÉ

et

THE UNIVERSITY OF SYDNEY

Résumé en français

CNRS, PIIM

Faculty of Science, School of Physics

pour obtenir le grade de
Docteur de l'Université Aix-Marseille

Une étude des dispositifs de fusion nucléaire électrostatique en tant que décharge à cathode creuse à basse pression

présenté par Nicholas RANSON

Les décharges par confinement inertiel électrostatique (IEC en anglais) sont des réacteurs plasma permettant de réaliser la fusion nucléaire à l'aide d'un système simple. Pendant de nombreuses années ce type de décharge était composée d'une cathode sphérique à grille polarisée en continu, à basse pression, faisant converger les ions en son centre créant ainsi un noyau de fusion à haute énergie et densité. La grande transparence de la grille cathodique permet de confiner les ions qui oscillent à l'intérieur du noyau formant ainsi une anode virtuelle avec une charge d'espace positive. Ces dernières années cependant, des preuves se sont accumulées remettant en cause le fonctionnement des IEC: les ions, créés à haute densité et à faible énergie au centre de la cathode divergent ensuite vers l'extérieur sous l'accélération d'une anode virtuelle. Un taux élevé d'ionisation interne et des faisceaux divergents de particules chargées rappellent plutôt un effet de type cathode creuse. Dans cette thèse, nous entreprenons une étude expérimentale, informatique et analytique pour prouver que les dispositifs IEC fonctionnent en fait comme une forme hybride de décharge anormale à cathode creuse.

Une cathode hybride IEC/creuse composée de deux anneaux coaxiaux est analysée à l'aide du diagnostic de fluorescence induite par laser (LIF en anglais). Une densité plus élevée d'ions divergents est observée par rapport aux ions convergents. Ce comportement a été expliqué en considérant l'accélération des ions d'une anode virtuelle au centre de la cathode telle que déterminée par un modèle de calcul de la gaine cathodique. Cette décharge à deux anneaux est censée être cohérente avec une décharge à cathode creuse mais la formation d'une anode virtuelle ne peut pas être expliquée par un effet de type cathode creuse. Une analyse LIF d'une cathode creuse cylindrique à parois pleines dans des conditions de décharge IEC à basse pression a été

entreprise pour clarifier le lien entre chaque type de décharge. Bien qu'il n'ait pas observé de divergence ionique, le signal de fluorescence a indiqué une augmentation de la densité ionique à l'approche de la cathode alors que la plupart des théories de pré-gaine prédisent le contraire. Ce phénomène de densité apparemment anormal avait déjà été observé dans la littérature et a des conséquences importantes pour l'analyse LIF, mais aucune explication n'avait été donnée. Il est proposé que des électrons secondaires spatialement inhomogènes présents dans la pré-gaine cathodique puissent entraîner localement un accroissement de la création des ions métastables ArII 3d′ ^{2}G$_{9/2}$ qui sont observés par le diagnostic LIF. La thèse se tourne ensuite vers la validation de cette hypothèse pouvant avoir des conséquences pour l'analyse de l'expérience à deux anneaux.

Une tentative est ensuite faite pour observer la distribution spatiale des populations d'électrons secondaires à travers une pré-gaine cathodique en utilisant une analyse par sonde de Langmuir. Un programme d'estimation bayésienne est développée pour mieux clarifier les incertitudes expérimentales lors de la mesure de plusieurs populations d'électrons avec une seule sonde. En utilisant cette méthode, une population d'électrons, représentée par une Mawellienne dérivante, est détectée et se thermalise avec la distance parcourue à travers le plasma, ainsi que les populations d'ions et d'électrons du plasma. La population maxwellienne dérivante est supposée provenir d'une émission secondaire d'électrons. Ces paramètres de décharge sont utilisés à leur tour pour résoudre une équation des taux de collision de la population ArII 3d′ ^{2}G$_{9/2}$ à travers une pré-gaine cathodique. On montre que les populations d'électrons secondaires énergétiques peuvent conduire à une augmentation de la densité d'ions métastables à l'approche d'une cathode alors que la population de l'état fondamental se comporte comme prévu. Cela suggère qu'utiliser le signal de fluorescence des ions métastables comme représentant de l'état fondamental n'est pas valide en présence de populations d'électrons spatialement inhomogènes. Magré tout, cet effet est considéré comme insuffisant pour expliquer le mode de décharge de la cathode à deux anneaux comme étant celui d'une cathode creuse. À la suite de ces arguments, il est suggéré que les systèmes de fusion IEC soient reclassés en tant que dispositifs de fusion électrostatique sans confinement.

Acknowledgements

A PhD project is a daunting prospect from the outset. Without the people I leaned upon to get me through it, I never would have had the courage to start one, let alone the wherewithal to finish one. Trying to list of all of these incredible people that now I inevitably owe big favours to makes me realise how lucky and supported I've been throughout it all.

To Joe Khachan, Richard Bowden-Reid, and Daan Van Schijndel, the last Aussie knights of the spherically gridded table. You have my undying gratitude for your patient support, seemingly endless physics knowledge, and for your merciless use of the open plan office to punish my resistance to procrastination. Joe, your commitment to truth, humility, and integrity makes you the best scientist that I know. I am honoured that you took the time to patiently try to confer your incredible standard despite a packed schedule, let alone to also discuss philosophy, schemes, and all sorts of intrigues acidic to the concept of a deadline. Your generosity has allowed me to appreciate the beauty of learning for its own sake. To Richard, who had to undo my bodgy soldering jobs, show me the real meaning of duct tape, and educate me delicately on the correct pairings of beer and sausages. I should be kissing your overly protective boots in gratitude, but instead I chose to show it by having you shout me coffees and Thai lunches. Never fear, I shall be annoying you three well into the future when I feel nostalgic about these glory days.

A mes amis Marseillais et aux personnes légendaires du PIIM qui ont fait de mon année en France l'une des meillures années de ma vie (grâce à une bone dose de débauche française). A Nicolas Claire et son 'méchante maitress' d'une laser. Tu as fait un gros pari sur un Australien inconnu simplement par ta générosité. Sans toi et Eric Rostang, je serais encore en train d'organiser mon arrivé en France. Merci mille fois pour tes conseils patients et précieux, et merci d'être resté avec moi durant tant d'heures dans ce labo sans fenêtre. A Madhu, Khalil, et Marylise, qui m'ont tous montré que la meilleure façon de découvrir le campus de Saint-Jérôme était d'être en dehors de celui-ci. Vous ne serez jamais débarrassé de moi!

To my physics friends, who taught me one of the most profound insights into physics that still comes up in my work every day; pawn to C3 is a terrible starting move. As inviting as the bleak, windowless halls of the Physics building were at first sight, your warm and constantly distracting presence heightened them to the realm of permanent rose tinted glasses. The difference from when I started my PhD on my own to looking forward to the joy of seeing all of your bright and ridiculous faces every day was astounding to me. If there was one way that I may hope to have repaid my debt to you all, it was in firmly establishing the French tradition of a two hour lunch break.

To my non-physics friends, or 'normal' friends as they like to be called (and obviously including my bridge friends who I'd never be so rude as to call normal). The list of those who deserve

thanks is too long for even my faint sense of humility to be put here. Your ability to avoid asking me about my thesis at all costs and, as a last resort, not listening to me at all when in physics rant mode, helped immeasurably in keeping me sane in my non-physics life. The weight of the world is light with you characters there to lift it.

To my impressive parents, Maria and David, who most incredibly managed to hold their smile without faltering as I asked if I could live with them while I wrote my thesis. It would be embarrassing to find out just how many phone calls I made to you both during these past years. That will continue to be the price of having been so consistently selfless, admirable, and dependable in my life. I've never met anyone else with the strength of courage, character, or of liver to lead such an exquisite life focused on love and food like yours. The same goes for my brother Lawrence, grandparents Anna and Ennio, and my entire family who sunk so many precious hours and groceries into lifting me up. I think there should be a section for the 'life supervisors' of a PhD with your names in large embossed gold.

To Lydia, my wife (that's *still* fun to say), whose patient understanding in the face of my insistent irrational fears was given so selflessly that I'll forgive the fact you have no idea what my thesis is about. A healthy perspective on my work has been forced by its comparison to the sheer obviousness of your value. I will never forget all of the times that you comforted me and distracted me without blinking when you were having a difficult time yourself. A PhD can be a self-centered pursuit, but you never made me feel that way. Instead, you make me feel strongly enough to run home to you every day like I do, and like I will always do, just to check that you're real.

Thank you all.

Contents

Symbols & constants, *in order of appearance.*

Symbol	Meaning	Unit
$\tilde{\boldsymbol{F}}$	force	N
$\tilde{\boldsymbol{E}}$	electric field	V·m^{-1}
$\tilde{\boldsymbol{B}}$	magnetic Field	T
q_{e}	fundamental charge	C
λ_{D}	Debye length	m
ϵ_0	Vacuum permittivity	F·m^{-1}
k_{B}	Boltzmann's constant	J·K^{-1}
T_{k}	population k temp	K *or* eV
n_{k}	pop. k number density	m^{-3}
L	characteristic size of plasma	m
p	background gas pressure	Torr
m_k	pop. k mass	kg
b	binary collision impact parameter	m
σ_k	interaction k cross section	m^2
r_k	int. k reaction rate	m$^{-3} \cdot$ s^{-1}
f_k	pop. k distribution function	m$^{-6} \cdot$ s^3
$f_{k,v}$	pop. k velocity dist. func.	m$^{-3} \cdot$ s^3
K_k	int. k rate coefficient	m$^3 \cdot$ s^{-1}
λ_k	int. k mean free path	m
ν_k	int. k collision frequency	s^{-1}
$\tilde{\boldsymbol{\Gamma}}_k$	flux of pop. k	m$^{-2} \cdot$ s^{-1}
μ_k	pop. k mobility	m$^2 \cdot$ V$^{-1} \cdot$ s^{-1}
D_k	pop. k diffusion coefficient	m·s^{-2}
$\bar{\epsilon}_k$	pop. k mean energy	J *or* eV
γ_{e}	2$^{\mathrm{ndry}}$ e^- emission coef.	
$\gamma_{\mathrm{e,i}}$	γ_{e} by ion bombardment	
α_{T}	Townsend 1$^{\mathrm{st}}$ ionisation coef.	m^{-1}
$d_{\mathrm{c}}, r_{\mathrm{c}}$	cathode sheath radius/width	m

Symbol	Meaning	Unit
V_c, U_{c}	cat. bias	V
j	discharge current density	A·m^{-2}
i_{k}	pop. k current	A
$\phi(x)$	electric pot. distribution	V
D/Dt	convective derivative	
μ_0	magnetic permeability	V·s $\cdot$ (A $\cdot$ m)$^{-1}$
$\tilde{\boldsymbol{v}}_k$	pop. k velocity	m·s^{-1}
$\tilde{\boldsymbol{u}}_k$	pop k macroscopic avg. vel.	m·s^{-1}
$\phi_{\mathrm{p}}, V_{\mathrm{p}}$	plasma potential	V
$d_{\mathrm{hc}}, r_{\mathrm{hc}}$	hollow cat. width/radius	m
Q	nuclear fusion Q factor	
c	speed of light in vacuum	m·s^{-1}
K_k	pop. k kinetic energy	J or eV
M_k	pop. k reduced mass	kg
n_f	den. of confined fusion particles	m^{-3}
τ_{E}	avg. energy conf. time	s
E_{y}	fusion energy yield	J or keV
r_{f}	fusion core radius	m
η	anode grid transparency	
$\zeta_{\mathrm{e}}, \zeta_{\mathrm{i}}$	N$^{\mathrm{o}}$ e^- or ion re-circulations	
γ_{l}	Lorentz Factor	
V_{a}	anode bias	V
g_k	statistical weight of state k	
ν_0	target transition freq. in vacuum	Hz
h	Planck's constant	J·s
ν_{l}	laser freq.	Hz
$I_{\mathrm{l}}(\nu_{\mathrm{l}})$	laser photon intensity	W·m^{-2}
$\tilde{\boldsymbol{k}}_{\mathrm{l}}$	laser beam wave vector	m^{-1}
γ_0	spontaneous decay rate	s^{-1}
W	induced rate of absorption	s^{-1}
P	laser power	W
I_{f}	fluorescence photon intensity	W·m^{-2}
$f_{m,v}, f_{g,v}$	metastable or ground state VDF	m$^{-3} \cdot$ s^3
$r_{m/g}$	$f_{m,v}/f_{g,v}$	
σ_{met}	ArI$\rightarrow$ArII met. by e^- impact	m^2
σ_{ion}	ionisation of ArI by e^- impact	m^2
u_0	ion sound speed	m·s^{-1}

Symbol	Meaning	Unit
x_0	loc. of sheath/pre-sheath boundary	m *or* mm
l	characteristic length of pre-sheath	m *or* mm
V_f	floating potential	V
SN	signal to noise ratio	
$l_\mathrm{p}, r_\mathrm{p}$	Langmuir probe length or radius	m
r_s	LP sheath radius	m
V_B	LP bias relative to V_p	V
$u_\mathrm{e,D}, u_\mathrm{e,D_{eV}}$	e^- drift velocity	m·s^{-1} *or* eV
u_th	thermal velocity	m·s^{-1}
E_tot	total avg. energy per particle	J *or* eV
subscript G	refers to ArII 3d$'$ ^{2}G$_{9/2}$ state	
ϵ_0	cross section threshold energy	eV
ϵ_pk	cross sec. peak energy	eV
Δx	Domain step size	m
$\varepsilon_\mathrm{r,tot}$	2$^\mathrm{ndry}$ e^- reduced E_tot	eV
ε_r	rate eqn. energy multiplier	
$T_\mathrm{r,e,s}, n_\mathrm{r,e,s}$	reduced 2$^\mathrm{ndry}$ e^- Temp./den.	eV *or* m^{-3}
subscript Cl	values taken from Fig. 5.4	

Chapter 1

Introduction

The study of the hollow cathode discharge has been a long and ongoing process invaluable to both plasma research and industry. Discovered in 1916 by Paschen [1], this minor geometric change from a classical glow discharge results in an increased energy efficiency, particle transport mechanisms, and spectroscopic output for otherwise identical discharge conditions. These advantages have led to the extensive use of the hollow cathode in fields ranging from spectral emission and absorption spectroscopy [2] to thin film deposition [3]. Historically, the majority of hollow cathode research was carried out at gas pressures greater than $100\,\mathrm{mTorr}$ ($10^{-4}\,\mathrm{Atm}$), with extremely few experiments conducted under $10\,\mathrm{mTorr}$ [4]. Studies below this pressure have usually been incidental within areas that use a hollow cathode as either a means to an end, as in satellite thruster physics [5, 6], or even where the discharge type may have been misclassified, as in electrostatic nuclear fusion devices [7]. There remains ample opportunity for fundamental physical discoveries in low pressure hollow cathode research that could be of benefit to a diverse range of applications. In particular, we aim to clarify disagreements about ion transport mechanisms in electrostatic fusion devices by linking them to the hollow cathode effect.

The work presented below is experimental, analytical, and computational to reclassify a type of electrostatic nuclear fusion device as a form of hollow cathode discharge. The pursuit of this goal required some development of the Langmuir probe and laser-induced fluorescence (LIF) diagnostic techniques to ensure the validity of our conclusion. In doing so, we hope to solidify the understanding of the fundamental plasma diagnostics used in the experimental analysis.

Inertial electrostatic confinement (IEC) nuclear fusion devices were conceptualised [8, 9] as a method of heating and confining a plasma of fusion fuel like deuterium using a spherically symmetric potential well. The aim of creating this well was to converge highly accelerated ions into a high density 'fusion core' at its centre where they have an increased chance of fusing. Different techniques have been suggested to create the potential well while avoiding the use of

absorbing boundaries that remove ions from the system. In this way, the accelerated ions are free to oscillate balistically about the fusion core such that their effective confinement time is increased by the number of their recirculations through it. For many years it has been proposed that this can be achieved using a highly transparent spherical cathode grid in the centre of a low pressure discharge [7]. The gridded cathode is supposed to contribute to the ionisation of the background gas while allowing for the convergence of ions into IEC about its centre. We shall build on existing evidence to argue that these discharge operated IEC devices do not exhibit ion convergence nor confinement in reality. Instead, ions are seen to diverge outward from a region of positive space charge at the cathode centre reminiscent of the hollow cathode effect. In order to approach these conflicting arguments, it will first be necessary to distinguish the subtle yet important differences between the generic concept of a plasma and a real discharge system that may have resulted in this misunderstanding. The change in operation away from the convergent IEC model may then allow for orders of magnitude improvement in the overall fusion efficiency, thus improving the concept's viability as a safe, portable, and inexpensive neutron generator [10].

The attempt to disprove the discharge IEC mechanism using the (LIF) diagnostic method encountered an apparently anomalous plasma pre-sheath phenomena likely attributable to metastable ions in the discharge. The cause of this phenomena represented a possible flaw in our LIF analysis of discharge IEC devices and in previous uses of the LIF diagnostic in the literature. Resolving this issue required a Langmuir probe analysis of the entire cathodic pre-sheath to determine the spatial distribution of energetic electron populations that were suspected to be influencing this anomalous metastable ion phenomenon. This allowed for a collisional rate analysis that indicated a flaw in a common inference made to relate metastable and ground state ion populations when using the LIF diagnostic. The principal aim for this work was to change the view of discharge IEC devices as instead being a form of hollow cathode discharge operating in the abnormal glow regime. It is hoped, however, that the additional contribution to the understanding of Langmuir probe and LIF analyses may clarify future research of the low pressure DC glow discharge in general.

The treatment of electrostatic fusion devices as hollow cathode discharges requires the unified use of the somewhat disparate fields of discharge physics and its relevant modelling, nuclear fusion, IEC systems, low temperature plasma diagnostics, and collisional-rate analysis. As a result, there is a review of the literature for each topic prior to the analysis relevant to it. In this chapter, we review the state of the literature for the first three of these major topics, after which a detailed summary of the aims in this thesis will be given.

1.1 Glow discharge physics

1.1.1 The difference between a plasma and a glow discharge

An excellent general introduction to plasmas and their uses has been given by Chen [11] while a more experimentally focused treatise on discharges has been given by Raizer [12]. A comprehensive summary of particle collisions as they relate to plasma diagnostics has also been given by McDaniel [13].

Plasmas are colloquially defined as the fourth state of matter, achieved by increasing the mean energy of a gas so that many of its constituent particles become ionised. More specifically, a plasma is a self-interacting, quasi-neutral state of matter comprising electron and ions populations that exhibit collective behaviour with each other alongside possible neutral gas atoms [11]. Plasmas can be characterised by the density and mean energy (or temperature in most cases) of the electrons and positive ions as well as the electromagnetic fields they exist within, manifest, and respond to [12]. Plasmas have been observed in a vast variety both experimentally and in nature [14], ranging from the cold and incredibly sparse plasmas found to form the majority of interstellar media to the extremely dense and energetic plasmas found in fusion reactors, stellar cores, and lasers. An incomplete list of the more common types of plasmas and how they can be classified by the plasma density and temperature is given in Figure 1.1.

The physics of a plasma is a vast interplay of various particle species coupled through complex collisional and field forces. Each charged particle of type k within a plasma creates its own electromagnetic fields whilst simultaneously interacting with the electric and magnetic fields $\tilde{\boldsymbol{E}}$ and $\tilde{\boldsymbol{B}}$ due to other charges and external sources. A charged particle with velocity $\tilde{\boldsymbol{v}}_k$ travelling through electromagnetic fields will experience a Lorentz force [15]

$$\tilde{\boldsymbol{F}}_{\mathrm{L}} = q_k \left(\tilde{\boldsymbol{E}} + \tilde{\boldsymbol{v}}_k \times \tilde{\boldsymbol{B}} \right), \tag{1.1}$$

where $q_k = Z q_{\mathrm{e}}$ is the integer multiple Z of the elementary charge q_{e} of the particle. The level of coupling between populations is therefore dependent on the charge and motion of each particle, and is further complicated by collisional interaction with neutrals and boundaries near to it.

If disturbances that affect the charge distribution are introduced to the plasma slowly relative to the inverse of the plasma frequency ω_{p}, the plasma will develop a space charge that serves to shield itself from the disturbance [15]. The disturbance is generally screened over a characteristic distance that can be parameterised in most discharges by the electron Debye length λ_{D} [16]

$$\lambda_{\mathrm{D}} \approx \sqrt{\frac{\epsilon_0 k_{\mathrm{B}} T_{\mathrm{e}}}{n_{\mathrm{e}} q_{\mathrm{e}}^2}}, \tag{1.2}$$
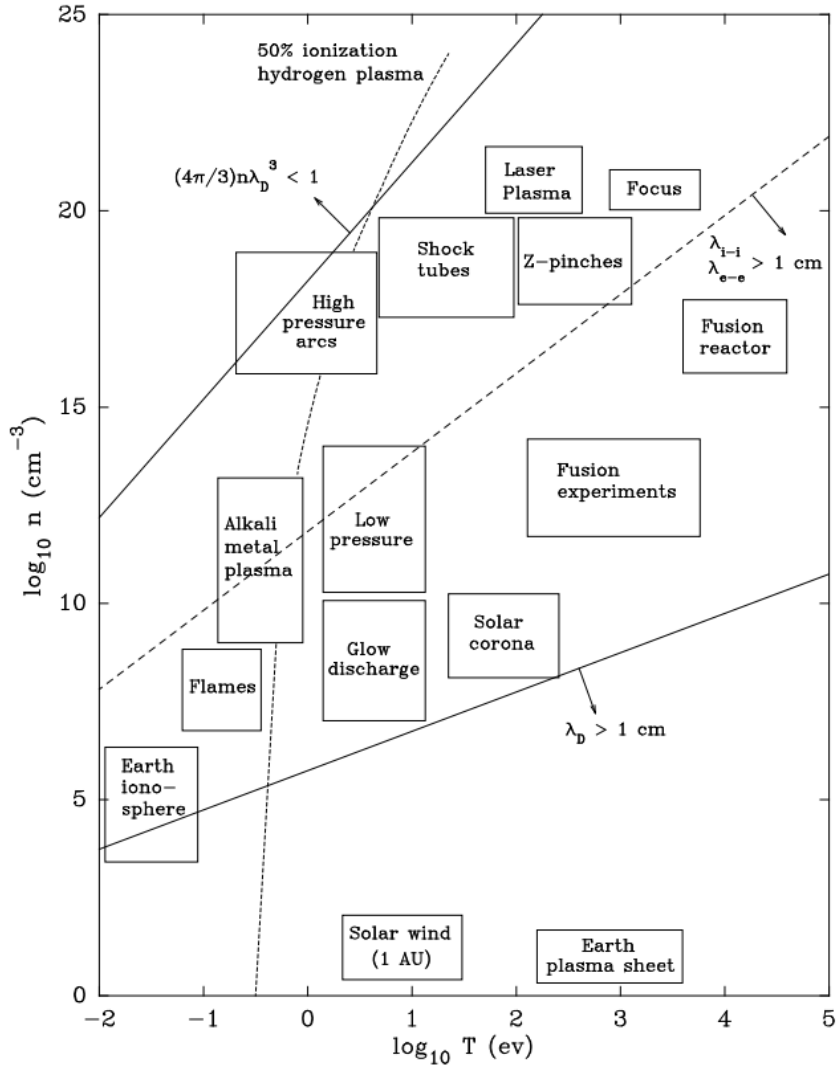
FIGURE 1.1 – The many categories of plasma observed in nature, displaying many orders of mangitude of variation in densities and temperatures. Different types of plasmas are often distinguished by the density n and temperature T of the most populous charged species within them. Taken from the NRL plasma formulary [14].

where ϵ_0 is the permittivity of free space, k_{B} is Boltzmann's constant, and T_{e} and n_{e} are the temperature and density of the predominant electron population. The quasi-neutrality criterion requires that the total density of oppositely signed charges is approximately equal over a distance larger than λ_{D}, meaning that the characteristic size of the plasma L must follow $L \gg \lambda_{\mathrm{D}}$. Under these conditions, the plasma forms a coherent, self-interacting whole that re-arranges to each given set of external conditions. Plasmas are therefore extremely responsive to the shape of applied fields, containment vessels, and all sorts of particular experimental conditions [17]. This severely complicates the researchers ability to simplify physical models or make comparisons between different experimental systems. The choice of simplifying assumptions that can be used to reduce the complexity of plasma modelling is a continuing source of disagreement

and confusion in the literature (for some examples, see the reviews by Little and Von Engel [18], Riemann [19], Phelps [20], and Bogearts *et al.* [21]). Any experimental or analytical simplification used to reduce this complexity must therefore present reasoning supported by validated precedence from the literature. For these reasons, the experiments presented in this thesis were designed to isolate the mechanics of particular physical principles such as the hollow cathode effect. As such, we shall analyse DC (hence steady state), weakly ionised, unmagnetised plasmas in non-thermal equilibrium in the particular form of a glow discharge. We further restrict the analysis to discharges in argon to avoid dealing with the complicated additional excited states and interaction mechanisms that must be considered in the presence of molecular species.

More than 99 % of regular matter in our universe exists in a plasma state, and yet natural, sustained plasmas are rare on Earth [14]. Plasmas are therefore usually studied using discharge chambers, which require few operating parts without inhibitive expense. Here, ionisation of a pure background gas admixture is sustained within an evacuated chamber using a possible combination of electrically biased boundaries (electrodes), magnetic fields, electromagnetic waves, or through charge sources like electron emitting (thermionic) filaments [12]. Much of the electromagnetic power input into the system manifests as a current of charges through the background gas, which is converted through collisions into heat, electromagnetic radiation that is characteristic of the gas, and the sputtering of surfaces within the discharge. For this reason, discharges have found many industrial applications beyond the study of plasmas that began in the mid to late nineteenth century [22], including as light sources and lasers [23], for chemical deposition [24], in material processing [25] and ion implantation [26], in the generation of ozone using dielectric barriers [27], in medicine [28, 29], and many more active areas of research [21]. A regular discharge chamber will usually contain a region of weakly ionised, non-thermal equilibrium plasma. Despite this, discharge dynamics can differ from plasma dynamics in significant ways that have not always been well accounted for, particularly in the case of discharge IEC devices. A discharge in its steady state need not be quasi-neutral and is most commonly partially ionised with ionisation fractions of much less than 1 % [17]. Discharges can instead be largely characterised by the net current that flows between the cathode and the anode, the electrode bias, and the background gas pressure. We must therefore review collisional interactions between charges and the neutral background gas before charged particle transport phenomena can be approached.

1.1.2 Charge-neutral collisional interactions

Let us first consider an energetic electron in a discharge travelling with velocity $\tilde{\boldsymbol{v}}_{\mathrm{e}}$ along x through the background gas of pressure p. Electron-neutral elastic collisions are an illustrative example from which to view more complex collisional processes. The low mass of the electron

m_e relative to that of the target background gas neutral m_t significantly increases its speed for an equivalent kinetic energy. The background gas can therefore be accurately modelled as a volume of uniform, stationary targets. Consider a slab of neutral targets of thickness Δx which the electron is incident upon that contains N gas atoms, as illustrated in Figure 1.2. It is important that this volume contains few enough target gas atoms to avoid 'shadowing', such that the cross-sectional area of targets do not overlap when viewed from the path of the electron, but also enough particles that the statistical nature of population interactions is captured [30]. If
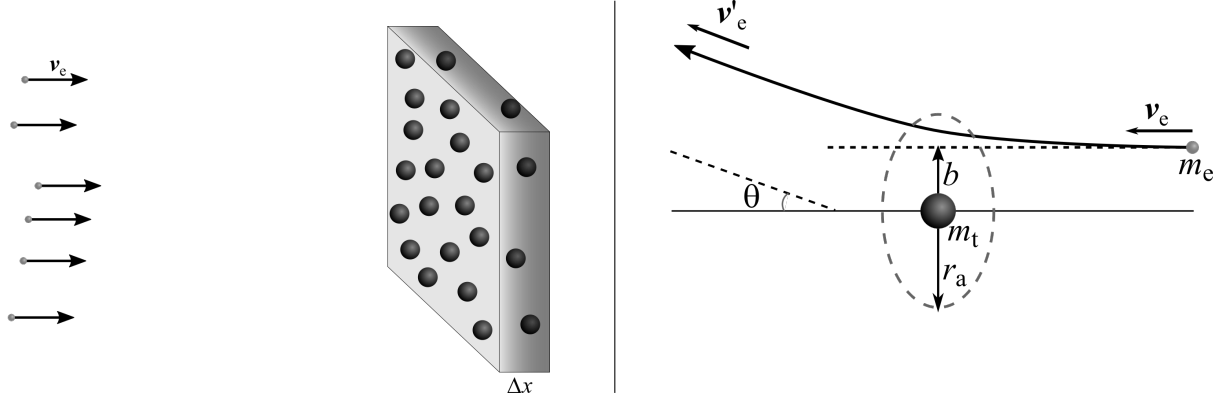
FIGURE 1.2 – *Left:* A flux of particles with velocity $\tilde{v}_e$ incident on stationary targets withing a volume of thickness Δx. *Right:* An electron with impact parameter b being deflected by an angle θ from a target atom with cross-sectional area σ.

the electron passes within a defined radius r_a of a target atom, it will experience forces through complex quantum interactions that are difficult to ascertain[1]. Experimentally, the electron will only be defined as having interacted if it experiences a measurable deflection θ that depends on the impact parameter b and relative momentum of the interaction, as depicted in Figure 1.2. In this way, we can view the atom as having a definite cross-sectional area $\sigma(v_e)$ analogous to the cross-section of a billiard ball. Each annulus representing a surface element of impact parameter db will eventually receive similar numbers of incident electrons, such that the total area of all annuli that represent a collision will be dependent on the *speed* v_e of the interaction. With these simplifications, we can extend the analysis from that of a single electron (or any incident particle) into a flux of electrons $\tilde{\Gamma}_e = n_e \tilde{v}_e$ travelling within a small velocity interval $d\tilde{v}_e$ of $\tilde{v}_e$ incident on the slab. The experimentalist can then abstract this cross-section concept for any collision type, elastic or inelastic, by considering the area in which all detectable interactions take place [30];

$$\sigma(v_e) \ [\text{m}^2] = \frac{\text{№ reactions per target nucleus per unit time}}{\text{№ incident particles per unit area per unit time}}. \tag{1.3}$$

Using this definition, the non-linear dependence of the cross-section on the incident particle velocity can be experimentally determined without exact knowledge of the true nature of the interaction. Experimental results for interaction cross-sections have been painstakingly collated

---

[1]For an in-depth treatment of collision interactions at the quantum level, see *Scattering Theory* by Taylor [31].

over centuries into vast repositories such as the archives of the National Institute of Standards and Technology [32]. And still, the available interaction data are not exhaustive nor definitive. It is common that reports of the cross-section for the same interaction will lie well outside of their respective uncertainty values (see [33, 34] as an example). Theoretically determined cross-sections are frequently used where experimental results are lacking [31], but these are dependent on assumptions of the form of the interaction potential that is extremely difficult to observe in practice.

The number of interactions of type k that occur at a given speed v_e per unit volume and time at a location $\tilde{\boldsymbol{x}}$ is then defined by the reaction rate [30]

$$r_k\left(\tilde{\boldsymbol{x}}, v_\mathrm{e}\right) = \sigma\left(v_\mathrm{e}\right) v_\mathrm{e} n_\mathrm{e}\left(\tilde{\boldsymbol{x}}\right) n_\mathrm{t}, \tag{1.4}$$

where $n_\mathrm{e}\left(\tilde{\boldsymbol{x}}\right)$ is the number density of electrons at location $\tilde{\boldsymbol{x}}$ that we have defined as having a uniform flux Γ_e and n_t is the uniform number density of targets. In reality, the beam of electrons we have considered will represent a single phase space element $\mathrm{d}\tilde{\boldsymbol{x}}\mathrm{d}\tilde{\boldsymbol{v}}_\mathrm{e}$ of the entire distribution function $f_\mathrm{e}\left(\tilde{\boldsymbol{x}}, \tilde{\boldsymbol{v}}_\mathrm{e}\right)$ at $\tilde{\boldsymbol{x}}$, where $\int f \mathrm{d}\tilde{\boldsymbol{v}} = n\left(\tilde{\boldsymbol{x}}\right)$. We can find the total reaction rate at $\tilde{\boldsymbol{x}}$ by integrating over all possible velocities of the interaction weighted by the distribution function of electron velocities [30]

$$r_k\left(\tilde{\boldsymbol{x}}\right) = n_\mathrm{t} \int_{-\infty}^{\infty} |\tilde{\boldsymbol{v}}_\mathrm{e}|\, \sigma\left(|\tilde{\boldsymbol{v}}_\mathrm{e}|\right) f_\mathrm{e}\left(\tilde{\boldsymbol{v}}_\mathrm{e}\right) \mathrm{d}\tilde{\boldsymbol{v}}_\mathrm{e} = n_\mathrm{t} n_\mathrm{e}\left(\tilde{\boldsymbol{x}}\right) \langle \sigma \cdot v \rangle = n_\mathrm{t} n_\mathrm{e} K_k, \tag{1.5}$$

where K_k [m$^3\cdot$s^{-1}] is the rate coefficient for process k and $\langle \chi \rangle = \frac{1}{n} \int \chi f_\alpha \mathrm{d}\tilde{\boldsymbol{v}}$ denotes the mean value of a parameter χ for a particle system with total distribution function f_α. This can be extended to the case in which two concurrently moving populations with distribution functions $f_1\left(\tilde{\boldsymbol{v}}_1\right)$ and $f_2\left(\tilde{\boldsymbol{v}}_2\right)$ at $\tilde{\boldsymbol{x}}$ collide to [35]

$$r_k\left(\tilde{\boldsymbol{x}}\right) = \int_{-\infty}^{\infty} \int_{-\infty}^{\infty} |\tilde{\boldsymbol{g}}|\, \sigma\left(|\tilde{\boldsymbol{g}}|\right) f_1\left(\tilde{\boldsymbol{v}}_1\right) f_2\left(\tilde{\boldsymbol{v}}_2\right) \mathrm{d}\tilde{\boldsymbol{v}}_1 \mathrm{d}\tilde{\boldsymbol{v}}_2, \tag{1.6}$$

where $\tilde{\boldsymbol{g}} = \tilde{\boldsymbol{v}}_2 - \tilde{\boldsymbol{v}}_1$ is the relative velocity of the interaction. It is common to define a population α by its velocity distribution function $f_{\alpha,\mathrm{v}}\left(\tilde{\boldsymbol{v}}\right)$, where $\int f_\mathrm{v} dv = 1$ and $f_\alpha\left(\tilde{\boldsymbol{x}}, \tilde{\boldsymbol{v}}\right) = n_\alpha\left(\tilde{\boldsymbol{x}}\right) f_{\alpha,\mathrm{v}}\left(\tilde{\boldsymbol{v}}\right)$, at a location $\tilde{\boldsymbol{x}}$ since many types of analyses are more dependent on the particle distribution than their absolute density. The most common example of a particle velocity distribution function is the Maxwellian distribution

$$f_\mathrm{v}\left(\tilde{\boldsymbol{v}}_x, \tilde{\boldsymbol{v}}_y, \tilde{\boldsymbol{v}}_z\right) = \left(\frac{m}{2\pi k_\mathrm{B} T}\right)^{3/2} \exp\left[-\frac{m}{2k_\mathrm{B} T}\left(\tilde{\boldsymbol{v}}_x^2 + \tilde{\boldsymbol{v}}_y^2 + \tilde{\boldsymbol{v}}_z^2\right)\right] \tag{1.7}$$

that describes a population that has collisionally thermalised into the maximum entropy distribution for a given temperature. The projectile-target calculation (Equation 1.5) is used where

possible since the relative velocity calculation (Equation 1.6) is a computationally expensive six-dimensional integral in many laboratory cases. Most discharges are weakly ionised and contain electron species of much higher mean energies than that of the ion or neutral populations so that Equation 1.5 is an accurate approximation.

Many useful parameters which characterise a discharge in homogeneous regions can be defined once the reaction rate has been calculated. The mean free path λ_k for an interaction of type k is the characteristic distance a projectile particle will travel before interacting through that mechanism [36],

$$\lambda_k = \frac{\langle v \rangle}{n_t \langle \sigma v \rangle}. \tag{1.8}$$

Projectiles travelling in a beam with initial density n_0 through a background of targets that have not undergone the interaction of type k will decay as

$$n\left(\tilde{\boldsymbol{x}}\right) = n_0 \exp\left[-\frac{x}{\lambda_k}\right]. \tag{1.9}$$

The average number of collisions experienced by a particle per unit time in homogeneous discharge regions is expressed as the collision frequency [36],

$$\nu_k = n_t \langle \sigma v \rangle = \frac{\langle v \rangle}{\lambda_k}. \tag{1.10}$$

These descriptive parameters are useful in approaching bulk statistical collisional processes of drift and diffusion that govern the current flow in a discharge.

1.1.3   Mobility and diffusion

Discharges require externally applied electromagnetic fields of sufficient magnitude to be able to accelerate charged particles to energies capable of ionisation. Ionisation interactions are necessary to make up for the loss of charge particles to boundaries and by recombination so that a current can be sustained in the steady state. A balance must therefore be struck between charged particles being able to gain energy from these fields and in expending this energy in collisions with the background gas. Understanding the nature of this balance is particularly crucial for discharge IEC devices which attempt to source ions by ionisation of the background gas but also aim to accelerate those ions to fusion relevant energies.

Elastic collisions between charged particles and the background gas dissipate the momentum gained in the form of joule heating which occurs at a rate proportional to the electric field strength [17]. This limits the rate of inelastic collisions by restricting the majority of charged particles below the 10 eV threshold energy of ionisation and excitation of monatomic gases. In a

uniform electric field $\tilde{\boldsymbol{E}}$, a group of particles with charge q will pick up an average drift velocity $\tilde{\boldsymbol{v}}_\mathrm{d}$ that is dependent on the collision frequency of elastic momentum transfer collisions ν_mt [17],

$$\tilde{\boldsymbol{v}}_\mathrm{d} = \frac{q}{m\nu_\mathrm{mt}}\tilde{\boldsymbol{E}} = \mu\left(\nu_\mathrm{mt}\right)\tilde{\boldsymbol{E}}. \tag{1.11}$$

The coefficient of proportionality μ between the drift velocity and the applied field is the *mobility* of the species. The mobility is an important parameter that characterises the resistance a particle faces when travelling through a medium.

Equation 1.11 is non-linear since the collision frequency ν_mt is itself dependent on the electric field strength. The significant analytical simplification offered by assuming that μ is constant for each species has been the norm in discharge modeling. The value of μ for a given gas can then be more easily determined by experiment or Monte-Carlo numerical methods if the momentum transfer cross section is already known. It has been shown that this assumption does not always affect the qualitative validity of numerical models [37, 38], particularly in low field or homogeneous systems. Furthermore, this assumption allows for the use of similarity laws [39], discussed below in Section 1.1.5, in which experimental parameters are given together as a *ratio* for ease of comparison. In many cases, however, theories based on assuming a constant mobility can not be rectified with experiment, for example in determining the Townsend ionisation coefficient [40] (also discussed in Section 1.1.5). Particle mobilities parallel and transverse to the electric field have also been shown to diverge from each other in regions of strongly inhomogeneous $\tilde{\boldsymbol{E}}$ fields [41, 42].

Absorbing boundaries introduced into a plasma create local spatial inhomogeneity in population densities as charged particles are removed in bulk from the system. Particles will then tend to be driven from regions of high density to regions of low density in a random walk collisional process known as *diffusion*. The total flux $\tilde{\boldsymbol{\Gamma}}_k$ of particles of type k in an external field $\tilde{\boldsymbol{E}}$ will be the sum of the drift and diffusion components [43]

$$\tilde{\boldsymbol{\Gamma}}_k = n_k\tilde{\boldsymbol{v}}_k = \frac{n_k q_k}{m_k \nu_\mathrm{mt}}\tilde{\boldsymbol{E}} - \left\langle\frac{v_k^2}{3\nu_\mathrm{mt}}\right\rangle\nabla n_k = n_k\mu_k\tilde{\boldsymbol{E}} - D_k\nabla n_k, \tag{1.12}$$

where D_k is the diffusion coefficient. The diffusion coefficient is therefore a measure of the transparency of a medium to particles that are diffusing within it. If we assume that ν_mt is independent of $\tilde{\boldsymbol{E}}$, then [43]

$$\frac{D_k}{\mu_k} = \frac{2}{3}\frac{\bar{\epsilon}_k}{q_k} = \frac{k_\mathrm{B}T_k}{q_k}, \tag{1.13}$$

where $\bar{\epsilon}_k$ is the mean energy of the population and the rightmost equality is the Einstein relation. Einstein's relation is applicable when the species k is in a Maxwellian distribution (Equation 1.7). From these, analytical expressions for the spatial and temporal density evolution within simple discharge geometries can be found. Phelps [44] has given a useful guide for when charged

particle losses to the wall of common discharge tube geometries will be dominated by diffusion (collisional) or free-fall (collisionless) processes, reproduced in Figure 1.3.
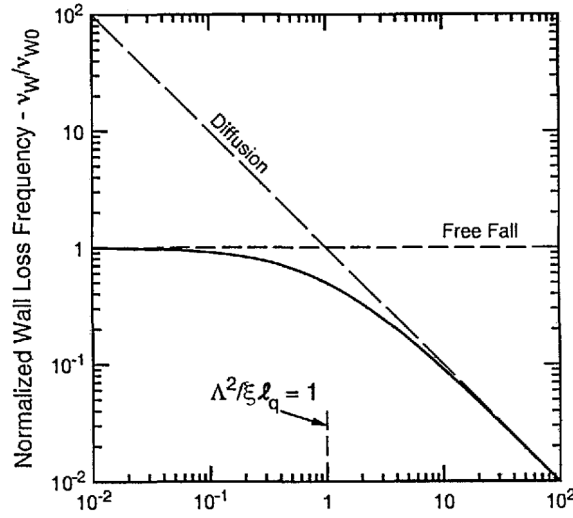

FIGURE 1.3 – The criterion for when the normalised frequency of charge particles losses to the walls ν_W in a cylindrical discharge will be dominated by diffusion (collisional) or free-fall (collisionless) processes, taken from Phelps [44]. The x-axis characterises the collisionality of the discharge relative to the size of the discharge tube.

Both the mobility and diffusion coefficients are inversely dependent on the mass of the particle in question. Since the mass ratio of an electron to the lightest possible ion, a proton, is $m_e/m_p \approx 1/1800$, electrons will drift and diffuse more rapidly than ionic populations. This works in conjunction with the fact that electron populations usually have higher mean energies than ion populations in non-thermal equilibrium discharges [36] and therefore carry the majority of the discharge current. In this way, electrons are responsible for most notable discharge processes, including ionisation and excitation of the background gas (and therefore radiative emission) [13], joule heating [17], Bremsstrahlung radiative losses [45], and many of the plasma instabilities in discharge systems [46].

The mobility of electrons in various gases has historically been measured in swarm experiments [47, 48], microwave experiments, [49], and in time-of-flight ionisation experiments [50]. These experiments are all based on determining the drift velocity of a known current of electrons through a homogeneous background gas and minimising diffusion parallel to the drift. Diffusion coefficients are more difficult to isolate from other discharge processes, and are frequently 'determined' from the mobility using Einstein's relation in which ν_{mt} is assumed constant. Methods of measuring D_e directly using electron showers in low field discharges [51, 52] show reasonable agreement with theory despite the requirement that the electron drift velocity be determined and subtracted from the mean energy of the distribution. Ion mobilities have largely been captured with reasonable agreement to predictions from theory for low field values [53], particularly for

noble element and nitrogen ions in their parent gases [34, 54–56]. Diffusion coefficients measured in high field regions where Equation 1.13 is invalid remain rare [57] to non-existent. In these cases, one must rely on the Einstein relation despite the unknown level of inaccuracy caused by its use.

1.1.4 Ambipolar processes

The difference in mobilities between ions and electrons means that electrons created within a discharge are lost from the system much more quickly. In the steady sate, the separation of charge will grow until the positive space charge restricts electron flow and increases ion flow to the point that their fluxes out of the region are equal [36, 43]. The collective motion of charges of opposite sign in response to a space charge is denoted as 'ambipolar'. The ambipolar flow of ions and electrons from a centre of positive space charge at the cathode centre (otherwise known as a virtual anode) will be shown to be a viable candidate to explain ion divergence from both low pressure IEC and hollow cathode discharge systems.

Ambipolar motion can be a diffusion dominated process if in the absence of strongly inhomogeneous external electric fields or a drift dominated process otherwise [43, 58]. Ambipolar processes generally cause plasma to flow from regions of high density and low electric field towards regions of low density and high field. Ambipolar diffusion to absorbing boundaries is responsible for the 'plasma potential', a positive space potential relative to the anode bias that is observed multiple Debye lengths from boundaries in the vast majority of discharges. The opposite is usually only observed in extremely low pressure systems that feature significant contribution from electron sources in magnetically contained plasmas [59, 60] or if negative ions exist in very high densities [61].

Ambipolar diffusion occurs instead of ambipolar drift when the separation of charge is small, such that $|n_i - n_e| \ll n_e \approx n_i$ [43]. An illustration of the ambipolar diffusion process is given in Figure 1.4. The rate of ambipolar diffusion along a direction x from a region without sources of charge or strong external fields can be quantified by setting the ion and electron flux to be equal [43]:

$$\tilde{\mathbf{\Gamma}}_i \approx \tilde{\mathbf{\Gamma}}_e = \mu_e \tilde{\mathbf{E}}_x n_e - D_e \frac{\delta n_e}{\delta x} = \mu_i \tilde{\mathbf{E}}_x n_i - D_i \frac{\delta n_i}{\delta x}$$

$$\Rightarrow \tilde{\mathbf{\Gamma}}_x = -\frac{D_i \mu_e + D_e \mu_i}{\mu_e + \mu_i} \frac{\delta n}{\delta x} = -D_a \frac{\delta n}{\delta x}, \tag{1.14}$$

where n is the number density of either species in the quasi-neutral region, and D_a is the *ambipolar diffusion coefficient*. Inspection of Equation 1.14 shows that $D_i < D_a < D_e$, such that ion diffusion is significantly enhanced by the ambipolar process. The necessary criteria
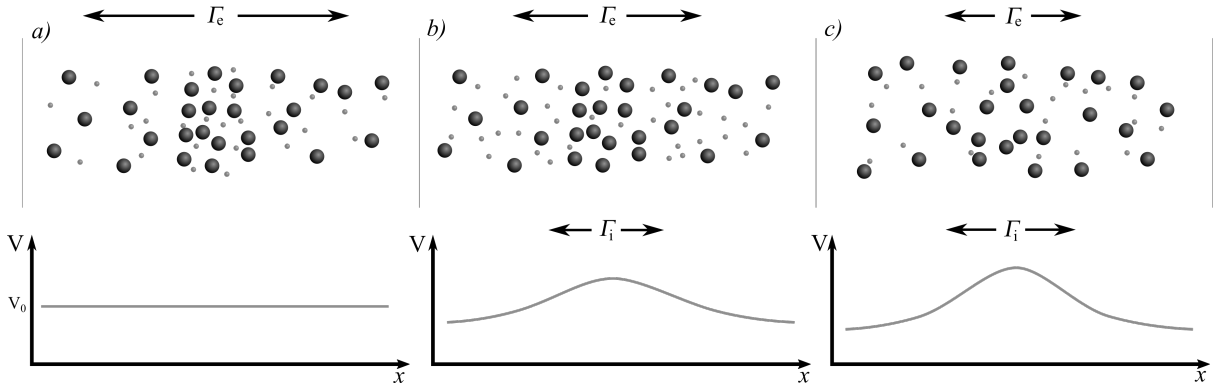
FIGURE 1.4 – The ambipolar diffusion process in an illustrative quasi-neutral but inhomogeneous system of ions and electrons (background gas not shown). *a)*: The electrons begin to diffuse with flux $\tilde{\mathbf{\Gamma}}_e$ at a rapid pace relative to the ions, leaving them in place. Before movement, the smoothed potential distribution in space is zero. *b)* The electron diffusion to regions of low density creates a positive space charge, which begins to accelerate the ions and decelerate the electrons. *c)* The ion and electron fluxes out of the dense region equalise.

$|n_i - n_e| \ll n$ will only occur if the characteristic length of the density gradient L (usually corresponding to the characteristic length of the plasma region) follows $L \gg \lambda_D$ [44]. Otherwise, the resulting polarisation field will be too large to validate the assumption of quasi-neutrality. The total electric field is then the sum of externally applied fields and the ambipolar polarisation fields that develop via diffusion following Fick's law [36]:

$$\tilde{\mathbf{E}}_{\text{tot}} = \frac{\tilde{\mathbf{j}}}{q_e n \left(\mu_i + \mu_e \right)} - \frac{D_e - D_i}{\mu_e + \mu_i} \frac{\nabla n}{n}, \tag{1.15}$$

where $\tilde{\mathbf{j}}$ is the discharge current. It is impossible to distinguish between the externally applied field (the first term on the RHS) and the ambipolar diffusion field (the second term on the RHS) at a point in a single measurement.

In the presence of a strongly inhomogenous electric field, an *ambipolar drift* flux develops that is equivalent in many ways to the diffusion flux [43]. The common method of determining the value of the ambipolar drift coefficient D_E again relies on assuming the particle mobilities to be constant, despite the fact that this will not be true in inhomgeneous fields [43]:

$$D_E = -\frac{\epsilon_0 \mu_i \left(\tilde{\mathbf{E}} \right)^2}{q_e n} \qquad \Rightarrow \qquad \frac{D_E}{D_a} = \frac{\epsilon_0 \left(\tilde{\mathbf{E}} \right)^2}{n k_B T_e}, \tag{1.16}$$

where we have used the fact that $\mu_e \gg \mu_i$ for the RHS relationship. Both drift and diffusion ambipolar effects will be present in any typical glow discharge, combining to increase the total ion flux above otherwise expected levels [62]. Ambipolar drift will dominate over diffusion within a glow discharge of density $n = 1 \times 10^9 \text{ cm}^{-3}$ and $T_e = 1 \text{ eV}$ if $E \gtrsim 50 \text{ V} \cdot \text{cm}^{-1}$ [43].

The true nature of ambipolar processes in realistic discharges has been shown in many cases to differ from the idealised conception given above. Some of the development in ambipolar research was performed within the USSR and unfortunately remains difficult to access. Kolobov and Tsendin [63] use a kinetic analysis to show that ambipolar diffusion field $\tilde{\boldsymbol{E}}_a$ (the RHS of Equation 1.15) is valid for an isothermal, two species discharge system with at least approximately constant particle mobilities. They present an ambipolar model for multiple electron populations as are commonly found in glow discharges, which was then generalised to any number of charged species by Rogoff [64]

$$\tilde{\boldsymbol{E}}_a = \frac{\Sigma_k q_k D_k \nabla n_k}{\Sigma_k q_k^2 \mu_k n_k}. \tag{1.17}$$

Thompson [65] showed in a molecular oxygen discharge that the formation of negative ions by electron attachment significantly increases the ambipolar diffusion of positive ions if $n_-/n_+ \gtrsim 10^{-1}$. Ambipolar effects have even been observed to initiate entire field reversals in DC glow discharges in some cases [66]. Hairapetian *et al.* [67] measured the diffusion of an electron beam into a vacuum region to show that the ambipolar field is significantly dependent on energetic electrons not trapped by the plasma potential. Godyak *et al.* [68] warn that the commonly made assumption that electron populations are thermalised in order to use the Einstein relation leads to an underestimation of the ambipolar drift.

Overall, the processes that contribute significantly to charged particle transport in a particular discharge can be determined by the ratio of the ion mean free path in neutral gases and the Debye length, λ_i and λ_D respectively, to the characteristic size of the chamber Λ [44], shown in Figure 1.5. This is a useful guide to determine which discharge model will be an appropri-
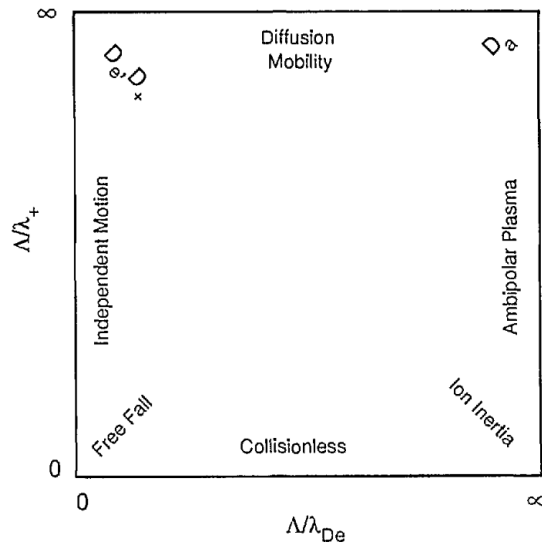

FIGURE 1.5 – A guide giving which processes will govern charged particle transport in a discharge given the ratio of typical mean free paths in neutral gases to the characteristic size of the discharge chamber Λ, taken from [44].

ate approximation for an experiment given that much cross-sectional data for charge-neutral collisions exists in the literature. Lowering the plasma density of a discharge would increase the Debye length relative to Λ and correspond with moving to the left of Figure 1.5 towards a regime in which ions and electrons move independently of each other. Decreasing the system pressure increases λ_i and corresponds to moving downwards in Figure 1.5 towards a collisionless or possibly inertial regime.

1.1.5 Discharge regions

We have seen how the difference in ion and electron mobilities causes the flux of positive and negative charges through a discharge to be unequal and how this can cause regions far from boundaries to exhibit non-zero electric fields. Furthermore, a discharge can be sustained in a system such that the characteristic size of the discharge L is no longer much greater than the Debye length λ_D [69], breaking one of the defining criterion of a plasma. Hence, a DC discharge can have a majority of the chamber exhibit significant density imbalance, as is the case for discharge IEC devices. In this section we shall outline the important features and regions that can exist in most types of discharge with a particular focus on the plasma-cathode interface. We shall then discuss the specific case of the glow discharge that pertains to the experimentally applied voltages and pressures used in this thesis.

A self-sustaining DC discharge is the steady state flow of gaseous current between an anode and a cold cathode that emits secondary electrons predominantly due to positive ion bombardment [17]. Secondary electron emission is the process in which a particle striking a surface can eject one or more electrons from it[2]. The number of ejected electrons emitted per incident particle on average is characterised by the secondary electron emission coefficient γ_e [72], which is usually within $10^{-4} \lesssim \gamma_e \lesssim 10^{-1}$ for most cathodes unless within very energetic systems. The incident particle may be an electron or a positive, negative, or neutral particle, with γ_e heavily dependent on the type of particle, its state of excitation or ionisation, and its incident energy on the surface. The surface material and its state of cleanliness also affect γ_e while the temperature of the material does not [73]. This suggests that secondary electron emission proceeds as a coulomb interaction between incident particles and the free electrons in the material [74].

Glow discharges predominantly consist of a lower mean energy, high density, and approximately thermalised population of electrons and ions (often referred to as 'bulk' or 'cold' populations), and sometimes feature multiple higher mean energy electron populations [17, 36]. Multiply ionised and negative ion species are usually observed in significantly lower densities than the singly ionised positive ion within discharges [75–77] due to the higher threshold energy and

---

[2]For in depth reviews on secondary electron emission, see [70, 71]

lower magnitude of the cross-sections of their creation mechanisms. Therefore, it is often sufficient to consider the bulk charges and a single source of high energy electrons to derive the fundamental analyses of discharge physics that will follow. In the case of a glow discharge, the cathode accelerates positive ions towards it and decelerates electrons, so that the largest contribution to γ_{e} is from the coefficient for ion bombardment, $\gamma_{\mathrm{e,i}}$ [20]. The positive electric field of the ion reduces the surface potential barrier confining electrons to the surface, increasing $\gamma_{\mathrm{e,i}}$ relative to that for electrons and neutrals and causing ejections with non-zero kinetic energy [78, 79]. Experimental values found by different groups for practical cathodes vary enough that Phelps recommends $\gamma_{\mathrm{e,i}}$ be treated as an unknown in cathode sheath models [20].

Each electron emitted from the cathode in a parallel plane system must gain sufficient energy to create enough ions that themselves will create a further electron at the cathode in a reproductive cycle. This will only occur if enough ions reach the cathode to reproduce the electron that created them, a criterion that is given by [40, 80]

$$\int_0^L \alpha_{\mathrm{T}}(x)\,dx = \ln\left(1 + \frac{1}{\gamma_{\mathrm{e}}}\right) \tag{1.18}$$

where L is the total distance of the discharge gap and α_{T} is the empirically determined Townsend first ionisation coefficient that is dependent on the discharge pressure and voltage. It is possible to reduce this requirement for a self-sustaining discharge without significantly altering the main discharge mechanisms by introducing external charge sources like thermionic filaments that emit electrons. These can be useful as a method to manipulate the requisite applied electric field or experimental pressure for a desired type of discharge that may otherwise have been difficult to achieve.

The externally applied accelerating field between the cathode and anode would be uniformly distributed in a one-dimensional system in the absence of charged species. The majority of electrons emitted from the cathode are unlikely to reach ionising energies in such a system as their slow acceleration by the field is overcome by collisional processes. Still, a few of the electrons emitted from the cathode in this case will ionise the background gas, causing a positive space charge to begin to build. This space charge cumulatively restricts the entire cathode potential to drop over a much smaller distance $d_{\mathrm{c}} \leq \lambda_{\mathrm{e}}$ than the entire discharge gap L [17]. This allows for the efficient acceleration of electrons to high energies over a distance in which they are unlikely to undergo a collision. The discharge can then proceed with an appreciable current density and without the need for inhibitively large applied biases to the electrodes. This mechanism explains why the voltage required to sustain a discharge is less than that required to initiate one.

The developed space charge divides the discharge into three significantly distinct regions [17]:

1. the 'cathode fall' or 'cathode sheath', a highly energetic, high field region containing significantly imbalanced positive space charge. The cathode sheath is crucial to sustaining the discharge (region 1 in Figure 1.6);

2. the negative glow region, also crucial to the discharge, of relatively high charged particle density approaching quasineutrality (region 2);

3. A low field, superfluous and alternately luminous region containing multiple structures that is often approximated as quasi-neutral (region 3).
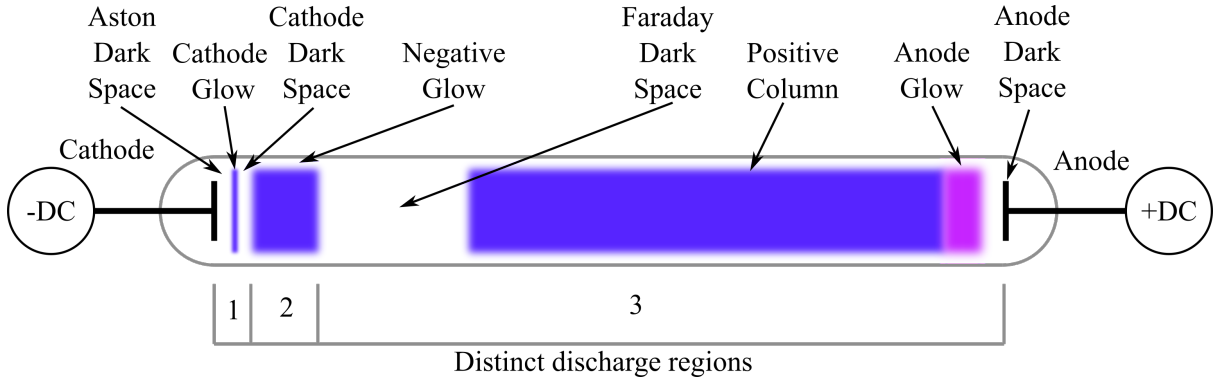

FIGURE 1.6 – The historically recognised sections of a discharge tube grouped into important regions for analysis: the cathode sheath (1); the negative glow (2); the remaining quasi-neutral region superfluous to self-sustainment.

1.1.6 The cathode sheath

The development of the cathode sheath has been studied extensively from the time of Langmuir [81] after it was quickly discovered to be the most important region for maintaining the discharge. Von-Engel and Steenbeck [82] showed in 1934 that the electric field in the cathode fall of a glow discharge follows

$$V_c = \int_0^{d_c} \left| \tilde{\boldsymbol{E}} \right| dx = \int_0^{d_c} E_c \left(1 - x/d_c \right), \qquad (1.19)$$

where V_c and E_c are the applied potential and electric field at the cathode respectively and d_c is the width of the cathode sheath. This integral has no closed analytical solution, and so was traditionally simplified by assuming that the electric field is homogeneous in the cathode fall following $E = V d_c$ [17]. With this assumption, we can relate properties of the cathode fall to experimental parameters through the 'similarity laws' [83]

$$E_c/p = \frac{B}{C + \ln\left(pd_c\right)}, \qquad \frac{V_c}{pd_c} = \frac{B}{C + \ln\left(pd_c\right)}, \qquad C = \ln\left(\frac{A}{\ln\left(1 + 1/\gamma_e\right)}\right), \qquad (1.20)$$

where A and B are experimentally determined constants [40]. Many experimental results in discharge physics are displayed with axes given in E/p or in pd to reduce the number of free

parameters that can vary between different research groups. Equation 1.20 implies that the voltage required to maintain a sheath of width d_c is a function of pd_c that has a stable minimum voltage $V_{\min}$. The discharge will adjust itself in the steady state so that the criteria are met to be able to operate at $V_{\min}$.

The use of the homogeneous field approximation was first experimentally verified by Paschen [84] in simple discharges as well as with numerical solutions of Poisson's equation [83] (discussed in Section 1.2). We can then estimate the cathode sheath thickness if we know the discharge current density j and cathode bias using [18]

$$d_c \approx \left(\frac{\epsilon_0 \left(1 + \gamma_{e,i}\right) \mu_i}{jn} \right)^{\frac{1}{3}} V_c^{\frac{2}{3}}. \tag{1.21}$$

This method implicitly treats the cathode fall region as an analogy of the low charge density Townsend dark discharge between two plates separated by d_c with a source of ions in place of the anode (see Figure 1.8). Although frequently used, the original basis for why these similarity laws apply relied on a flawed energy minimisation argument that did not withstand the tests of time. The similarity laws have been modified and extended since then for more complex discharges, for example involving non-Maxwellian populations [85] or pulsed applied fields [86]. Despite all of this, the relations in Equation 1.20 remain a valid method for the comparison of simple discharges.

So far, we have been modelling the potential drop between the cathode and the plasma as stopping at a definite point referred to as the 'sheath edge'. The Debye shielding of charge instead results in the exponential decay of potential with distance from the electrical disturbance [15]. Historically, the sheath edge was somewhat vaguely defined as the 'point' at which the potential difference from the plasma potential had become significantly less than the mean energy of bulk electrons. The implications of this vague definition will be detailed in the discussion of Bohm theory and the cathodic pre-sheath in Chapters 3 and 4. Child [87] and Langmuir [81] followed a similar analysis to Von Engel and Steenbeck [88] to relate the sheath thickness to the discharge characteristics in an infinite plane, collisionless gap without ions, finding that

$$d_c^2 = \frac{\sqrt{2}}{9\pi} \sqrt{\frac{q_e}{m_e}} \frac{V_c^{\frac{3}{2}}}{j}. \tag{1.22}$$

Langmuir extended this analysis to discharges between concentric cylinders [89]

$$r_c = \frac{2\sqrt{2}}{9} \sqrt{\frac{q_e}{m_e}} \frac{V_c^{\frac{3}{2}}}{j\beta^2}, \tag{1.23}$$

where r_c is the radius of the cathode sheath and β is a given quantity. Equation 1.23 shall be useful for estimating the operating regime in both the cylindrical hollow cathode and Langmuir probe analyses given in Chapters 3 and 4. Langmuir then showed [89] that including an ion current i_i in this calculation increases the electron current i_e by reducing the build up of negative space charge near the cathode that served to contain emitted electrons there, according to

$$\frac{di_e}{di_i} = A\sqrt{\frac{m_i}{m_e}}, \tag{1.24}$$

where $0.378 \leq A \leq 3.455$ is itself dependent on $\sqrt{m_i/m_e}$. Langmuir and Child's analysis [81, 87] successfully described the development of the plasma potential as well as properties of the cathode sheath in simple discharges. Equations 1.20, 1.22, and 1.23 will be frequently used as a quick method for determining the size of the cathode sheath and, therefore, the discharge regions that will likely be present in experiment.
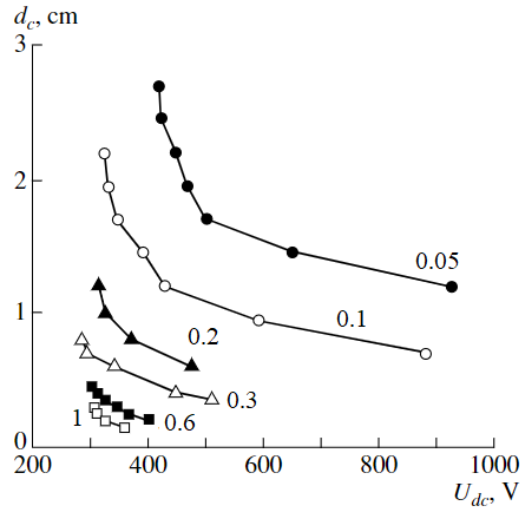

FIGURE 1.7 – The cathode sheath length as a function of the cathode bias in a DC glow discharge in air, adapted from [90]. The pressure for each experiment is given next to the data in Torr.

In experiments, the width of the cathode sheath has been found to be inversely proportional to the background pressure [90], and has been somewhat linked to charged particle mean free paths [91]. An example of cathode sheath lengths as a function of cathode bias in a DC cylindrical glow discharge in air with $L = 33\,\text{mm}$ is given in Figure 1.7, adapted from Lisovskiy and Yokovin [90]. More complex relationships have been derived to include the effects of collisions [92], metastable atoms and molecules [93] and other lesser considerations such as the effect of cathode sputtering on the discharge current [94] and non-linear particle drift velocities [25]. The complexity of these models has made comparison with experiment intractable given the difficulty in controlling multiple variables in a discharge [18]. d_c can only be determined in higher

dimensional or asymmetric systems by solving Poisson's equation for the electric potential ϕ,

$$\nabla^2\phi = \frac{1}{\epsilon_0}\left(\Sigma_k q_k n_k\right), \tag{1.25}$$

for each charged species k in the discharge. Equation 1.25, however, represents a highly non-linear differential equation that is strongly dependent on the plasma boundary conditions. Solving Equation 1.25 analytically without simplifications is therefore difficult to impossible in higher order geometries [95]. Historically, if an analytical solution to Equation 1.25 could be found, it had to rely upon reductive simplifying approximations followed by pain-staking integration performed by hand. This process has been dramatically improved by computational methods, discussed in Section 1.2, to an extent that has led to their development as independent fields of study.

1.1.7   The normal and abnormal glow discharge

Discharges come in many distinct forms that can be defined by the ratio of voltage applied to the electrodes to the current collected by them. This manifests as separate regions of the $V-i$ or $i-V$ curve (or 'characteristic') of the discharge tube, as shown in Figure 1.8. The
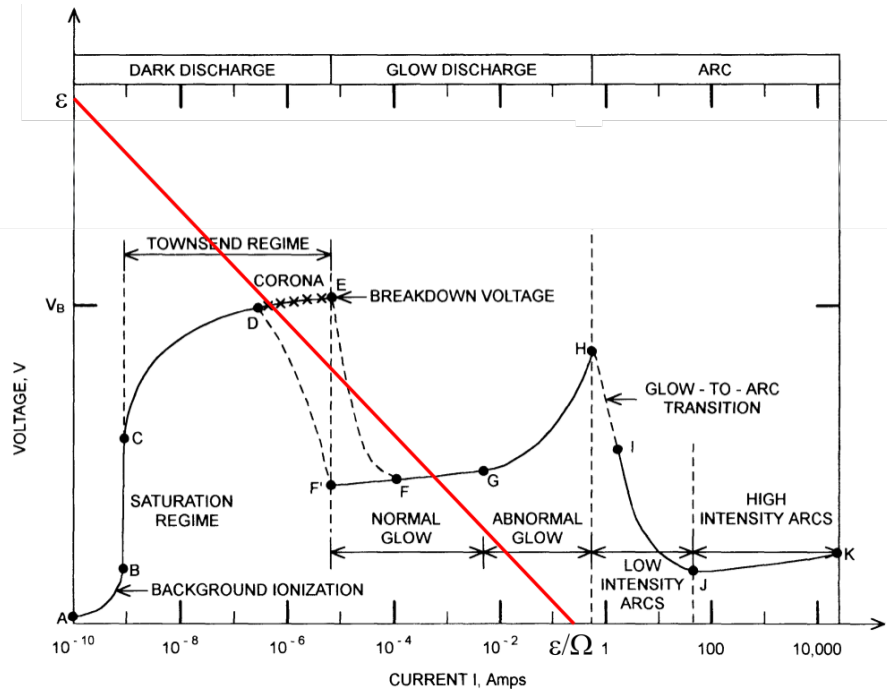
FIGURE 1.8 – The $V-i$ curve of a DC discharge tube. The labelled regions are the distinct discharge types. In red is a typical load line of the discharge circuit (with applied EMF ε and internal resistance Ω). Adapted from *Industrial Plasma Engineering* by Roth [96].

$V-i$ curve for a particular experiment is affected by many factors, the most influential being the background gas pressure pumped through the tube, the type of gas used, and the internal

resistance of the electrode circuit. The type of discharge manifested is given by the intersection of the load line of the circuit applying the voltage to the electrodes with the $V - i$ curve of the discharge. The general behaviour of each discharge type remains apt for higher order discharge geometries, although the $V - i$ curve may change quantitatively [17].

The IEC and hollow cathode discharges of relevance to this work largely fall into the closely related normal and abnormal glow discharge regimes. A characteristic feature of the normal glow discharge is the relatively constant cathode bias that is maintained for changing discharge currents (region F to G in Figure 1.8). This is the result of a spatially non-uniform current density at the cathode, in which the discharge only partially covers the cathode surface [17, 20]. As the applied bias varies, so does the surface area of the cathode involved in the discharge rather than the average current density. If the applied bias is increased (or the circuit resistance decreased) to the point that the entire cathode surface is involved in the discharge, the average current density must begin to increase along with it. This discharge mode has been labelled the 'abnormal glow discharge' (region G-H in Figure 1.8). Abnormal discharges usually occur at very low experimental pressures and high applied voltages [17]. At a certain limit of applied bias, the emission of electrons from the cathode will begin to avalanche into the arc discharge, a high current mode that occurs in sparks or in arc welding [96]. The normal glow discharge usually has a chamber volume of characteristic widths $L \sim 1 - 100$ cm, pressures of $p \sim 10^{-2} - 10^2$ Torr, and discharge currents $i \sim 0.1 - 100$ mA, with room to trade between the E/p and pd values [17]. Abnormal glow discharges can be achieved by reducing the experimental pressure or external circuit resistance [97] and by increasing the applied bias, resulting in a relatively large cathode fall region. Discharge IEC devices discussed in Section 1.5 are often operated in chambers of radius less than 1 m, with electrodes at ~ -50 kV and pressures close to 10^{-2} Torr [7], resulting in currents in the order of $1 - 1000$ mA, falling between a normal and abnormal glow discharge.

1.1.8 Electron populations in glow discharges

Experiments performed using electrostatic probes and analysers [98–100] regularly exhibit the presence of multiple electron species in glow discharges rather than a single, thermalised population. Including these energetic electron populations contributes to a marked improvement in the accuracy of discharge modelling [63, 101] and has improved general understanding considerably. The various electron populations have been historically distinguished from each other by their method of creation and the population mean energy. The great variety of charge sources available in discharge physics outweighs the number of common names available, and has unfortunately confused nomenclature such that one must carefully outline what is meant by terms like 'secondary' or 'primary' electrons. The nomenclature established in the following Section shall be used throughout the thesis, in particular in chapters 3 to 5.

The vast majority of electron density in regions of a glow discharge outside of the cathode sheath is carried by an approximately Maxwellian population with temperatures typically between 0.1-3 eV and densities between $10^{14} - 10^{16} \, \mathrm{m}^{-3}$ [14]. This population exists in an approximately quasi-neutral, non-thermal equilibrium state with singly ionised particles of the background gas of significantly lower temperature [102, 103] when outside of the cathode sheath. These high density electron and ion populations are created in the 'bulk' of the discharge (many Debye lengths from boundaries) by electron impact ionisation of the background gas [104] and are usually used to parameterise the type of plasma as in Figure 1.1. As such, they are usually designated as the 'cold' or 'bulk' populations, and in some cases as 'ultimate' electrons [105].

A higher temperature, lower density, and often approximated as Maxwellian 'hot' electron population is the next most common population found in the bulk plasma [17, 105]. Distinct from the high energy tail of the bulk electron population, these are suspected to arise from the thermalisation of energetic electrons emitted from surfaces and external charge sources [98, 99, 106]. The terms 'hot' or 'energetic' are often used within the literature to refer to any electron population of higher mean energy than the cold electron population, however, even if the hot population is not Maxwellian. Before thermalisation, electrons that are emitted directly from charge sources like thermionic filaments are frequently called 'primary' electrons (see N. D. Twiddy [107], for example). This is due to the fact that they are often the source of the electron avalanche that initiates a discharge [17]. Electrons emitted from the cathode by secondary electron emission of any process or created by ionisation within the sheath are collectively known as 'secondary' electrons [73, 108]. Secondary electrons have been shown to form a beam near to the cathode with energy roughly equivalent to the cathode bias V_c [109] or otherwise have been measured to have thermalised when within the bulk of the discharge [78, 100]. The spatial development of the secondary electron distribution function travelling away from the sheath had not been observed at the time of publication to the best of the author's knowledge. The determination of such measurements for the first time using a Langmuir probe analysis shall be the focus of Chapter 4. Otherwise, how the distribution function of secondary electrons develops from a beam into a thermalised population with distance from the cathode has only been numerically modelled, with an example given in Figure 1.11.

Other electron distributions are possible depending on the experimental equipment. Mono-energetic populations with an isotropic velocity distribution have been observed in low pressure multipole systems [100] that feature particle trapping and reflection methods. Energetic electron populations with more complex forms of distribution function have been experimentally observed [63, 98] and given various names as shown in Figure 1.9a). It is difficult to distinguish whether such populations arise from a single mechanism or are the amalgamation of multiple lesser populations, meaning they can be difficult to reproduce in computational or analytic models. Hot and secondary electron populations are usually observed with densities at least 100 times smaller than the bulk population except in the most extreme discharge conditions, and are sometimes
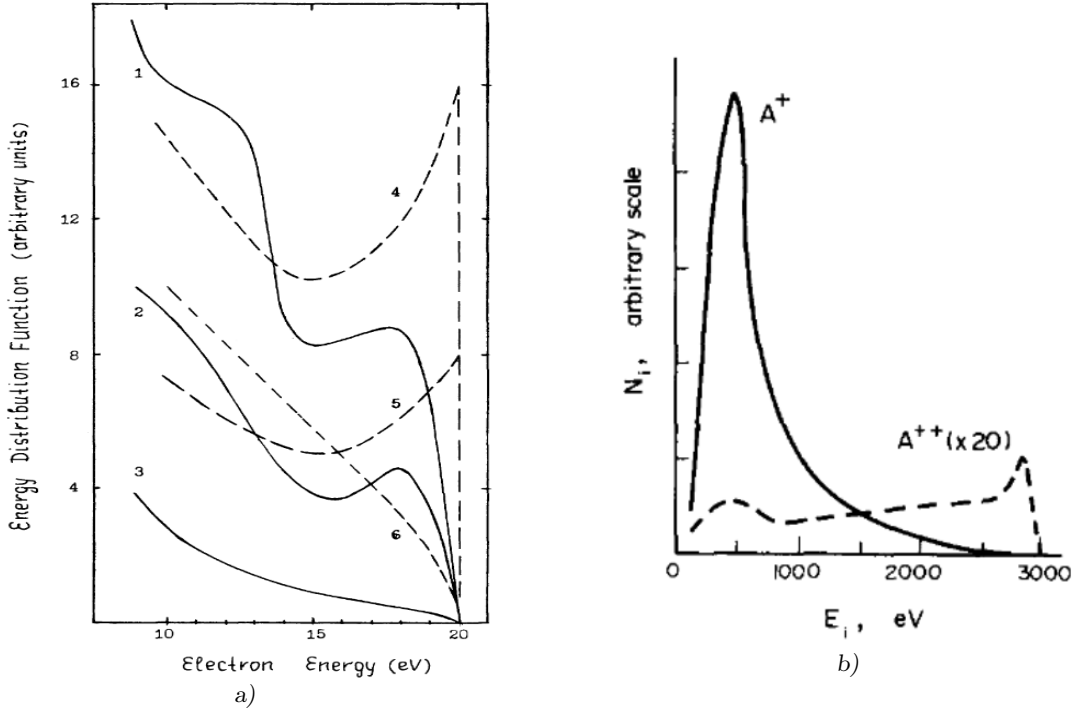
FIGURE 1.9 – *a)*: The energy distribution functions of 'intermediate' electrons proposed by Kolobov and Tsendin [63] at different locations within a discharge as measured from electron-metastable collisions [110] (solid lines). The dashed lines represents an analytic model of a kinetic equation attempting to reproduce the electron distribution functions ($1 \equiv 4, 2 \equiv 5, 3 \equiv 6$). *b)*: The normalised ion energy distribution functions of singly and doubly ionised argon captured by mass spectrometry at the cathode in an abnormal glow discharge in a 0.1 Torr argon discharge tube with -3 kV cathode bias, taken from Bondarenko [76].

not observable at all with insensitive diagnostics [17]. However, the minimum threshold energy for the ionisation of a background gas is above 10 eV [104] (being 15.76 eV for neutral argon in the ground state). The density of energetic populations able to ionise can therefore be large relative to that of the bulk population so that they contribute significantly to or dominate inelastic discharge processes. Many of the higher order discharge processes such as the formation of double sheaths, radiative emission processes, and the hollow cathode effect cannot be recreated in modelling without including at least one type of energetic electron population [111, 112].

Secondary electron dynamics have been attempted to be captured by kinetic computational models, to moderate success [112]. These energetic electrons deliver energy gained in high field regions of the discharge to low field regions like the negative glow. The velocity distribution function of positive ions at the cathode has similarly been shown to contain information developed in other regions of the discharge [75–77], with an example shown in Figure 1.9b). Here, mass spectroscopic measurements demonstrate the acceleration of positive ions with resistance due to charge transfer collisions. Altogether, this means that a glow discharge system can be non-local[113], in that the energy distribution function of a population at a location is not solely dependent on electric fields less than a Debye length away from it. In other words, a charged

population can carry information between otherwise unrelated phase space elements in the system. This severely limits the accuracy of models that implicitly assume locality, such as Von Engel's model [82] in Equation 1.19 and the similarity laws in Equation 1.20 that are so often relied upon. Tsendin states [114] that approximating a discharge as local only holds if the distance to the nearest wall is far greater than the characteristic length of energy relaxation for a population. The issue of locality can be addressed in some cases by numerical models which offer greater control over which reductive assumptions are made to simplify the analysis in question.

1.2 Numerical discharge modelling

We have seen that the complexity of a discharge means that analytical descriptions rely upon linearisation, assumed constancy, or by otherwise enforcing strong restrictions on particle dynamics in ways that are not always experimentally verified. Analytical models serve as an excellent method for determining values within an order of magnitude, but regularly fail to capture higher order non-linear processes. Instead, a discharge with particular boundary conditions may be more accurately modelled by solving the plasma equations describing particle motions numerically. This is achieved through two main methods: models that track phase space elements of a statistical number of particles, most notably fluid and kinetic models; and models that track or approximate individual particle motions. Each method has significant advantages and disadvantages that a researcher may choose between depending on the particular class of particle or field dynamics that is the focus of the analysis. Phase space models have shown greater success at capturing phenomena that depend on slight differences in particle number density like the development of space charge [115]. Particle models are considered the more appropriate choice for capturing non-linear particle dynamics, particularly instabilities in magnetised nuclear fusion plasmas [116]. In all cases, one must be aware of the multitude of artificial artefacts numerical models suffer from that can easily be misinterpreted as physical phenomena [112].

1.2.1 Statistical methods

Computational models that have here been described as statistical solve particular forms of Boltzmann's equation for each particle species α coupled with analytical expressions that describe collisional processes as well as with electromagnetic fields. These methods are statistical in that they track the motion of phase space elements $\mathrm{d}\tilde{\boldsymbol{x}}\mathrm{d}\tilde{\boldsymbol{v}}\mathrm{d}t$ of each populations distribution function $f_\alpha\left(\tilde{\boldsymbol{x}}, \tilde{\boldsymbol{v}}, t\right)$ that contain many individual particles of type α. Here, $\tilde{\boldsymbol{x}}$ and $\tilde{\boldsymbol{v}}$ describes all positions and velocities that are within $\mathrm{d}\tilde{\boldsymbol{x}}$ or $\mathrm{d}\tilde{\boldsymbol{v}}$ of the mean position $\tilde{\boldsymbol{x}}$ and velocity $\tilde{\boldsymbol{v}}$ under consideration. Averaging over phase space elements significantly reduces the immensity of calculating all of the particles in a discharge in a way that is beneficial in describing many-particle processes like

the development of space charge, diffusion, and the sources and sinks of particle populations by collisions. The proceeding discussion is given in greater depth in *Fundamentals of Plasma Physics* by Bittencourt [113]. Boltzmann's Equation is a complete description of the development of all phase space elements from a frame of reference travelling with the mean velocity of each element in consideration:

$$\frac{\mathrm{D}f_\alpha}{\mathrm{D}t} = \frac{\delta f_\alpha}{\delta t} + \tilde{\boldsymbol{v}} \cdot \nabla_{\tilde{\boldsymbol{x}}} f_\alpha + \frac{q_\alpha}{m_\alpha} \left[\tilde{\boldsymbol{E}} + \tilde{\boldsymbol{v}} \times \tilde{\boldsymbol{B}} \right] \cdot \nabla_{\tilde{\boldsymbol{v}}} f_\alpha = \sum_k f_k C_k, \tag{1.26}$$

where $\nabla_{\tilde{\boldsymbol{x}}}$ and $\nabla_{\tilde{\boldsymbol{v}}}$ are the spatial and velocity derivatives respectively, $\tilde{\boldsymbol{E}}$ and $\tilde{\boldsymbol{B}}$ describe the sum of all electric and magnetic fields, both externally and internally generated, and $\Sigma_k f_k C_k$ describes collisional processes from all particle species k that interact with particles of type α. Here, $\mathrm{D}/\mathrm{D}t$ is the convective derivative, and all external forces acting on the system have been simplified as the Lorentz force (Equation 1.1) since it dominates over lesser forces in a discharge like those of viscosity, pressure, and gravity.

Collision processes can be solved either by assuming properties of the particle distribution function or directly by using the collisional integral methods described in Section 1.1.2. The former method offers significant simplification at the cost of forcing the system towards an expected result, as in Krook's relaxation model [117]

$$\sum_k f_k C_k = -\nu \left(f_\alpha - f_{\alpha 0} \right), \tag{1.27}$$

which describes the tendency of a system towards a thermal equilibrium solution f_{α_0}. Treating collisions fully, Equation 1.26 is a non-linear, integro-differential, coupled set of equations that must be closed using Maxwell's equations:

$$\nabla \cdot \tilde{\boldsymbol{E}} = \nabla^2 \phi = \frac{\sum_k q_k n_k}{\epsilon_0} \tag{1.28}$$

$$\nabla \cdot \tilde{\boldsymbol{B}} = 0 \tag{1.29}$$

$$\nabla \times \tilde{\boldsymbol{E}} = -\frac{\delta \tilde{\boldsymbol{B}}}{\delta t} \tag{1.30}$$

$$\nabla \times \tilde{\boldsymbol{B}} = \mu_0 \left(\tilde{\boldsymbol{J}} + \epsilon_0 \frac{\delta \tilde{\boldsymbol{E}}}{\delta t} \right), \tag{1.31}$$

where the first equality in Equation 1.28 is Poisson's equation, μ_0 is the magnetic permeability, and $\tilde{\boldsymbol{J}}$ is the total current density of charged particles.

Directly solving the system of Equations given by 1.26 and 1.28 to 1.31 is a notoriously difficult and generally unsolved problem. Instead, different conservation rules that describe particle behaviour can be derived from Boltzmann's equation by taking consecutive 'moments' of it [113].

This involves multiplying Equation 1.26 by the property to be conserved $\tilde{\boldsymbol{\chi}}_\alpha$ and integrating the result over velocity space. This takes quite a bit of manipulation, given in Bittencourt chapter 8 [113]. The first moment results in the continuity equation which describes the change in the total amount of a macroscopic quantity within a fluid element. In other words, the continuity equation tracks the transport of a quantity $\tilde{\boldsymbol{\chi}}_\alpha$ through space. In plasma physics, the quantity in question is usually the particle mass ($\tilde{\boldsymbol{\chi}}_\alpha = m_\alpha$) or charge ($\tilde{\boldsymbol{\chi}}_\alpha = m_\alpha q_\alpha$), so that the continuity equation is given by [113]

$$\frac{\delta\left(n_\alpha m_\alpha\right)}{\delta t} + \nabla \cdot \left(n_\alpha m_\alpha \tilde{\boldsymbol{u}}_\alpha\right) = S_\alpha, \tag{1.32}$$

where $\tilde{\boldsymbol{u}}_\alpha$ is the macroscopic average velocity of the particles $\tilde{\boldsymbol{u}}_\alpha\left(\tilde{\boldsymbol{x}}, t\right) = \langle\tilde{\boldsymbol{v}}\rangle$ and S_α is the total collisional loss or production of particles of type alpha. In the absence of collisions in the steady state, Equation 1.32 describes the decrease in the local density of a population as it accelerates such that the total flux remains constant, given by $n_\alpha \tilde{\boldsymbol{u}}_\alpha = \text{Const}$. This version of the continuity equation is referred to as the conservation of flux.

The second moment of Boltzmann's equation uses $\tilde{\boldsymbol{\chi}}_\alpha = m_\alpha \tilde{\boldsymbol{u}}_\alpha$ (or $\tilde{\boldsymbol{\chi}}_\alpha = m_\alpha q_\alpha \tilde{\boldsymbol{u}}_\alpha$) to capture the flow of momentum in the discharge [113],

$$\frac{\delta n_\alpha \tilde{\boldsymbol{u}}_\alpha}{\delta t} + \nabla \cdot \left(n_\alpha \langle\tilde{\boldsymbol{v}}\tilde{\boldsymbol{v}}\rangle\right) - \frac{q_\alpha}{m_\alpha}\left[\tilde{\boldsymbol{E}} + \tilde{\boldsymbol{u}}_\alpha \times \tilde{\boldsymbol{B}}\right] = \sum_k n_k \langle C_k \tilde{\boldsymbol{v}}\rangle. \tag{1.33}$$

The collisional term on the RHS of Equation 1.33 captures all methods of momentum transfer for a species α between itself and with other species and boundaries in the plasma. Higher moments of the Boltzmann equation can be found indefinitely by using higher order powers of the average velocity, $\tilde{\boldsymbol{\chi}}_\alpha = m_\alpha \langle\tilde{\boldsymbol{v}}^n\rangle/n$. The next moment results in the energy transport equation, and so on. Equations 1.32 and 1.33 can also be derived using a purely fluid argument and the Navier-Stokes equation, showing the relationship between kinetic and fluid models.

Each moment of Boltzmann's equation introduces a term of higher order in velocity that itself requires the next higher order moment of the Boltzmann equation in an infinite loop. For example, we note the $\langle\tilde{\boldsymbol{v}}\tilde{\boldsymbol{v}}\rangle$ term in Equation 1.33 can only be determined by taking the next moment of Boltzmann's equation using $\tilde{\boldsymbol{\chi}}_\alpha = m_\alpha \langle\tilde{\boldsymbol{v}}\tilde{\boldsymbol{v}}\rangle/2$. The $\langle\tilde{\boldsymbol{v}}\tilde{\boldsymbol{v}}\rangle$ term would then need a further moment of the Boltzmann equation involving a $\langle\tilde{\boldsymbol{v}}\tilde{\boldsymbol{v}}\tilde{\boldsymbol{v}}\rangle$ term. Thus, the system of equations must be cut off at an arbitrary point that must be argued to be a reasonable choice by the modeller. Once chosen, the system of closed equations can be numerically approximated to a given accuracy by discretising the solution space into a finite grid and using Taylor expansions to approximate derivatives (the finite difference method) [118].

In fluid systems, the set of equations 1.28 to 1.33 can be represented in general using the non-linear operator form $\delta\mathbf{g}/\delta t = \mathbf{L}\left(\mathbf{g}\right)$ [111], where $\mathbf{g}\left(\tilde{\boldsymbol{x}}, t\right)$ represents the independent physical

variables that describe the discharge and **L** contains spatial derivatives. Then, solutions can be solved by advancing in discrete 'time steps' Δt (which can represent real time evolution or can be arbitrary to advance towards a steady state solution), so that the solution g^{n+1} at time step $t^{n+1} = t^n + \Delta t$ is given by [111]

$$\frac{\delta \mathbf{g}}{\delta t} = (1 - \Theta) \mathbf{L}^n (\mathbf{g}^n) + \Theta \mathbf{L}^{n+1} (\mathbf{g}^{n+1}) . \tag{1.34}$$

$0 \leq \Theta \leq 1$ is then a chosen variable which determines if the approximation is *explicit* ($\Theta = 0$), *implicit* ($\Theta = 1$), or somewhere advantageously in between as in the Crank-Nicolson [119] and Runge-Kutta [120] methods. Explicit methods are generally simpler to solve than implicit methods, but suffer stability limitations based on the time step size. In all methods, there is no way to guarantee that a final solution accurately represents reality without reference to experiment.

One of the most simple and pertinent examples of a fluid model is the description of the potential distribution in a basic discharge [36]. Here, the cathodic sheath due to a planar, steady state, collisionless, two species plasma trapped between floating boundaries is solved using Poisson's equation. The continuity equation (Equation 1.32) is used to determine the ion density against their expected drift velocity u_0 at each location while Boltzmann's relation (derived by treating the electron population as Maxwellian in a repulsive potential) is used to determine the electron density, such that [36]

$$\frac{d^2 \phi}{dx^2} = \frac{q_e n_0}{\epsilon_0} \left[\exp \left(\frac{q_e \phi}{k_B T_e} \right) - \left(1 - \frac{2 q_e \phi}{m_i u_0^2} \right)^{-\frac{1}{2}} \right] . \tag{1.35}$$

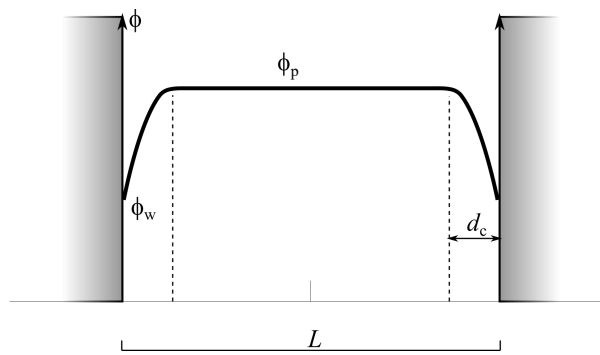A typical sheath potential distribution using Equation 1.35 is given in Figure 1.10.

FIGURE 1.10 – The potential distribution ϕ in a one dimensional discharge gap of width L between two absorbing floating walls at potential ϕ_w found by numerical solution of Equation 1.35. Despite the strong assumptions involved to arrive at Equation 1.35, this model captures the development of a cathodic sheath of width d_c containing a potential drop from the plasma potential ϕ_p.

This approximation only solves the first moment of the Boltzmann equation, cutting off higher order moments by neglecting collisions and assuming the form of the particle distribution functions. Indeed, many stringent simplifications beyond those already mentioned have been included: that the ions are cold ($T_i = 0$), so that their velocity distribution function at a location is entirely defined by the electric field there; that the ions enter the cathode sheath with a drift velocity u_0; and that the potential ϕ decreases monotonically from the system centre. Why ions enter the sheath with a non-zero drift velocity u_0 has to do with a concept called the cathode 'pre-sheath' introduced by Bohm in 1949 [121]. The pre-sheath has become its own field of study [19] and shall become a significant focus of the analysis in chapters 3 to 5 where it it discussed in greater detail. Despite the potential problems arising from this set of assumptions, numerical solutions of Equation 1.35 have proven sufficiently accurate for characterising simple DC glow discharges at an experimentally distinguishable level. Many different methods have been employed to numerically solve for the different regions in discharges at different levels of complexity, and have been summarised by Lister [111].

1.2.2   Individual particle methods

Fluid and kinetic methods gain the statistical advantages of phase space calculations, in which the bulk structure of both fields, particle density distributions, and most collisional processes are captured well in relatively few numerical calculations. However, most statistical methods require homogeneous fields that interact with charged species locally, failing to capture ionisation and excitation processes due to highly energetic, non-local primary and secondary electrons. Individual particle models like Particle In Cell (PIC) and Monte Carlo Collision (MCC) methods attempt to better model non-local dynamics. This is usually done by approximating the behaviour of individual particles by tracking the trajectories of representative 'superparticles' as well as their electromagnetic interactions self consistently using Equations 1.28 to 1.33. Collisions between virtual particles can then be calculated using probabilistic methods. Individual particle methods are therefore better at capturing significant energy changes that occur within less than a collisional mean free path of the particle in question [122]. Boeuf *et al.* [123], for example, use an MCC analysis to demonstrate the experimentally illusive thermalisation of the secondary electron beam travelling away from the cathode plate in a normal glow discharge, given in Figure 1.11. The computationally expensive nature of PIC and MCC methods that used to be a significant barrier for their use is being surmounted by the rise of cheap computing power in recent years. As such, they have become popular for capturing non-linear instabilities in energetic plasmas such as in magnetic confinement fusion reactors or low density space plasmas [116]. Fundamental limitations on the superparticle representation in PIC-MCC codes, however, fail to properly conserve energy and momentum in the system [124]. Any individual
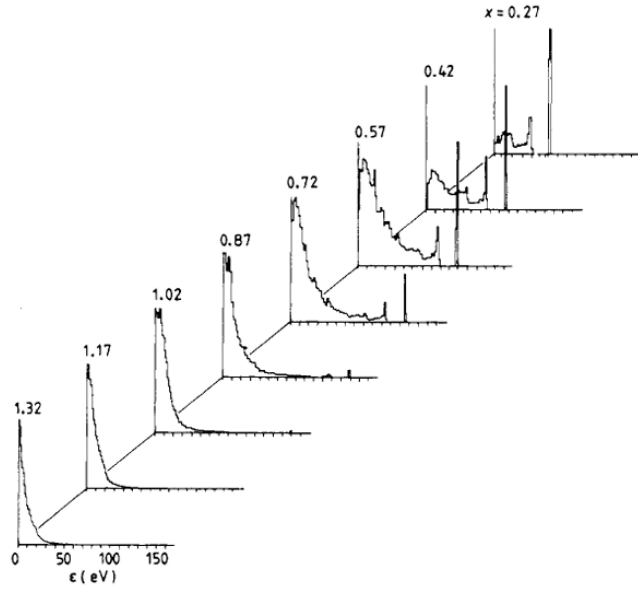
FIGURE 1.11 – The energy distribution function with distance x (in cm) from a planar cathode with $E/p = -240 \, \text{V} \, \text{cm}^{-1} \text{Torr}^{-1}$ calculated by a numerical Monte-Carlo model in a normal glow discharge operated at 1 Torr, taken from [123]. The density of the beam of secondary electrons that manifests as the individual, high energy spike in the energy distribution function can be seen to decrease with increasing x.

particle model that does not include a sufficient number of particles will also suffer in capturing bulk particle effects that arise from small discrepancies in particle number densities like the development of space charge [125].

Many discharge systems incorporate different features that are not all well suited to either bulk or individual particle modeling alone. The most relevant to this thesis is that of the hollow cathode discharge, which features bulk effects like the development of a virtual anode [97] as well as highly non-local electron populations that dramatically change the discharge mode. In the next section, we shall introduce the hollow cathode discharge following the reviews by Pillow [91], Little and Von-Engel [18], and Arslanbekov [3]. This shall lead to a discussion of hybrid fluid-particle models in section 1.3.2 and the development of a virtual anode in low pressure hollow cathode discharges in preparation for the analysis of discharge-mode IEC devices.

1.3 The hollow cathode discharge

Early in discharge physics research it was observed that changing the shape of the cathode had a strong effect on the discharge as a whole [17, 126]. Cathode geometry was unexpectedly related to discharge parameters like the bulk plasma density and resistivity [91]. The most dramatic example of this is when the cathode is made to surround a volume of space of characteristic width

d_{hc} or radius r_{hc}, forming what is known as a hollow cathode as shown in Figure 1.12. This can
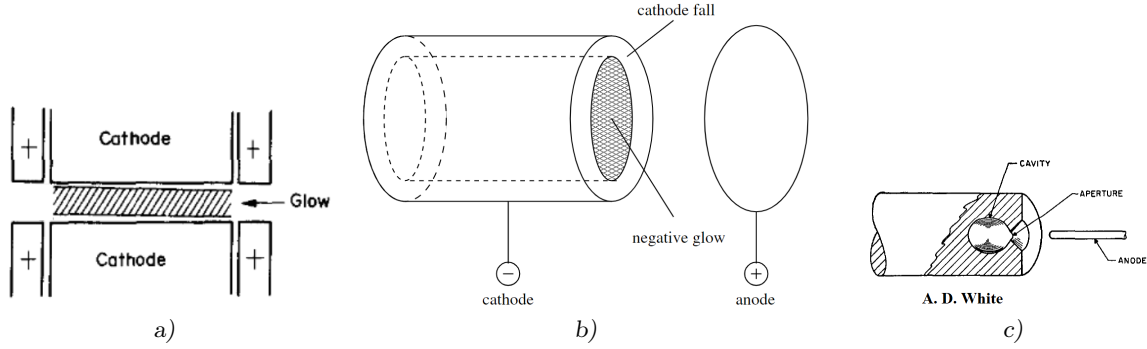

FIGURE 1.12 – Example hollow cathodes taken from the literature. *a)*: An example of a plane hollow cathode [18]. *b)*: A cylindrical hollow cathode [127]. *c)*: A micro-cavity within the cathode, forming a hollow cathode discharge [128].

be achieved in multiple ways, ranging from hollow cylinders [127], cups [97], micro-cavities in a cathode surface [128], capacitor-style flat plates, or more complex hybrid designs [126, 129]. An external anode faces at least one of the open apertures of the cathode in each system.

If the negative glow from opposite facing interior surfaces of the hollow cathode overlap, the hollow cathode effect is observed [4, 91]. The hollow cathode effect is known for a number of curious and potentially beneficial phenomena. A dramatic increase in the discharge current density occurs within the hollow cathode compared to a diode system for the same applied voltage and pressure, increasing the discharge efficiency [3]. Along with this comes the formation of electron, sputtered neutral, and even ion beams that diverge out from the cathode centre [18]. Intense radiation with narrow spectral lines are emitted from the hollow cathode volume since the hollow cathode effect proceeds without significantly raising the temperature of the background gas [2]. This has led to the frequent use of the hollow cathode discharge as a spectral lamp source [130]. The total discharge density within the cathode has been observed to increase by several orders of magnitude [18, 131] relative to an equivalent diode discharge, and the sheath width d_{c} at each cathode surface decreases [132].

If the discharge pressure is raised high enough that opposing negative glows no longer overlap, the hollow cathode effect disappears and each cathode surface acts more like an independent glow discharge cathode [18]. The dramatic change between this state and a true hollow cathode discharge is shown by the dependence on the discharge (or cathode) voltage given as U_{d} against the background gas pressure by Kolobov and Metel [4], shown in Figure 1.13. The 'optimal' conditions for a hollow cathode discharge occur between the minimum at $p = 20\,\mathrm{Pa}$ and the maximum at $p = 105\,\mathrm{Pa}$. Beyond $p = 150\,\mathrm{Pa}$ the negative glows separate and the hollow cathode effect is no longer observed, reducing the discharge efficiency. If the pressure becomes too low such that few electron-neutral collisions occur, the discharge voltage begins to increase until the discharge is 'extinguished'. Helm first proposed [133] that this was due to secondary
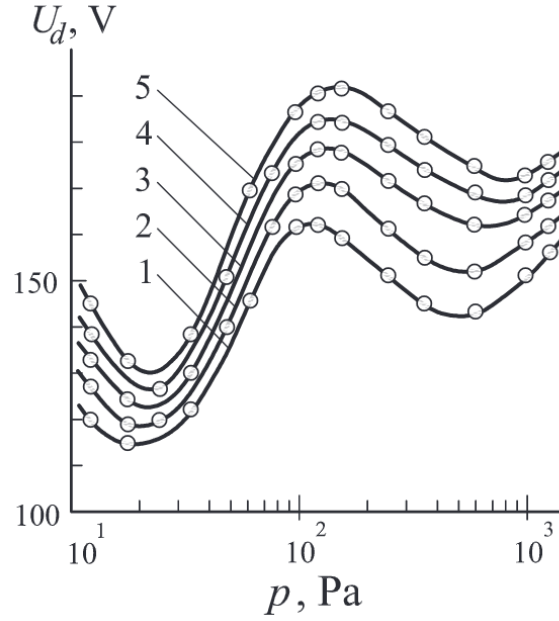
FIGURE 1.13 – The dependence of the discharge voltage U_d on helium pressure for a nickel hollow cathode with $r_{hc} = 15$ mm and length 250 mm for discharge currents $I = 25$ (1), 50 (2), 100 (3), 150 (4), 200 (5) mA, taken from [4]. The hollow cathode effect is shown to optimally occur for low pressures between the minima and maxima, while after $p = 150$ Pa the cathode operates as a regular glow discharge.

electrons being able to reach the opposite cathode surface and be absorbed there. Before this point, the hollow cathode has been observed to become filled with a positive space charge [134] with focused diverging electron beams from it [125, 135], reminiscent of ambipolar effects. This observation is supported by the fact that an electron beam can maintain a small longitudinal spread in velocities beyond what might otherwise be expected [136]. This low pressure regime (near to 1 mTorr) will characterise the pressure of the hollow cathode and planar abnormal glow discharges analysed in this thesis.

The change in d_c from that predicted in Equations 1.19 to 1.23 due to the hollow cathode effect is not well characterised. The similarity laws are in fact technically invalid for hollow cathode discharges since V_c, d_c, and the current density $\tilde{J}$ become somewhat independent of each other. This disadvantage is well compensated by instead being able to isolate a single variable in experiment [18]. Also, the tendency of a low pressure hollow cathode to behave somewhat as an abnormal glow discharge has been somewhat verified by the observation that $\tilde{J}$ arrives evenly distributed across the inner cathode surface [137]. The electric field of the cathode fall within cylindrical cathodes has been measured as remaining linear [138] and has been approximated as following [18]

$$\tilde{\boldsymbol{E}}\left(r\right) = \frac{2V_c}{d_c^2}\left(r + d_c - r_{hc}\right).\tag{1.36}$$

Stockhausen and Kock [127] have addressed the unknown cathode sheath width with reasonable success against experiment by introducing a free scaling parameter $d_c \to \alpha d_c$ into MC modelling

of the spectral emission output from a cylindrical hollow cathode, finding that $2 \leq \alpha \leq 4.5$. Hagelaar *et al.* [139] derived an analytic self-sustainment condition analogous to Equation 1.18 for a hollow cathode discharge:

$$\frac{\exp\left(\alpha_{\mathrm{T}} d_{\mathrm{c}}\right) - 1 - \alpha d_{\mathrm{c}}}{2\left(\alpha_{\mathrm{T}} d_{\mathrm{c}}\right)^2} \gamma_{\mathrm{e}} q_{\mathrm{e}} V_{\mathrm{c}} = W, \tag{1.37}$$

where W is a parameter that describes the total power lost by electrons in all collisions divided by their ionisation rate. This criterion describes how the sheath thickness in a hollow cathode discharge adjusts such that enough energy is spent in ionisation to sustain the discharge through secondary electron emission. Many experimentalists have further noted that the $V - i$ characteristic of hollow cathodes are generally more stable than that of a regular glow discharge [130, 140, 141] and can even exhibit 'negative resistance' [140, 142] where the cathode bias decreases with increasing discharge current.

1.3.1 Pendular electron motion

The cause of the hollow cathode effect has been attributed to *pendular electron motion* [127], a processes depicted in Figure 1.14. Pendular electrons are a population of secondary electrons
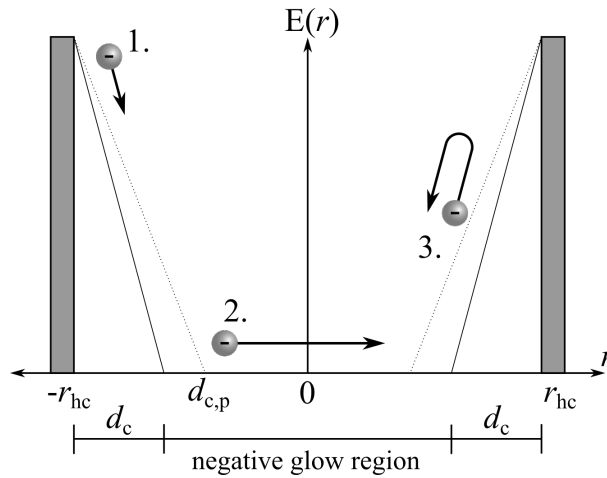

FIGURE 1.14 – The pendulum effect for secondary electrons within the radial electric field of a hollow cathode of radius r_{hc}. The solid line demonstrates the approximately linear electric field within the cathode sheath of radius d_{c}, demonstrating the reduction in sheath width due to hollow cathode effect from that of an equivalent plane discharge $d_{\mathrm{c,p}}$ discussed in Section 1.1.6 (with corresponding field shown by the dotted line). 1. A secondary electron is created within the cathode sheath and accelerated towards the cathode centre. 2. The electron traverses the overlapping negative glow at maximum energy, efficiently ionising and exciting the background gas. 3. The electron decelerates and reverses direction in the opposite cathode sheath, repeating the process in a pendulum-like motion.

that oscillate within the electric potential well created between opposite surfaces of the cathode, or indeed within any electrostatic potential trap [4]. Their repeated motion through the enclosed negative glow results in a significant increase in their effective inelastic mean free path through

this region. Pendular electrons were first detected by replacing part of a hollow cathode wall with an electrostatic energy analyser which was able to detect the significant density of radial beam electrons [133]. The confining potential well manifests as low internal electric fields axially and high electric fields radially in hollow cathode discharges with pressures above 0.1 Torr [97, 143–145]. The highly energetic pendular electrons are thus reasonably well confined to the hollow cathode centre at a rate inversely proportional to the reduced cathode separation $d_{\mathrm{hc}}p$ [18]. The amount of energy transferred from secondary electrons to the contained discharge is increased, manifesting as an increased ionisation and radiation densities there [139, 143]. Electrostatic probe [146] and analyser [144] measurements within cylindrical hollow cathodes have found similar or greater local densities of non-Maxwellian and often isotropic energetic electron populations to the low temperature bulk population.

The relatively high space charge caused by the increased rate of ionisation contributes to forming a virtual anode within the cathode. This in turn decreases the cathode sheath width [91, 97, 127, 132], allowing a greater proportion of ions and electrons created there to reach high energies. Ions and photons created within the negative glow of the hollow cathode are much more likely to reach an inner surface of the cathode by ambipolar diffusion or purely geometric considerations than in a plane cathode system [132]. The large fraction of radial ion diffusion increases the number of secondary electrons generated within the cathode, creating further internal ionisation in a feedback loop. Given the right conditions, this effect has been observed [91, 139] to cause the majority of discharge generation to occur within the cathode cavity even in discharge systems much larger than the cathode itself. Indeed, the distance of the maximum density of charged particle populations from the cathode centre has been found to be inversely proportional to the applied pressure, consistent with the pendular electron model [129, 143]. Ions that manage to drift axially from the cathode interior or charge exchange along the way form the divergent ion and neutral beams associated with the hollow cathode effect.

The hollow cathode effect has led to the wide use of hollow cathodes in both research and industry as a line source for analytical chemistry [91], as spectral lamps [130], as a laser component [109, 147], in thin film deposition and plasma processing [148], for holographic recording [149], and in circuit voltage stabilisation [142]. Most of these applications use high operating pressures towards the upper end of a normal glow discharge regime and into atmospheric discharges and arcs (regions H onwards in Figure 1.8). Hollow cathode discharges at pressures below 100 mTorr have received relatively little analysis [131], to the best knowledge of the author. When hollow cathodes are used below this pressure range, the analysis of the hollow cathode is often incidental within a study intended for other purposes like in satellite thrusters [5, 6] and IEC nuclear fusion systems [150, 151]. Little is known as to how the hollow cathode effect is changed if the discharge pressure is decreased to a point that opposite facing cathode sheathes begin to overlap and the negative glow region disappears. Evidence has been published that the neutral

and electron beams are still produced in hollow cathode discharges with pressures as low as 2 mTorr [125, 150, 151]. Furthermore, diverging neutral and ion beams have been observed in satellite thruster systems which have a cathode geometry similar to a hollow cathode with a single aperture operated in the 10s of mTorr [6, 152]. The neutral beams are suspected to be caused by charge exchange interactions with diverging ions, suggesting that the hollow cathode virtual anode still manifests to some extent. Finally, whether the hollow cathode effect could contribute sufficiently to the formation of a virtual anode similar to those observed in IEC systems at these low discharge pressures remains to be seen.

1.3.2 Hybrid fluid hollow cathode modelling

The direct measurement of a discharge using electrostatic probes and analysers requires the introduction of a physical boundary as well as a further external field to the region being scrutinised. This undermines the value of measurements made internally to a hollow cathode given above. The closed nature of a hollow cathode also means that most optical measurements must either be taken along an integrated line of sight through the cathode or be taken around its exterior. The combination of these factors make it difficult to take reliable, spatially resolved measurements of the internal mechanics of the hollow cathode. Similarly, neither pure fluid or individual particle models have been able to capture all aspects of the hollow cathode effect to date. As a result, a hybrid MC fluid model has been developed by Bogaerts *et al.* [153–155] that has demonstrated great success in predicting the density and flux of both local and non-local charged species, as well as electric fields, emission, and even sputtering processes in hollow cathode glow discharges in argon. Here, ions and slow electrons are treated as a fluid while energetic electrons are tracked with an MC model. The solution to each model is fed in as updating parameters for the other model in iterative, staggered time steps. The energetic electron collision processes determine the source terms for the continuity equations governing the fluid species, while the fluid species determine the electric field as well as the source of energetic electrons from secondary electron emission by ion bombardment. This successfully predicted the development of a virtual anode with a negative plasma potential at the cathode centre as well as an increase in axial electric field (and hence in the energy of the diverging ion and neutral beams) with decreasing pressure. This type of virtual anode will be shown to match the description of the virtual anode that has been previously argued to instead arise from inertial ion confinement in discharge IEC devices [7]. The similarity between IEC discharge phenomena and many aspects of the hollow cathode effect such as this shall be used in Chapter 2 to argue that IEC devices in fact operate as a hybrid form of abnormal hollow cathode discharge.

1.4 Nuclear fusion and the IEC method

We have now established the requisite context to discuss the inertial electrostatic Confinement (IEC) method of achieving nuclear fusion. In this section we introduce nuclear fusion in the context of producing both electrical energy and controlled neutron radiation and lead to a review of the existing literature surrounding the IEC concept. The existing literature both in support of and opposing the ion convergence model shall then be discussed.

1.4.1 Nuclear development

Nuclear research proliferated rapidly from the start of the second world war as physicists quickly managed to control the atom well beyond previous expectation [156]. The rapid rise in nuclear fission research followed by the development of the hydrogen bomb by the 1950s led many nuclear scientists to believe that controlled nuclear fusion, hereby named 'fusion', was just around the corner. It was quickly shown that both fusion and fission could be utilised for the production of zero-carbon electricity as well as useful radio-isotopes for medical and industrial purposes that were previously unavailable to humanity [157]. Today, nuclear fission represents an available leading candidate for producing energy economically, being an on-demand, continuous, reliable source that can sustain vast electric grids, while also reducing humanities contribution to climate change [158]. Creating a single system that can maintain a controlled fusion reaction capable of releasing net positive total energy, however, has proven incredibly difficult. The ratio between the power output from a fusion reactor and the power input required to sustain the fusion reaction is quantified by the Q factor. Achieving a sustained fusion reaction with a Q factor above unity remains an era-defining milestone for modern physicists. Only now does this seem attainable in the near future, buoyed by the promise of a first plasma at ITER in 2025 [159] as well as recent successes in superconducting magnet technology and nuclear plasma confinement time [160]. These successes have heightened fusion research activity to a frenzy with immense levels of funding from both private industry and government agencies.

1.4.2 The benefits of nuclear fusion over fission

Fusion power stations and reactors in general offer many significant advantages over their fission counterparts. Fusion avoids the use or creation of heavy radio-nuclides, solving the contentious issues of nuclear waste storage or possible runaway nuclear explosions made infamous by the Chernobyl, Three Mile Island, and Fukushima disasters [161]. These events have swayed public support away from the use of fission reactors in many countries across the globe. The absence of heavy radio-nuclides means that fusion experimentation is not nearly as limited by the restrictive international regulations [162].

	Reaction pathway					%	Yield (MeV)
(1)	$^2_1$D	$+^3_1$T	$\rightarrow$	$^4_2$He (3.50)	$+$ $^1_0$n (14.1)	100	17.6
(2)	$^2_1$D	$+$ $^2_1$D	$\rightarrow$	$^3_1$T (1.01)	$+$ $^1_1$p (3.02)	50	4.03
(3)			$\rightarrow$	$^3_2$He (0.82)	$+$ $^1_0$n (2.45)	50	3.27
(4)	$^2_1$D	$+$ $^3_2$He	$\rightarrow$	$^4_2$He (3.6)	$+$ $^1_1$p (14.7)	100	18.3
(5)	$^1_1$p	$+$ $^{11}_5$B	$\rightarrow$ $3\,^4_2$He (8.7)			100	22.4

TABLE 1.1 – The most common fuels and reactions used in nuclear fusion reactors, taken from [158] and from [163] for the p-B pathway. The D-D reaction has two equally likely product pathways. The energy yield for each reaction is given.

The nuclear fusion reaction involves overcoming the immense coulomb repulsion between light nuclei to bring them to separations at which the strong force dominates, combining them into a single nucleus. This process directly converts a significant fraction of the reactant rest mass into a large amount of energy following Einstein's famous relation $E = mc^2$, where c is the speed of light in vacuum. This fundamental difference from the controlled explosion nature of a nuclear fission reactor means that fusion reactions require a constant input of energy to proceed. This stops fusion reactions from being able to proliferate exponentially. The emitted energy from fusing nuclei is largely proportioned into the lighter of the fusion products [164]. These can be captured and directly converted to electricity if the product is charged or indirectly through the heating of water into steam. The most common nuclear reactions used in controlled fusion reactors, the products they create, and the total energy yield per reaction are listed in Table 1.1. Collisional cross sections for each of these reactions are given on the left of Figure 1.15. Fusion occurs naturally in stars via the intense compression and heating of the stellar plasma by its immense gravitational potential well. On Earth, fusion reactions are predominantly achieved by creating a highly energetic plasma consisting of the desired fusion fuel [160]. The most common reaction type is currently the D-T reaction due to its high cross section at lower energies. However, tritium is radioactive with a half life of 12 years, meaning that is has a low natural abundance and adds significant engineering and supply issues to the design of a fusion reactor [165].

The fusion engineering challenge is not merely of achieving astronomical plasma temperatures, but in *containing* the plasma in such a way that the energy input to the device goes towards fusion reactions rather than damaging the containment vessel. The six-dimensional velocity integral used to calculate the fusion reaction rate for a given system (Equation 1.6) can be vastly simplified by instead being expressed as a function of the relative kinetic energy and effective temperature of the plasma [164];

$$\langle \sigma(K) v \rangle_{\text{rel}} = \sqrt{\frac{8k_\text{B}T_\text{eff}}{\pi M}} \left(\frac{1}{k_\text{B}T_\text{eff}} \right)^2 \int_0^\infty K_\text{rel}\sigma(K_\text{rel}) \exp\left[-\frac{K_\text{rel}}{k_\text{B}T_\text{eff}} \right] dK_\text{rel}, \quad T_\text{eff} = \frac{m_1 T_2 + m_2 T_1}{m_1 + m_2}, \tag{1.38}$$
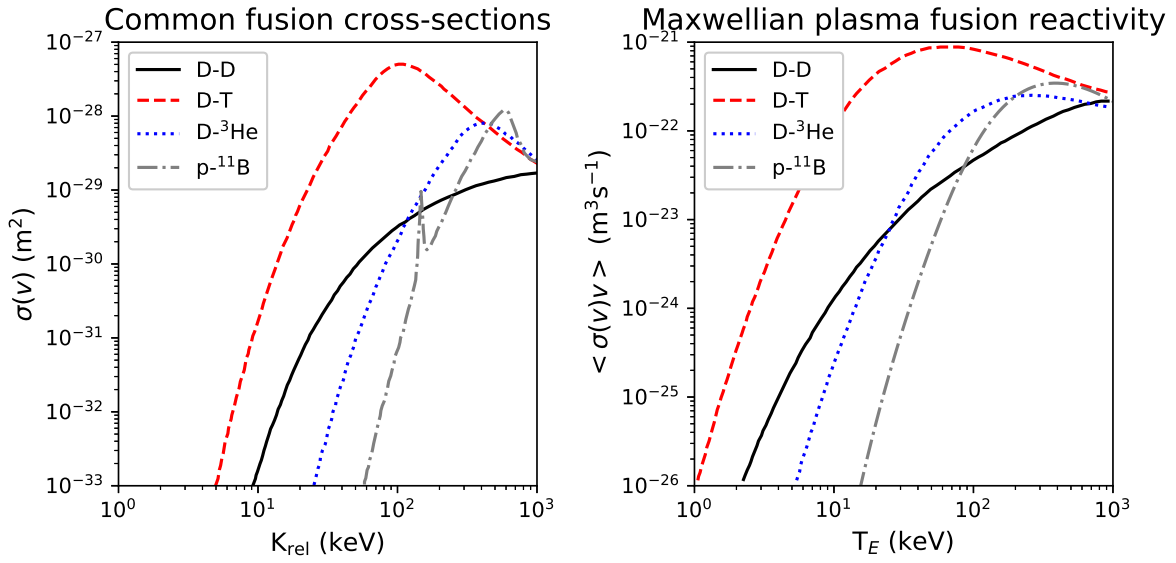
FIGURE 1.15 – *Left)* Cross sections for the common fusion reaction pathways listed in Table 1.1. *Right)* The fusion reactivity for each reaction pathway. Data taken from [158, 163, 166]

where $M = m_1 m_2/(m_1 + m_2)$ is the reduced mass of the interacting populations with masses m_1 and m_2. The reaction rate of nuclear fusion reactions for each reaction pathway in Table 1.1 for thermalised reactants in equal proportion are given on the right in Figure 1.15. Whether a fusion system of a contained Maxwellian plasma will meet the requirement for self-heating and subsequently a positive energy output is given by the Lawson criterion [167, 168],

$$n_f \tau_{\mathrm{E}} \geq \frac{12 T_{\mathrm{eff}}}{E_{\mathrm{y}} \langle \sigma v \rangle_{\mathrm{rel}}}, \tag{1.39}$$

where n_f is the density of confined fusion particles in the steady state, τ_{E} is the average confinement time of energy input into the system, and E_{y} is the energy yield of the reaction. The Lawson criterion describes the minimum of the $n_f \tau_{\mathrm{ec}}$ curve for each reaction type, corresponding to $T_{\mathrm{eff}} \approx 25$ keV for the D-T reaction and to a much less manageable $T_{\mathrm{eff}} \approx 85$ keV for the D-D and D-^{3}He reactions [168]. As a guideline value, achieving $Q \geq 1$ using a D-T plasma within an experimental system that can achieve $T_{\mathrm{eff}} = 15$ keV would require that

$$n_{\mathrm{f}} \cdot \tau_E \geq 10^{20} \ \mathrm{m}^{-3} \mathrm{s}. \tag{1.40}$$

This is a very difficult set of requirements to achieve, and as a result fusion energy reactors have to be designed on a massive and expensive scale in order to improve their plasma confinement and heating capabilities.

1.4.3   Neutrons as a fusion by-product

A more easily achieved output of a nuclear fusion reactor are the valuable resources that the products of some fusion reactions represent. Some of the reactions listed in Table 1.1 produce neutrons as a by-product; a useful commodity only otherwise available in significant quantities from fission reactors or radioactive substances. A neutron's lack of electric charge allows it to penetrate deep into a target substance and either excite, be captured into, or scatter directly from atomic nuclei. In this way, neutrons can be used in neutron imaging [169], Neutron Activation Analysis (NAA) [170, 171], and the production of radio-pharmaceuticals [157]. Each of these uses represents widespread and heavily depended upon markets of significant value to scientific, governmental, and commercial communities.

NAA is the high precision analysis of the characteristic gamma and neuclide emission from atomic nuclei that have been excited by the absorption of a neutron [171]. As each spectrum is unique to each isotope and is independent of the molecule the isotope exists within, it is possible to identify trace components of as little as 10^{-12} grams of a material otherwise inaccessible to direct observation. Similarly, the production of radio-isotopes by neutron capture for medical and industrial use is currently limited to viable nuclear reactors, cyclotrons, and synchrotrons. An example of this process is the production of ^{177}Lu, a common radionuclide used in cancer therapy and dosimetry [157],

$$^{176}_{71}\mathrm{Lu} + ^1_0\mathrm{n} \rightarrow ^{177}_{71}\mathrm{Lu}, \tag{1.41}$$

which has a half life of 6.647 days. Both NAA and radio-pharmaceutical production via neutron capture require a tune-able neutron flux in the order of $10^{13}\,\mathrm{cm}^{-2}\mathrm{s}^{-1}$ when considering transport delays and sample half-lives [157]. Radio-pharmaceutical production is currently listed as a critical technology in the national interest by the Australian government for which new methods of production are desired [172].

As of 2022, $Q = 1.5$ has reportedly been achieved using inertial confinement fusion [173, 174], in which the photon pressure from an immense laser is used to compress a pellet of D-T fusion materials into a reaction. These reports are promising and symbolic but are still at the stage of press reports and have not yet been replicated at the time of submission of this thesis. Further, inertial confinement methods do not provide an obvious pathway to achieving a sustained reaction useful within a power station. The best funded and currently leading candidate for achieving a sustained $Q > 1$ fusion reaction is that of magnetic confinement devices, with the ITER tokamak the most prominent example [159]. Magnetic confinement devices make use of the magnetic aspect of the Lorentz force (Equation 1.1) to trap charged particles along restricted paths that do not intersect with the chambers walls of the device [160, 175]. Large scale inertial and magnetic confinement methods suffer from requiring expensive, state of the art experimental

equipment. Project timelines can extend for decades with costs in the order of billions to tens of billions of USD before a fusion reaction is achieved.

The work in this thesis is instead focused on the substantially simpler, cheaper, and experimentally conducive nuclear fusion mechanism of inertial electrostatic confinement. There are multiple reasons for this angle of approach despite the fact that IEC devices are unlikely to achieve $Q > 1$ in a reasonable time frame. Mainly, the IEC mechanism shows promise for the design of small scale, safe, and tune-able neutron production devices that can be readily transported a desired location [170, 176–178]. It is also hoped to be a simpler mechanism for energy production if IEC research was ever to receive funding at a similar level to other fusion methods.

1.5   IEC devices

Inertial electrostatic confinement in its ideal conception [8, 179–183] is a method of accelerating positive ions to high energies and confining them into an inertial oscillation about a high density core using electrostatic forces alone. In this way, it is proposed that fusion fuel can be contained at high densities in the core with long confinement times. To date, rudimentary IEC devices largely intended as a proof of concept have demonstrated neutron production rates up to 10^8 using the $D - D$ reaction [176, 177, 181, 184–186], with orders of magnitude of improvement yet available [178]. The fusion reaction rate in IEC systems has also been shown to scale in proportion with the system current and with the square of the applied voltage [187, 188]. The maximum fusion rate achievable by scaling the size and power input of an IEC device towards levels that would be required for a positive energy gain is not known. It may therefore be possible to close the many orders of magnitude gap between current IEC neutron rates and the fluence required for NAA and radio-nuclide production. For this reason, IEC devices have been studied in Australia [150, 189–193], Europe [194, 195], Iran [196–198], Japan [199–202], and the United States [10, 203–207]. Continuing research into IEC devices has slowed in recent decades as the maximum fusion reaction rate achieved has remained stagnant. This limit may be attributable not to insurmountable issues with the electrostatic fusion concept but rather to a fundamental misclassification of the physics of the IEC device.

There are two over-arching designs of IEC device which we here label according to their main fusion reaction pathway: charged beam IEC devices and discharge operated IEC devices. Examples of the critical components of each design is given in Figure 1.16 and will be discussed below. The proposed physical mechanism of both designs is to create a deeply negative and spherically symmetric electrostatic potential well at the centre of a highly evacuated chamber. Positive ions that are created throughout the vacuum chamber by a discharge or injected as a beam radially converge into the well under acceleration by its potential. The spherical symmetry

of the theorised convergence causes ions to simultaneously reach high energies as well as a high density at the centre of the device, creating a 'fusion core' there [7]. Ions that do not undergo a fusion reaction are supposed to be carried through the potential well by their inertia and decelerated to a stop at the equipotential radius at which they were created. The ions can pass through the fusion core multiple times due to this oscillatory inertial confinement, increasing both the fusion core density and the total effective confinement time. Any ion that is instead absorbed by surfaces in the system, neutralised by electron recombination, or is scattered out of the potential well or loses energy through a collision reduces the fusion efficiency of the device. The beam-beam and discharge IEC methods differ in their methods of creating the potential well in a trade off between producing uniform charge distributions, maximising ion re-circulations, and simplicity of the design.

1.5.1   Charged beam IEC devices

Similar proposals for the first IEC designs were proposed by Elmore, Tuck, Watson [179] (Figure 1.16a)) and by Farnsworth and Hirsch in their 'Fusor' concept [9, 181, 208–210] (Figure 1.16b)) to achieve fusion reactions between radially converging ion beams. Elmore *et al.* [179] proposed the use of a spherical, highly transparent gridded anode contained within a concentric, electron emitting cathode in a system with less than 1 mTorr of background gas. Electrons are emitted from the surface with a spherically symmetric distribution, and are accelerated to system centre by the anode grid. If the electrons have a purely radial velocity, they are theorised to decelerate as they approach a high density core of negative space charge with characteristic radius r_f due to their mutual repulsion. The electrons form a deep potential well or 'virtual cathode' there as outlined in the potential diagram in Figure 1.16a). This analysis was an extension of Langmuir's proposal for space charge limited current between concentric spheres [211] to higher electron energies. Ions that are introduced within the anode grid using external beams or otherwise are then confined to the virtual cathode. The lack of a physical cathode grid and the low probability of scattering events due to the system pressure improves the number of possible ion re-circulations ζ_i. Two ion beams with velocities $\tilde{\boldsymbol{v}}_1$ and $\tilde{\boldsymbol{v}}_2$ that intersect in the fusion core at an angle θ gain an increase in relative kinetic energy compared to a beam-target system according to

$$K_{\text{rel}} = \frac{1}{2}M\tilde{\boldsymbol{v}}_{\text{rel}}^2, \quad \tilde{\boldsymbol{v}}_{\text{rel}} = \left(\frac{v_2 \cos\theta + v_1}{1 - v_1 v_2 \cos\theta/c^2}, \ \frac{v_2 \sin\theta}{\gamma_l \left(1 - v_1 v_2 \cos\theta/c^2\right)}, \ 0 \right), \qquad (1.42)$$

where $\tilde{\boldsymbol{v}}_{\text{rel}}$ is found by considering a co-ordinate frame moving with velocity $\tilde{\boldsymbol{v}}_1$ and $\gamma_l = 1/\sqrt{1 - v_1^2/c^2}$ is the Lorentz factor. This makes it easier to reach collision velocities that maximise the fusion reaction rates given in Figure 1.15. The anode grid will have a transparency $\eta = A_{\text{trs}}/A_{\text{tot}}$, where A_{trs} is the surface area of the anode that is transparent and A_{tot} is the total surface area of the sphere with radius equal to the anode radius. The total electron current entering the core through this anode in the steady state $i_{\text{e},0}$, and hence the magnitude of the
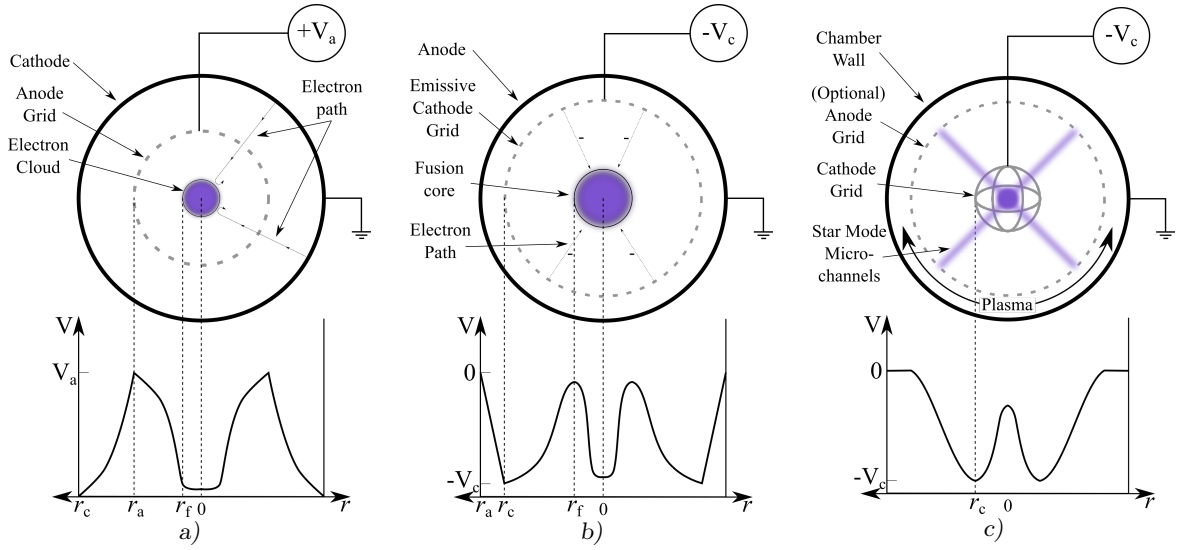
FIGURE 1.16 – The main IEC configurations (above) with examples of possible electric potential distributions within the system (below). *a)* The charged-beam IEC design by Elmore *et al.* *b)* The charged-beam Farnsworth-Hirsch Fusor. *c)* A typical discharge operated IEC system.

potential well formed, is then a multiple of the electron current emitted from the cathode $i_{e,c}$ [212]

$$i_{e,0} = \left(\frac{r_c}{r_f}\right)^2 \frac{\zeta_e i_{e,c}}{2} = \left(\frac{r_c}{r_f}\right)^2 \frac{\eta}{1-\eta^2}\frac{i_{e,c}}{2}, \tag{1.43}$$

where r_c is the radius of the cathode and ζ_e is the average number of times an electron passes through the anode grid before it is lost. Even within this highly idealised system, Elmore *et al.* [179] show that the requirements for a break-even fusion power output of such a device is given by

$$Q = \frac{n_{i,f}^2 r_f^3 \left[\frac{\pi}{3} E_{\text{D-T}} \langle \sigma_f \tilde{\boldsymbol{v}}_{\text{rel}} \rangle\right]}{i_e V_a} \zeta_e \geq 1, \tag{1.44}$$

where $n_{i,f}$ is the ion density at the fusion core, $E_{\text{D-T}}$ is the energy released in the D-T fusion reaction, and V_a is the positive bias applied to the anode. This implies a necessary electron current of $i_{e,c}$ in the order of 10^{14} A given the suggested operating conditions for charged beam IEC devices. This is not feasible even in a rapidly pulsed system. Pulsing the applied voltage to the anode has been suggested to improve the formation of alternating potential wells at the cathode centre [213, 214], although these results could not be exactly reproduced by Bandara and Khachan [215].

The Farnsworth-Hirsch fusor [9, 181, 208] follows the same principle but uses the radially converging electron beams to ionise a low density background gas within a cathode grid (Figure 1.16b)). The presence of a background gas will increase collisional losses from the system but adds the benefit of the creation of space charge in the fusion core, significantly reducing the required power input to manageable levels. This must be carefully balanced since converging ions will create their own positive potential well within the fusion core that acts to counteract

the virtual cathode that confines them.

If electrons and ions are created in symmetric distributions on equipotential surfaces at different radii without any angular momentum relative to their trajectories, they will form a possibly infinite series of nested alternating potential wells at the fusion core, termed 'Poissors' [7]. In practice, charged particles are created at various radii within the system and gain angular momentum through collisions, causing possible Poissors to combine into a lower order of alternating wells. The resulting 'double well' virtual anode that is proposed to form is demonstrated in the potential diagram in Figure 1.16b). Swanson *et al.* [216, 217] have used the diameter of an electron beam as observed on a phosphor screen that passed through the fusion core of a Fusor in deuterium to infer that it is possible to form a triple well structure. Otherwise, a lone virtual anode in a beam IEC system would reduce the expected fusion efficiency according to the converging ion theory by decreasing the maximum kinetic energy of ions in the fusion core.

Ions are argued to largely thermalise into a Maxwellian distribution within the fusion core of a Fusor system [7]. In this case, particles that up-scatter into the high energy tail of the distribution can escape the potential well and are lost to the system. The remaining population can be confined with achievable anode voltages as compared to the system shown in Figure 1.16a). Farnsworth and Hirsch have given a theoretical treatment to show that useful fusion yields are possible in these highly idealised conditions [181, 208, 212]. Rider [218, 219] gave a theoretical counter-argument showing that the rate of energy loss through up-scattering will always outweigh the fusion energy gain. Chacón *et al.* [220] later criticised the assumptions used by Rider with an argument that used a uniform, collisionless Fokker-Plank computational model of a Fusor to show the possibility of achieving $Q > 100$. The stability and depth of the electrostatic potential well can also be theoretically increased by injecting external ion beams into the system [221]. This would reduce the angular momentum of the ion population relative to its radial momentum, causing steeper potential gradients at the fusion core. In practice, it remains difficult to inject ions into the system with low enough kinetic energy such that they are not able to escape the virtual cathode and be absorbed by the cathode surface opposite to its starting point. This, combined with increased losses due to electron and ion scattering with the background gas, limit the functionality of the Fusor relative to its experimental complexity. Hirsch [181] has reported maximum neutron production rates in the order of $10^9 \, \text{s}^{-1}$ using D-T fuel (approximately equivalent to $10^7 \, \text{s}^{-1}$ using D-D fuel), although Gardner *et al.* [176, 221] report achieving only 0.1-0.5 of this rate in a similar system. The lack of high rates of ion confinement has led to the Polywell IEC design by Bussard [222], in which magnetic fields are used without a cathode grid to confine electrons and deflect ions from surfaces. Both types of charged beam systems discussed in this section are beset by defects in both the fundamental physics and experimental design that are difficult to overcome [218]. For this reason, many experimentalists instead use discharge operated devices.

1.5.2 Discharge operated IEC devices

A basic schematic of a discharge operated IEC device is given in Figure 1.16c). The discharge operated IEC device represents the balance between experimental expedience and optimising the theoretical yield of a device, and has been shown to produce neutrons using D-D fusion in the order of $10^7 \, \text{s}^{-1}$ [185]. Here, the negative potential well is formed using a physical cathode grid. Maintaining a high number of average ion recirculations ζ_i requires that the cathode grid be highly transparent. The source of ions is then generated by a discharge that is initiated within the system. According to the majority of IEC literature, ions are drawn towards the highly transparent cathode grid, converging to form the fusion core and virtual anode there [10, 177, 180, 186, 194–199, 205, 207, 223–226]. In recent years, however, experimental evidence has been building towards the exact opposite mechanism; ions diverging from low velocities at the cathode centre under acceleration by a virtual anode [150, 151, 189–192, 227, 228] resulting in a majority of fusion reactions occurring exterior to the fusion core [187, 200–202]. That such a discrepancy could exist is hypothesised here to be due to the inferential nature of plasma diagnostic techniques. In this case, an experimenter's bias can influence the interpretation of any inferred discharge parameters. The prevalence of this issue will also be discussed in Chapters 3 and 5 where a common assumption used in the analysis of the laser-induced fluorescence diagnostic is tested for its validity. In this section, we present both supporting and detracting arguments for the discharge IEC concept from the literature as they stood before the work presented in this thesis.

Maintaining a discharge with a high ion density requires that the background gas pressure be large enough for electron-neutral ionisation collisions to occur frequently. However, any ion travelling in its parent neutral gas experiences a high rate of inelastic collisional energy loss through charge exchange as well as other collisional processes [229]. Ions or the highly energetic neutrals created by their charge exchange with the background gas can both undergo fusion in collisions with the background gas. This has led to observations of a greater total fusion reactivity outside of the cathode region [187, 207]. IEC devices are usually operated between 1 - 50 mTorr as a balance between these collisional loss processes, maximising the fusion reactivity, and maintaining the discharge [7]. Most ion-neutral inelastic collisional process cross-sections decrease monotonically beyond 100 eV of collisional kinetic energy [13], resulting in a mean free path that increases with the ion velocity (see Section 1.1.2). It has been argued [7] that so long as ions are accelerated to high energies within single mean free path by the cathode grid, they will still be able to recirculate multiple times in the system. The question remains as to the high probability of undergoing the charge exchange reaction as the ion is decelerated before reflection for each re-circulation [230]. The double well distribution given in Figure 1.16c) is thus the highest order series of potential well that has been observed by proton collimation

[201], Doppler spectroscopy [189, 190], dusty plasma diagnostics [191], and Langmuir probe measurements [231]. The magnitude of the virtual anode recorded is on the order of 25 % of the potential difference applied to the cathode.

The theoretical possibility of multiple ion re-circulations is reduced by the fact that ions are created at different radii along the potential well and suffer significant elastic collisions. This increases the angular momentum of the population and thermalises them to some extent, reducing the likelihood of clean re-circulations through the cathode grid in useful quantities. Miley [185, 224] states that this issue is rectified by a peculiar discharge state particular to IEC grids known as the 'star mode'. This name arises from the radial spokes of light that emanate from a highly emissive region at the cathode centre, as has been illustrated in Figure 1.16c). IEC devices are therefore usually operated in this mode. It is posited that the radial spokes of light emission (named 'microchannels' in IEC literature) that pass through openings in the cathode grid are caused by radially converging ion beams. Miley [7] states that this behaviour has been verified by "magnetic deflection experiments", although no further detail is given. It is interesting to note that a radially converging ion current would be magnetically deflected in the same direction as a radially diverging electron current. It is asserted that the positive ions travel through the grid openings rather than being attracted to the more negative grid wires due to a self-selection process. If only the ions that travel in the microchannels survive, they will ionise within these trajectories that can cause more ions to travel within the microchannel. This behaviour has been demonstrated using the SIMION computational code [224] (initially designed for very low current particle guns) which calculates the vacuum potential created by an electrode by solving Poisson's equation 1.25 in the absence of charges. This method is used to predict the trajectories of ions while ignoring the effect of the ionic space charge, a fundamental feature of the IEC discharge. Furthermore, proponents of the converging microchannel argument agree that emissive beams in other IEC discharge modes come from diverging electrons [10, 196].

The converging ion argument relying on directed microchannels for discharge operated IEC devices has not stood up to experimental verification. Multiple experimental methods have provided strong evidence that ions are being created in high densities at the cathode centre and then being accelerated outward [150, 151, 189–192]. Ions begin with low velocities at the cathode centre in these experiments and are observed to have velocities directed predominantly outwards from it that exhibit acceleration up to the cathode radius. Converging ion beams that passed through the cathode centre would instead register as velocities in both radial directions along with a maximum velocity occurring toward to the cathode centre.

Furthermore, it has been demonstrated that the majority of total fusion reactions that occur in a discharge operated IEC do not occur within the originally defined 'fusion core' [187, 200–202,

207, 227]. Both the cathode and anode material in these cases have been shown to be a dominant factor in determining measured neutron rates in low power IEC discharges in deuterium. If the cathode is kept at low enough temperatures such that surface adsorption of the background gas is likely, a majority of the total fusion yield can occur on the cathode surface [228]. The adsorbed gas on the cathode forms a measurably high density of targets that ions strike after having experienced the maximum accelerating potential difference available to them. Bakr *et al.* [186] have demonstrated that even the vacuum chamber material significantly affects the neutron production rate, consistent with high energy neutrals striking its surface. They posit that this is due to converging ions undergoing charge exchange and passing through the fusion core rather than diverging ion motion, but provide no supporting evidence for this claim. The diverging ion and surface fusion mechanisms represent a truly fundamental change in discharge IEC design for maximum fusion yield considering the possibility of cooling the cathode using an exterior coolant system. Maximising the cathode transparency to ensure ion convergence and re-circulation may not be fruitful.

Many facets of discharge theory also point away from ion convergence and towards the ion divergence theory. The majority of the optical emission processes in most discharges are caused by electron flow, as discussed in Section 1.1.3. This would lead to the conclusion that the observed microchannels in the star mode be comprised of radially divergent electron beams. Fitzgerald [125] demonstrated that the microchannel of a cylindrical IEC operated in star mode excited a phosphor-coated screen as expected for a highly collimated electron beam with an energy equivalent to the anode-cathode potential difference; the microchannel consisted of a diverging electron beam. Furthermore, much of the analysis of the converging ion theory has involved the calculation of the potential distribution in vacuum. The formation of a cathode sheath by the discharge would shield much of the discharge volume from the negative potential of the cathode, reducing the radii at which ions are collected towards the cathode.

In fact, the formation of a virtual anode with diverging ion, neutral, and electron beams in a region of a discharge surrounded by a cathode is a description of the hollow cathode effect (discussed in Section 1.3). Despite the transparency of IEC cathodes, some pendular electron motion could still occur that may bring the majority of the discharge to the cathode interior. In fact, this is a well known mechanism for cathodes that form an electrostatic trap for electrons at pressures near to 1 mTorr [4]. In this case the electrostatic trap was defined as any cathode that forms a cavity, including the use of wires in various encapsulating shapes. Early observations of solid hollow cathodes at very low pressures found focused diverging electron beams [135] as well as the formation of positive space charge interior to the cathode [134]. Similar work on cathodes formed by wires into various spiral shapes that enclosed a volume of space noted many aspects of the hollow cathode effect at low pressures [126]. For example, Stephenson [126] noted the formation of a "bright bead of glow ... in the centre of the cathode" of much greater brightness

than the rest of the discharge volume, as well as a decrease in the cathode sheath width once opposing negative glows overlapped.

Work on glow discharges with pressures at or below 10 mTorr aimed at producing fast neutral beams regularly note the prevalence of diverging fast electron beams when the cathode geometry, as a gridded or solid hollow cathode, forms an electrostatic potential trap for them [4, 232, 233]. Builth-Williams has also demonstrated [234] that replacing the traditional IEC spherical grid with various hollow cathode geometries improved the fusion neutron yield by more than an order of magnitude. This result is in line with the surface fusion observations discussed above. Altogether, these results are a description of the hollow cathode effect. This points to the fact that discharge operated IEC devices seem to operate as a hybrid form of hollow cathode discharge. It is possible that these various cathode geometries result in the pendular trapping of secondary electrons such that a virtual anode is formed. This virtual anode could in turn accelerate the high density of positive ions created within it outward from the cathode, resulting in the observed ion divergence phenomenon. Converging ions will always occur to some extent in a discharge IEC system. However, the majority of diverging ions are likely to form the dominant fusion pathway. In summary, these observations correlate with the hypothesis that gridded IEC devices are better described as a hollow cathode discharge. If this is true, then discharge IEC devices do not exhibit ion convergence and fusion reactions are not being enhanced by confinement mechanisms. Further research is needed to confirm this hypothesis and distinguish which exact aspects of the hollow cathode effect would be most responsible for improving the magnitude of virtual anode that accelerates diverging ions.

1.6 Aim of this thesis

When this work was begun, the original aim was to investigate the hypothesis that the ion divergence phenomenon observed in gridded IEC cathodes was a result of the hollow cathode effect. In attempting to prove this, however, it became necessary to analyse the laser-induced fluorescence diagnostic itself, involving discharge measurements taken with a Langmuir probe. This was to address evidence that arose that implicated a common inference that we had made in using LIF to observe ion divergence was flawed. As a result, this thesis contains a second body of work related more closely to improving the use of the Langmuir probe and LIF diagnostic methods so that the analysis of low pressure discharges may be more reliable in future.

In Chapter 2 we present the first experimentation that directly observes the relative rates of ion convergence and divergence in a discharge IEC device. This is achieved using LIF along the axis of a hybrid IEC/hollow cathode consisting of two co-axial wire rings that was intended to display characteristics of both discharge types. A virtual anode is shown to result from a cathode sheath

calculation, and the dominant diverging ion population can be replicated from it. In Chapter 3 we attempt to link different aspects of the hollow cathode effect to ion divergence in IEC using an LIF analysis on a cylindrical hollow cathode with solid walls. This instead reveals an anomalous increasing ion density in the cathode pre-sheath approaching the cathode. This implies that the metastable ions targeted for LIF analysis may be selectively created by energetic secondary electrons differently to the ground state ion population that they are assumed to be a representative of. In Chapter 4 we undertake a Langmuir probe analysis to determine the spatial distributions of secondary electron populations across a cathodic pre-sheath. A Bayesian estimation routine is developed to quantify experimental uncertainties and to address the over-fitting issue that arises in the analysis of multiple electronic currents to a single probe. The discharge parameters determined in Chapter 4 are then used in Chapter 5 to solve a simplified collisional rate equation of ArII metastables in a cathodic pre-sheath. An explanation for the anomalous ion density phenomenon is given, and more concrete boundaries on the validity of inferences made when using the LIF diagnostic are set. In summary, this information is used to re-analyse the conclusions of Chapters 2 and 3, such that the ion divergence phenomenon in discharge IEC devices is more firmly linked to the hollow cathode effect.

Chapter 2

The divergent ion model

In Chapter 1 we reviewed the literature both in favour of and opposing the proposed physical mechanism driving nuclear fusion interactions in discharge based IEC devices. The majority of research groups suggested the confinement of positive ions occurs due to their convergence to a high density fusion core. Ions that are absorbed by surfaces in the discharge represent energy losses, and the majority of fusion interactions are from accelerated ions striking each other or the background gas at high energies within the cathode. More recent evidence pointed toward effectively the opposite mechanism. Ions seem to be created at low velocity and high density at the cathode centre and accelerate outward in a divergent manner from a virtual anode that is established there. Ions reach their maximum velocity near the radius of the cathode surface, and fusion interactions occur between ions and both the background gas as well as adsorbed deuterium on surfaces. If this is true, it questions a large body of published work to an extent that requires very strong justification.

It then becomes an issue that the majority of the research demonstrating the ion divergence phenomena has been published by a single body; the Sydney University applied plasma physics research group that includes the author of this manuscript. The diagnostic methods used to observe the ion divergence phenomena also do not have excellent spatial resolution such that only inferences could be made about ion velocity distribution functions (IVDFs). For example, the dusty plasma diagnostic used by Khachan *et al.* [191] relied on the transfer of momentum between atoms or molecules to micro-particles to detect ions diverging from a central virtual anode. The Doppler analysis of the emission spectra in IEC [189, 190, 192] also required that ions first undergo charge transfer with deuterium neutrals since deuterium ions have no electron available for spectroscopic emission. These types of analyses determine information about the history of an ion through a different particle that has interacted with it.

Any counter-argument against the theory of IEC needs to be based on a proposed physical mechanism that can both explain the observed ion divergence and be tested in a direct way. The ideal experimental evidence for such a model needs to have enough spatial resolution to distinguish between ions that have converged and passed through the cathode centre or have diverged from it. In the following chapter we shall present the work relating to the measurement of IVDFs inside a hybrid IEC/hollow cathode using the laser-induced fluorescence diagnostic method. First, a summary of the key unpublished results from the author's honours thesis shall be given to provide context for the approach. This work indicated that low pressure hollow cathodes can develop a large virtual anode due to ambipolar effects and that the cathode geometry can significantly enhance the nuclear fusion rate when operated in IEC discharge conditions. Second, the laser-induced fluorescence diagnostic method will be introduced, followed by a description of the multipole discharge method used in the proceeding work. The research included in the first publication of this thesis [193] will then be given. Experimental evidence was confirmed by a rudimentary cathode sheath calculation in favour of the ion divergence theory in a hybrid IEC hollow cathode. A discussion is then given toward the hypothesis that most IEC devices operated in the normal or abnormal glow discharge regime are in fact operating as a hybrid form of a hollow cathode discharge. The absence of ambipolar effects in the hybrid IEC hollow cathode that were present in solid hollow cathodes is then discussed.

The work given in this chapter was performed before the anomalous ion behaviour was discovered that indicated flaws in the assumptions relating general and metastable IVDFs that are used in the laser-induced fluorescence diagnostic. As such, the diagnostic was used at a surface level without in depth analysis, and only a rudimentary introduction to the relevant literature is given below. Instead, the laser-induced fluorescence literature relevant to the anomalous ion density phenomenon will be presented in Chapter 3.

2.1   Motivation from previous work

Multiple observed factors summarised below seemed to indicate that IEC devices were operating as a form of hollow cathode discharge:

- A high density of low velocity ions and energetic electrons seem to be created within the cathode followed by their outward acceleration (given that the observed microchannels in IEC devices are likely to be diverging electron beams, discussed in Chapter 1.5.2);

- Previously unpublished experimental work within the Sydney University group [234] indicated that the use of a solid hollow cathode in place of a gridded spherical cathode resulted in an *increase* in the nuclear fusion yield for otherwise identical discharge conditions.

Furthermore, the flux of ions and electrons in the same direction given only a local negative electrostatic potential distribution within the cathode is a very close description of ambipolar effects, discussed in Chapter 1.1.4. This leads to a plausible hypothesis for the ion divergence phenomena. An IEC cathode would be able to trap pendular electrons similarly to a hollow cathode depending on its geometry. We consider if this could occur to the extent that the majority of ionisation is localised to the cathode centre in most discharge IEC devices. Electron beams would then leave this centre of high charge density and electric field more rapidly than ions, developing a positive space charge and hence a virtual anode there as a result of ambipolar drift or diffusion. Ions created by electron impact bombardment (the main creation mechanism in a glow discharge, see Section 1.1.8) gain negligible momentum from the ionisation process relative to their potential energy due to the cathode bias. The magnitude of this virtual anode relative to the cathode bias would therefore govern the maximum kinetic energy of this majority of centrally created ions, and hence be related to the nuclear fusion rate. A solid hollow cathode would result in a stronger manifestation of the hollow cathode effect than a gridded cathode since its geometry is more conducive for trapping pendular electrons, increasing the magnitude of the virtual anode. Finally, the increased surface area of a hollow cathode could actually contribute to an increased nuclear fusion rate [227, 228] for the low discharge powers often used in diagnostic experiments due to the high density of adsorbed fusion fuel there. If this ambipolar divergence hypothesis is correct, then the nuclear fusion rate should be highly dependent on the magnitude of the virtual anode that results from the cathode geometry.

The following work in Section 2.1 was submitted as part of the author's honours thesis and should not be considered for the examination of this thesis.

The ambipolar divergence hypothesis was tested by measuring the neutron production rate as a result of the D-D fusion reaction, listed in Table 1.1, for various hollow cathode geometries under otherwise identical filament mediated glow discharge conditions. The stainless steel hollow cathode geometries that were used are given in Figure 2.1. Each cathode was biased at -20 kV in 10 mTorr of deuterium gas with the thermionic filaments at a significantly lower magnitude of bias. The filaments were intended solely to initiate the discharge that was not self-sustaining using the cathode alone at this pressure. These cathode parameters represent a lower discharge power than is typically used in an IEC discharge that is intended to achieve a maximum nuclear fusion rate. In those cases the cathode is often biased at the order of -100 kV relative to the grounded vacuum chamber walls. A reduced discharge power is easier to achieve and remains useful for the diagnostic testing of nuclear discharges if the abnormal glow discharge regime can be maintained. This also avoids the dangerous radiation levels that a -100 kV discharge creates. It should be noted, however, that a lower discharge power does not heat the cathode to incandescence as is often the case when aiming for high fusion rates. Therefore, gases would remain
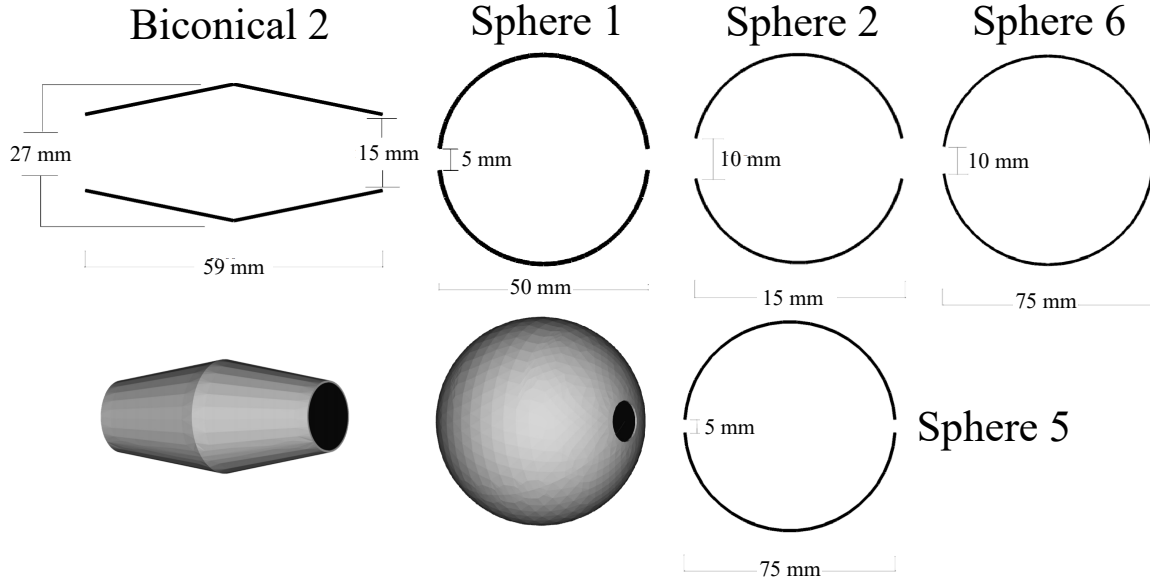
FIGURE 2.1 – The cathode geometries used in the author's honours work. The cathode names and their specifications are given alongside example CAD images.

adsorbed to the cathode surface at higher densities than is likely for a high power IEC discharge, increasing the contribution of the cathode surface to the fusion reaction rate. However, it would be possible to liquid cool an IEC device operated at high powers so that the benefit of surface fusion could still be maintained.

In the honours experiments the nuclear fusion rate was found to change by up to a factor of 14 with the different cathode geometries. The fusion rate was highest for Biconical 2 and Sphere 2, and decreased with a decreasing ratio of the aperture to cathode radius. The virtual anode created as a result of ambipolar diffusion (and not drift) was then numerically modelled for each cathode geometry. The potential distribution in vacuum was first calculated using a centered difference approximation of Laplace's equation (Poisson's Equation 1.25 in the absence of charges) in 2-D cylindrical co-ordinates and solved using a relaxation method as described in Chapter 1.2. An electron population was subsequently assumed to be created at a thermal velocity with $T_e = 3\,\text{eV}$ and a given density n_e at the cathode centre and to be accelerated outward by the vacuum potential, leaving behind an assumed stationary ion population of density $n_i = n_e$ (see Chapter 1.1.7). The resulting ambipolar field was calculated using the conservation of flux in one dimension without collisions (Equation 1.32) to track the electron density gradient $\nabla_{\tilde{x}} n_e / n_e$. The ambipolar field approximation (Equation 1.15) was then discretised and solved by ignoring ambipolar drift and assuming that $\mu_i, D_i \ll \mu_e, D_e$, such that

$$\tilde{E}_a \approx \frac{-D_e}{\mu_e} \frac{\nabla_{\tilde{x}} n_e}{n_e} \approx -\frac{k_B T_e}{q_e} \frac{\nabla_{\tilde{x}} n_e}{n_e} \tag{2.1}$$

This represents a zeroth order, collisionless approximation that should only be valid in the

absence of strong electric fields where Einstein's relation, given by Equation 1.13, is valid. Despite these issues, the calculation revealed a strong linear correlation between the average fusion rate and the magnitude of the predicted virtual anode created by ambipolar diffusion, shown in Figure 2.2. The R^2 value of a linear fit to the data is astonishingly close to 1, supporting the
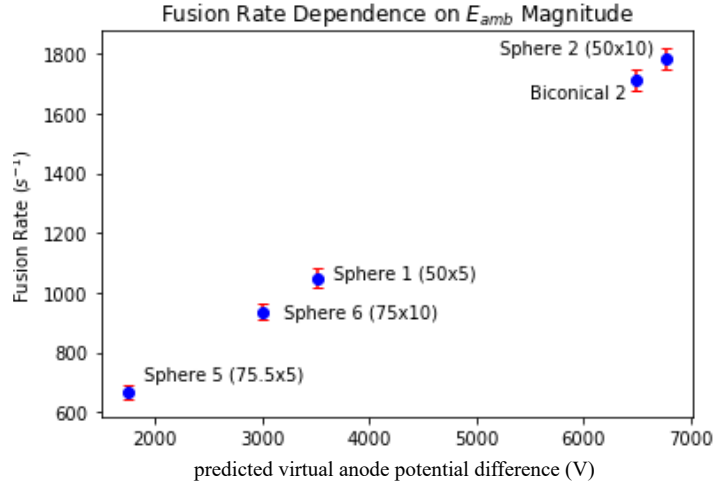

FIGURE 2.2 – The nuclear fusion rate against the predicted magnitude of the virtual anode for the cathode geometries given in Figure 2.1. $R^2 > 0.99$ for a linear fit.

ambipolar hypothesis. It should be noted, however, that an incorrect unit conversion was later discovered that had artificially increased the magnitude of the predicted virtual anodes by a factor of 100 towards more realistic values. This factor error did not affect the strength of the linear relationship given in Figure 2.2. Instead, this implied that a numerical factor based on an excluded physical mechanism was missing from the model, with likely possibilities including ambipolar drift effects and electron beam divergence in the radial dimension.

2.1.1 Implications for current research

The numerical model used in the work above contained too many unrealistic approximations to be considered rigorous enough for publication. However, the correlation given in Figure 2.2 implied that ambipolar effects were involved in the physical mechanism of IEC devices. A more sophisticated ambipolar model would need to be closely guided by experimental measurements of the magnitude and spatial distribution of virtual anodes. These measurements might be best achieved by the direct observation of the interior of a cathode that exhibits both the hollow cathode effect and is similar enough to a traditional IEC gridded cathode for a valid comparison. This set of criteria could be matched by using the laser-induced fluorescence diagnostic method on a 'two-ring' hybrid hollow cathode, shown in Figure 2.3. The two-ring cathode featured two loops of stainless steel wire with a diameter of 2 cm separated by a wire bar of length 2 cm. This type of cathode allows for a direct line of sight to the cathode interior and may exhibit enough internal reflection of secondary electrons to establish the hollow cathode effect.
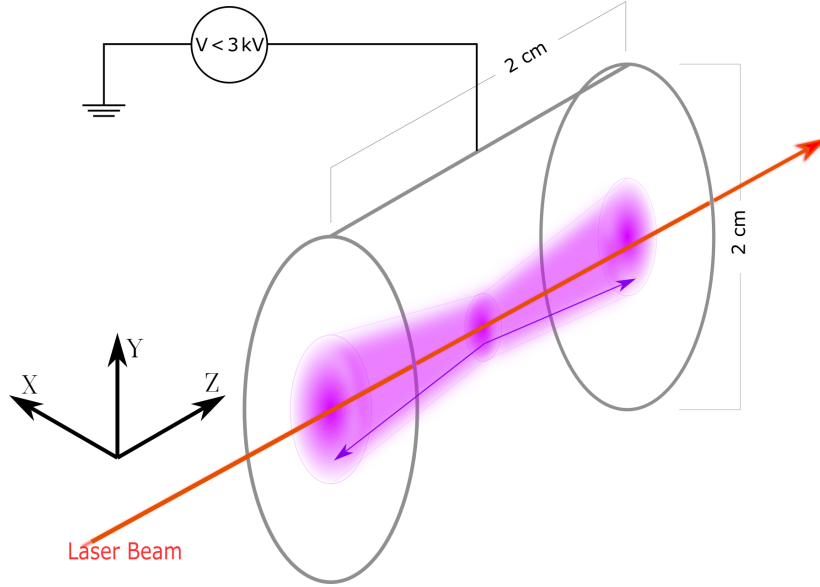
FIGURE 2.3 – Schematic diagram of the two-ring cathode showing the divergent plasma column between the cathode rings as described in Sec 2.6. The laser beam, used for LIF measurements, was aligned along the axis of symmetry of the rings along the center of the indicated discharge.

Furthermore, the cathode geometry would not interrupt ion convergence if that happens to be the dominant mechanism of ion transport. However, if ion divergence is found to be dominant, then this will likely be the case for a spherical cathode grid as well. The proceeding laser-induced fluorescence experiments were performed in a low pressure multipole discharge system. Both of these experimental systems have important impacts on the analysis, and are introduced below.

2.2   The laser-induced fluorescence (LIF) diagnostic method

The LIF method uses the laser pumping of a selected transition between two optically connected quantum levels of a particle in a target population to infer information about its velocity distribution function (VDF), $f_{t,v}$ [235]. More broadly, LIF uses the Doppler shifting of the absorption of a laser due to the relative motion of a target particle to relate the induced fluorescence spectrum to its VDF. The target transition between quantum states for a particle at rest will be pumped by photons with a frequency ν_0 that corresponds to the energy difference between the states $h\nu_0$, where h is Planck's constant. A laser that can produce a beam that can be scanned over a frequency range that contains ν_0 must be selected. The lasers used for LIF analysis ideally have a linewidth much less than the natural linewidth of the target transition that are a result of Doppler shifting induced by particle temperatures [236]. This ability to scan in frequency while maintaining a very narrow linewidth is usually achieved by having a powerful pumping laser excite a dye laser. Dye lasers use a liquid gain medium that can be tuned in frequency using a prism or diffraction grating [237]. An example of a common laser system used for LIF analysis is
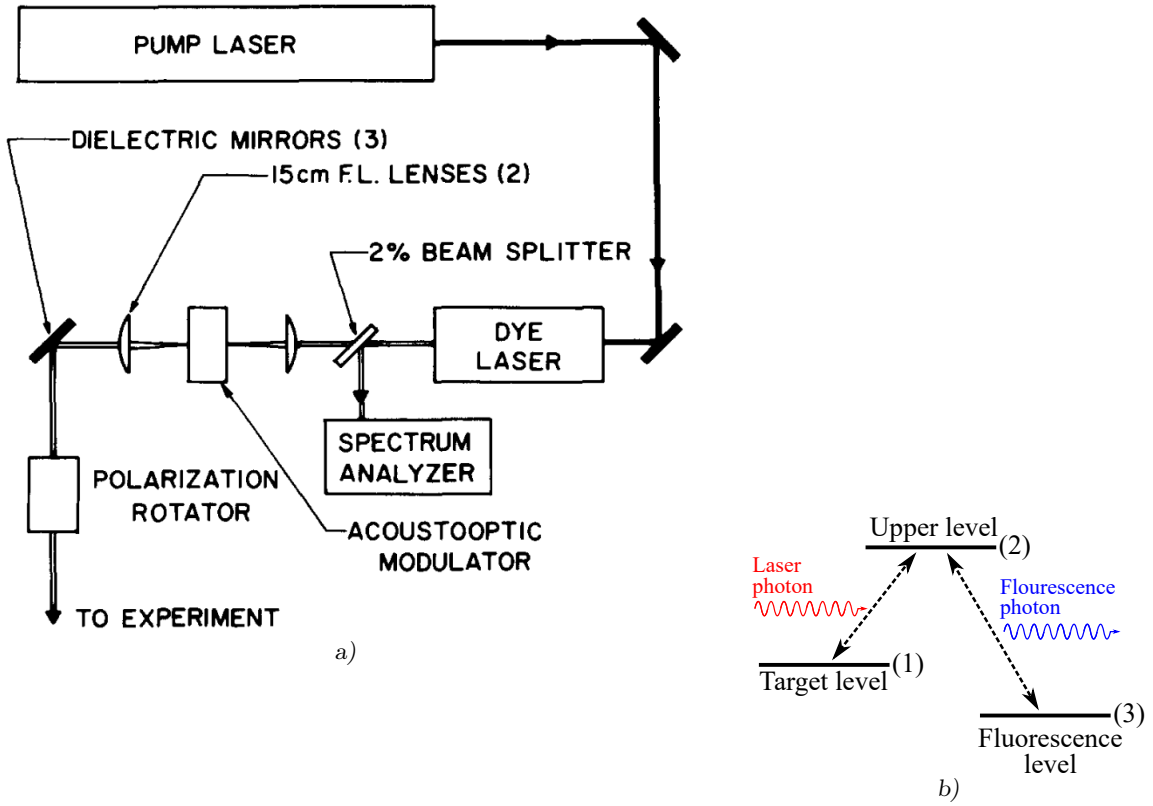
FIGURE 2.4 – *a)*: A tunable laser system used for LIF analysis, repurposed from Hill *et al.*
[236]. *b)* Laser-induced fluorescence of a set of quantum levels.

given in Figure 2.4a). A portion of the laser beam is diverted into an optical spectrum analysis
system so that the laser photon intensity entering the discharge, $I_l(\nu_l)$, for a laser frequency ν_l at
a particular time during a scan is known. This was achieved in the following experiments using
a Fabry-Pérot interferometer [238], which reflects the laser beam between mirrors surrounding
an optical cavity of a fixed length that contains a gas or discharge with a well known absorption
spectrum. A pure iodine discharge was used in this work. The Fabry-Pérot design allows for
a distinct absorption spectrum to be collected at the same time as the LIF signal with very
high precision in the wavelength domain. A laser photon with known frequency ν_l in a beam
with wave-vector $\tilde{\boldsymbol{k}}_l$ will only be absorbed by the target particle in the discharge if its velocity
along the direction $\hat{\boldsymbol{k}}_l$, $\tilde{\boldsymbol{v}}_{t,k}$, shifts the absorption frequency transition due to the Doppler effect
according to [235]

$$\tilde{\boldsymbol{v}}_{t,k} = c\frac{\nu_l - \nu_0}{\nu_l}. \tag{2.2}$$

The target transition is chosen such that the upper quantum level spontaneously decays in
typically $\gamma_0^{-1} \leq 10\,\text{ns}$ [235], where γ_0 is the spontaneous decay rate, through an optically allowed[1]
emissive transition to a third quantum level. This entire process has been depicted in Figure
2.4b). The induced rate of absorption of the laser beam $W(\tilde{\boldsymbol{v}}_t)$ by a target particle with total

---

[1]Transitions between particle states according to the Russel-Saunders notational scheme will be reviewed in
Chapter 3

velocity $\tilde{\boldsymbol{v}}_{\mathrm{t}}$ is then given by [236]

$$W\left(\tilde{\boldsymbol{v}}_{\mathrm{t}}\right) = \frac{c^2}{8\pi\nu_0^3}\gamma_0 \int I_{\mathrm{l}}\left(\nu\right) R\left(\nu - \tilde{\boldsymbol{k}}_{\mathrm{l}} \cdot \tilde{\boldsymbol{v}}_{\mathrm{t}}\right) d\nu, \tag{2.3}$$

where R is the resonance function of a stationary ion evaluated at the Doppler shifted frequency. If the transition is pumped weakly (i.e. if $W\left(\tilde{\boldsymbol{v}}_{\mathrm{t}}\right) \ll \gamma_0$), then the VDF of the upper quantum level, $f_{2,v}$, is related to the VDF of the lower level, $f_{1,v}$, by [236]

$$f_{2,v}\left(\tilde{\boldsymbol{v}}_{\mathrm{t}}\right) = \frac{W\left(\tilde{\boldsymbol{v}}_{\mathrm{t}}\right)}{\gamma_0} f_{1,v}\left(\tilde{\boldsymbol{v}}_{\mathrm{t}}\right). \tag{2.4}$$

W is usually approximated as a constant for laser line-widths small enough such that instrumental artefacts are avoided [236]. In this case, the fluorescence emission spectrum induced by the laser pumping becomes proportional to $f_{2,v}$ in the idealised case. The intensity of fluorescent emission from the target particles for an input laser frequency ν_{l} can then be related to the density of particles with a corresponding velocity in the direction of $\hat{\boldsymbol{k}}_{\mathrm{l}}$.

A small volume along the laser beam is then isolated using an optical array and the induced fluorescence spectrum is separated from the background plasma emission by 'chopping' the laser signal [235] in conjunction with using a lock-in amplifier. Chopping amounts to pulsing the laser on and off such that the emission from the observed volume can be compared with and without the LIF signal. This can be achieved mechanically by passing the laser beam through a rotating wheel containing slits separated at equal angles from each other, as was the case in this thesis. The lock-in amplifier then uses a process called 'heterodyning' [239], in which a total signal s_{tot} is formed by mixing two input signals, s_1 and s_2, in a way that a single one of signals can be isolated. In the case of LIF, the chopping process results in a sinusoidal reference signal of only the background radiation of the plasma when the laser is chopped off and a separate sinusoidal signal including the background plasma radiation and fluorescence signal when the laser is not being chopped. Integration of the combined signals over a specified time (known as the 'time constant') that must contain multiple oscillations of each signal attenuates other signals that are out of phase with the reference signal [239]. The time constant is usually chosen on the order of milliseconds to seconds as a trade-off between increasing the signal detection capabilities and a longer averaging of the detected signal so that it is slower to respond relative to the frequency scanning speed of the laser. This, in combination with a low-pass filter, allows signals of up to a million times smaller magnitude than that of the random background noise to be isolated [240]. By scanning the laser through a frequency range, then under ideal conditions, the intensity of the fluorescence signal remains proportional to the one-dimensional VDF along $\hat{\boldsymbol{k}}_{\mathrm{l}}$ at a location $\tilde{\boldsymbol{x}}$ across all velocities [236]. Furthermore, if certain criteria are met, the fluorescence signal intensity at two or more different locations can be compared to the input laser power P. This would mean that the relative density of the particle distribution functions at each location may be compared. In this way, the distributions of particle species can be locally determined by only

changing their state of excitation. This lack of discharge perturbation represents a significant advantage over other local discharge diagnostics such as electrostatic probes that are discussed in Chapter 4.

The term "ideal conditions" refers to a set of experimental restrictions and assumptions that must be carefully analysed for each situation in which LIF is being used. The most relevant of these to the current chapter is saturation of the LIF signal, which will be summarised in Section 2.2.1. Otherwise, one of the most notable issues with LIF arises from the fact that tuneable dye lasers are most commonly available for lasing frequencies in the visible spectrum [235]. The lowest available transition from the ground state of an atom or ion requires a photon energy of above 10 eV, corresponding to the UV range. A long-lived or metastable excited state of the target particle population must therefore be selected as the target level for laser pumping. However, only a small fraction of a population usually exists in a particular excited state, while the majority of discharge theory is determined by the majority ground state. Therefore, knowledge of a particular metastable state of a population on its own is not always helpful, and a relationship between the metastable and ground state VDFs is frequently assumed. The accuracy of this assumption and its implication on the use of the LIF diagnostic will be the subject of chapters 3 and 5. For now, we shall follow the frequent assumption [236] that the observed metastable VDF, $f_{m,v}$, is a proportionate representation of the ground state VDF, $f_{g,v}$, at a measurement location x.

2.2.1 Laser saturation effects

If the target state population density $n_t(\nu_l, x)$ that will absorb laser photons of frequency ν_l at a location x is much greater than the equivalent intensity of photons, $I_l(\nu_l, x)$, then the rate of photon absorption by the population will be proportional to both n_t and I_l [235, 241]. As the laser is scanned through frequencies, the intensity of emission at each frequency is then proportional to the local particle density for each frequency, such that an accurate VDF can be reconstructed from it. Furthermore, this will be true across measurement locations, and the relative signals can also be corrected for a wandering input laser power. The LIF signal is then said to be *unsaturated*, and the full one-dimensional distribution function can be determined within an experiment.

If $n_t(\nu_l, x)$ is instead of a similar order of magnitude or lower than $I_l(\nu_l, x)$, few of the particles remain in the target optical level (1) given in Figure 2.4b) [242]. Therefore, an increase in the photon intensity I_l (laser power P) will not result in a linear increase in observed fluorescence [243], since the additional photons are less likely to be absorbed. Stimulated emission from the upper level to the target level can also begin to occur at high enough laser intensities,

complicating the relationship with the fluorescence signal further. The state is *saturated*, and the relationship between P and the target phase space density becomes complicated and unreliable [243, 244]. This is a well known experimental phenomenon given that low density metastable states of a population are usually selected as a target.

Whether or not an experiment is in a saturated LIF regime can be determined by observing the fluorescence signal intensity at ν_l while changing P. Pigeon *et al.* [245] have demonstrated the non-linear asymptotic relationship between P and the fluorescence signal intensity I_f beyond a saturation threshold in the same multipole discharge system as used throughout this thesis, given in Figure 2.5. However, the generality of this relationship is not well understood. Efforts have been made to relate a fully saturated LIF signal to the particle density [246, 247], but have been impeded by the difficulty in determining the exact distribution of the laser beam profile. The cross-sectional power distribution of a laser beam exiting the lasing cavity is usually approximated as Gaussian [248]. The rate of scattering of the laser beam as it travels through a plasma is dependent on the laser power [103] so that the true laser profile at a given location is not known unless using high enough laser powers that scattering is irrelevant [249]. More recent efforts have been aimed at untangling the effects of general signal saturation from the target particle VDF. This is usually attempted by creating various models of the connection between the quantum levels involved in the fluorescence process [250], with some success at the laser saturation threshold powers [251]. Eckbreth [241] has observed that an I_f just above the saturation threshold increases as $P^{0.33}$. However, this was for limited laser powers and ignores the transition from the linear, unsaturated regime. Experimentalists preferably avoid operating in a saturated regime given the complexity of models and their limits of applicability even when all of the experimental parameters are well known. This is particularly true when comparing VDFs at multiple locations since it is difficult to know the rate of attenuation of a laser beam
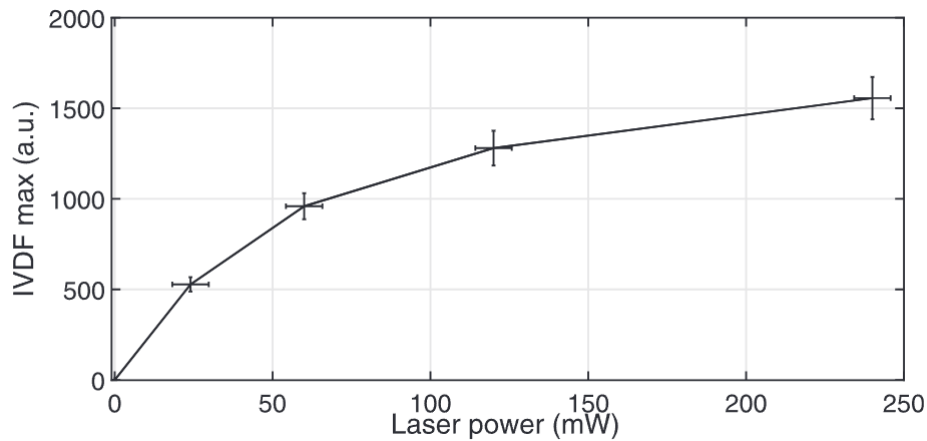

FIGURE 2.5 – The relationship between the maximum magnitude of the fluorescence signal intensity from a constant multipole discharge system to the power of the laser beam used, taken from Pigeon *et al.* [245].

through a discharge which affects the laser intensity profile at a particular location x. However, reducing the laser intensity comes at the cost of reducing the signal to noise of the fluorescence spectra relative to the plasma emission. This sets a lower bound for the input laser power that often forces the experimentalist into a saturated signal regime.

There are many other experimental artefacts to consider when using the LIF diagnostic, such as: electromagnetic influences on energy levels such as the Stark effect [252] and Zeeman splitting [253]; reflection of the laser beam through the observation volume [245]; and so on. An LIF experiment must therefore be a delicate balance between setting experimental parameters to meet these criteria while being able to produce the physical effects that one wants to observe. This means that it is not always possible to eliminate all deleterious artefacts from a diagnostic. Noble gases are frequently used in the spectroscopic analysis of discharge ions, for example, due to their inability to readily form molecules [242]. This eliminates the complex structure of rotational or vibrational states that comprise molecular emission spectra. However, the difference in energy $h\nu_{\mathrm{m},0}$ between the metastable states of noble gas ions relative to the ground state of the corresponding neutral atom is on the order of 30-40 eV [32, 254]. Therefore, the frequently modelled version of a glow discharge that only contains an ion and cold electron population (see Chapter 1.2) will contain too low of a density of metastable ions to produce reliable fluorescence signals. Increasing the metastable density by changing experimental variables like the discharge voltage is also not desirable since this may change the discharge regime that contains the desired plasma phenomena to be observed. This was one of the main intentions of the design of the multipole discharge system that was used in the proceeding experiments, and which we overview below.

2.2.2 The multipole discharge system

The multipole (or multidipole) system consists of a grounded stainless steel vacuum vessel with alternating bar magnets aligned on its exterior. An example of a multipole system has been given in Figure 2.6. The alternating magnetic poles produce a strong yet short ranged magnetic field along the chamber wall that reflects charged particles back into the discharge volume [255]. This has been shown to increase the plasma density, uniformity, and quiescence for otherwise equivalent discharge conditions without the magnetic multipole [255–257]. Multipole devices can therefore be used for discharges at very low pressures and discharge voltages, sometimes to the extent of having charge-neutral mean free paths larger than the characteristic size of the chamber L. In this case, external charge sources are required to achieve breakdown. This is commonly achieved by placing thermionic filaments within the unmagnetised discharge volume and heating them with an external bias so that they emit primary electrons in large numbers. The bias on the filaments can also provide the entire discharge potential if desired. Primary electrons in a
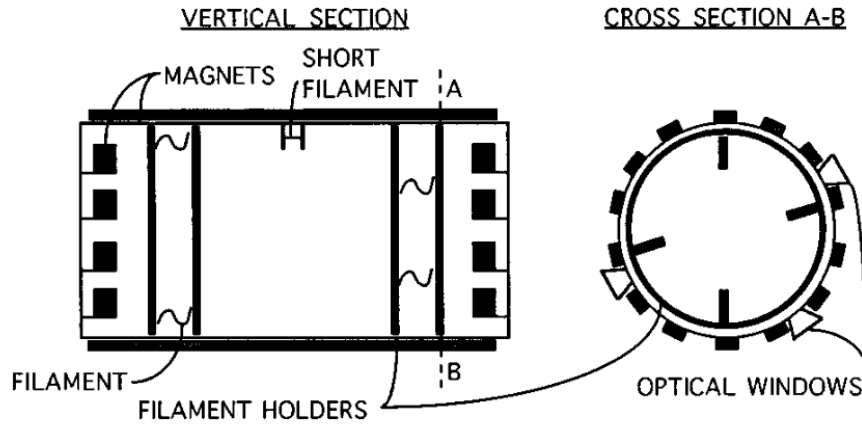
FIGURE 2.6 – A typical multipole chamber, showing the magnetic multipole and thermionic filament arrangement. Taken from Carrére *et al.* [257].

multipole system in which $\lambda_e \gtrsim L$ are accelerated rapidly by the filament bias and can reflect from the encasing magnetic field multiple times before undergoing an inelastic collision. This tends to randomise their direction without significantly losing energy, such that the population is isotropic and mono-energetic[2]. Isotropic mono-energetic primary electron populations with mean energies equivalent to the filament bias have been observed in multipole systems below 1 mTorr of pressure [255, 258–260]. The primary electron population has been observed to have collisionally thermalised into a high energy Maxwellian population as the discharge pressure increases [257]. The uniformity of the primary electron population has been proposed as the leading mechanism behind the spatially uniform ionisation density and hence plasma uniformity observed in multipole systems [260]. The multipole system can therefore be used to reduce undesirable collisional effects and for the manipulation of the plasma potential even below the anode bias [261] to improve Langmuir probe diagnostics. Otherwise, the multipole system creates ideal LIF conditions, with high metastable densities and an optically thin plasma [262]. For these reasons, a multipole system was used in the following analysis and for the LIF experiments given in Chapter 3.

2.3   The hybrid IEC hollow cathode

We are now in a position to approach the work contained in the first publication of the thesis [193], titled 'Measurements and modelling of ion divergence from a gridded inertial electrostatic confinement device using laser induced fluorescence'. The experiments included in this publication were designed by Valentin Pigeon, Nicolas Claire, and Joe Khachan, and were performed by Valentin Pigeon and Nicolas Claire.

---

[2]The isotropic mono-energetic distribution function is discussed more closely in Chapter 4.1.2

In the following sections we present laser induced fluorescence measurements on argon ions generated by a cathode grid that consisted of two parallel rings with a common axis of symmetry. The intention was to observe the relative rates of ion convergence and divergence at the cathode centre for an IEC style of cathode operated in an abnormal glow discharge regime. The laser light was directed along the axis of symmetry in order determine the spatial distribution of ion velocities. The shift in the wavelength required to produce fluorescence determined the magnitude and direction of singly ionized argon along the axis. Measurement along this axis of symmetry was chosen because it has been shown [189] that the ion velocity was highest compared to all other directions and with a greater density per unit velocity. We reiterate that the linear nature of the majority of the discharge along the axis is commonly known as a microchannel in publications about gridded IEC discharges. We shall also present a model based on the development of a sheath between the rings in order to explain the measured magnitude and direction of flow of ions.

It was discussed in Chapter 1.5.2 that discharge IEC devices are operated in the abnormal glow regime characterised by a monotonic increase in discharge current with the magnitude of applied cathode bias. Reports have been given of dominant fluxes of high speed neutral deuterium or hydrogen atoms emerging from within the cathode grid in a direction toward the anode in these systems using Doppler shift emission spectroscopy [150, 192], and dusty plasma diagnostics [191]. This divergent motion may be due to a virtual anode being established within the cathode grid and accelerating ions outward. Although the virtual anode is also consistent with a convergent ion focus, it has been noted [50] that Doppler spectroscopy gives a much larger density of divergent ions than that of convergent ions. This is not consistent with a convergent ion focus model where the density of convergent ions should at least be equal to that of divergent ions. The low collisonality of abnormal glow discharges tends to allow for a higher rate of secondary electron emission such that a higher proportion of ionisation occurs near to the cathode (see Chapter 1.1.7). We shall argue that when the cathode is a grid that contains a volume of space, this results in a discharge within it similar to a hollow cathode discharge. Moreover, these devices have operated with a very low ionization fraction so that ion and electron collisions with the neutral background gas have dominated the ion kinetics such as charge exchange collisions [151, 189, 230, 263].

2.4   Experimental apparatus

A schematic diagram of the multipole experimental set-up is presented in Fig. 2.7. A total thermionic emission current of 500 mA from two heated tungsten filaments, at a bias that ranged from 10 to 150 V, initiated a discharge within a grounded cylindrical vacuum chamber with a diameter and length of 40 cm and 80 cm, respectively. The discharge produced from the
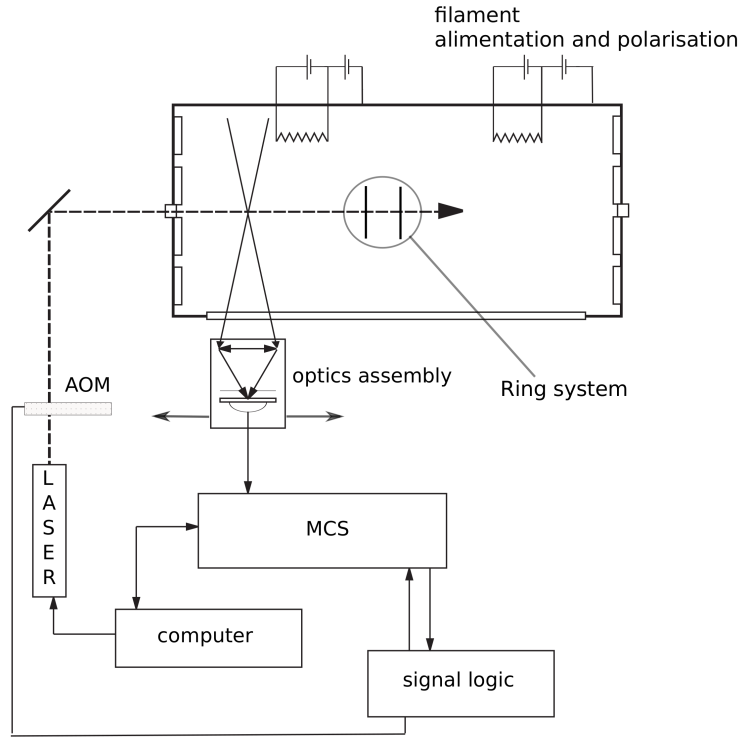
FIGURE 2.7 – Schematic diagram of the multipole and LIF acquisition apparatus. For each wavelength the laser is modulated by the AOM in order to remove spontaneous emission light from the fluorescence signal. The MCS device counted the pulses generated by the fluorescence detection system.

thermionic emission was aided by cusp magnetic fields on the surface of the vacuum vessel. The magnetic cusps were produced by alternating polarities of permanent magnets. The short, 8 cm range of the alternating magnetic fields meant that the bulk of the plasma generated within the chamber could be considered unmagnetized [255, 257]. A cathode was placed approximately at the chamber centre.

There were no permanent magnets on the ends of the vacuum chamber. The discharge voltage and current were kept constant by regulating the filament current; electron temperature was typically a few eV, and the bulk plasma outside of the cathode sheath was homogeneous and isotropic with a density of approximately 10^{15} m^{-3} for previous experiments with the same experimental procedure and apparatus but differing cathode geometries [257].

The cathode consisted of two parallel stainless steel rings of 2 cm in diameter and separated by a 2 cm conducting metal bar, given in Figure 2.3. The cathode was connected to a voltage supply that could deliver up to 3 kV. LIF was performed along the axis of the rings shown in Figure 2.3: off axis measurements resulted in a poor signal-to-noise ratio. The LIF diagnostic used a 899 coherent CW ring dye laser chopped by an external acousto–optic modulator (AOM). The emitted laser line, whose frequency can be manually fixed anywhere in the dye tuning range,

has a bandwidth of 0.5 MHz, which is much less than the 14 MHZ natural line width of the transition used. This natural line width determines the minimum velocity resolution of the diagnostic. The laser line could scan a frequency interval up to 30 Ghz. The three argon atomic levels used for the laser induced fluorescence are the ArII $3d'\,^2G_{9/2}$ metastable level, which is laser excited to the $4p'\,^2F_{7/2}$ level (611 nm) with observed decay to $4s'\,^2D_{5/2}$ (460.9 nm). The laser beam was propagated through the plasma along the axis of symmetry of the rings. The fluorescence light induced by the laser beam was captured by collection optics transverse to the axis of the rings, meaning that positions behind the cathode were obscured. The spatial resolution for the movement of these collection optics was 0.125 mm.

A 1 nm band pass optical filter isolated the fluorescence light from spontaneous emission. The fluorescence signal was detected by a photomultiplier tube (PMT) whose pulses were amplified and counted by a Multi-Channel Scalar (MCS) that set the time resolution up to 5 ns, however, no time resolution was used for this experiment. The PMT was set on a movable trolley in order to spatially scan the fluorescent signal along the axis of the rings.

2.5 Experimental results and discussion

LIF measurements were performed along the parallel direction of both the interior and exterior of the ring system, as shown in Figure 2.3. The rings bias was set to -200 V with a -50 V bias on the filaments at a working pressure of 0.19 mTorr. These operating parameters initiated an abnormal glow discharge with a low ionisation fraction of the gas and a Debye length of around 0.4 mm such that a complete cathode sheath of similar dimensions to the cathode was formed. Such conditions cause the majority of ionisation and charge flux to occur within or in the immediate vicinity of the cathode and isolate it from the electric fields of the filaments. These discharge conditions match those of regular IEC operating conditions despite differences in applied voltage to the cathode so that similar physical processes occur in both systems. Multiple peaks were recorded within the measured longitudinal IVDF at each position along the axis of the ring system as shown in Figure 2.8. The sign of the recorded ion velocities was taken to be positive if their motion was in the direction of the laser beam and negative if in the opposite direction. The peaks of interest are those located at non-zero velocities and are called the principal peak (PP) and the secondary peak (SP) with respect to their amplitudes.

The peak centered at zero velocity, named the ionisation peak (IP), was always present within observations of shifted distribution functions and was likely due to thermal ions caused by ionisation. Consequently, this peak is irrelevant to the following discussion.

The evolution of argon ion velocities at the maximum amplitude of the PP and SP as a function of position is shown in Figure 2.9. The SP was only discernible above the background noise within the rings and indicates velocities directed towards the cathode center and decelerating.
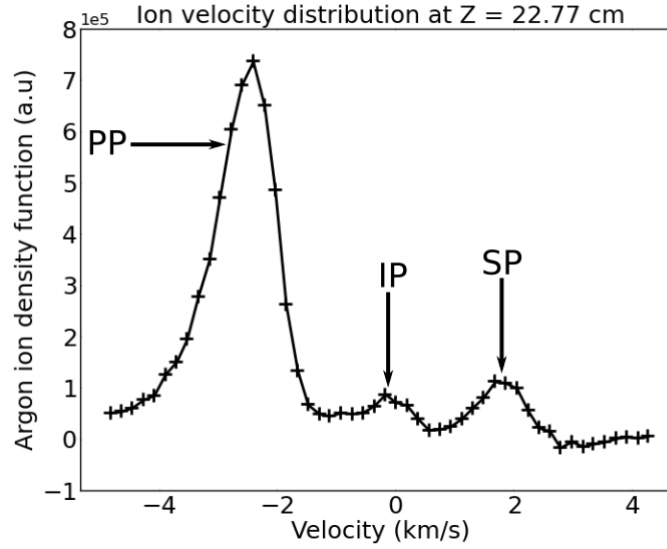
FIGURE 2.8 – Plot of a typical distribution function measured between the rings at $x = 22.77$ cm. The highest peak is the principal peak (PP), SP stands for secondary peak, IP for ionization peak.

The majority of moving ions within the cathode, represented by the PP, are diverging from the cathode center in the direction of the rings. This is in direct contrast to the conventionally accepted ion focus model that would predict a majority of converging ions. The acceleration outwards observed in the PP and the subsequent deceleration inwards once past the cathode rings, along with the deceleration inwards of the SP, both indicate the existence of a virtual anode at the cathode center. However, the virtual anode cannot be established from the convergent ions (SP peak) since their density is much less than the divergent ions (PP peak within the cathode). Furthermore, the maximum velocity of the PP group indicates a relatively small magnitude of virtual anode relative to the cathode bias. Therefore, the low velocity of the SP group decelerating towards zero velocity would not be expected for ions created outside of the region that experienced the full potential drop of the cathode sheath. The observed distribution function of the PP is instead consistent with the creation of thermal ions within the interior of, and nearby to, the cathode, and with subsequent motion that is largely determined by the spatial profile of the established virtual anode. In Section 2.7, it will be shown that the virtual anode can be formed by sheaths that develop between the cathode rings, and, subsequently, causes the divergence of the majority of ions that form within the cathode interior. This can be demonstrated by considering a steady state ion sheath at the cathode, as will be explained in Section 2.6, which develops the necessary virtual anode at the cathode center.

The presence of these processes causing ion divergence from the cathode center is further highlighted by the spatial evolution of densities within the ring system. This evolution is plotted in Figure 2.10, representing the relative densities of the peak velocity of groups of moving ions. The
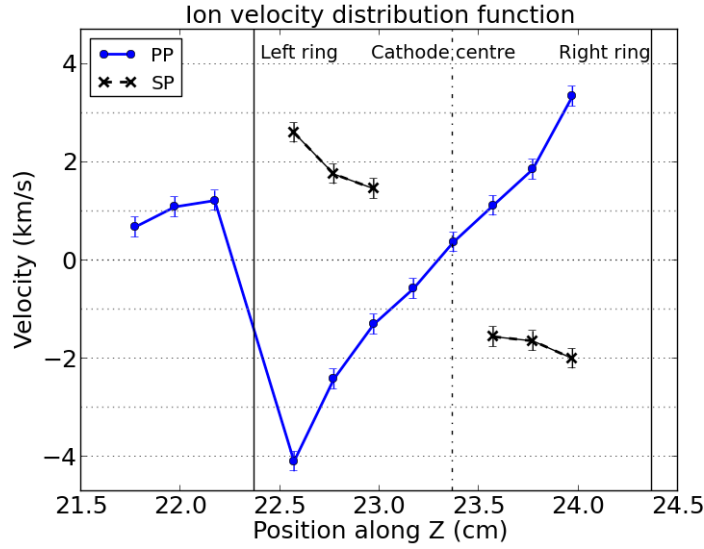
FIGURE 2.9 – Positions of the principal and secondary peak as a function of position. Positions of the two cathode rings and the center of the cathode are displayed. The IVDF scan was not performed after the right ring assuming the symmetry of the system. The error in position is ±1 mm. The error in velocity is the scanning velocity step of 185 m/s.

slight asymmetry in Figures 2.9 and 2.10 is likely caused by the proximity of the left side of the cathode in Figure 2.7 to a filament within the chamber. Bombarding ions partially maintain the discharge by causing secondary electron emission at the cathode which subsequently continues the discharge process. Ions entering the cathode sheath asymmetrically due to proximity to a filament would thus cause asymmetry in the discharge at the cathode. Furthermore, the small asymmetry in velocities in Figure 2.9 implies that the shape of the virtual anode is symmetric, even if the ion densities are not. The evolution of densities of the PP ions again matches the case that ionisation mostly occurs within the cathode and the cathode sheath. The data points to the left of the cathode, namely those at z positions less than 22.4 cm, are of much greater density and lower velocity than expected for convergent ions created outside of the cathode sheath. This implies that these ions were created by secondary electron emission or electrons leaving the cathode interior. These data points were included in the PP due to their higher densities and further since they are likely to contain divergent ions that have been decelerated outside of the cathode and become convergent.

In the ion divergence model proposed above, we would expect ions created near the cathode center to accelerate outwards, reach a maximum velocity amplitude at the boundary of the virtual anode, and decelerate inwards again as their momentum carries them beyond this point. By the conservation of flux, an increase in particle velocity will correspond to a decrease in particle density. Such a velocity profile for the PP would thus result in a local density maxima within the cathode at some point near to the cathode center, followed by a decrease in density as the ions accelerate, and finally another region of high density where the PP ions are slowed to
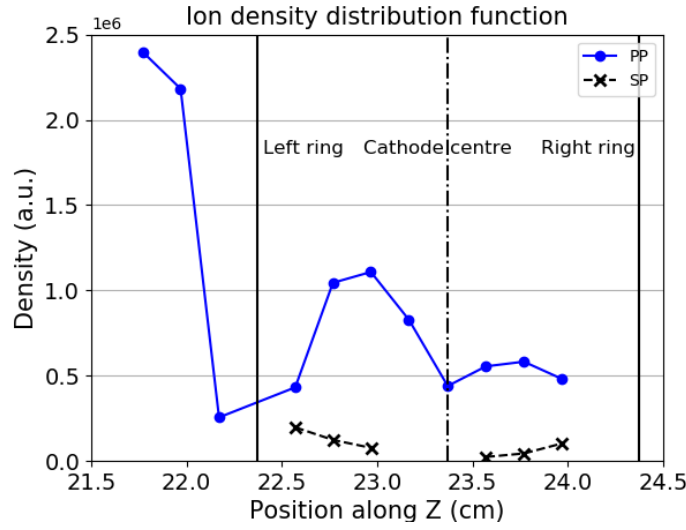
FIGURE 2.10 – Densities of the PP and the SP as a function of position. Densities were obtained by integration of the IVDF over velocities. The relative error is $\pm 10\,\%$ due to the choice of integration limits.

a halt and are reflected to become convergent. Ions are unlikely to remain permanently on the cathode axis as the steepest potential gradient points towards the cathode rings, likely decreasing the density of diverging ions that have reflected outside of the cathode. There, however, the density of ions with converging velocities will be contributed to by further ionisations within the exterior cathode sheath from secondary electron emission and from electrons exiting the cathode interior in the focused microchannels [125]. The results of Figure 2.10 demonstrate this phenomena. The following sections propose novel physical models for IEC discharges to explain the observed majority of ionisation within the vicinity of the cathode and subsequent ion divergence from an established virtual anode.

2.6   Formation of the virtual anode

Two physical phenomena from these experiments require a novel analytical explanation: the high rate of ionisation occurring within and in the immediate vicinity of the cathode, and the outward acceleration of ions from thermal velocities at the cathode center. In the following we neglect the background multipole plasma of the experiment as a high-voltage cathode in such a system generates its own dominant discharge that is responsible for the majority of the creation of charge. The primary electron population with an energy near to -50 V emitted from the thermionic filaments is likely to be deflected to some extent by the sheath of the cathode biased at -200 V.

The first of the two criterion can be achieved by identifying the two-ring cathode discharge, as well as more regular IEC discharges that use a spherical grid, as an intermediate form of a hollow cathode discharge. Although regular IEC discharges are operated with applied cathode voltages on the order of 100 kV, most are operated well within the abnormal glow discharge regime with a low ionisation fraction of the gas [20, 179, 189, 192, 212, 224, 264]. In such cases, the governing plasma physics will be similar to those occurring in the experiment presented in Section 2.5; that is, abnormal discharge physics involving a cathode sheath with a Debye length in the order of 0.4 mm with collisional process dominated by charge exchange interactions. As most of the potential drop is contained within a maximum of 10 Debye lengths from the cathode, we must investigate the sheath structure around and within the grid to explain the direction of ion flow. Furthermore, previous research [191] carried out on a similar two-ring cathode operated at -9 kv in a 13 mbar hydrogen discharge presented similar plasma densities and ion divergence as the experiment given above.

That IEC devices operate as an intermediate hollow cathode discharge is supported by considering the similarities between the originally suspected abnormal discharge mode of the two-ringed cathode and that of a hollow cathode discharge. A hollow cathode discharge is characterized by the hollow cathode effect, in which temporarily trapped pendulum electrons oscillating between inner walls of the cathode localise the vast majority of ionisation, and hence the discharge, to the cathode interior and immediately in-front of its apertures [91, 127, 139]. This also produces relatively dense diverging electron beams from the cathode interior, otherwise known as microchannels, as well as an increase in discharge current density and a reduction in sheath width for otherwise identical conditions to a regular discharge. Previous literature demonstrated these features for the two-ring cathode: a discharge localised to the cathode interior (which can be observed as the location of the majority of the plasma glow) and the typical diverging electron beams [125, 191]. Both phenomena were observed in the present experiment. Furthermore, gridded IEC cathodes satisfy the necessary conditions for pendulum electrons, having a volume of space enclosed by a negative electrode that emits secondary electrons due to ion bombardment. Figure 2.10 supports the identification of the two-ringed device acting as a hollow cathode discharge as the increased density of the PP compared to the SP indicates that the majority of ions within the cathode originated from within it. It is therefore very likely that IEC discharges are at least an intermediary stage between an abnormal glow and hollow cathode discharge. Consequently, this is in contrast to the ion-focus model, considering that the majority of ions are formed within the cathode and cannot be subsequently accelerated further inwards.

The second criteria requires that a virtual anode is established at the cathode center and must be explained from discharge phenomena outside of the ion-focus model. There has been empirical evidence of diverging ion motion within hollow cathode discharges and in discharges using the regular IEC concentric spherical grid electrodes [127, 150, 191, 192, 265, 266]. However, to-date, there has been no model to explain this ion flow direction. This is addressed in the following

section, where a three-dimensional steady state computational plasma sheath model is presented that forms a virtual anode at the cathode center capable of reproducing the experimentally obtained diverging ion velocity distribution function.

2.7   Computational modelling

The plasma potential for the system was found by computationally solving Poisson's equation,

$$\nabla^2 \phi = -\frac{\rho}{\epsilon_0}, \tag{2.5}$$

via relaxation where ρ is a given charge density profile. The explicit form of Poisson's equation given in [267] for a planar sheath extended to three spatial dimensions was used such that the non-symmetric cathode geometry of Figure 2.3 can be solved computationally;

$$\nabla^2 \phi = \frac{q_e}{\epsilon_0} \left(n_e - n_i \right) = \frac{q_e n}{\epsilon_0} \left[\exp\left(\frac{q_e \phi}{k_B T_e} \right) - \left(1 - \frac{2 q_e \phi}{m_{\mathrm{Ar}^+} u_0^2} \right)^{-1/2} \right], \tag{2.6}$$

where m_{Ar^+} is the argon ion mass, and u_0 is the argon ion thermal plasma velocity. The effect of secondary electron emission from the cathode is not included explicitly in this equation, which is likely to affect the accuracy of the solution in the immediate vicinity of the cathode. Further work is necessary to include the effect of secondary electron emission on sheath profiles for complex cathode geometries. However, secondary electron emission is implicitly included in Equation 2.6 due to its involvement in establishing the plasma density n_0, which has been experimentally measured for this system. Although this method ignores changes in fluid volume elements for ions in the conservation of particle flux as they focus towards the cathode wires, an assumption likely to cause inaccuracies near the cathode surface, the calculated potential distribution will be valid along the central axis of the cathode where the surfaces of equipotential vary slowly in space. The number density of the experiment also allows for the selection of fluid elements that are small compared to changes in the potential gradient to further negate this effect. Testing with more exhaustive methods for calculating the cathode sheath for the two-ring device using electrostatic force terms from Vlasov-Poisson equation reproduced negligibly different results from Equation 2.6 for increased likelihood of relaxation instabilities and computation time.

A Gauss-Seidel Successive Over-Relaxation (GS-SOR) time-stepping method was implemented for the experimental parameters outlined above. The computationally expensive nature of a three dimensional GS-SOR model restricted the calculable space to a cube with ubiquitous 0 volt Dirichlet boundaries representing the grounded chamber at least 20 Debye lengths from any part of the cathode, well beyond the sheath edge. Considering that each filament was placed more than 100 Debye lengths from the cathode, this choice only ignores higher order plasma processes that have little effect on the formation of a virtual anode that cannot be being formed

by converging ions. The only unknown input parameter to the computational model of noticeable effect was that of the bulk plasma density, n. Whilst previous research on the same chamber produced bulk plasma densities of $n \approx 10^{15} \, \text{m}^{-3}$ [257], the interior nature of the hollow cathode discharge is known to reduce the plasma density outside of the cathode [97, 129, 266]. For this reason, the results of the computational model are given including all final values originating from bulk plasma densities within the values of $10^{14} \, \text{m}^{-3} \leq n \leq 10^{15} \, \text{m}^{-3}$. The asymmetry in figures 2.9 and 2.10, likely due to uneven proximity to emissive filaments, was excluded for simplicity in the computational model.

2.7.1 Sheath modelling results and discussion

The potential distribution taken along the Y-Z and X-Z planes of Figure 2.3 within the cathode and positioned at the cathode center are shown in Figure 2.11. The potential distribution along the longitudinal axis (the dashed line in Figure 2.11 (a)) of the cathode with a final time-step tolerance of $2.5 \times 10^{-3} \, \%$ is shown in Figure 2.12. The geometry of the cathode and the positive ion sheath establishes a virtual anode at the cathode center of similar form found by Motoyasu *et al.* [265] in a multiple ring discharge and Khachan *et al.* [191] with a two-ringed cathode. This occurs as the sheath reduces the potential from the cathode over distance such that the center of the cathode is positive relative to other regions of space that are in closer proximity to the cathode wires, such as the center of each cathode rings. Ions formed within this region would be accelerated outwards towards regions of lower potential near the rings, whilst ions formed outside of the cathode would be decelerated upon approach by the virtual anode, as seen experimentally in both the PPs and SPs of Figure 2.9. Furthermore, electrons that escape radially from this potential distribution, parallel to the X-Y plane of Figure 2.3, would diffuse
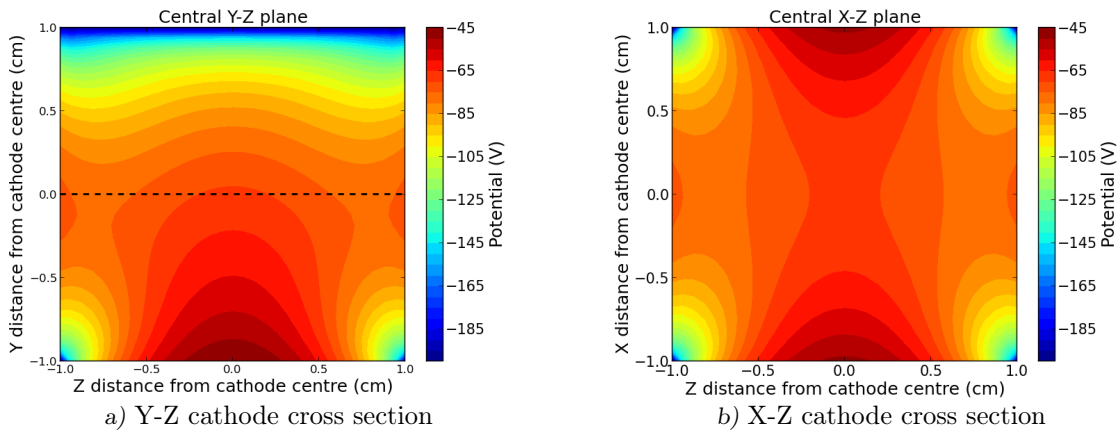

a) Y-Z cathode cross section   b) X-Z cathode cross section

FIGURE 2.11 – Cross sections of the cathode interior centered at the cathode center including both cathode rings and connecting bar (see Figure 2.3) of a typical plasma potential with ion sheath. *(a)*: The Y-Z plane. The dashed line shows the values of potentials used to make Figure 2.12 *(a)*. *(b)*: The X-Z plane.

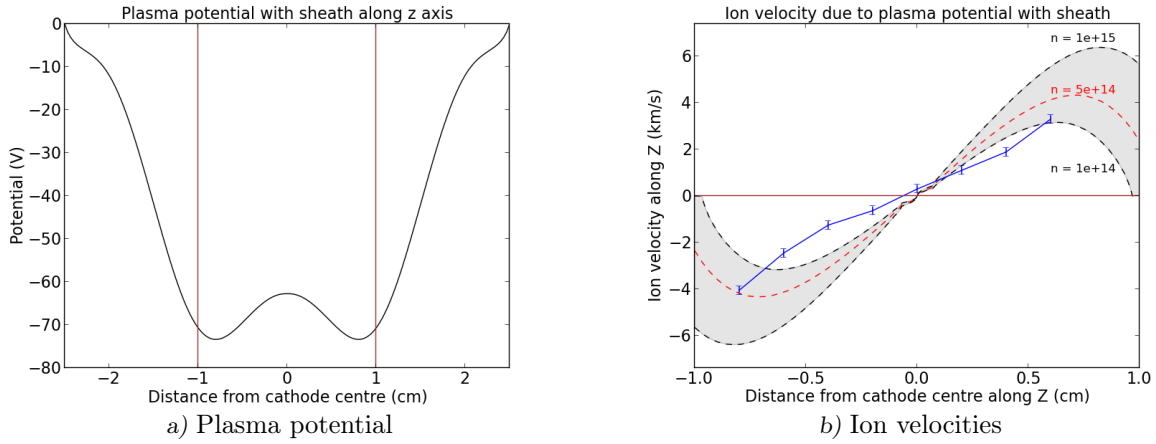*a)* Plasma potential   *b)* Ion velocities

FIGURE 2.12 – *(a)*: A typical plasma potential along the cathode longitudinal axis after sheath calculation. The two vertical lines represent the cathode ring positions. *(b)*: Experimentally obtained ion velocities (blue line) against ion velocities (grey area) due to charge exchange modelling on a range of possible plasma potential distributions. The dashed lines represent the minimal, median, and maximal ion velocity distributions for the varying bulk plasma density, n, and the initial standard deviation of the Gaussian ion density distribution function, f_i.

with distance, while electrons escaping through the rings would be electrostatically lensed into the focused beams that are observed during the discharge.

To demonstrate ion divergence, consider a Gaussian ion density distribution, f_i, of ions continually generated along the central axis. Previous studies show that the majority of thermal ions from a hollow cathode discharge are created at the cathode center with a Gaussian density spread [97, 125, 129, 139, 265]. We calculate the response of these ions to this potential while implementing the charge exchange model outlined by Shrier *et al.* [263], adapted for a non-monotonically decreasing potential, as our only collisional process. As the exact nature of f_i is not accurately known, the model results are given with error bars that include the combination of possible choices of both realistic varying standard deviations for f_i taken from Khachan *et al.* [191] and initial choice of n. The $Ar^+ + Ar \Rightarrow Ar + Ar^+$ charge exchange reaction dominates collisional processes within $0.1 - 17$ eV of relative energy [12] and has the following cross section [268]:

$$\sigma_{ce}^{1/2} = 7.49 \times 10^{-8} \text{ cm} - \left(0.73 \times 10^8 \text{ cm}\right) \log E_i, \tag{2.7}$$

where E_i is the argon ion energy in eV. As an example, a typical SP or PP ion travelling at roughly 2 km/s has a mean free path for charge exchange of roughly 3 cm, in the order of the separation of the cathode rings. Ions that have undergone charge exchange at some point along their acceleration by the potential are replaced with an ion of zero velocity, which is the average result of a charge exchange interaction. The velocities of ions as they accelerate and charge exchange at each point along the distribution is stored so that we have a new ion distribution function along the cathode axis, similar to the PP shown in Figure 2.8. The peak velocities from each position along the axis are displayed in Figure 2.12 *(b)* alongside the peak velocities from the LIF spectroscopy given in Figure 2.9. The computational model displays a significant range

of realistic input values that produce ion velocities that successfully match the results given in Figure 2.9. Disagreement between the exact form of the experimental and computational ion velocity distribution functions are likely due to simplifications in the initial Gaussian form of f_i, ignoring the effects of secondary electrons from the cathode, and the exclusion of lesser collisional effects such as elastic scattering.

It should be noted that while vacuum modelling of the system produced a virtual anode due to the cathode geometry alone, this virtual anode could only produce ion energies an order of magnitude less than those observed in Figure 2.9. A sufficient virtual anode is only formed after including the cathode sheath in the calculation. It may be possible that the cathode sheath is serving to amplify this geometric virtual anode rather than being responsible for creating one. However, the phenomena of ion divergence from the cathode centre has been observed in similar systems without a geometry-induced virtual anode. Thus, if true, this concern would require a different physical theory to explain the observed ion divergence phenomena in IEC systems. That such phenomena match well with known cathode sheath theory indicates that this method of geometric virtual anode amplification, while possible, is unlikely to be the case, particularly for spherical IEC cathodes.

Divergent ions accelerated by the virtual anode will have lower energies than that of convergent ions that have been accelerated by the entire potential difference of the cathode sheath, reducing their fusion cross section. However, diverging ions exist in much greater densities than high energy converging ions which were not measurable above background noise in this experiment. A previous study [192] showed divergent ion energies within microchannels reaching 20 % of the applied cathode voltage in a spherical IEC device. Furthermore, virtual anodes of higher magnitudes will increase the potential difference between the cathode interior and the cathode surface for ions formed within the virtual anode. Bowden-Reid *et al.*[227] have demonstrated that a significant proportion of fusion events from IEC devices can occur between bombarding ions and neutral gas on the surface of the cathode depending on the cathode temperature. The full mechanism of the production of fusion reactions in IEC devices is therefore more detailed than the traditional model of solely convergent ions. Future cathode designs for IEC cathodes need not aim for maximal transparency since ion convergence is minimal and since ion bombardment of the cathode significantly contributes to the total fusion rate. Instead, this model predicts that a cathode geometry that can maximise the magnitude of the virtual anode will increase the average energy of a large fraction of the accelerated ions within the system and potentially the overall fusion rate.

Ion divergence from the cathode center would also contribute to the explanation of the significant dependence of the fusion rate on anode materials as discovered by Bakr *et al.*[186] in their recent work on IEC systems. The cross-section for charge exchange reactions between ionised forms of hydrogen and neutral hydrogen gas has been shown to be nearly identical to that of deuterium and increases to a peak in the tens of keV of relative impact energy [44]. Energetic neutrals from

charge exchange with ions at high energies after they are accelerated outward from the cathode center would be less likely to experience collisions before reaching the deuterium on the anode surface than in the ion-focus model. This increase in average energy of neutrals reaching the anode surface would increase the number of fusion events depending on the density of targets there, which is itself dependent on the anode material.

2.8   Summary and implications for further work

The ion distribution function along the central axis of a two-ringed IEC cathode was determined by LIF in an argon discharge under abnormal glow discharge conditions. The majority of ions were found to be created near the cathode center at thermal velocity and subsequently accelerated outwards, in direct disagreement with the previously accepted ion-focus model. Evidence was given to support the argument that gridded IEC devices operate in an intermediate regime between an abnormal glow discharge and a hollow cathode discharge. The formation of the virtual anode at the cathode center was computationally replicated by an ion sheath model which successfully reproduced the experimentally obtained ion velocity profile using charge exchange modelling. This change in fundamental theory of the operation of IEC devices has relevance for the field of IEC neutron production as the diverging ion model changes the process in which ions reach fusion-relevant energies.

The LIF work given in this chapter represents a further experimental technique that corroborates the argument given in Chapter 1.5.2 that IEC is in fact a misnomer. If the two-ringed cathode reflects the physical mechanics of a classical spherical IEC gridded cathode, then ion convergence is unlikely to be the major contributor to forming a high density fusion core. We have also developed a possible alternative theory based on the hollow cathode effect that could explain the divergence phenomena. It is based on this combination of evidence that we suggest the renaming of discharge based IEC devices to only 'electrostatic' nuclear fusion devices. However, three issues arose at the publication of these results:

1. We received referee comments that the two-ring cathode does not behave like an IEC discharge, although these were without supporting evidence or references. Proponents of the convergent ion theory may not be sufficiently convinced by the analysis given above;

2. There was no need for the ambipolar hypothesis which linked the fusion rate to the magnitude of virtual anode created by ambipolar diffusion;

3. The ratio of the magnitude of the virtual anode to the cathode bias for the two-ringed cathode at -200 V does not match values in the order of 25 % indicated by ion kinetic

energies in previous observations of ion divergence for cathode biases in the order of -10 kV [189–192].

The vacuum solution of Equation 2.5 showed that the creation of a virtual anode due to the cathode geometry alone could be avoided if the ratio of the ring diameter to their separation, $r_{\text{d-s}}$, was limited to $r_{\text{d-s}} \geq 3/2$. The geometric virtual anode that is created by the two-ring cathode was sufficiently enhanced by cathode sheath such that ambipolar effects were not necessary to reproduce the ion velocity results given in Figure 2.9. The two-ring cathode would also be worse at trapping pendular electrons than a spherical grid or traditional hollow cathode, reducing the magnitude of the hollow cathode effect. This is since the centre of the two-ring cathode is not surrounded by cathode wire except for the connecting bar, such that the majority of possible electron trajectories would not pass near to a cathode surface.

The authors were of the opinion that ambipolar effects were likely still involved in creating virtual anodes of greater magnitude relative to the cathode bias in both IEC-type discharges and low pressure hollow cathode discharges. However, both cathodic sheaths and ambipolar effects result in the creation of positive space charge due to the difference in responses of electrons and positive ions to their environment. Untangling these two processes would be difficult if they occur to similar extents. The exact geometry of the two-ring cathode may not be ideal for connecting these arguments. Ideally the relationship between hollow cathodes and spherical IEC grids could be solidified by a direct observation. This would be best achieved for the interior of a cathode that establishes a virtual anode of sufficient magnitude that it could not be attributed to sheath effects alone. It was thought necessary to first observe the relevance of ambipolar processes in a low pressure hollow cathode discharge before attempting to link them to spherical grid cathodes that are significantly more complex to model. Therefore, in the following chapter we shall present an LIF analysis of various low pressure multipole discharges in argon using a cylindrical hollow cathode with solid walls.

Chapter 3

The low pressure hollow cathode discharge

It was demonstrated in Chapter 2 that a small virtual anode magnitude V_a relative to the cathode bias V_c could be replicated by only considering geometric and sheath effects for the hybrid two-ring hollow cathode. The space charge created by the cathode sheath exacerbated the very small, geometric virtual anode that existed due to the cathode bias in vacuum. A spherical gridded cathode or hollow cathode with solid walls would not produce a geometric virtual anode in vacuum, as can be determined by solution of Laplace's equation. We may therefore not expect that sheath effects alone would replicate the previously observed virtual anodes for such cathodes. Furthermore, these types of cathodes as well as previous studies involving the two-ring cathode [190, 191] in high power IEC discharge conditions have displayed diverging ion velocities that correspond to $V_a \approx |0.25V_c|$. We must also consider the strong linear relationship that was determined between ambipolar diffusion and virtual anode formation in low pressure hollow cathode discharges discussed in Chapter 2.1. The connection between these problems could perhaps be illuminated by observing a cathodic discharge in which the formation of a virtual anode is unlikely to be attributable to sheath effects on their own. This type of virtual anode was considered more likely to occur in a solid cylindrical hollow cathode operated at similar discharge conditions as the two-ring experiment. The LIF measurement of IVDFs created by the hollow cathode could perhaps strengthen the relationship between the ion divergence phenomena and the low pressure hollow cathode discharge.

In this Chapter we shall present LIF measurements involving multiple laser orientations in various low pressure hollow cathode discharges in the same multipole system used in Chapter 2.3 and Reference [193]. This also represents further work in characterising ionic distribution functions for hollow cathode discharges below 100 mTorr of operating pressure. The initial attempt to observe the hollow cathode interior using an angled double lens array will be presented and

its failure discussed. Then, the LIF observations across the pre-sheath and sheath directly in front of the hollow cathode shall be given. These results do not demonstrate ion divergence observable exterior to the cathode, but this may not be due to the absence of a virtual anode or ambipolar effects. Some possible causes of the lack of observed ion divergence shall be listed. The fluorescence signals will also be shown to contain much more significant results concerning a previously observed but unexplained anomalous spatial distribution of the target metastable ion density. The literature regarding this anomaly, the possible flaw with the LIF diagnostic that it represents, and previous research that may be affected by this flaw will be discussed, including the arguments made in Chapter 2. An analysis of the experimental LIF results will be given with the necessary research to be undertaken before the cause of this anomaly can be identified.

It will first be necessary to understand the relationship between the ArII $3d'\,^2G_{9/2}$ metastable ion population selected as a target in our LIF experiments and the transitions between the electronic configuration of quantum levels that may contribute to it. We therefore begin with an introduction to the coupling schema used for many electron atoms. This understanding will be important for the collation of the many possible sources and losses that could contribute to the ArII $3d'\,^2G_{9/2}$ state from the interaction of the multiple species in a discharge.

3.1 Quantum levels in many electron atoms

The energy levels in multiple electron atoms result from the complex simultaneous interaction of electrons with each other and with the potential well of the nucleus. The field of optical spectroscopy concerning transitions between levels began as an experimental pursuit well before the formation of quantum mechanics [269]. This resulted in a complicated set of nomenclatures that attempted to describe energy spectra that did not seem to follow the physical laws known at the time. As a result, many different nomenclatures are used in the literature that only apply in certain cases and yet still have many exceptions. We shall focus on the Russel-Saunders, or $L-S$, coupling scheme [270] that is most applicable to atoms with fewer than 30 protons like argon. We shall also discuss how $L-S$ coupling relates to both the Paschen and Racah notations that are often given in literature concerning the ArII $3d'\,^2G_{9/2}$ metastable state. We shall follow the summaries given by Kitchen [269] and Raju [271].

3.1.1 Individual electron quantum numbers

The electron quantum numbers that determine the energy levels of a single electron atom are [271]:

1. n, the *principal quantum number*, relating to the total energy of the electron orbit, and is restricted to $n \in \mathbb{N}$.

2. l, the *azimuthal quantum number*, derived from the quantisation of the electron's orbital angular momentum vector $\tilde{\boldsymbol{l}}$, and relates to the shape of the electron's orbit.

$$l = 0, 1, 2, \cdots, n-1 \qquad (l = s,\ p,\ d,\ f,\ g,\ h,\ i,\ \cdots). \qquad (3.1)$$

3. m_l, the *magnetic quantum number*, arising from the spatial quantisation of $\tilde{\boldsymbol{l}}$ with respect to an external reference direction usually given by an external electromagnetic field, where

$$m_l = 0, \pm 1, \pm 2, \cdots, \pm l.$$

4. m_s, the *spin quantum number*, due to the half integer spin of the electron, such that $m_s \pm 1/2$.

In a single electron atom, these quantum numbers combine to determine the atomic energy levels as a result of Pauli's exclusion principle. The m_l states remain degenerate in the absence of external fields, and there is only a small dependence of the energy level on m_s since the electron spin angular momentum vector $\tilde{\boldsymbol{s}}$ couples with $\tilde{\boldsymbol{l}}$ to form the total angular momentum

$$j = \left| \tilde{\boldsymbol{l}} \pm \tilde{\boldsymbol{s}} \right|. \qquad (3.2)$$

3.1.2   Multiple electron atoms

Without excitation, the possible electron quantum states (different combinations of n, l, m_l, and m_s) are filled in ascending order, grouping first into shells with smaller divisions into subshells (with some exceptions). The electronic configuration of an atom can be listed by writing the n and l of each occupied subshell with the number of electrons occupying it as a superscript. For the argon atom ground state, we have

$$1s^2 2s^2 2p^6 3s^2 3p^6.$$

In multiple electron atoms, however, complex coupling between each electron's quantum numbers and possibly those of the protons in the nucleus dominates the vectors that determine the number of levels and their associated energy. This results in a much larger set of possible quantum states that can not be described by the electron quantum numbers alone. For atoms with fewer than 30 protons, the interactions between the orbital angular momenta of different electrons dominates over spin-orbit coupling and forms a new set of total angular momentum vectors [270]. How this coupling produces an electron energy configuration is categorised by the Russel-Saunders or

L-S coupling scheme [270]. Beyond 30 protons, in the case of certain excited atoms like Neon, or when considering relativistic effects, the j-j or j-l coupling scheme categorising dominant spin-orbit interactions of individual electrons is employed[1].

3.1.2.1   *L-S* or Russell-Saunders coupling

Fortunately, all closed subshells contribute nothing to the total angular momentum of an atom. In this way we can determine the possible electron configurations by coupling the quantum vectors of only outer-shell electrons:

1. $\tilde{\boldsymbol{L}} = \sum_k \tilde{\boldsymbol{l}}_k$, the *total orbital angular momentum*, where $\tilde{\boldsymbol{l}}_k$ is the orbital angular momentum of an electron in an open sub-shell. This vector is constrained such that that the total azimuthal quantum number L (from $|\tilde{\boldsymbol{L}}| = [L(L+1)]^{1/2} \hbar$) is a positive integer or zero. For two interacting electrons with azimuthal quantum numbers l_1 and l_2, we have that

$$L = (l_1 + l_2),\ (l_1 + l_2 - 1),\ \cdots,\ |l_1 - l_2|. \tag{3.3}$$

   Each value of L has its own associated energy, despite l_1 and l_2 remaining the same. For historical reasons, the values of L are given by a capital letter following the scheme given in 3.1, such that

$$L = 0, 1, 2, 3, \cdots \qquad (L = S,\ P,\ D,\ F,\ G,\ H,\ I,\ \cdots). \tag{3.4}$$

   For each additional electron, we find all possible L values from coupling the first two electrons, $L_{1,2}$, and then use the same schema above between each possible value of $L_{1,2}$ and l_3 to form a new set $L_{1,2,3}$, and so on. Unfortunately, the energies from the same magnitude of $L_{1,2,3}$ formed via different values of $L_{1,2}$ combined with l_3 and following System 3.3 will generally differ, quickly forming extremely complex configurations.

2. $\tilde{\boldsymbol{S}} = \sum_k \tilde{\boldsymbol{s}}_k$, the *total spin angular momentum*, where $\tilde{\boldsymbol{s}}_k$ is the spin angular momentum of an electron in an open subshell. This is found in the same way as above but is simplified by the fact that $m_{\mathrm{s}} = \pm 1/2$. For n relevant electrons,

$$S = \left(n \cdot \frac{1}{2} \right),\ \left(n \cdot \frac{1}{2} - 1 \right),\ \cdots,\ 0 \text{ or } \frac{1}{2}. \tag{3.5}$$

3. $\tilde{\boldsymbol{J}} = \tilde{\boldsymbol{L}} + \tilde{\boldsymbol{S}}$, the *total angular momentum* from which the name $L - S$ coupling arises. The total angular momentum quantum number J determines the final energy level configuration of an atom or ion. We find J by combining all possibilities of L and S that obey Pauli's

---

[1]For a detailed description of j-j coupling, see Chapter 8 of Principles of Modern Physics [272]

exclusion principle:

$$J = (L + S), (L + S - 1), \cdots, |L - S|. \tag{3.6}$$

The set of energy levels corresponding to the values of J for a given L and S is called a *term*. A specific value of J is called a *level*. The number of levels in a term, called the multiplicity of the term, is given by $2S + 1$.

The total angular momentum $\tilde{\boldsymbol{J}}$ takes quantised directions in space relative to an external reference direction analogously to m_l. This gives rise to M, the magnetic quantum number, which splits each J level into $g = 2J + 1$ non-degenerate energy *states* in the presence of an external magnetic field, where

$$M = -J, -J + 1, \cdots, J. \tag{3.7}$$

Although the different M states are degenerate without an external field, it changes the number of available positions in that state that an electron can occupy. That is, it changes the *statistical weight g* of the level. Thus, for an electron excited to a particular term, the likelihood it will occupy a particular level is given by the ratio of its statistical weight to that of the entire term [269].

3.1.3 The *L-S* notation scheme

In $L - S$ notation, all of the information necessary to describe multiple-electron atoms is present; the multiplicity (hence the total spin angular momentum), the total orbital angular momentum L, the total angular momentum J and the quantum numbers of all electrons. Finally, we include the *parity* of the level, which manifests as a circle subscript above L. The parity of a state refers to whether the wave-function of a level is symmetric or anti-symmetric, and is described as 'even' if the sum of each electron's orbital angular momentum, $\Sigma_k l_k$, is even and odd if the sum is odd. The L-S state is presented like so;

$$^{2S+1}L_J \ \ (even\ parity) \qquad \text{or} \qquad ^{2S+1}L_J^\circ \ \ (odd\ parity), \tag{3.8}$$

and is given after the electronic configuration, as is demonstrated for the ground state of singly ionised argon, ArII;

$$1s^2 2s^2 2p^6 3s^2 3p^5 \ ^2\mathrm{P}^\circ_{3/2} \to 3p^5 \ ^2\mathrm{P}^\circ_{3/2} \tag{3.9}$$

where $S = 1/2$ and $L = 1$, and the RHS is a common abbreviation that excludes closed sub-shells. This abbreviation can be more clearly outlined by grouping electrons into the electronic configuration of an equivalent ground state noble gas atom in square brackets, such that $1s^2 2s^2 2p^6 \to [\mathrm{Ne}]$.

Ar$^{+,m}$ metastable state	Excitation energy (eV)
$3s3p^6\ ^2P^\circ_{1/2}$	0.1775
$3s^23p^4(^3P)3d\ ^4D_{7/2}$	16.4065
$\cdots\ 3d\ ^4F_{9/2}$	17.6289
$\cdots\ 3d\ ^4F_{7/2}$	17.6947
$\cdots\ 3d\ ^2F_{7/2}$	18.4958
$3s^23p^4(^1D)3d\ ^2G_{9/2}$	19.1161
$\cdots\ \overline{3d\ ^2G_{7/2}}$	19.1187
$\cdots\ 3d\ ^2F_{7/2}$	20.2722

TABLE 3.1 – The known metastable states of singly ionised argon at the time of Varga *et al.* [274]. The selected metastable state for the LIF diagnostics used throughout this thesis has been underlined.

For atoms or ions with a single excited electron, it is common to include the $L-S$ configuration of the 'parent' ion in closed brackets before the description of the excited electron begins [269, 273]. The parent ion is the ground state of the atom or ion without the excited electron. This is done in an attempt to align the $L-S$ coupling scheme more closely with that of Racah notation since singly excited atoms sometimes break the $L-S$ coupling rules. As an example, the ArII $3d'\ ^2G_{9/2}$ state can be fully represented as

$$[\text{Ne}]3s^23p^4\left(^1D\right)3d\ ^2G_{9/2} \tag{3.10}$$

where $[\text{Ne}]3s^23p^4\left(^1D\right)$ represents the ground state of the parent ion (which is doubly ionised argon in this case), on top of which we have the excited electron occupying the $3d\ ^2G_{9/2}$ level. If a parent ion is common to many levels for an atom or ion it can be abbreviated with an apostrophe on the excited electron quantum numbers, such that $3s^23p^4\left(^1D\right)3d \Leftrightarrow 3d'$. The known metastable states of singly ionised argon relevant to the LIF diagnostic as determined by Varga *et al.* [274] are given using the $L-S$ coupling scheme in Table 3.1

3.1.4 Transition selection rules

When an electron transitions between different energy levels, the total angular momentum of the system must be conserved. This means an electron can transition between any state if the change is caused by a binary or higher order collision with other massive particles. Optical transitions, however, are limited by the momentum change that is offered by absorbing or emitting a photon that is restricted to a spin angular quantum number of $\{-\hbar, 0, \hbar\}$. This results in a set of optical selection rules individual to each notational scheme that govern the likelihood that a transition will take place. This fact also explains why emission and absorption spectra do not involve all possible transitions between $L-S$ states. Paschen notation, for example, was an attempt

to explain the electronic configuration of neon using hydrogen like theory based on observed transitions [269], and is still used in the literature today.

The rules for optically allowed transitions between L-S coupling levels are as follows:

1. L must change by 0 or ± 1. $\Delta L = 0, \pm 1$ (*L can't go from 0 to 0*)

2. J must change by 0 or ± 1. $\Delta J = 0, \pm 1$ (*J can't go from 0 to 0*)

3. The parity *must* change.

4. S must not change. $\Delta S = 0$.

An optical transition is either allowed (follows the rules above) or forbidden. Forbidden transitions can in fact occur, but much more rarely than their allowed counterparts resulting in transmission lines that are usually 10^5 to 10^{12} times fainter [269]. There are some intermediate transition cases with transition probabilities lying somewhere between these two extremes, giving transmission lines known as *intercombination* lines. The set of spectral lines resulting from all allowed transitions between two terms is called a *multiplet*, with specific names such as 'singlet', 'doublet', 'triplet' if the number of possible J values is known. An indicator that the $L - S$ coupling parameters are breaking down is when emission lines between states are observed that can not be predicted by the $L - S$ coupling scheme alone.

3.1.4.1 Transition probabilities and emission/absorption coefficients

Transmission probabilities are a microscopic description of the average time a transition will take to occur between an upper state (2) and lower state (1), and can be broken up into spontaneous emission (with associated Einstein coefficient A_{21}), absorption (B_{12}), and stimulated emission (B_{21}) components [269]. The lifetime of a level is the average of the inverse of all downward spontaneous transitions from that level. These range from 10^{-8} s for allowed transitions, 10^{-5} s for intercombination transitions, and from 10^{-3} s up to millions of years for forbidden transitions. The number of spontaneous emissions between levels (2) and (1) per unit time and volume in a system is a constant that depends only on the transition probability and the local number of atoms in that state, $n_2 A_{21}$, where n_2 is the number density of atoms with an electron in excited state 2. The number of absorption transitions also depends on the available intensity of photons with the required frequency, I_{21}, to facilitate the upward transition, $n_1 B_{12} I_{21}$.

Stimulated emission occurs when an excited state of an atom is induced into releasing a photon with the same phase, direction, and even polarisation as an external photon interacting with the system. This process therefore depends on both the local intensity of photons with the necessary transition frequency as well their phase relative to equivalent photons emitted from the atom.

Stimulated emission is possible instead of absorption since an oscillator can impart energy to a wave instead of the other way around if they are out of phase with each other. Stimulated emission is also important when considering saturated LIF signals as the laser can begin to depopulate the upper fluorescent state at an unknown rate. The number of stimulated emissions per unit volume and time is given by $n_2 B_{21} I_{21}$.

3.1.5 Other notation schema

The $L - S$ coupling scheme sometimes fails to describe energy levels in atoms where you would otherwise expect it to apply[2]. Paschen notation is adequate for explaining many transitions in neon and argon, however, and is commonly used in the literature. Racah or j-l notation was a subsequently developed quantum mechanical framework to describe the energy levels in low-proton atoms with a single excited electron.

3.1.5.1 *j-l* or Racah notation

The Racah notation scheme works by treating the single excited electron in an atom and the remaining parent ion as two separate entities that couple together [275]. The spin-orbit interaction in the parent ion dominates over the electrostatic interaction between the excited electron and the core, which in turn dominates over the spin coupling of the electron to the core. The total angular momentum of the parent ion, $\tilde{\boldsymbol{J}}_{\mathrm{i}}$, is coupled with the orbital angular momentum of the excited electron, $\tilde{\boldsymbol{l}}_{\mathrm{e}}$, to arrive at a new quantum vector, $\tilde{\boldsymbol{K}}$, with associated quantum number

$$K = |J_{\mathrm{i}} + l_{\mathrm{e}}|, \ |J_{\mathrm{i}} + l_{\mathrm{e}} - 1|, \ \cdots, \ |J_{\mathrm{i}} - l_{\mathrm{e}}|. \tag{3.11}$$

We then couple $\tilde{\boldsymbol{K}}$ to the spin of the excited electron, $\tilde{\boldsymbol{s}}_{\mathrm{e}}$, to find the total angular momentum of the excited electron with the parent ion $\tilde{\boldsymbol{J}}_{\mathrm{e}}$ which takes values

$$J_{\mathrm{e}} = K + s_{\mathrm{e}}, \ \ J_{\mathrm{e}} > 0. \tag{3.12}$$

To write a state fully in Racah notation, we put the L-S state of the parent ion first in round brackets, followed by the quantum numbers of the excited electron, followed by the value of K in square brackets with J_{e} as a subscript;

$$\left(^{2S_{\mathrm{i}}+1}L_{\mathrm{i}\,J_{\mathrm{i}}}\right) n_{\mathrm{e}} l_{\mathrm{e}} \left[K\right]_{J_{\mathrm{e}}}. \tag{3.13}$$

---

[2]See Appendix 2 from Gaseous Electronics: Theory and Practice [271] for greater detail.

For argon with a single electron excited to the 4p level, a possible state would be $\left(^2P^{\circ}_{3/2}\right)4p\,[5/2]_3$ where in this case $K = J_\mathrm{i} + l_\mathrm{e} = 3/2 + 1 = 5/2$, $J_\mathrm{e} = K + s_\mathrm{e} = 5/2 + 1/2 = 3$, and the parent ion has even parity. Sometimes the parity symbol is put as a superscript on the square bracket.

In the special cases of neon and argon (after which many of these notation schemes were based), the parent ion has two nearly equivalent ground states, $^2P^{\circ}_{3/2}$ and $^2P^{\circ}_{1/2}$, where the former is slightly lower in energy. A common abbreviation in Racah notation is to differentiate between these higher and lower possible ground state with an apostraphe on the excited electron's quantum numbers, avoiding the need to write out the parent ion's L-S configuration. For example,

$$\left(^2P^{\circ}_{1/2}\right)ns \Leftrightarrow ns', \qquad \left(^2P^{\circ}_{3/2}\right)ns \Leftrightarrow ns, \qquad \left(^2P^{\circ}_{1/2}\right)np \Leftrightarrow np', \cdots. \tag{3.14}$$

3.1.6   Paschen notation

Paschen notation is an upward list of excited states in energy that maintains the structure of allowed transitions between levels. The ground state atom is always designated as 'ground state'.

Ne electronic configuration	Ar electronic configuration	Paschen notation
$1s^2 2s^2 2p^6$	$[\mathrm{Ne}]3s^2 3p^6$	Ground state
$1s^2 2s^2 2p^5 3s^1$	$[\mathrm{Ne}]3s^2 3p^5 4s^1$	$1s_{1-4}$
$1s^2 2s^2 2p^5 3p^1$	$[\mathrm{Ne}]3s^2 3p^5 4p^1$	$2p_{1-10}$
$1s^2 2s^2 2p^5 4s^1$	$[\mathrm{Ne}]3s^2 3p^5 5s^1$	$2s_{1-4}$
$1s^2 2s^2 2p^5 4p^1$	$[\mathrm{Ne}]3s^2 3p^5 5p^1$	$2p_{1-10}$
$1s^2 2s^2 2p^5 5s^1$	$[\mathrm{Ne}]3s^2 3p^5 6s^1$	$3s_{1-4}$

TABLE 3.2 – Paschen notation for excited neon or argon

Then, the first excited state is designated as $1s$, followed by $2p$, then $2s$, $3p$, and so on. Here, the letter corresponds to the orbital angular momentum l_e of the excited electron, and increasing values correspond to increasing energy of the level. The $\Delta l_\mathrm{e} = \pm 1$ rule for allowed transitions is maintained in Paschen notation. Finally, from Racah notation we can see that each ns level of the excited electron corresponds to 4 possible states and each np level to 10 possible states. These are listed as np_1, np_2, $\cdots$, np_{10}, where increasing subscript value corresponds to a lower energy state. Paschen notation for neon and argon is outlined in Table 3.2.

3.2   Historical assumptions concerning the use of LIF

The assumed relationships between the observed metastable VDF, $f_{m,v}$, and the ground state VDF, $f_{g,v}$, at a measurement location x that are sometimes used in LIF literautre were briefly discussed in Chapter 2.2. $f_{m,v}$ was assumed to be a proportionate representation of $f_{g,v}$ at x in order to draw conclusions about the diverging ion hypothesis in Chapter 2.3. It may well

be that ArII 3d′ $^2G_{9/2}$ metastable ions are created at different proportions within and without of the cathode to ArII ions in general, however, leading to an overstated importance of the hollow cathode effect than was actually the case. The possible invalidity of these sorts of assumptions would have ramifications not only for the conclusions drawn concerning the diverging ion hypothesis but also in past published research that has used them. We therefore review the prevalence of this assumption in the literature as well as existing publications that demonstrate the anomalous ion density phenomenon before approaching the hollow cathode experiments.

The LIF diagnostic has been fundamental in plasma analysis since its conception near to 1970 [276, 277]. The non-perturbative detection and relative comparison of local atomic or ionic distribution functions at multiple locations throughout a discharge has been used for the confirmation of many plasma and discharge phenomena. These include the measurement of ion transport [248, 253, 278–280], properties of the cathodic sheath [281–283], plasma population densities [243, 284, 285] and temperatures [102, 103, 286–290], electromagnetic field strengths [262, 291–293] and atomic hyperfine structure [236, 294, 295], plasma dynamics and waves [296–300], and many biological phenomena [301]. Many of the theories involved with these types of analyses do not distinguish between the excited state of the population under investigation and therefore require knowledge of its majority states, usually the ground state. This is not possible for most typical scanning lasers used in LIF analysis that are restricted to optical wavelengths [241]. A pumped transition from a long lived metastable state must be chosen that results in nearly immediate fluorescence.

However, it is not given that this metastable state will behave in a way that accurately reflects its equivalent ground state. The ratio of the density of all metastable states to the ground state in argon glow discharges is reportedly on the order of 10^{-5} for ArI [302–305] and at most 10^{-2} for ArII [254, 287, 306, 307], and frequently much less than this [277]. This means that the observation of the VDF of a single metastable quantum level is usually insufficient for the comprehensive solution of plasma theories. As an example of this, models of the cathode sheath thickness discussed in Chapter 1.1.6 require knowledge of the total population of singly ionised particles and are insensitive to the state of excitation of any particular particle. Therefore, determining the distribution function of a metastable ion population alone that comprises less than 1 % of the total ion population that may be distributed entirely differently will not accurately reflect the organisation of the cathode sheath. For these sorts of reasons an assumption is sometimes made in the literature concerning the information that can be inferred about a ground state population from an observed VDF. The true nature of this relationship for IVDFs at different locations within a plasma has not been comprehensively determined, to the best knowledge of the author. We shall focus our analysis on the known metastable states of singly ionised argon, listed in Table 3.1, in comparison to the most densely populated ArII $3s^23p^5\,^2P^{\circ}_{3/2}$

ground state in a typical argon glow discharge [308].

Some researchers draw comparisons between $f_{m,v}$ and $f_{g,v}$ by citing the similarity in the mass and charge of two species. Stern and Johnson [277] began this trend by comparing the linear relationship of both spontaneous and LIF emission to increasing current in a low pressure hot cathode argon discharge, arguing that the LIF diagnostic is therefore a sensitive probe of $f_{g,v}$. The claim that the ratio of VDFs, $r_{m/g} = f_{m,v}/f_{g,v}$, will remain proportionate throughout velocity space and that this relationship will be maintained across multiple measurement locations has been made at various strengths in some following works, as noted by Skiff *et al.* [280]. In some cases an analysis has been made that implicitly relies on this comparison without stating so directly [236, 248, 281, 283, 296, 299]. This was the case in the publication by the author given in Chapter 2.3 in which the relative density of ArII populations within the two ring cathode was discussed whilst having only measured the IVDFs of the ArII 3d' ^{2}G$_{9/2}$ state [193].

Otherwise, it is more frequently assumed that the shape of each VDF will remain in proportion at an individual location, particularly when outside of electromagnetic fields [242]. In these cases it is argued that the equivalent mass and charge of each population will likely cause them to respond equally to local electromagnetic fields. The ArII 3d' ^{2}G$_{9/2}$ metastable state, for example, has a lifetime of at least 10 μs for purely spontaneous emission [254, 309, 310], and is therefore recognised for its assumed ability to react to the local discharge environment in a manner that reflects the behaviour of the ArII ground state population. However, this assumption necessarily implies that $r_{m/g}$ will be representative throughout phase space. Altkorn and Zare [243] have noted this trend in the literature and proceed to indicate that this assumption will only be invalid if the optically pumped transition is saturated. Goeckner *et al.* [102, 311] go further to explicitly state that the relative density of a metastable ion population at different locations will be a proportional representative of the ground state density even in the cathode sheath and pre-sheath. Although Goeckner *et al.* demonstrate that this is indeed the case between two of the ArII metastable states listed in Table 3.1, the cross-sections for the main creation and destruction mechanisms of various ArII metastable states (discussed in Chapter 5.1) are similar to each other. This would imply that the various metastable states are likely to form in similar distributions to each other but not in comparison to other states that have different formation mechanisms. Severn *et al.* [312] have shown that the VDfs of the ArII metastable states given in Table 3.1 indeed remain in proportion but make no comment on $r_{m/g}$.

The assumption that the unsaturated LIF signal of an ionic metastable population at a location x will be qualitatively representative of $f_{g,v}$ depends on the differences between the mechanisms that generate and destroy each population. The rate processes that contribute to each population will be discussed at length in Chapter 5.1 for the collisional rate analysis of the ArII 3d' ^{2}G$_{9/2}$ state. For now, it is enough to know that the cross-section for the creation of
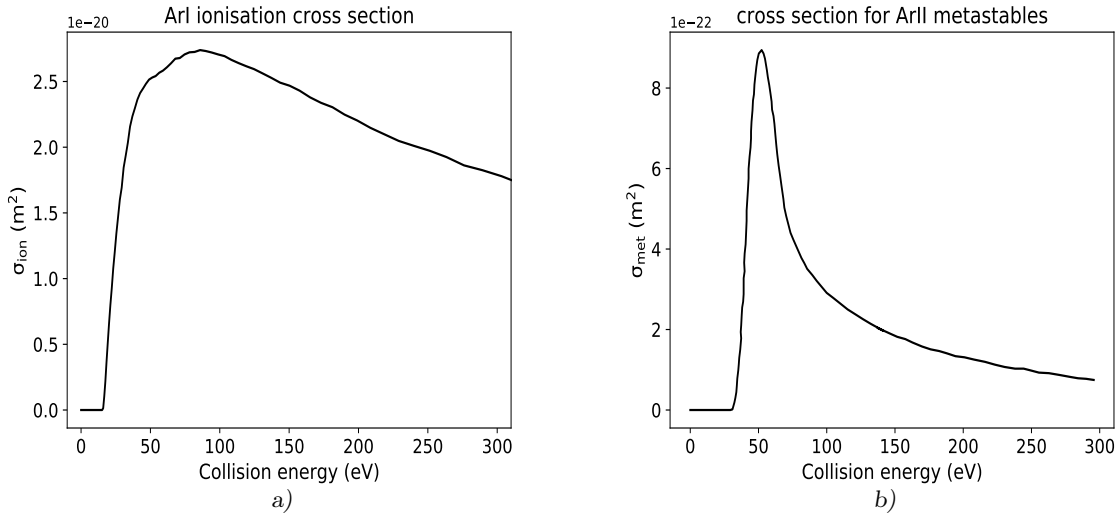
FIGURE 3.1 – *a)* The average cross-section for the electron impact ionisation of ArI to all ArII states, σ_{ion}, taken from the literature [313–317]. *b)* The cross-section for the simultaneous ionisation and excitation of ArI to all ArII metastable states listed in Table 3.1 [254, 306, 309], σ_{met}, of which the ArII 3d′ ^{2}G$_{9/2}$ state will represent only a fraction (discussed in Chapter 5.1.1.1)

metastable ions by electron impact processes, σ_{met}, has a high threshold energy followed by a sharply peaked maximum [254, 306, 309], shown in Figure 3.1b). This means that the spatial distribution of energetic electron populations likely has a strong influence on the spatial distribution of metastable ions. This may not be true to the same extent for the ionisation of neutral argon to the ground state by electron impact, which has a relatively constant cross-section σ_{ion} up to 300 eV beyond its threshold of relative collision energy [313–317] as shown in Figure 3.1a). Keeping this in mind, the VDF of ground state ions at a location x within a cathodic pre-sheath, for example, will be formed not only by the generation of ions at x but also by ions that have been accelerated there from other locations by electromagnetic fields and diffusion processes. If metastable ions are generated at a different ratio at x as compared to outside of the pre-sheath, or if they experience a different rate of collisional deceleration, then $f_{m,v}$ at x will likely be qualitatively different to $f_{g,v}$. This is a pertinent example as the pre-sheath in a glow discharge has been observed to contain secondary electron populations with rapidly varying mean energies [100, 318] that likely affect the local production of metastable ions. Skiff *et al.* [280] have argued that a strongly perturbed electron distribution or systematic distortions of the LIF signal as discussed in Chapter 2.2.1 can cause both a spatial and velocity dependence of $r_{m/g}$ for the ArII 3d′ ^{2}G$_{9/2}$ state. They show that metastable quenching by binary collisions affects $r_{m/g}$ by removing high energy metastables from the population at a greater rate than the ground state ion population is decelerated by charge exchange collisions in a double-plasma device. The deviation from a representative $r_{m/g}$ has also been shown to occur in hybrid fluid-Monte Carlo modelling of ArI metastables in hollow cathode discharges at low pressures [304, 305]. Skiff *et al.* note [280] that the presence of electron populations that are changing in energy or density will

affect $r_{m/g}$ due to the more frequent metastable quenching by electron collisions compared to pure recombination. Romadonov *et al.* [300] compared the cross-sections for the electron impact ionisation and excitation of xenon neutrals into metastable states to that of ionisation as a whole to argue that $r_{m/g}$ will similarly not remain representative. However, no further analysis to the general validity or invalidity of the constancy of $r_{m/g}$ has been made to the best knowledge of the author, particularly in the presence of energetic electron populations.

3.2.1 Anomalous density increase in cathodic pre-sheaths

A further indication that the comparison between metastable and ground state ions may not be valid has arisen in LIF observations of an apparently anomalous ion density distribution within a cathodic pre-sheath [103, 257]. In the following discussion of the pre-sheath it is very important that the nomenclature used for different electron populations is agreed upon given the varying conventions that exist. We use the definitions given in Section 1.1.8; the Maxwellian 'cold' or 'bulk' population found in vast majority at temperatures on the order of 1 eV in the bulk plasma; 'primary' electrons emitted directly from thermionic filaments, and 'secondary' electron populations emitted from surfaces such as the cathode by particle bombardment. Populations of an undetermined source with higher mean energy than that of the bulk electrons are referred to as 'hot' or 'energetic' electron populations.

The plasma pre-sheath was first proposed by Bohm [121] to resolve the previously ill-posed transition from the cathode sheath to the plasma in a collisionless, two-species, planar diode discharge. A low temperature ion population must be slowly accelerated to at least their sound speed $u_0 > \sqrt{k_B T_{e,c}/m_i}$ by the pre-sheath potential while consequently reducing in density due to the conservation of flux. Otherwise, if the ion temperature follows $T_i \ll T_{e,c}$ as is usually the case (see Chapter 1.1.7), the ion density will decrease more quickly in the cathode sheath than the cold electron population [36]. This would lead to a non-monatonic sheath potential, depicted illustratively in Figure 3.2, that causes the boundary value problem given by Equation 1.35 to become ill-posed. We follow Riemann's proposal for the most common definition of the cathodic pre-sheath [19] as the region in which ion motion is inertia dominated. Riemann proposed that the potential drop $\phi(x)$ from the plasma potential ϕ_p at a location x to the sheath boundary at x_0 is given by [319]

$$\phi(x) = \phi_p + \frac{T_{e,c}}{q_e}\sqrt{\frac{x_0 - x}{l}}, \tag{3.15}$$

where $T_{e,c}$ in this case is the temperature of the cold electron population in the bulk plasma that begins at $x = x_0 + l$, and l is the characteristic length of the pre-sheath. l has been shown to be proportional to the total ion-neutral collisional mean free path $\lambda_{i,n}$ in low pressure discharges using LIF analysis of the ArII 3d' ^{2}G$_{9/2}$ state [282, 320]. The multiple definitions and

theories concerning the pre-sheath within the literature that have since been developed [19] share the general trend of a decreasing ion density approaching the cathode sheath. This behaviour has also been routinely observed in experiment [267, 321]. The expected ion density profile and relationship between the sheath, pre-sheath, and plasma potential has been qualitatively illustrated as the solid black lines in Figure 3.2.

In contrast to this, Claire *et al.* [103] reported LIF measurements of an anomalous increase in density of the ArII $3d'$ $^2G_{9/2}$ population across the pre-sheath approaching a negatively floating planar plate in a low pressure multipole discharge in argon, shown in Figure 3.3. The rapid acceleration that occurs once the metastable ions enter the potential drop of the cathodic sheath results in a density distribution that is sharply peaked at the sheath/pre-sheath boundary. The peak in the ArII $3d'$ $^2G_{9/2}$ population density reaches four times its value observed in the bulk plasma [103]. This indicates either an unexpected disruption from classical pre-sheath theory if indeed $r_{m/g}$ is representative or otherwise the possible unreliability of making this comparison. Claire *et al.* suggest the possible influence of energetic electron populations, but no further analysis was given.

The anomalous increase had been previously observed without identification in a similar LIF analysis of a multipole discharge in argon [257]. Severn *et al.* [283] also gave LIF measurements of the ArII $^4F_{7/2}$ in front of a biased cathode that demonstrate the anomalous behaviour, again without comment. Goeckner *et al.* [102] presented an LIF analysis of the ArII $3d'$ $^2G_{9/2}$ metastable state within a planar cathode sheath in a multipole discharge in argon in which the density increase effect is not confirmed but would remain possible if measurements were taken further into the pre-sheath.
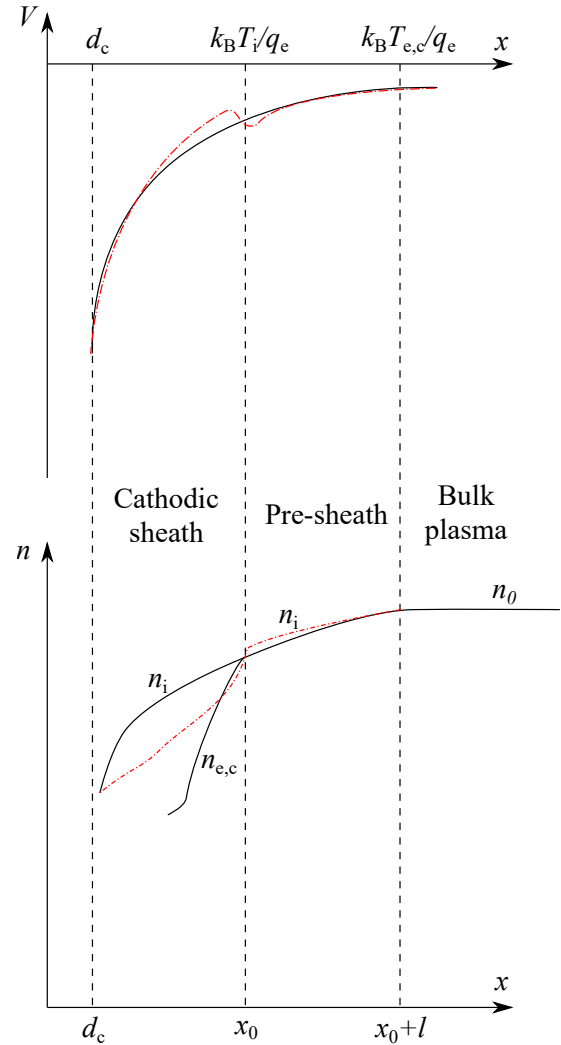
FIGURE 3.2 – An indicative illustration of how the potential and charge particle densities change towards a cathodic sheath as described by Bohm's pre-sheath theory [121] (solid black lines) and without the pre-sheath acceleration of the ions (red dot-dashed lines).
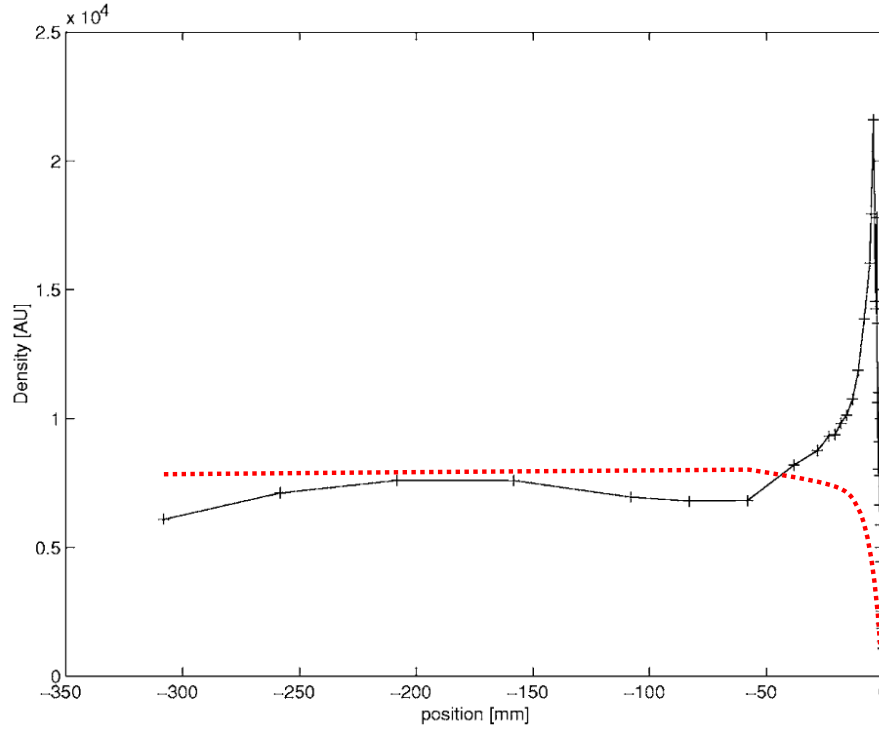
FIGURE 3.3 – The LIF observation of the anomalous ArII $3d'\,^2G_{9/2}$ density distribution in front of a floating plate (at 0 mm) in a multipole discharge with 3.6 mTorr of argon and -50 V applied to the thermionic filaments, reproduced from Claire *et al.* [290]. An example of an expected ion density profile according to Bohm theory [121] is given as the red dotted line.

3.2.2 Implications for the two-ring experiment

The claims made about the diverging ion theory based on the experimental results for the two-ring cathode experiment given in Chapter 2.3 could be questioned if $r_{m/g}$ is indeed not representative. The very basis of the hollow cathode theory presented as an explanation of the observed ArII $3d'\,^2G_{9/2}$ IVDFs in Figure 2.9 relied on the presence of highly energetic secondary electron populations. These secondary electrons may preferentially create ArII $3d'\,^2G_{9/2}$ metastables over ground state ArII ions within the cathode, contributing at an unknown extent to the high ratio of diverging to converging metastable ions shown in Figure 2.10. However, it is unknown whether the preferential ionisation of ArII $3d'\,^2G_{9/2}$ metastables could fully account for the roughly 10 times greater diverging ion density observed at 23 cm along z in Figure 2.10. The LIF analysis of a low pressure hollow cathode discharge in a multipole system would likely help clarify the cause of this anomalous ion density phenomenon. First, the admittance of a laser beam through the hollow cathode cavity avoids the increase in density near surfaces that would be caused by laser reflection from a planar surface through the observation region [245]. Second, the highly energetic secondary electron beam produced by the hollow cathode effect (discussed in Chapter 1.3) should affect the creation of ArII $3d'\,^2G_{9/2}$ metastables. It may be possible to isolate the contribution of the beam from the primary electron population (discussed in Chapter 2.2.2) by comparing both filament mediated and self-sustaining low pressure hollow cathode discharges. A

primary electron population was always present in the previous cases that exhibited the anomalous density increase, but other electron populations and possibly geometric effects may also contribute to it.

Furthermore, the experiments given below were simultaneously intended to clarify the formation of a virtual anode by ambipolar effects, and in doing so, shed light on the low pressure hollow cathode discharge. It was discussed in Chapter 1.3 that the hollow cathode effect occurs when the negative glow from opposite interior surfaces of the hollow cathode overlap, and that the sheath width may be approximated by Equation 1.36. The high voltage and low pressures of typical IEC operating conditions may cause the interior cathode sheaths to expand to an extent that they overlap, so that no interior negative glow region exists (sometimes called an 'obstructed discharge' [322]). This has been previously observed [4, 131, 133, 134] to create a positive space charge in the cathode interior, highly focused diverging secondary electron beams, and a dramatic increase in the required cathode voltage to achieve the same discharge current. By observing IVDFs near or within the hollow cathode at various discharge pressures near 1 mTorr, we may well be able to observe the transition between an abnormal and an obstructed hollow cathode discharge mode. It may well be the case that all IEC discharges are operating in this obstructed mode with an increased interior sheath width, resulting in a virtual anode either through ambipolar effects or other mechanisms.

3.3   Experimental arrangement

Experiments were performed within the same grounded cylindrical multipolar discharge chamber as in Chapter 2.3, with an inner diameter and length of 40 cm and 80 cm respectively. The discharge chamber as well as the region of magnetisation has been given again in Figure 3.4. Alternating bar magnets were axially aligned on the cylindrical wall of the vacuum vessel alone, such that the plasma could be considered unmagnetised beyond 8 cm into the discharge [257]. The multipole chamber was evacuated to a base pressure in the order of 10^{-6} Torr with an Arlikan-Leyhold AMM71ZBA4 vacuum pump supported by a Pfieffer-Balzer TCP130 turbomolecular pump. Pure argon gas was then admitted to the chamber up to the operating pressures that were measured simultaneously by a Pfieffer compact IK2251 cold cathode gauge and a TPG 035 Balzers needle gauge. The pressure gauges were maintained such that they agreed within 20 % of each other. The discharge for experiments performed at 0.19 mTorr and 1.9 mTorr were mediated by two thermionic tungsten filaments placed within the un-magnetized discharge volume. The filaments were biased at -50 V relative to the grounded vessel wall and a heating current applied such that a stable 0.5 A current was drawn from each filament. A cylindrical hollow cathode of 1.25 cm inner radius and 6 cm length was held in the centre of the discharge and aligned symmetrically with the discharge chamber. This rather long aspect ratio
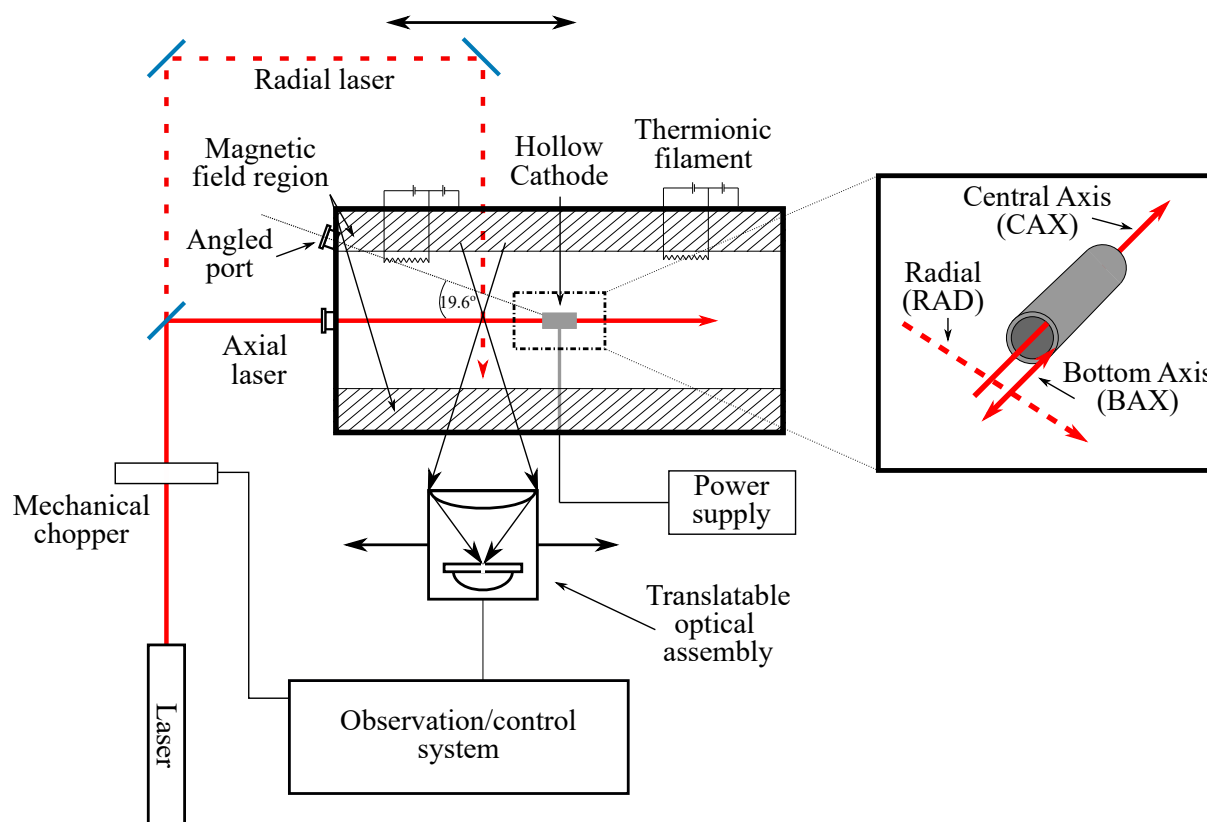
FIGURE 3.4 – The experimental arrangement used for the LIF analysis, with the multipole chamber and its internals to scale. The attempted observation of the cathode interior through the angled port is shown. The inset displays the laser orientations relative to the hollow cathode.

was designed such that the interior axis of the cathode could be viewed beyond the cathode centre from the angled port, shown in Figure 3.4. Furthermore, it was initially hoped that the length of the hollow cathode would create a wider virtual anode, such that the development of the IVDF might be better distinguished by the optical array. The cathode was connected to a Technix SR1-N-1200 1.48 kW power supply via a thin stainless steel rod that extended to a port on the curved cylindrical wall. This was limited to a maximum bias magnitude below 2 kV, such that discharges could not be tested in the 10-100 kV range often used in IEC analyses. The hollow cathode was biased to -200 V in the filament mediated discharges and drew between 4-5 mA of current in the experiments performed at 0.19 mTorr and 12 mA at 1.9 mTorr. A further, self-sustaining discharge was conducted without the use of the thermionic filaments in which the cathode was biased at -1000 V with 38 mTorr of background gas, drawing 7-10 mA of current. The discharge conditions correlated to being within an abnormal glow discharge regime, as was tested by determining an increasing rate of change of cathode current with increasing cathode bias.

Discharges were run for at least 10 minutes with each set of experimental parameters before LIF observations were recorded to allow the discharge to reach a steady state. Primary electrons emitted by filaments and trapped within a magnetic multipole arrangement have either

been observed in an isotropic mono-energetic distribution at pressures below 1 mTorr [106, 255, 257–259, 323] or in an energetic Maxwellian distribution otherwise [260]. This primary population is intended to significantly increase the creation rate of metastable argon ions in the bulk plasma. It has also been observed [259, 260, 290, 324, 325] that the floating potential V_f in similar thermionic systems without a cathode is a function of the applied potential to the filaments V_D and the neutral pressure p, where $V_f \rightarrow V_D$ as $p \rightarrow 0$.
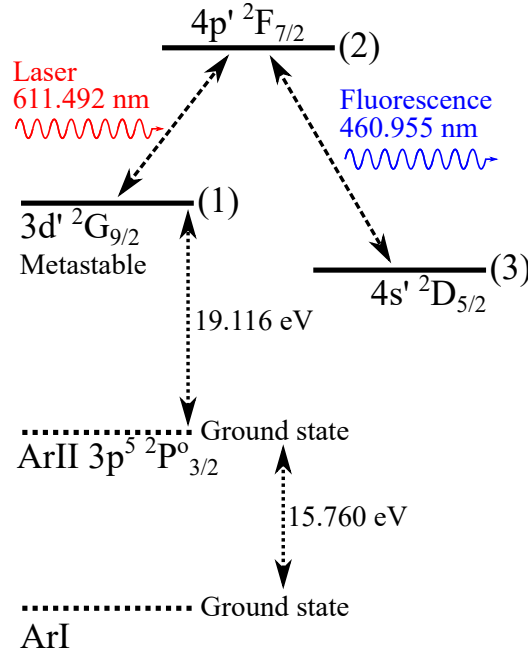
FIGURE 3.5 – The most important states of argon for the LIF analysis.

The laser beam used in the LIF analysis was produced by a coherent 899 tunable dye laser pumped by a 5 W coherent Verdi solid state laser, identical to that used in Chapter 2. The laser signal was mechanically chopped at 1 kHz and frequency calibrated using an iodine plasma absorption spectrum within a Fabry-Pérot interferometer system. The laser line was manually fixed near to the 611.5 nm vacuum pumping line of the ArII $3d'\,^2G_{9/2}$ metastable to $4p'\,^2F_{7/2}$ transition, shown in Figure 3.5, with a 20 GHz scanning range and 0.5 MHz bandwidth. This allows for sufficiently high frequency resolution to determine thermal background gas particle temperatures relative to the natural 14 MHz natural linewidth of the transition [236]. The 460.957 nm fluorescent emission from the $4p'\,^2F_{7/2}$ to the $4s'\,^2D_{5/2}$ with spontaneous emission lifetime of 7.4 ns [326, 327] was detected by a slit, double lens, and photomultiplier optical array. The optical array could be axially translated in 0.1 mm steps when viewing radially into the discharge chamber. The $4s'\,^2D_{5/2}$ state has a dipole transition to the ground state, such that the fluorescence photon is not well absorbed by the plasma [248], improving the signal-to-noise ratio of the experiment. The laser through the discharge had an 8 mm diameter profile that can

be approximated as Gaussian [248] as was assumed in this work.

The laser could be admitted into the discharge chamber either along the hollow cathode axis, pumping the reduced metastable ion longitudinal VDF (ILVDF), or radially to the hollow cathode, measuring the ion radial VDF (IRVDF) as shown in the inset of Figure 3.4. The flat ends of the vacuum vessel were coated in a rugged absorbing layer [103] to minimise specular laser reflection that can confuse recorded IVDFs [245]. The fluorescence signal was isolated using two 3 nm optical bandpass filters centered at 460 nm and collimated using a 1 mm slit opening. This caused a laser volume with an axial length of at most 0.5 mm to arrive at the photomultiplier due to the double lens magnification, described below. An extended observation volume has been known to result in the convolution of the observed IVDF when the potential gradient across the observation volume is high [262, 328], as is the case within the cathode sheath. IVDFs measured in this region are therefore unlikely to display a population with a sharply peaked drift velocity. The chopped photomultiplier signal was processed using an EG×G Princeton 5210 lockin amplifier with 10 mV sensitivity and 1 ms time constant, isolating the fluorescence signal from background. Each measurement taken at every location within an experiment was the average of 5-10 frequency scans of the laser taking 50 s each such that the signal-to-noise ratio of the peak LIF signal, SN, was well above 4 for the majority of an experiment. SN was calculated using the variance from the mean value of each signal for its most negative velocities where no flourescence signal was apparent, as indicated as the overlayed red line in Figure 3.7.

3.3.1 The double lens arrangement

Experiments were performed using three laser orientations that are identified in the inset of Figure 3.4: with the laser beam passing through the central axis of the hollow cathode (labelled as CAX); with the laser aligned axially with the bottom lip of the hollow cathode (BAX), in which laser reflection will be present in the signal; and with the beam oriented radially through the discharge and translated axially (RAD). The exact radial distance from the central axis of the hollow cathode in the RAD arrangement could not be determined. Attempts were made to ensure this distance was less than the hollow cathode radius, but it could not be guaranteed. The optical array and radial laser position could be axially translated in unison in 0.1 mm increments.

At first it was attempted to observe the interior of the hollow cathode directly by using an optical port that was angled at 19.6° to the axis of the chamber and focused on the chamber centre, depicted in Figure 3.4. The double lens array, or 'lens doublet', was created in order to isolate narrow volumes along the laser beam while collecting as much fluorescent light as

possible. Additional degrees of freedom were granted by relative translation of the lenses [329]. The angle between the line of sight of the optical array and the laser beam meant that the length of beam captured by the observation volume was increased by approximately three times. This would serve to increase the effects of observation volume convolution [328]. Drilling a hole in the wall of the hollow cathode such that its interior could be viewed radially has been previously shown to significantly reduce the nuclear fusion rate in deuterium discharges [234]. The angled approached was therefore used since the ambipolar hypothesis that relates the magnitude of the virtual anode to the nuclear fusion rate could be too greatly affected by the introduction of an additional hole.

We assume the lenses to be infinitely thin, an approximation that only slightly affects the predictive accuracy of double lens theory [329]. Consider an arrangement of two convex lenses of focal lengths $\mathcal{F}_1$ and $\mathcal{F}_2$ separated by a distance $d < \mathcal{F}_1, \mathcal{F}_2$ focused on an object O of distance $\mathcal{S}_1$ from $\mathcal{F}_1$ (as depicted in Figure 3.6). This style of arrangement was forced by the optical
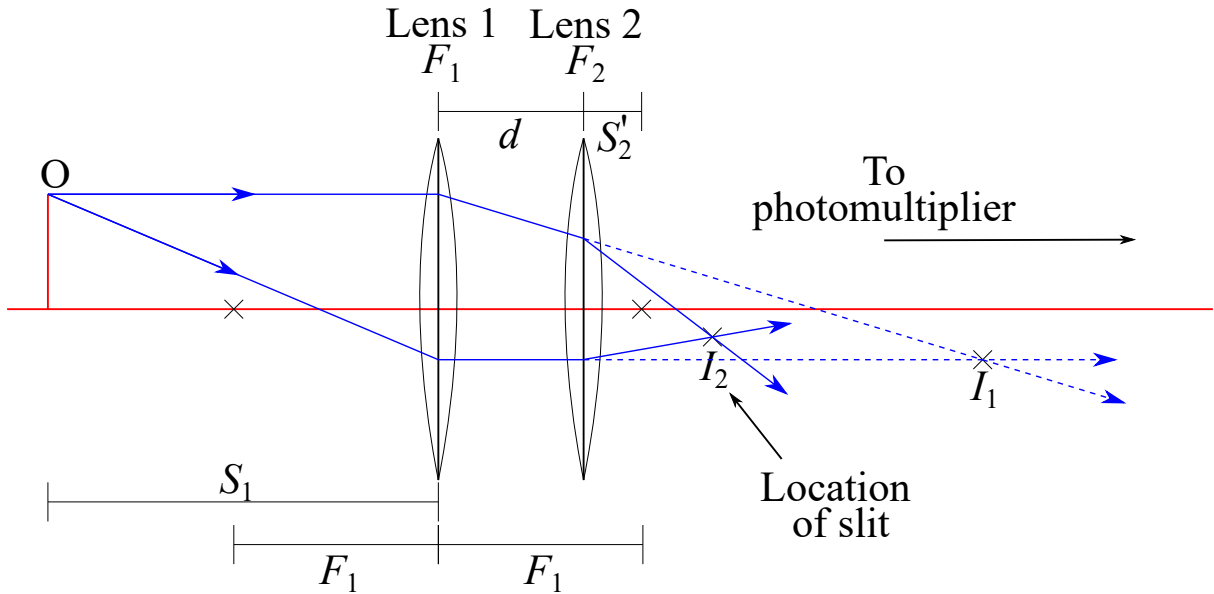
FIGURE 3.6 – Double lens array theory when the lens separation d is less than the focal length of the first lens $\mathcal{F}_1$.

alignment systems available during the transport restrictions of the Covid-19 pandemic. The second lens changes the location of the focused image of the first lens $\mathcal{I}_1$ to a new location, $\mathcal{I}_2$, as a function of $\mathcal{S}_1$ and d. The magnification of this image will follow

$$M = \frac{\mathcal{S}_1'}{\mathcal{S}_1} \frac{\mathcal{S}_2'}{\mathcal{S}_2}, \tag{3.16}$$

where $\mathcal{S}_1'$ is the distance from the first lens to the image it would create without the second lens at $\mathcal{I}_1$, $\mathcal{S}_2$ is the distance from the second lens to $\mathcal{I}_1$, and $\mathcal{S}_2'$ is the distance from the second lens to the final image at $\mathcal{I}_2$. The first lens had to be fixed to the angled port to exclude ambient light and capture the maximum fluorescence photons, such that $\mathcal{S}_1$ was constant. In this case,

the relationship between $\mathcal{S}_2'$ and d follows

$$\mathcal{S}_2' = \frac{(-\mathcal{S}_1' + d)\,\mathcal{F}_2}{-\mathcal{S}_1 + d - \mathcal{F}_2}. \tag{3.17}$$

The lenses available had focal lengths of 20 cm and 30 cm; if we chose $\mathcal{F}_1 = 30$ cm, then the domain of experimentally achievable lens separations d corresponded to almost no change in $\mathcal{S}_2'$, which was inadequate. However, it was discovered that the projection of the viewing angle along the laser beam as well as the enforced magnification of $M \leq 0.5$ of this arrangement given an object distance of $\mathcal{S}_1 \approx 45$ cm meant that IVDFs could not be determined with meaningful SN values. This was not the case when the double lens optical array viewed the laser beam radially with $\mathcal{S}_1 \approx 20$ cm, as shown in Figure 3.4. Thus, measurements of the interior of the hollow cathode had to be abandoned. It was hoped that it may be possible to view diverging IVDFs radially by observing the immediate vicinity of the hollow cathode.

3.3.2 The measurement of IVDFs

The laser intensity emitted from the laser system was measured before and after an observation at each location using a thermopile sensor. The fluorescence signal was only kept if the laser power had varied by less than 5 % over the photon collection period. The laser power exiting the system was kept between 300-400 mW for all measurements such that fluorescence peaks with $SN \geq 4$ were regularly visible without laser beam absorption effects [103]. The relative
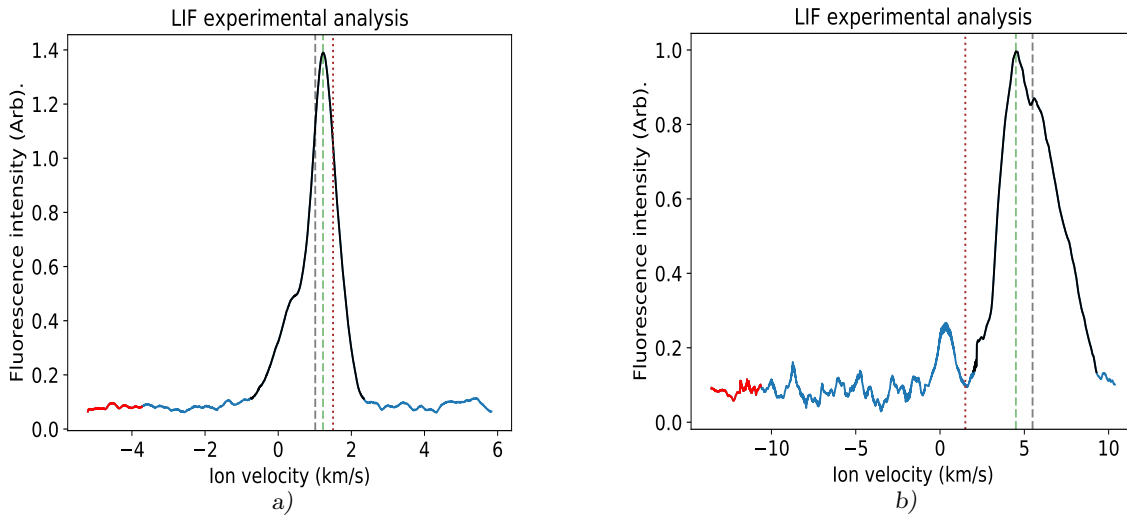
FIGURE 3.7 – Examples of the determination of the density and velocity from a typical LIF signal. Blue line, the LIF signal, with red section giving values included in the SN calculation. Grey and green dashed vertical lines, the mean and peak velocity respectively. Brown dotted line, $\tilde{v} = 1.5$ km/s. *Left:* The portion of the LIF signal in black, the values used in both the density and velocity integration since $v_{\mathrm{pk}} \geq 1.5$ km/s. *Right:* The values used in the mean velocity calculation only, excluding the ionisation peak since $v_{\mathrm{pk}} \geq 1500$ km/s.

laser power was also measured throughout each experiment by determining the relative intensity of a fraction of the laser beam line diverted using silvered mirrors. The laser power varied by at most 15 % over all observations for a set of discharge conditions and each fluorescence signal was subsequently normalised against the mean laser power during that time. It has been previously shown in the same experimental system, however, that the ArII $3d'\,{}^2G_{9/2}$ state can become saturated with a laser power above 50 mW [245], as described in higher detail in Chapter 2.2.1. Saturation causes an increase in metastable ion density between two subsequent locations to be underestimated, particularly with diminishing laser power over distance. Therefore, an anomalous density increase across the cathodic pre-sheath as discussed previously would occur in spite of these effects. The effects of saturation were therefore excluded from the following analysis of the density phenomena. However, inferences concerning the hollow cathode discharge in general using observed IVDFs are likely affected by saturation in a manner that was not accounted for given the lack of specific knowledge concerning the laser beam in the discharge. The low laser power variation throughout an experiment will minimise negative influences between measurement locations but the signal intensity may no longer be representative of an IVDF throughout velocity space. The high lasing power was required to avoid an insufficient rate of pumping of the ArII $3d'\,{}^2G_{9/2}$ state in regions where the population had a large drift velocity, so that saturation was unfortunately unavoidable.

3.4   Experimental results

The normalised fluorescence signals with axial distance from the nearest hollow cathode edge for each experimental arrangement, voltage, and pressure are given in Figure 3.8. A positive velocity corresponds to the direction approaching the cathode for the axially aligned laser experiments and is arbitrary in the radial case given in Figure 3.8f). The results have been presented as waterfall plots with an arbitrary offset between signals corresponding to a measurement location. Each continuous line corresponds to an ArII $3d'\,{}^2G_{9/2}$ IRVDF in Figure 3.8f) or an ILVDF in Figures 3.8 a)-e) measured at an axial distance from the cathode that is given next to the signal in millimetres. We refer to the axial location of the hollow cathode edge closest to the laser throughput port as $x = 0$ with increasing axial distance from the cathode as an increase in x. IVDF signals from different frequency scanning ranges at a single location have been averaged together where they overlapped to form a single continuous IVDF, such as in the measurements for $x \leq 7$ mm in Figure 3.8a). The value of the offset between IVDFs as well as the scale of normalisation within an experiment was chosen for clarity, and was not consistent across separate experiments. Figure 3.8c) indicates the experiment with a self-sustaining cathode discharge in which the thermionic filaments were not used. It should be noted that Figure 3.8e) contains the results of the BAX laser alignment and therefore includes the effect of laser reflection through the optical detection volume as described by Pigeon *et al.* [245].
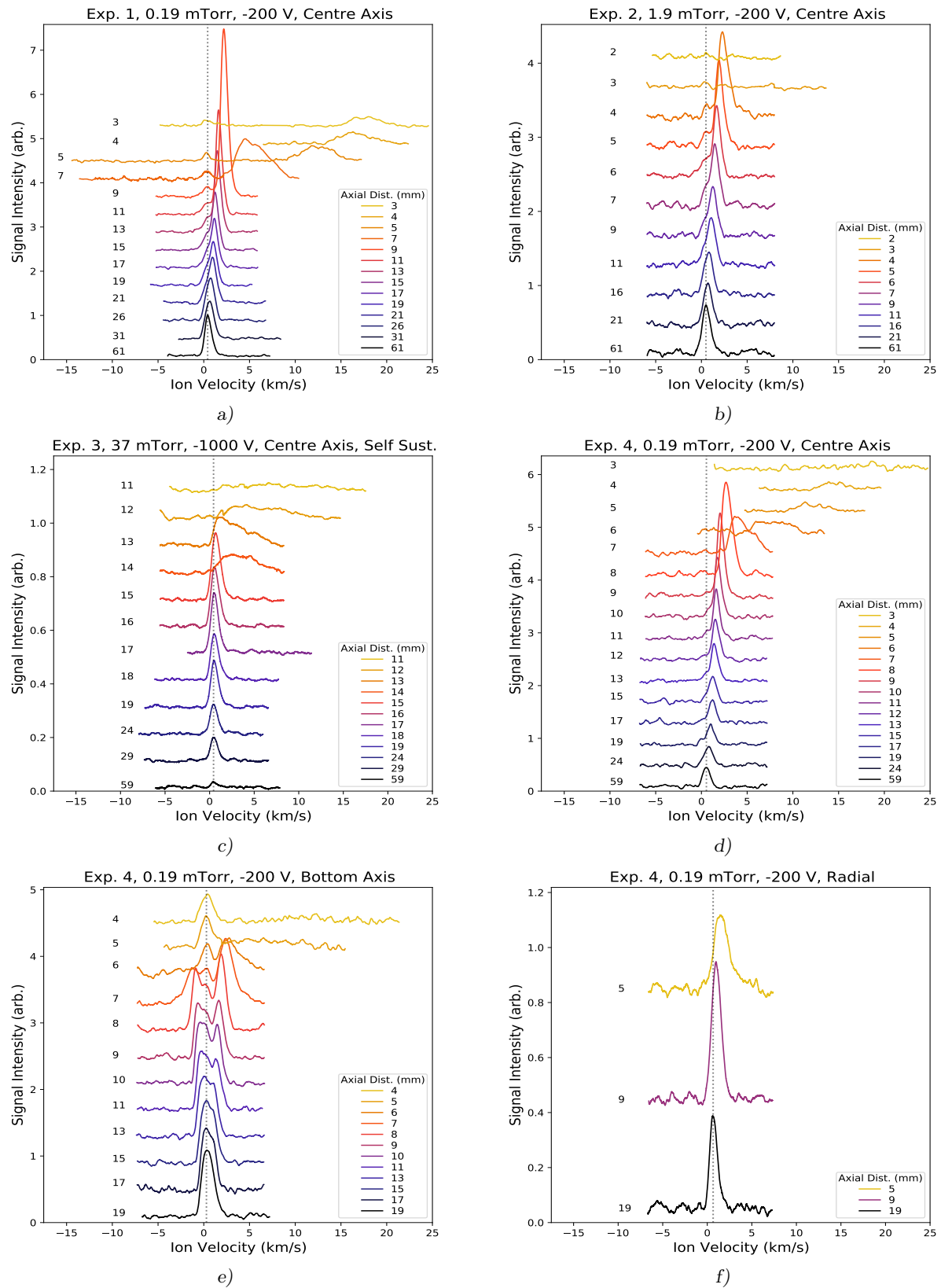
FIGURE 3.8 – The ILVDfs [*a)-e)*] and IRVDF [*f)*] for the hollow cathode experiments as waterfall plots. The axial distance of each measurement from the cathode is given in mm. ν_{p} of each IVDF furthest from the cathode is indicated by the vertical dashed line.

The target emission frequency in vacuum, ν_0, may not correspond to the actual fluorescence transition frequency in a plasma, ν_p, that should correspond to a population without a drift velocity. This is due to the shifting of a natural emission line that occurs for a population of ions in a plasma[3]. This could cause a population without a drift velocity to manifest as appearing to having one due to this shift of the transition frequency caused by the discharge medium. Instead, ν_p may be better indicated by the mean velocity of the IVDFs measured at distances furthest from the cathode, given by the vertical dashed line in each sub-figure. The true ion velocity is therefore likely to be better represented by its difference in velocity space from the vertical dashed line. The laser could not be reliably scanned to frequencies corresponding to ion velocities above 25 km/s (≈ 130 eV) or below -15 km/s (≈ 45 eV) without frequently losing the lasing mode.

The normalised density of the IVDFs at each location within an experiment is given in Figure 3.9a), excluding the BAX results given in Figure 3.8e). The density was calculated by integrating under all peaks in a signal that had $SN > 4.5$ between endpoints given by a signal magnitude of $SN = 4.5$. An example of this procedure being performed on a typical LIF signal from those in Figure 3.8 is given in Figure 3.7a). This formulation was manually checked for each IVDF given in Figure 3.8 so that peaks consisting of few data points that were likely the result of noise were not included in the calculation. All experimental densities have been normalised to the value taken furthest from the cathode that would most closely represent the bulk plasma values.

---

[3]For greater detail on this subject and the theory of radiative equilibrium, see the textbook by Hubeny and Mihalas [330]
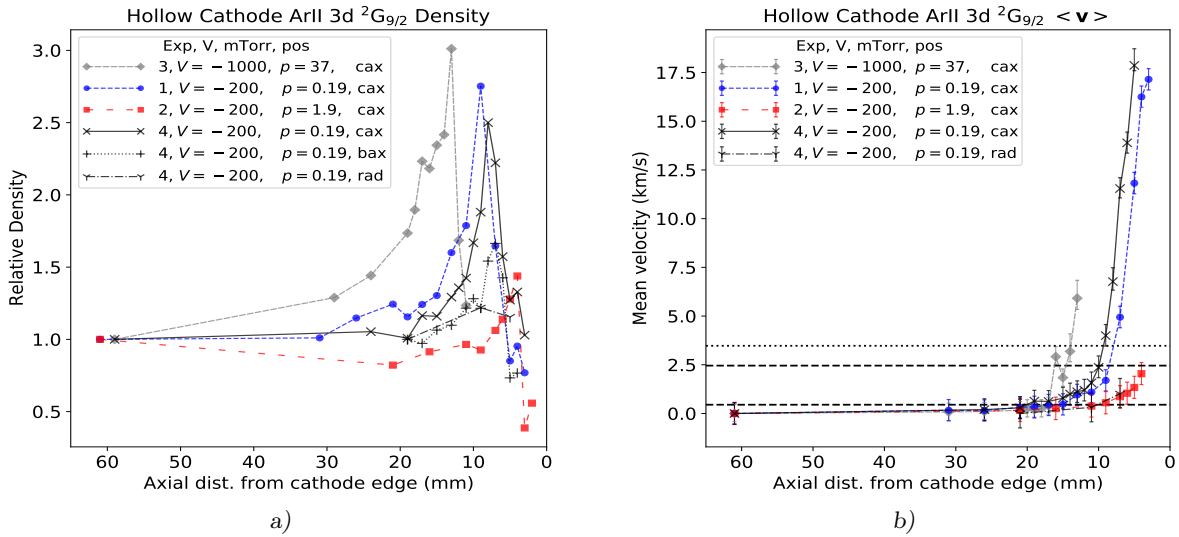
FIGURE 3.9 – *a)*: The relative population density at each measurement location within an experiment, normalised to the density furthest from the cathode. The cathode bias, experimental pressure, and laser alignment is given in the legend. *b)* The mean velocity of the bulk groups in the IVDFs. The upper horizontal dashed and dotted lines refer to u_0 according to Bohm's [121] and Riemann's [319] theories respectively. The lower dashed line gives the maximum ion thermal velocity given by previous experiment as $k_B T_i = 0.1$ eV [286, 331, 332].

3.5 Discussion of experimental results

Multiple phenomena relating to the different processes of ion transport, the apparent rethermalisation of the IVDF, and the anomalous metastable ion density approaching the cathode sheath are present within the data given in Figure 3.8. Each phenomena will be discussed separately in its own subsection. Before these are approached, we need to define what is meant by the particle drift velocity more clearly, as well as the regions corresponding to the sheath, the pre-sheath, and the bulk plasma. Here we shall use the definition of the cathode sheath originally given for a diode discharge [95] as the region in front of the cathode in which the plasma potential drops rapidly. It is important to note, however, that in the CAX experiments we are analysing the central axis of the hollow cathode which is not likely to be parallel to the gradient of maximum potential drop.

The pre-sheath between the sheath boundary at x_0 and the bulk plasma at $x_0 + l$ according to Equation 3.15 can be defined by the mean drift velocity of ions. In Figure 3.8a), the acceleration of the majority of the ArII $3d'\,^2G_{9/2}$ population toward the cathode slowly increases until we can see a separation between the accelerated 'bulk' group and a small 'ionisation' group near to zero velocity. This separation of the ionisation group is also visible in Figure 3.7b), while in Figure 3.7a) we can see an instance where it seems the ionisation group is present but not clearly separate to the bulk group. The ionisation group is so named as the occurrence of stationary ions within the high electric field indicated by the drift velocity of the accelerated bulk group was most likely a result of local ionisation. It is apparent in Figures 3.8a), 3.8b), and 3.8d) that the ionisation group contributes to the bulk group of accelerated ions across the cathodic pre-sheath. The ILVDFs shown in all filament mediated experiments performed along the central axis exhibit the merging of these two groups. This requires that a decision be made as to how to define the overall population mean drift velocity.

The 'peak' velocity, $\tilde{\boldsymbol{v}}_{\mathrm{pk}}$, was first calculated as the mean velocity of the largest 5 % of the ILVDF that was above $SN \geq 4$ weighted by the signal intensity, and is indicated by the green dashed vertical line in Figure 3.7. One can see in Figure 3.7b) as well as in Figures 3.8c) and 3.8d) that the peak velocity would not be representative of the bulk group once significant acceleration of the population has begun (at $x = 14\,\mathrm{mm}$ and $x = 7\,\mathrm{mm}$ respectively). Instead, the peak velocity was used to define the upper and lower bound of the signal included in the calculation of the 'mean' velocity $\langle \tilde{\boldsymbol{v}} \rangle$. If $\tilde{\boldsymbol{v}}_{\mathrm{pk}} \leq 1500\,\mathrm{km/s}$, the mean velocity was calculated analogously to the density by integrating the IVDF for all values with $SN \geq 4.5$. Otherwise, the bulk group was considered to be separate to the ionisation group, which was fit using a Gaussian profile centered at ν_{p} and removed from the calculation. The uncertainty upper and lower limits were determined by performing the same calculation with $SN = 4$ and $SN = 5$ respectively. The results are given in Figure 3.9b). Each data set shown in Figure 3.9b) has had the velocity corresponding to ν_{p} subtracted from all values. The Bohm velocity u_0 at x_0 for $T_{\mathrm{e,c}} = 2.5\,\mathrm{eV}$ as has

been reported previously in the same discharge system at 0.36 mTorr in argon [290] is indicated in Figure 3.9b) with the upper dashed horizontal line. The velocity of ions at x_0 as predicted by Equation 3.15 is given as the dotted horizontal line. The peak (not shown) and mean velocities remained within the experimental uncertainty of each other for measurements taken within the pre-sheath. The spatial mean velocity distribution qualitatively follows that expected in front of the cathode of a 1-D glow discharge system as described in Section 3.2.1. This indicates that the axial potential distribution created by the sum each ring element of the front-facing surface of the hollow cathode results approaches that of a planar cathode with increasing axial separation.

The chosen definition of the sheath/pre-sheath boundary at $x = x_0$ can now be refined using the data presented in Figure 3.9. We define this location as the point in which the ArII 3d$'$ ^{2}G$_{9/2}$ density rapidly decreases while the mean velocity increases above the dotted horizontal line. This corresponds to $x = 7$ mm in Figures 3.8a) and 3.8d), and at $x = 14$ mm in Figure 3.8c). The sheath boundary is suspected to have occurred at $x = 3$ mm from the cathode edge in Figure 3.8b) but was not able to be resolutely observed. This could be due to the narrow cathode sheath width of less than 4 mm. A narrow sheath width may have accelerated the bulk ion group to well above 10 km/s within 1 mm of separation from the measurement at $x = 4$ mm, such that it could no longer be observed. The signal intensity in the cathode sheath may also be flattened by the resulting convolution this would cause.

The width of the cathode sheath that is indicated by the above definition of $x = x_0$ increases with experimentally applied voltage and decreases with applied pressure, as has been observed in glow discharge tubes generally (see Chapter 1.1.6). However, it must be noted that the plasma density is likely to have varied in a manner not predicted by simple discharge parameter relationships due to the varying presence or absence of primary electrons from the thermionic filaments. It is also interesting to note the visible presence of metastable ion creation within the cathode sheath and pre-sheath most clearly evidenced in Figures 3.8a) and 3.8e). The magnitude of the ionisation peak in the cathode sheath for the BAX experiment in Figure 3.8e) was disproportionately increased by laser reflection relative to the measurement taken at $x = 19$ mm due to the increasing proximity to the reflecting cathode surface. We define the beginning of the pre-sheath to correspond to a mean metastable ion velocity greater than that in the bulk plasma by at least the ion thermal velocity at an upper bound of 0.1 eV of ≈ 450 m/s, indicated by the lower dashed line in Figure 3.9b). Langmuir probe experiments were not performed in conjunction with the LIF experiments so that the variation in discharge parameters between experiments was not known.

3.5.1 The lack of ion divergence

In none of the experiments presented in Figure 3.8 can we observe any evidence of a diverging ion population. There are multiple possible reasons for why this may have happened apart from discounting the diverging ion and ambipolar hypotheses given in Chapter 2. First, it was difficult to scan the laser to frequencies that correspond to large negative ion velocities without losing the lasing mode. It may be possible that an additional peak in the fluorescence signal corresponding to an ion population travelling away from the cathode would be present at speeds greater than 15 km/s. This is particularly the case as metastable ions that have reached the edge of the hollow cathode will likely have passed through their maximum kinetic energy afforded by the internal virtual anode. Second, the absence may be due to the cathode geometry, originally designed to allow for greater optical resolution within the cathode interior. Ions diverging from a central virtual anode are unlikely to have trajectories remaining on the cathode axis for a long distance as the maximum potential gradient is most likely toward the cathode walls. Therefore, we may not be able to see the equivalent of the PP population in the two-ring experiment shown in Figure 2.9 due to deflection of ions off the axis given the greater length of the hollow cathode relative to its radius. Third, internal ionisation within the longer length of the cathode is unlikely to be isolated to a single location. This would spread the diverging ion signal over a large range of negative velocities rather than forming sharp peaks. That sharp peaks are observed exterior to the cathode is likely due to the small acceleration of metastable ions across the pre-sheath relative to the laser scanning range. A small spread of ion velocities relative to the entire velocity range recorded would manifest as a narrow peak, and vice versa as is visible within the cathode sheaths in Figure 3.8. These issues may always be present when attempting to use the LIF diagnostic to determine IVDFs within high power IEC or hollow cathode discharges. In summary, the experiments shown in Figure 3.8 are certainly not supportive of the diverging ion or ambipolar hypotheses for low pressure hollow cathodes, but are also inadequate to disprove it.

For this reason, a series of new hollow cathodes and spherical grid cathodes were designed with better aspect ratios for testing the diverging ion hypothesis given the experimental constraints. The hollow cathodes had a 2 cm 'square' aspect ratio (equal inner diameter to length) such that they would have the same aspect ratio as the two-ring cathode as well as reducing the distance that diverging ions would need to travel along the cathode axis before being able to be observed. These were created after the author's access to the LIF multipole system at Aix-Marseille Université had expired due to Covid-19 restrictions. The cathodes have been sent to Aix-Marseille for experimentation which has not been completed at the time of submission, and will therefore be presented in Chapter 6.1 in which future research projects are discussed.

3.5.2 Rethermalisation of the IVDF in the pre-sheath

These results shed further light on the discussion of the apparent rethermalisation of the IVDF across a cathodic pre-sheath [260, 262, 324, 333–335]. The discussion arose over the observation of ArII 3d$'$ ^{2}G$_{9/2}$ IVDFs that appear to re-thermalise within the cathode sheath [290] or at the pre-sheath/sheath boundary [260] at x_0 after having developed an asymmetric low velocity tail across the pre-sheath. The development of the tail was initially proposed in a model by Emmert *et al.* [333] for a collisionless diode discharge featuring ions and bulk electrons only. LIF measurements in various low pressure argon glow discharges have shown the temperature of positive ions in the plasma bulk to be at approximately room temperature, with an upper bound of $k_{\mathrm{B}}T_{\mathrm{i}}/q_{\mathrm{i}} \approx 0.1$ eV [103, 287, 289, 290, 331, 332, 336]. This can be seen in the ionisation peaks shown in measurements taken for $x \leq 9$ mm in Figure 3.8a) as well as in measurements taken in what is likely the bulk plasma near to $x = 60$ mm in Figures 3.8a) to 3.8f). In these cases, the full width at half maximum of the peaks as well as a least-squares regression fitting of a non-drifting Maxwellian distribution to the population corresponds to a mean temperature of the drifting Maxwellian population of less than 0.1 eV. The behaviour predicted by Emmert *et al.* [333] was qualitatively observed using LIF in a multipole discharge in argon [262], although the analysis required that an arbitrary manipulation of the temperature of the IVDF be made at each measurement location. An explanation of the subsequent observation of rethermalisation was first attempted by Baalrud, Callen, and Hegna [334, 335], currently known as BCH theory. BCH theory posits that ion-acoustic instabilities formed at the sheath/pre-sheath boundary increase the rate of charged particle thermalisation by collisions by a factor of up to 100. Yip *et al.* [260] then argued in 2015 that their LIF observations supported BCH theory. In the same year, Coulette and Manfredi [324] discounted BCH theory by proposing a velocity bunching mechanism that describes the ballistic accumulation of fast and slow particles to a narrow section of the population's phase space.

The data-sets given in Figure 3.8 do not seem to prominently feature the rethermalisation of the particle population when within the cathode sheath as observed by Claire *et al.* [290]. However, the effects of the convolution of the fluorescence signal across the 0.5 mm observation width used in this experiment are likely the largest contributor to the observed asymmetries, compared to the 0.1 mm width used in Reference [290]. The apparent rethermalisation of the IVDF, or at least the increase in the bulk peak symmetry, seems to occur at the separation of the ionisation group (at $x = 9$ mm in Figure 3.8a), for example). This is unlikely to be due to an enhanced binary collision rate since these are likely to also change the state of excitation of the metastable ion involved, as will be argued in Chapter 5.1. The results shown in the CAX filament mediated experiments of Figure 3.8 seem to indicate rather the separation of a main group of accelerating particles from a group of particles ionised at each measurement location without a drift velocity. The contribution of these ionised particles to the ILVDF could be

distorting it only in intermediate pre-sheath locations, matching the velocity bunching theory of Coulette and Manfredi [324].

3.5.3   Discussion of the anomalous density phenomenon

In all experiments presented in Figure 3.8 we observe the same form of anomalous increase in the ArII 3d' ^{2}G$_{9/2}$ metastable density approaching a negatively biased surface as has been previously observed in front of planar plates [257, 283, 290]. The ion populations in all of the axial experiments are seen to start in an approximately thermalised distribution centered with a low mean axial drift velocity at the furthest point from the hollow cathode and then to slowly accelerate towards it. At the sheath edge, for example at $x = 7$ mm in Figures 3.8a) and 3.8d), the ions begin to accelerate rapidly, decreasing in density. This results in a population density distribution that is sharply peaked within the cathodic pre-sheath, as shown in Figure 3.9a). The sheath acceleration does not occur in the radial experiment shown in Figure 3.8f) as was expected given that the IRVDF should not be accelerated in the absence of radial electric fields. Despite this, the metastable ion density increases from $x = 19$ mm to $x = 9$ mm, and then decreases again to $x = 5$ mm, suggesting that a similar phenomenon affects the IRVDF as affects the ILVDF.

The peak of ions at the plasma drift velocity observed at the furthest distances from the cathode in the filament maintained experiments demonstrates the efficacy of the primary electron population emitted from the filaments in creating ArII 3d' ^{2}G$_{9/2}$ metastables. If the primary electron population were spatially homogeneous with a known density and energy, one could calibrate the observed fluorescence intensity in the bulk plasma to an absolute value. However, the authors are not aware of an experimental verification of this proposal. Indeed, both Langmuir probe results and LIF results of charged populations in multipole devices regularly show at least slight spatial inhomogeneity at different locations throughout the vacuum chamber [257, 290, 337]. The lack of an ionisation peak far from the cathode surface in the self-sustaining discharge given in Figure 3.8c) confirms the importance of primary electrons to the creation of ArII 3d' ^{2}G$_{9/2}$ metastables. Only a relatively small ArII 3d' ^{2}G$_{9/2}$ population could be detected at $x = 59$ mm in this case, suggesting the lack of energetic plasma particles far from the cathode. Low pressure hollow cathode glow discharges have been shown [125, 150, 151, 154] to exhibit secondary electron beams that exit outward from the hollow cathode apertures with energies at a high fraction of the cathode bias relative to the plasma potential. Secondary electrons are therefore the most likely candidate for the observed metastable ions in the self-sustaining discharge. A secondary electron beam that loses kinetic energy or density with increasing x through collisions and beam divergence in the self-sustaining experiment may explain the corresponding decreasing creation rate of ArII 3d' ^{2}G$_{9/2}$ metastables shown in Figure 3.8c).

Secondary electrons may also contribute in the filament mediated discharges. This may be indicated by the small ionisation peak visible in the cathode sheath region beginning at $x = 7$ mm in Figure 3.8a). The bulk population mean velocities observed at $x = 3$ mm and $x = 4$ mm in Figure 3.8a) correspond to an ion drift velocity of $\approx 60 - 80$ eV. The ion drift velocity is frequently used to indicated the local electrostatic potential in the sheath and pre-sheath [19, 95]. This potential barrier would be insurmountable to a mono-energetic electron population limited by the 50 V bias applied to the thermionic filaments. However, it is also possible that positive ions that have been accelerated to a high kinetic energy within the cathode sheath are able to create ArII 3d' ^{2}G$_{9/2}$ metastables there through collisions with the background gas. This would not explain the fact that the magnitude of the ionisation peak does not seem to change from the measurement at $x = 8$ mm in Figure 3.8a) where ions have insufficient energy to create metastable ions. In whichever case, the ionisation peaks shown in Figure 3.8a) indicate that a cathode sheath and pre-sheath is not well approximated as collisionless for metastable ions even at very low discharge pressures. This runs contrary to the collisionless assumptions used in much of the simplified discharge modelling discussed in Chapter 1.2.

The experimental conditions affect the magnitude of the ion density near to $x = x_0$ relative to that in the bulk plasma shown in Figure 3.9a) but not the fact that the peak density occurs there. It may be possible that the mono-energetic primary electron population observed in filament mediated multipole systems (discussed in Chapter 2.2.2) could cause the anomalous density phenomenon observed in Figures 3.8 and 3.3 by itself. The primary electron distribution would remain effectively homogeneous everywhere except for within the cathode sheath. It would therefore create ArII 3d' ^{2}G$_{9/2}$ ions at equal rates in the plasma bulk and within the pre-sheath. Metastable ions created within the plasma that reach the pre-sheath would be accelerated toward the cathode, successively adding to the density of locally ionised metastables. This would be counteracted to an unknown extent by the acceleration of locally created metastable ions in the pre-sheath, as well as the quenching of metastable ions travelling from the bulk plasma discussed in the following paragraph. If the isotropic mono-energetic primary electrons were solely responsible for the anomalous density phenomenon, however, then the same density profile should also be observed for ions in the ground state[4]. This certainly cannot be the case for the self-sustaining experiment given in Figure 3.8c). Even with the ArII 3d' ^{2}G$_{9/2}$ metastables likely being created near to the cathode by an emitted secondary electron beam in Figure 3.8c), the density increase phenomena is still observed. It may be the case that metastable ions converge somewhat to the laser axis when travelling from the bulk plasma towards the cathode, contributing to the peak in density. However, this would require an approximately spherical potential well formed by the cathode which is not likely to be the case due to screening by the

---

[4]It will be shown in Chapter 5.6 that homogeneous creation of ArII 3d' ^{2}G$_{9/2}$ metastables could not recreate the anomalous ion density phenomenon in front of a planar floating plate.

cathode sheath. Ion convergence also cannot explain the metastable density increase observed in front of a planar floating plate in a filament mediated multipole discharge with 0.36 mTorr of argon [290], as reproduced in Figure 3.3.

The same or lesser magnitude of anomalous density increase occurred in the planar systems [257, 283, 290] as compared to the experiments given in Figure 3.9a). The most significant contribution to the quenching of ArII 3d′ ^{2}G$_{9/2}$ metastables in low current discharges has been shown [280] to be from binary inelastic collisions with the background gas[5]. The ion-neutral inelastic collisional mean free path $\lambda_{i,n}$ in the filament mediated discharges was on the order of 1-10 cm, as indicated both by visual inspection of the pre-sheath length according to Equation 3.15 and by calculation of Equation 1.6 using the average of published cross-sections for all inelastic collision processes including charge transfer [34, 229, 338]. This corresponds with the gradual ion acceleration from zero drift velocity in the bulk plasma towards the cathode sheath observed in the 0.19 mTorr experiments in figures 3.8a) and 3.8d). As the pressure increases towards 37 mTorr, at which point $\lambda_{i,n} \approx 1$ mm, the acceleration of the bulk group across the pre-sheath up to $x = 3$ mm and $x = 14$ mm respectively is lessened, as shown in Figures 3.8b) and 3.8c). The metastable ions cannot traverse as far across the pre-sheath without being quenched such that the IVDF would be increasingly dominated by local ionisation. Also, the metastable acceleration by the cathode sheath in the self-sustaining experiment given in Figure 3.8c) is lopsided towards lower velocities and does not vary quickly. This effect could either be caused by collisional deceleration of the metastable ion population or instead by the rapid collisional quenching of metastables such that the population is dominated by recent ionisation. In either case, the findings support the theory given by Skiff *et al.* [280] that the difference between binary collisions that quench the ArII 3d′ ^{2}G$_{9/2}$ state and only decelerate ArII ground state ions likely affects the proportionality of $r_{m/g}$ over phase space. The fact that most collisional processes between ArII 3d′ ^{2}G$_{9/2}$ metastables and other particles are quenching in nature will be one of the subjects of Chapter 5.

The ionisation peaks in all experiments and particularly in the self-sustaining experiment point to the contribution to local ionisation and excitation of metastable ions by energetic electron populations. Secondary electrons emitted from metallic surfaces in filament mediated discharges below 1 mTorr in argon have been detected in greater densities than the primary electron population and at roughly 0.01 times that of the bulk electrons [100]. It is therefore possible that secondary electrons influence $r_{m/g}$ in discharges that contain a spatially homogeneous primary electron population emitted from thermionic filaments. Otherwise, primary electron populations are frequently spatially inhomogeneous in non-multipole discharge systems. We conclude that the anomalous metastable density phenomenon is likely dependent to some extent on the spatial distribution of energetic electron populations in the discharge. Such a proposition could only

---

[5]The rate processes that contribute to the production and loss of the ArII 3d′ ^{2}G$_{9/2}$ state in a low pressure glow discharge will be discussed in Chapter 5.1

be validated by a full collisional rate analysis of the ArII $3d'\,^2G_{9/2}$ population that includes its transport and diffusion through the discharge. This would require the simultaneous knowledge or estimation of the electric potential profile and parameters of charged particle distribution functions over the entire calculation domain. A collisional rate analysis of the hollow cathode discharge illustrated in Figure 3.4 would also involve complications arising from the experimental geometry. The difference between geometric effects and the influence of unmeasured discharge parameters could possibly be untangled using the hybrid fluid/Monte-Carlo hollow cathode computational method of Bogearts *et al.* [153, 305] that has been used analogously for ArI metastables. Otherwise, there has not been an experimental determination of the spatial distribution of these discharge parameters in front of a low pressure hollow cathode discharge to the best knowledge of the authors.

Instead, it may be possible to solve a one-dimensional collisional rate equation that replicates the conditions in front of a floating planar plate from Reference [290] and given in Figure 3.3. It may be possible to determine the cause of the anomalous density phenomenon if the parameters of the distribution functions of charged populations could be simultaneously observed at multiple locations in front of a planar cathode within a single experiment. Such experimental information could not be found within the literature by the author. The use of a computational model alone was also not considered reliable enough given the requirement to capture both kinetic and fluid aspects of multiple discharge populations, as discussed in Chapter 1.2. In the following chapter we detail Langmuir probe experiments undertaken to capture the spatial distribution of charge population parameters at multiple locations in front of a floating planar plate. This information shall then be used to numerically solve a collisional rate equation that was developed from the literature in Chapter 5.1.

Chapter 4

Energetic electrons in a cathodic pre-sheath

The solution of a collisional rate-equation in front of a planar floating plate will require the simultaneous determination of parameters of the distribution functions of ion and multiple electron species as well as the local electrostatic potential distribution. One of the only diagnostic methods capable of capturing all of this information at the same time is also one of the oldest and simplest plasma diagnostic methods; the Langmuir probe. The Langmuir probe introduces its own set of diagnostic issues that must be well understood before we could hope to analyse experimental results. We briefly review the Langmuir probe as it pertains to diagnosing low pressure DC glow discharges. We then give an analysis of cylindrical Langmuir probe measurements used to obtain the spatial evolution of ion, cold and hot electron parameters across a cathodic pre-sheath in front of a floating plate. This will require an extended analysis of existing Langmuir probe literature which sometimes disagrees on best practice or on the necessary level of uncertainty analysis. The knowledge of the distribution function of an energetic electron population will be discussed in terms of further pre-sheath theories in which they are sometimes neglected.

The work presented in this chapter has been published as 'Langmuir probe measurements of the secondary electron population across the cathodic pre-sheath of a DC argon discharge' [339].

4.1   The Langmuir probe

A Langmuir probe diagnosis of a discharge consists of inserting a conducting wire into the plasma and measuring the current drawn under various applied biases [340, 341]. This measures the 'current-voltage characteristic', or '$i - V$ curve' of the plasma at the location of the probe,

essentially capturing the aspects of its local conductivity. An $i-V$ curve allows us to distinguish between the parameters of different charged particle distribution functions in the plasma under the right conditions, so long as we have chosen an appropriate probe theory [17]. The physical simplicity of Langmuir probes makes for a cheap and readily made diagnostic technique available to all plasma physicists. One exposes a small amount of a refractory metal connected to a measuring circuit supported by an insulating holder (usually a ceramic) and places it in the region of plasma to be measured. By applying different biases to the probe, charged particles will be attracted or repelled by the resulting voltage in a way such that their current is indicative of their distribution at the probe surface. The enticing simplicity of the experimental method does not translate to probe theory, however, with a complex range of models available that can be misleadingly matched to spurious experimental data [99, 342].

Determining the physical quantities of a plasma or discharge is only meaningful if measuring the original, unperturbed plasma. A plasmas electromagnetic interaction with itself and its boundaries would then seem to preclude a Langmuir probe as a diagnostic. Non-perturbing optical diagnostic methods cannot observe electron populations directly and often present difficulties in determining absolute values for particle densities. One can instead mitigate the perturbing nature of a probe by making it as small as possible (thus drawing a negligible current from the plasma) and by applying an appropriate theory that accounts for the perturbation of the probe.

4.1.1 Types of probe

The way that a Langmuir probe collects current from the plasma is heavily dependent on its geometry. The geometries used are ones that simplify the ensuing theory as much as possible: planar disk probes; cylindrical wire probes; and spherical ball probes, shown in Figure 4.1. The simplification offered by these geometries technically requires that the probe shape is ideal, in that there exist no edge effects. The spherical probe is the only geometry that achieves this, but is difficult to make and the theory for it is not as well developed. A large disk probe has the simplest operational theory by reducing the problem of particles trajectories within the probe sheath to one-dimension [343], but significantly perturbs the plasma. Edge effects can be minimised for a cylindrical probe by making the probe radius to protruding wire length ratio, $r_{\rm p}/l_{\rm p}$, as small as possible, causing the end face of the wire to contribute negligibly to the wire's surface area. Otherwise, techniques exist to account for the contribution of the planar tip of a cylindrical probe [344] that involves rounding off the end of sheath to include a spherical component. Cylindrical probes are used in the following experiments as they can also easily be made small enough to draw a negligible current from the plasma. One must also be careful to design the probe support system so as to minimally eclipse the probe from charge particle trajectories that may reach it. Waymouth has shown [345] that the influence of a probe support will only be relevant in discharges at pressures of $p \gtrsim 100\,{\rm mTorr}$.
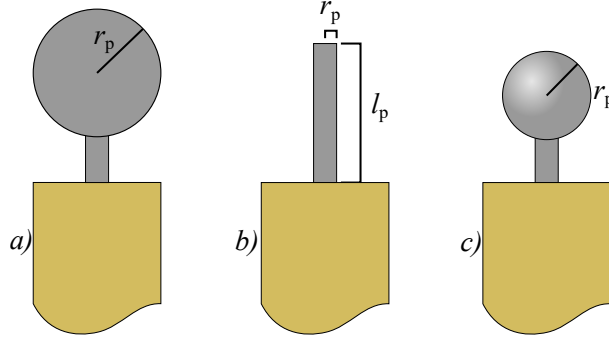
FIGURE 4.1 – Langmuir probes with ceramic holder (brown) and metallic geometries of radius r_p and length l_p: a) planar/disc probe; b) wire/cylindrical probe; c) spherical/ball probe.

4.1.2 Foundations of Langmuir probe theory

We shall approach Langmuir probe theory from the simplest foundations possible, adding complexity to the general formulae later as they are needed. For this, we assume that the Langmuir probe is perfectly absorbing and does not emit charged particles. The average potential between charged particles in a plasma is called the 'plasma' or 'space' potential, V_p, at which bias a reflective surface would not affect the plasma around it. The plasma potential is usually positive in the bulk plasma to confine electrons from being rapidly lost to boundaries, as discussed in Chapter 1.1.3. If a bias is applied to the probe relative to the plasma potential, V_B, a concentric cylindrical 'sheath' of oppositely charged particles will form around the probe whose space charge screens the probe potential. The part of the $i-V$ curve where $V_B \leq 0$ (and thus repelling electrons) is classically defined as the 'repulsion region' and otherwise as the 'saturation region' [346]. It is important to note that the experimentally applied voltage of a probe relative to ground, $V_{e/a}$ is given by $V_{e/a} = V_B + V_p$. Another important feature is the floating potential V_f at which the ion and electron currents to the probe are exactly equal, which is usually negative with respect to the anode. The floating potential of a probe may not be equivalent to the floating potential of electrically isolated surfaces within a discharge if its geometry relative to charge particle drifts causes it to collect different ratios of the population currents locally present.

The probe can only draw current if charged particles arrive at the probe surface. This will only occur when charged particles have original trajectories in the unperturbed plasma that now pass through the probe sheath and reach the probe surface after being repelled or attracted by V_B. We must first define the sheath edge as a hard boundary for this analysis, traditionally chosen to be the point at which $V_p = k_B T_{e,c}/2$ [121, 346], despite the actual asymptotic reduction of charge over distance depicted in Figure 3.2. This assumption allows us the relate the distribution function of particles that are collected from the probe's sheath edge to their distribution function in the "unperturbed plasma". Thus, the particle distribution at the probe surface will depend on its distribution at the sheath boundary, the size of the sheath relative to the probe, the potential difference between the sheath boundary and the probe V_B, and other operating

conditions [341, 343]. In order to obtain information about the discharge from an $i - V$ curve, we need a method to simplify the inputs to a model.

There are three important discharge characteristic lengths that restrict the final choice of Langmuir probe theory: the total mean free path for ions and electrons, $\lambda_{i,e}$, the characteristic size of the probe, L_p (defined by its radius and/or length), and the characteristic size of the sheath, λ_D. The influence of the ratio between these lengths on the appropriate choice of Langmuir probe theory has been characterised by Cherrington [342] as reproduced in Figure 4.2. Charged particles will reach the probe surface with minimal influence from the probe and its support mechanism if $\lambda_{i,e}/L_p \gg 1$ [342]. If charged particles do not undergo collisions within the probe sheath (given by the condition $\lambda_{i,e}/\lambda_D \gg 1$) then a phase space element of the population will remain unchanged along their trajectory since $Df_{i,e}\left(\tilde{\boldsymbol{x}}, \tilde{\boldsymbol{v}}, t\right)/Dt = 0$. This allows us to infer $f_{i,e}$ in the unperturbed plasma beyond the probe sheath if we know the form of the electrostatic potential within it. Finally, the set of assumptions used for a particular Langmuir probe the-
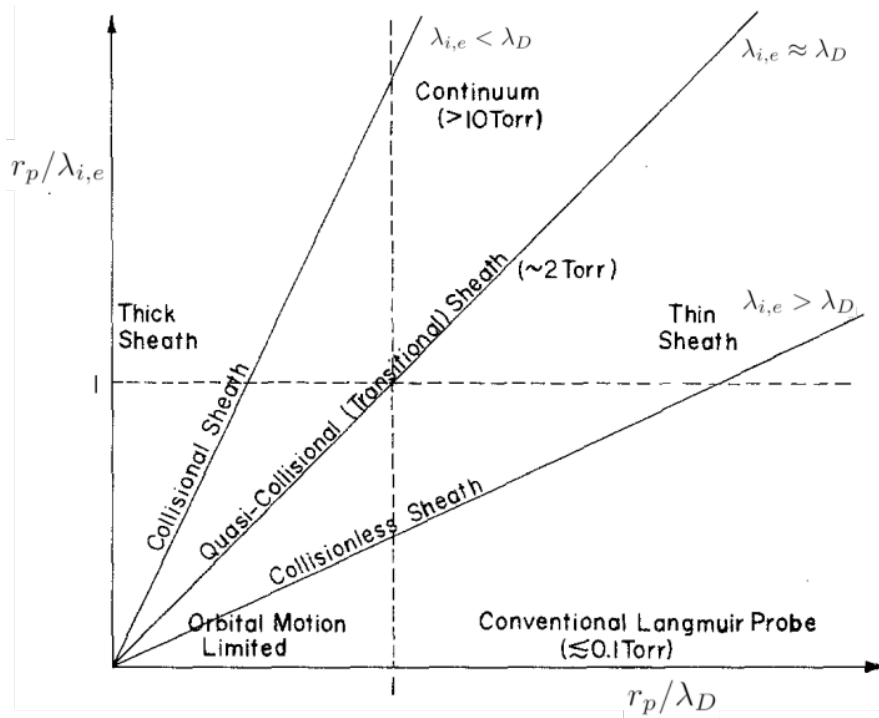
FIGURE 4.2 – Langmuir probe operation regimes for discharge characteristic lengths, taken from Cherrington [342]

ory depends on the ratio λ_D/r_p. If the sheath is thin relative to the probe radius such that $\lambda_D/r_p \ll 1$, the custom is to use 'thin-sheath' or 'semi-infinite plane' theory [343]. Here, we assume that the angular momenta of charged particle trajectories are irrelevant. This operation regime is characterised by the independence of the electronic saturation current on the size of the probe sheath, so that the current to the probe remains constant with voltage as shown in Figure 4.5. This is not observed experimentally for most plane probes [99, 341], since any real

probe will have non-planar edges, resulting in a non-planar sheath that can collect more charges as it grows. If instead $\lambda_D/r_p \gtrsim 1$, as is the case in low pressure glow discharges using probes with a small r_p, we use the 'orbital motion limited' theory of Mott-Smith and Langmuir [346].

4.1.3 Orbital motion limited theory

Orbital Motion Limited (OML) theory was introduced [346] to describe $i - V$ curves for probes in which charged particles that enter the probe sheath follow orbits that may not reach the probe surface. We first consider electrons as the theory for ions is either symmetric for opposite voltages or otherwise improved solutions have been found through alternative theories given in Section 4.3. In OML theory, the effective collecting area of the probe will be determined by

V_B repulsive $\qquad$ V_B attractive
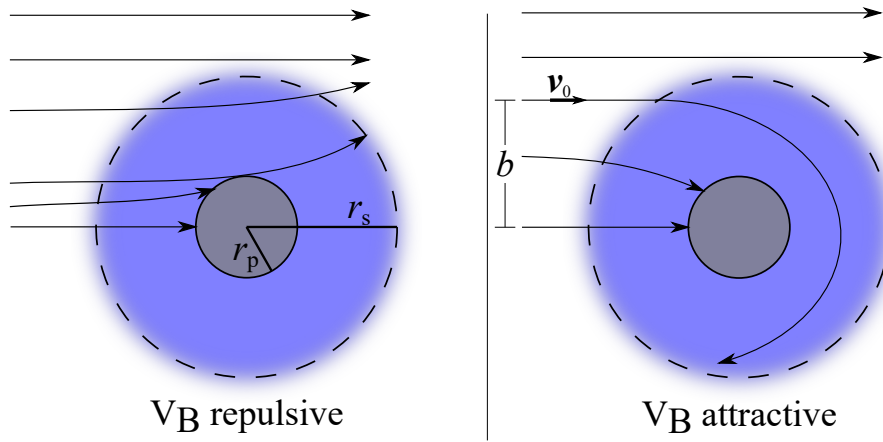
FIGURE 4.3 – Particle trajectories in a sheath (purple) around a cylindrical probe (grey) in the axial plane when $\lambda_D \gtrsim r_p$.

the co-axial sheath radius. An electron's original trajectory is repulsed ($V_B < 0$) or attracted ($V_B > 0$) by the sheath's space charge such that it may not reach the probe upon entering the sheath, as shown in Figure 4.3. The accelerated electron 'orbit' is instead defined by its angular momentum relative to the probe which is itself determined by the electron's initial velocity $\tilde{\boldsymbol{v}}$ and impact parameter b [346]. As V_B grows more positive, for example, the collecting sheath radius will expand to capture more of an electron population while the increased attractive force will increase the maximum angular momentum of electron trajectories that are captured. Thus, the current collected by the probe for even the simplest of electron VDFs, $f_{e,v}(\tilde{\boldsymbol{v}})$, will be dependent on the sheath radius as well as the potential drop within the sheath. The resulting function of two unknowns could only be solved directly using Poisson's equation, which is difficult given that the discharge parameters have not yet been determined. Instead, one searches for situations in which the probe current drawn becomes independent of the sheath radius as it increases towards the infinite limit. Each initially assumed $f_{e,v}(\tilde{\boldsymbol{v}})$ then predicts a different shape of i-V curve related to the plasma parameters of the electron population [346].

Mott-Smith and Langmuir [346] developed the OML method to remove the dependence on the sheath radius so that each $f_{e,v}$ that matches a set of necessary criteria predicts a different shape of $i - V$ curve from which the plasma parameters can be derived. We consider a cylindrical probe of length l_p and radius r_p such that $l_p \gg r_p$. The unperturbed plasma is assumed to be uniform with random electron velocities such that a probe placed there would have a symmetric and concentric sheath with radius r_s. We consider electrons in a small ring volume element $d\tilde{r}$ bordering the sheath and define the inwardly radial and tangential velocities, $\tilde{u}$ and $\tilde{v}$ respectively, in the plane normal to the probe axis, given in Figure 4.4. The total number of
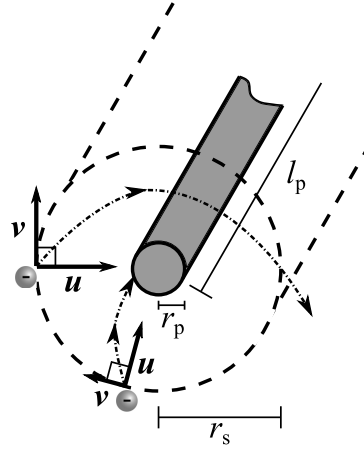
FIGURE 4.4 – The OML tangential and inwardly radial co-ordinate system for a cylindrical Langmuir probe. The probe sheath is indicated by the dotted lines. Two example electron orbits in an attractive sheath are given.

electrons in the phase space element $d\tilde{r}d\tilde{u}d\tilde{v}$ crossing the sheath per unit time will be [346]

$$2\pi r_s n_e \tilde{u} f_{e,v}\left(\tilde{u}, \tilde{v}\right) d\tilde{r}d\tilde{u}d\tilde{v}. \tag{4.1}$$

Letting $\tilde{u}_p$, $\tilde{v}_p$ be the velocity components of an electron that reaches the probe surface, the laws of conservation of energy and angular momentum give [346]

$$\frac{1}{2}m_e\left(\tilde{u}_p^2 + \tilde{v}_p^2\right) = \frac{1}{2}m_e\left(\tilde{u}^2 + \tilde{v}^2\right) + q_e V_B, \qquad r_p\tilde{v}_p = r_s\tilde{v}. \tag{4.2}$$

An electron that reaches the probe's surface fulfills the requirements

$$\tilde{u} > 0, \qquad \tilde{u}_s^2 > 0. \tag{4.3}$$

The total current i to the probe is found by multiplying Equation 4.1 by the electron charge and the total sheath surface area and integrating over electron velocities [346]

$$i = 2\pi r_s l_p n_e q_e \int_{0,u_1}^{\infty} \int_{-v_1}^{v_1} \tilde{u} f_{e,v}\left(\tilde{u}, \tilde{v}\right) d\tilde{u}d\tilde{v}, \tag{4.4}$$

where u_1, v_1 are boundary conditions defined by Equations 4.2 and 4.3 and the lower bound for the integral in $\tilde{\boldsymbol{u}}$ is 0 for attractive potentials ($V_\mathrm{B} > 0$) and $u_1 = \sqrt{-2q_\mathrm{e}V_\mathrm{B}/m_\mathrm{e}}$ for repulsive potentials ($V_\mathrm{B} \leq 0$). We can then remove the dependence on sheath radius from Equation 4.4 by considering when the sheath radius approaches infinity [346];

$$i_{r_\mathrm{s}/r_\mathrm{p}\to\infty} = 4\pi r_\mathrm{p} l_\mathrm{p} n_\mathrm{e} q_\mathrm{e} \int_{0,u_1}^{\infty} \tilde{\boldsymbol{u}}\sqrt{\tilde{\boldsymbol{u}}^2 + \frac{2q_\mathrm{e}}{m_\mathrm{e}}V_\mathrm{B}} f_\mathrm{e,v}\left(\tilde{\boldsymbol{u}}, 0\right) d\tilde{\boldsymbol{u}}. \tag{4.5}$$

The mathematical steps between Equations 4.4 and 4.5 in Mott-Smith's original paper [346] have been obscured in all available copies, but have been re-derived by Bowden-Ried [347]. For a known distribution function $f_\mathrm{e}\left(\tilde{\boldsymbol{u}}, \tilde{\boldsymbol{v}}\right)$, it is possible to derive the ideal $i - V$ curve of a probe directly from Equation 4.5 by numerical integration.

Only a few types of distribution functions can be easily expressed analytically or match the symmetry criteria required by OML theory. We shall go through the three distribution function types that are most relevant to this thesis.

The velocity distribution function for a Maxwellian population in this co-ordinate system is given by [346]

$$f_\mathrm{e,v}\left(u, v\right) = \frac{m_\mathrm{e}}{2\pi k_\mathrm{B}T_\mathrm{e}} \exp\left[-\frac{m_\mathrm{e}}{2k_\mathrm{B}T_\mathrm{e}}\left(u^2 + v^2\right)\right]. \tag{4.6}$$

Integrating Equation 4.6 using Equation 4.5 requires that the electron distribution function is integrated over its velocity space in $\tilde{\boldsymbol{u}}$ for each discrete probe potential V_B recorded, which can be computationally expensive. For this reason the original solutions were calculated analytically, sometimes involving complicated approximations. Solving in either way will form a particular ideal $i - V$ curve for a set of electron parameters T_e and n_e. An example of these for each probe geometry as determined by Mott-Smith and Langmuir [346] has been given in Figure 4.5.

Another possibility is the isotropic mono-energetic distribution function that was discussed in Chapter 2.2.2 as the likely form for primary electrons emitted from thermionic filaments in multipole discharges below 1 mTorr. In rectilinear velocity space, this distribution manifests as a spherical shell with radius of the velocity magnitude. The projection of a spherical shell of velocities onto our rectangular co-ordinate space results in [346]

$$f_\mathrm{e,v}\left(u, v\right) = 1/\left(2\pi v_c^2 \sqrt{1 - \frac{u^2 + v^2}{v_c^2}}\right), \qquad\qquad u^2 + v^2 < v_c^2, \tag{4.7}$$

$$= 0, \qquad\qquad u^2 + v^2 > v_c^2, \tag{4.8}$$

where v_c is the common magnitude of the electron velocities. This will divide a characteristic into three regions including the equivalent potential of the electron velocity V_c: $V_\mathrm{B} \leq V_\mathrm{c}$, where no electrons may reach the probe; and the remaining repulsion and saturation regions. An ideal
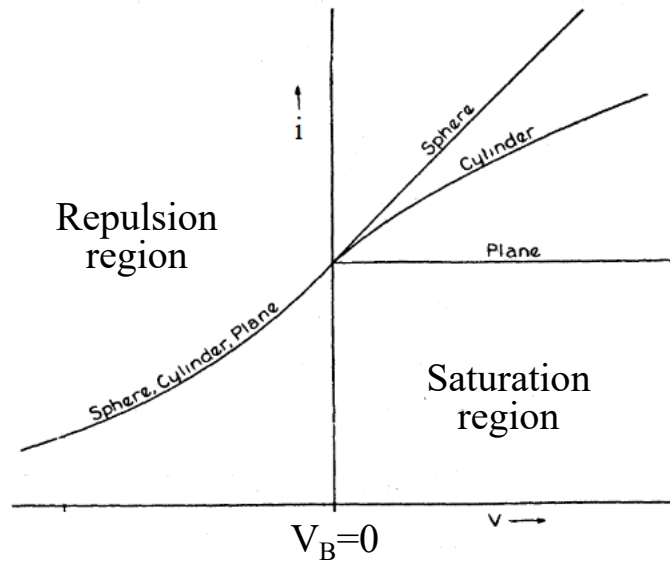
FIGURE 4.5 – An ideal Langmuir probe $i-V$ curve from a Maxwellian distribution of electrons for each probe geometry in Figure 4.1, taken from Mott-Smith and Langmuir [346].

$i-V$ curve found by integrating Equation 4.7 by Equation 4.5 is given in Figure 4.6. Inspection
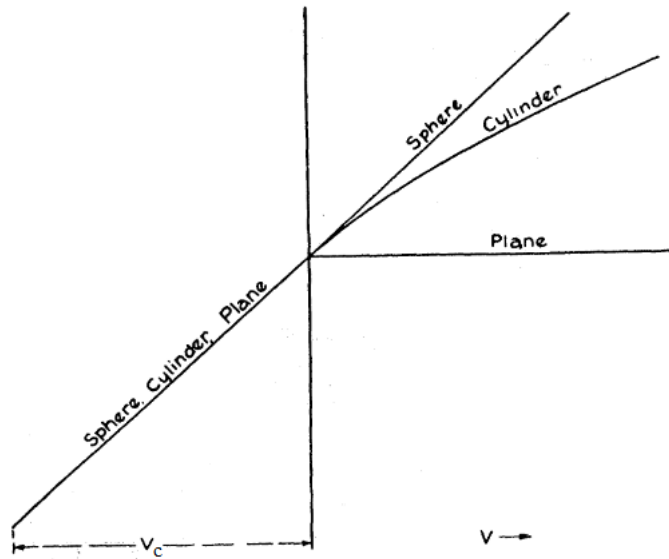

FIGURE 4.6 – Langmuir probe $i-V$ curves for the probe geometries in Figure 4.1 resulting from an isotropic, mono-energetic distribution of electrons [346].

of Figure 4.6 shows that the $i-V$ curve from an isotropic mono-energetic population could only be distinguished from a Maxwellian distribution by its linear nature in the repulsion region.

The final distribution type to consider is when a Maxwellian population has an additional mean drift velocity u_D; the drifting Maxwellian. This type of distribution occurs in discharge tubes that feature a total current of Maxwellian electrons between the cathode and anode [348], or

frequently from Langmuir probes used in orbiting satellites that are moving through a stationary space plasma [349]. A Maxwellian electron population with a drift velocity, u_D, perpendicular to the probe axis that is incorrectly modelled as a non-drifting Maxwellian may cause significant error when $u_D/u_{th} \geq 1.25$ [348]. Mott-Smith and Langmuir first showed [346] that, given an angle θ between the radial velocity of an electron u and its drift velocity u_D, the distribution function of the drifting Maxwellian population $f_{e,v}(u, v, \theta)$ becomes

$$f_{e,v}(u, v, \theta) = \frac{m_e}{2\pi k_B T_e} \exp\left\{ -\frac{m_e}{2k_B T_e} \left[u^2 + v^2 + u_D^2 - 2u_D(u\cos\theta + v\sin\theta) \right] \right\} \qquad (4.9)$$

The current to a probe given a drifting Maxwellian population can then be solved by further integration over the surface of the probe sheath to account for this angular dependence [346];

$$i_e = 2r_p l_p n_e q_e \int_0^{2\pi} \int_{0,u_1}^{\infty} u\sqrt{u + \frac{2q_e}{m_e}V_B} f_{e,v}(u, 0, \theta)\, du d\theta. \qquad (4.10)$$

Sheridan and Goree [348] give an experimental validation of the drifting Maxwellian population using a similar formulation to Equation 4.9 in which they take an angular average of the solution for a planar probe over the surface of a cylinder, neglecting end effects. An example of the effect of an increasing ratio of u_D/u_{th} for a drifting Maxwellian electron population on an ideal $i - V$ curve is given in Figure 4.7. These changes are the result of the fact that including a drift velocity is equivalent to adding an overall current to the system. An increased u_D allows electrons to overcome more repulsive probe biases while also reducing the values of impact parameter b of electron trajectories that will reach an attractive probe, flattening the characteristic overall. The shape of the $i - V$ curves with $u_D/u_{th} \geq 1$ are therefore significantly different to those predicted by the other known OML distribution functions according to Mott-Smith and Langmuir [346].

Although a drifting population will cause the probe sheath to become asymmetric, OML theory remains a valid approximation provided $r_s/r_p \gg 1$ [341, 346]. For OML theory the sheath formed in response to the bias applied to a cylindrical Langmuir probe is only approximately cylindrically concentric to the probe provided the potential $V(r)$ at a point r between the sheath edge at r_s and the probe surface at r_p follows the necessary condition [341, 346],

$$V(r) > \left(\frac{r_p^2}{r_s^2 - r_p^2} \right) \left(\frac{r_s^2}{r^2} - 1 \right) V_B, \qquad r_p \leq r \leq r_s, \qquad (4.11)$$

In the following work, it was assumed that the relatively low density between asymmetric and symmetric populations for the experimental conditions, meant that condition 4.11 was valid.[1]

---

[1] Contact the author for a DC discharge experimentalists review of Langmuir probe literature given in greater detail.
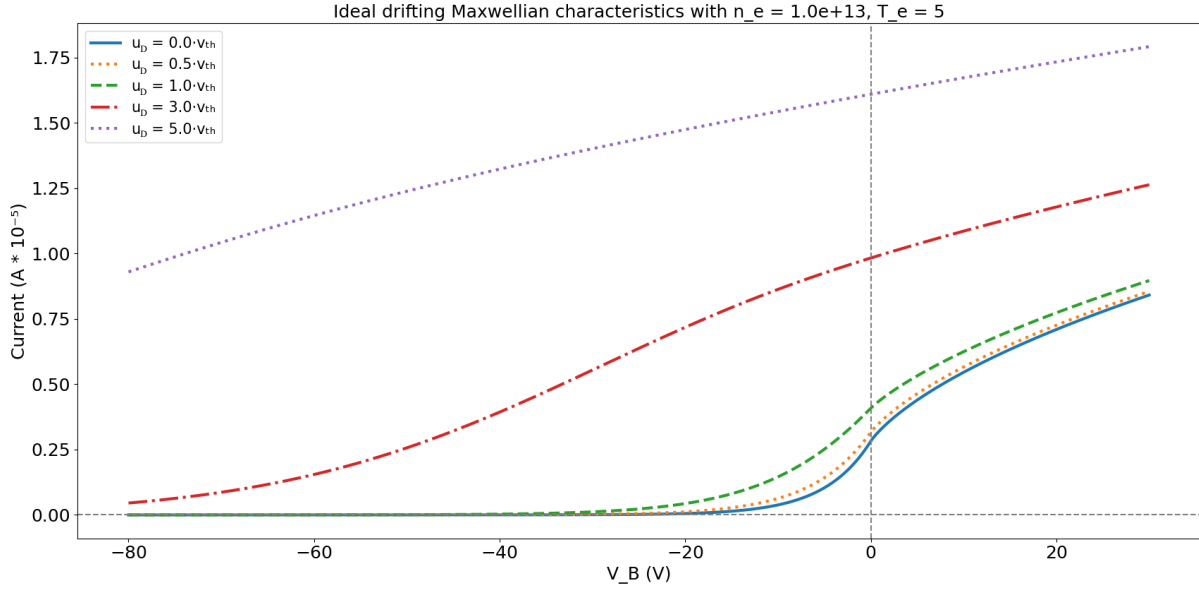
FIGURE 4.7 – Ideal $i - V$ curves for single electron populations with a drift velocity u_{D} increasing relative to the thermal velocity u_{th}. As u_{D} increases, the current collected by the probe increases overall, flattening toward a horizontal line as $u_{\mathrm{D}}/u_{\mathrm{th}} \to \infty$.

4.1.4 Using Langmuir probes in experiment

Experimental artefacts such as noise, imperfect probe tips, pickup from nearby electromagnetic radiation, and so on will deviate empirical $i - V$ curves [343] from those given in Figures 4.5, 4.6, and 4.7. The simplest example for Figures 4.5 and 4.6 would be the observation of a linear increase in current for $V_{\mathrm{B}} \geq 0$ for planar probes due to the increasing sheath size around its edges, as is always the case [99]. Cylindrical probe $i - V$ curves will no longer have a well defined transition (or 'knee') between the repulsion and saturation regions at $V_{\mathrm{B}} = 0$, making it more difficult to determine the plasma potential. Furthermore, an empirical $i - V$ curve will contain multiple collected currents from different populations at the same time that must have their individual contributions untangled. This is relatively easy if only a significant ion and cold electron population is present since the probe bias will reject one of the populations if swept to a repulsive magnitude well above its mean energy. However, one must be careful if a very energetic electron population is present, as this may contribute significantly to the probe current even for very negative probe biases. Deriving the parameters of the population distribution function then becomes an over-fitting issue since the ion and energetic electron parameters can be traded to form a similar $i - V$ curve in the repulsion region.

The work given in the remainder of this chapter is predominantly concerned with exactly that; solving the over-fitting issue to simultaneously and robustly detect ion, cold and hot electron populations given a single $i - V$ curve from a cylindrical Langmuir probe. The low pressure glow discharge conditions used in experiments described below are given in Table 4.1 that enable the use of OML theory [346] for the computation of electronic currents in a collisionless sheath

[340, 342, 350]. Typical Debye lengths, λ_D, and characteristic ion-neutral and electron-neutral collisional mean free paths $\lambda_{i,e}$ are shown in Table 4.1, such that $r_p \lesssim \lambda_D \ll \lambda_{i,e}$ allowing for the use of OML theory [351]. The length-to-radius ratio of the Langmuir probe is sufficiently large $(l_p/r_p = 600)$ that deviation from cylindrical probe theory caused by probe end effects can be ignored. Low pressures match the criteria given by Waymouth [345] to ignore eclipsing effects by the presence of the probe support.

4.2   Discharge parameters in the pre-sheath

Electron populations with greater mean energy than those of the bulk discharge govern many important discharge processes (including ionisation and excitation, see Chapter 1.1.2) and yet few direct measurements exist within the literature of their spatial evolution throughout sheaths and pre-sheaths. Spatially resolved measurements that do exist within discharges seem largely involved with determining the variation in plasma potential for inductively coupled plasmas [352–354] or otherwise in capacitavely coupled plasmas [355, 356] and are thus sparsely distributed throughout the discharge volume. Theoretical analysis has been applied to transition regions of high electric field that occur between boundaries and the bulk quasineutral plasma, particularly for the cathodic sheath and pre-sheath [19, 357]. Observations of energetic electrons originating within cathodic sheaths [100, 318, 325, 358–360] lack direct measurements of electron spatial and energy distributions, as well as the electric fields, which are difficult to obtain due to the perturbative nature of electrostatic probe diagnostics. Measurements of the spatial properties of plasma sheaths, the evolution of charged species within them, and the transition between the sheath and the quasineutral plasma are required to validate competing theoretical descriptions.

The concept of the plasma pre-sheath was briefly introduced in Chapter 3.2.1, over which cold ions acquire a drift velocity u_0 of at least their sound speed over the potential drop ϕ that was given by Bohm [121] as

$$\phi \geq -\frac{1}{2}\frac{k_B T_{e,c}}{q_e}. \tag{4.12}$$

Notably, u_0 is dependent on parameters of the cold electron population. Pre-sheath theory has been developed by many others in both scope and complexity since Bohm's proposition [19]. For example, it has been shown theoretically that for multiple Maxwellian electron populations, $T_{e,c}$ in Equation 4.12 can be replaced by an effective temperature, T_{eff}, given in terms of the harmonic mean electron temperatures weighted by their densities [361]

$$\frac{\sum_j n_{e,j}}{T_{eff}} = \sum_j \frac{n_{e,j}}{T_{e,j}}, \tag{4.13}$$

where $n_{e,j}$ and $T_{e,j}$ refer to the number density and temperature, respectively, of each electronic population present in the plasma. Non-zero ion temperatures have been shown to increase u_0 by a term proportional to $\sqrt{T_i}$ [362], where T_i is the ion temperature, although the effect remains small if $T_i \ll T_{e,c}$. Song *et al.* [361] demonstrated that energetic populations that are not in local thermal equilibrium have little effect on u_0. Riemann's asymptotic matching theory [319] that was given in Equation 3.15 will be analysed extensively in this chapter, and has been reproduced here for clarity;

$$\phi\left(x\right) = \phi_0 + \frac{T_{e,c}}{q_e}\sqrt{\frac{x_0 - x}{l}}. \tag{4.14}$$

This proposed that the pre-sheath potential drop equal $T_{e,c}$ occurred over a length l proportional to the ion-neutral mean free path λ_i between the sheath boundary at $x = x_0$ and the bulk plasma at $x = x_0 + l$, and has been experimentally verified by Oksuz *et al.* [281, 282] using emissive probe and laser-induced fluorescence measurements. The measurements given in Section 4.7 detailing the potential spatial profile, as well as the evolution of charged populations in the pre-sheath, will allow for a more complete comparison of competing pre-sheath theories.

The experiments described herein were also designed with a view to consolidate the extensive literature on low pressure, multidipole discharges in argon. In particular, Townsend values (pd) have been matched to earlier experiments [102, 103, 193, 281, 290, 360] that tracked the spatial evolution of the ion distribution function near unmagnetised surfaces at negative potentials using LIF. Knowledge of the energetic electron populations present within a cathodic pre-sheath may clarify the assumed relationship between metastable and ground state ion populations discussed in Chapter 3.

Finally, a complete model of the energetic electron population is also critical to the understanding of many of the bulk plasma parameters of the discharge such as floating potentials or the bulk electron density. The majority of energetic populations measurements made inside bulk plasmas show approximate Maxwellian distributions in higher pressures discharges [100, 106, 318, 363] or an isotropic mono-energetic form in low pressure multidipole discharges [259]. Otherwise, energetic electron populations are sometimes assumed to have been thermalised [364] over distances less than the electronic mean free path λ_e, following Langmuir's paradox [365]. Measurements of secondary electron populations have been carried out in the cathode sheath and bulk plasma using emissive and Langmuir probes, respectively [100, 325, 358, 360, 366]. Secondary electron emission from a floating metal plate, in a low pressure argon discharge, has been shown [325] to strongly influence both the magnitude and profile of the potential within the pre-sheath. However, to the knowledge of the authors there are no reports about the detailed evolution of the electron distribution function as it traverses the pre-sheath.

Analysis of Langmuir probe measurements to resolve the discrepancies outlined above present

some challenges. For example, calculating experimental uncertainties for multiple electron populations from a fit to any model of the current-voltage measurement is subject to over-fitting. In Section 4.6, we present a relative Bayesian likelihood estimation method that quantifies the uncertainty of a model fit by computing the goodness of the fit to the data over a scan of all possible plasma parameter combinations and models. This method will be shown to confirm a hot electron population within the pre-sheath that has a drifting Maxwellian distribution that thermalises over a distance proportional to the background gas pressure. Relevant analytical Langmuir probe models to the experiments are discussed in Section 4.3. The experimental method is given in Section 4.4 with analyses used to determine each plasma parameter (including the Bayesian analysis) in section 4.5. The argument for the form of the hot electron distribution and its source due to secondary electron emission from the floating plate, with a discussion of implications for pre-sheath theories presented above, is given in Section 4.8.

4.3   Selecting relevant Langmuir probe theory

4.3.1   The cold (bulk) electron population

The cold electron population, otherwise referred to as the 'bulk' electrons as defined in Chapter 1.1.8, refers to the relatively low temperature (usually having $k_B T_e \lesssim 3\,\text{eV}$) and high density electrons in the bulk of the discharge created predominantly by collisional ionisation. The cold electron population at each measurement location was approximated to be a local non-drifting Maxwellian distribution, given by Equation 4.6. This simplified approach has been shown to be accurate when hot electron populations are separately taken into account [100, 334, 343]. It has also been shown [367], however, that significant distortion of the $i - V$ curve due to the expected Maxwellian shape occurs in regions of strong electric fields such as a cathodic sheath. The likely but lesser presence of this effect in measurements within the pre-sheath can be taken into account by the increased uncertainty toward the sheath/pre-sheath boundary resulting from analytical methods for calculating the bulk electron density and temperature in these regions. Following Druyvesteyn's double derivative method [98] using the finite element method of Knapmiller *et al.* [366] validated the estimation of the bulk electron population as Maxwellian at all positions. These methods could not be used for the entire $i - V$ curve since the requirement of local isotropy for Druyvesteyn's method [98] would be violated for a drifting Maxwellian population. Furthermore, the experimental noise remained too high for the determination of energetic electron population characteristics using either differentiation method even after digital smoothing. This could only be rectified by using SG filters with window lengths large enough to significantly distort each experimental $i - V$ curve, as shall be discussed in Section 4.4.1. Schoenberg and Kunkel [106] note that the depletion of electrons with energies $\epsilon \leq k_B T_e/2$ can occur in glow discharges, which can cause the bulk electron density to be underestimated

by a factor of 2 or more [368]. This effect has been neglected in this chapter because there is no method to quantify it.

4.3.2 The hot electron population

Initial inspection of the measured $i - V$ characteristic showed an additional, anomalous current for $V_B < 0$, inconsistent with that expected from the bulk electron or ion models (see the inset in Figure 4.11). This additional current was consistent with a second, much more energetic population of electrons, in the plasma. A number of possible distribution functions for 'hot' electron populations are described in the literature; here we give a brief summary of the most likely distributions that may be consistent with our experimental conditions:

1. Isotropic and mono-energetic - occurs in low pressure discharges from chamber wall electron emission and acceleration toward the Langmuir probe by the potential difference between wall and bulk plasma [100]. This requires that $\lambda_e \gtrsim L/2$, where L is the vacuum chamber characteristic length, so that no significant thermalisation of the electron population occurs;

2. Higher temperature, lower density Maxwellian - can occur in glow discharges [98, 99, 106], and are created by ionisation processes, secondary electron emission [100, 318], or collisional thermalisation of high energy electrons in other distributions;

3. Drifting Maxwellian - chamber wall secondary electron emission, from ion collisions, have an approximate Maxwellian distribution with temperatures higher than that of the bulk electron population [100, 318] about a mean drift velocity away the surface. For an approximately planar and negatively biased surface with respect to the plasma, the energetic Maxwellian population will be accelerated by the cathodic sheath, resulting in a drift velocity with energy approximately equal to the potential drop in the sheath (provided $\lambda_D \ll \lambda_e$).

We posit a number of reasons for the hot electron population being either non-drifting or drifting Maxwellians. First, the isotropic, mono-energetic electron distribution has only been reported in significant densities in multipole systems or with lower gas pressures than the experiments described here [259, 290]. Second, the thermionic electron source (see Section 4.4), which may act as an alternate source of mono-energetic electrons, was shielded from the bulk plasma by placing it within a magnetic dipole array to disperse the emitted electron beam away from the Langmuir probe and pre-sheath region. A discussion of why a primary electron population is unlikely to be the source of the detected hot electron current even in the absence of having the magnetic dipole arrangement will be given in Section 4.8. Finally, the experimental configuration, consisting of a planar steel electrode floating at negative potentials and relatively large secondary electron

coefficients for metal surfaces from collisions with singly ionised argon ($10^{-3} \lesssim \gamma_{e,i} \lesssim 10^0$ for energies of 10-100 eV, see [73, 108]), are the conditions required for the formation of hot or drifted Maxwellian electron distributions.

4.3.3 The positive ion population

Laser-induced fluorescence experiments in filament mediated, low pressure, argon glow discharges have shown the temperature of positive ions to either be at approximately room temperature, follow $T_i/T_e \ll 1$, or have an upper bound $k_B T_i/q_i \approx 0.1$ eV [103, 287, 289, 290]. Reports of the ion temperatures in the range of $0.1 - 0.5$ eV by retarding field analysers have been discredited by Goeckner *et al.* [287] since these temperatures correspond to the minimum resolution of such devices. Therefore, the argon ion population has been modelled following Laframboise's radial ion theory [369] in the limit that $T_i/T_e \to 0$. In this work we assume mostly singly ionised argon due to the lower probabilities of higher ionisation states [104] coupled with the low characteristic energies of the experimental system.

Using OML theory to model the cold ion probe current has been shown to overestimate the ion density in the bulk plasma n_i. Bohm's pre-sheath theory reduced this discrepancy, however, overestimation remains an issue, thus there is a more common reliance on the measured cold electron density in the bulk, $n_{e,c}$. Laframboise [369] extended Bohm's work by numerically solving Poisson's equation for expanding sheaths about a cylindrical probe in the limit that $T_i/T_{e,c} \to 0$, such that

$$i_i = 2\pi r_p l_p q_e n_i \sqrt{\frac{k_B T_{e,c}}{2\pi m_i}} f\left(r_p/\lambda_D, \eta\right) = I_0 f\left(r_p/\lambda_D, \eta\right), \qquad \eta < 0, \qquad (4.15)$$

where $\eta = q_e V_B/(k_B T_{e,c})$ is the dimensionless probe potential normalised to the cold electron temperature, and $f\left(r_p/\lambda_D, \eta\right)$ is a numerically computed scaling function that includes a correction factor dependent on r_p/λ_D that is given in Laframboise's technical report. Hopkins and Graham's extrapolation technique [344] for Equation 4.15 beyond its original limit of applicability (that $q_e V_B \geq -25 k_B T_{e,c}$) was used to fit to data at all negative probe potentials. The semi-empirical simplification of $f\left(r_p/\lambda_D, \eta\right)$ given by Steinbruchel [370] for $r_p/\lambda_D \to 0$ in the case of a collisionless sheath was applied, such that

$$i_i = 1.15 I_0 \left(-\eta\right)^{1/2}. \qquad (4.16)$$

4.4   Experimental method and data preparation

Experiments were performed within a grounded cylindrical stainless steel vacuum chamber with an inner height and diameter of 304 mm and 314 mm, respectively (see Figure 4.8). The chamber pressure was monitored between $10^{-7} - 10^{-1}$ Torr by a Pfeiffer compact full range pirani/cold cathode gauge, Bayard-Aplert ionisation gauge, and an MKS capacitative Baratron. Regular maintenance of the pressure gauges was ensured such that readings between them agreed to within 20%. The chamber was pumped to a base pressure of at least 2×10^{-6} Torr by an Pfeiffer TPH 330 turbo-molecular pump with an Edwards E2M8 backing pump. Pure argon gas was then admitted to the chamber via a mass flow controller. Discharges were sustained by
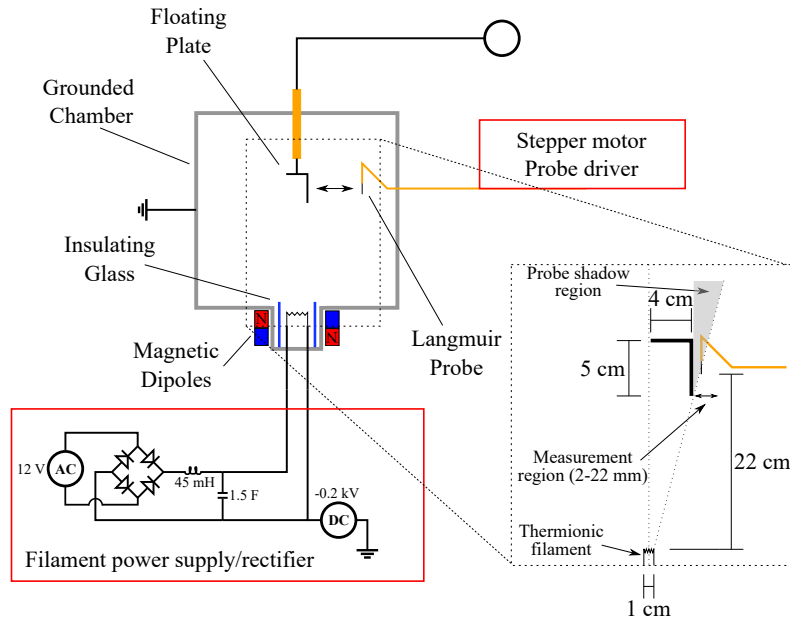
FIGURE 4.8 – The experimental apparatus, not to scale. The inset illustrates the position of the plate and thermionic filament as well as the shadowing of the Langmuir probe by the plate.

a thermionic filament electron source, heated by a floating, 12V DC power supply that had a ripple voltage of less than 1%. The filaments were able to float to a maximum of -1 kV relative to the chamber and emit an electron current of up to 150 mA. The discharge was operated at pressures between $1 - 10$ mTorr with filament biases between -50 and -200 V, corresponding to thermionic electron currents of between $30 - 100$ mA. An electrically isolated, L-shaped stainless steel plate was suspended by a ceramic support system connected to its uppermost surface into the centre of the vacuum chamber and allowed to float within the plasma. The plate had a flat, 5×5 cm^2 square region facing towards the Langmuir probe and was arranged such that the remainder of the plate and the support system likely had little influence on the discharge surrounding the probe. The filament was placed between two magnetic dipoles to increase the discharge current and shield the floating plate region from the emitted primary electrons. The magnetic field strength was measured with a Bell model G1/5 Gaussmeter to be in the order of 100 G immediately above the thermionic filament and at background levels within 5 cm of

the Langmuir probe or the floating plate. The magnetic dipole arrangement was intended to confine primary electrons emitted from the thermionic filament to the small magnetic volume surrounding it and divert them away from the volume containing the Langmuir probe.

Parameter	Symbol	Value
Cold electron temp	$T_{e,c}$	1 - 1.5 eV
Ion temp	T_i	≈ 0.026 eV
Cold electron/ion density	$n_{e,c}$, n_i	1 - 5$\times 10^{15}$ m^{-3}
Hot electron density	$n_{e,h}$	$\approx 10^{11}$ m^{-3}
Debye length	λ_D	0.18 - 0.21 mm
Pressure	p	1.0 - 10 mTorr
Ion/electron MFP	$\lambda_{i,e}$	2 - 200 mm
Thermionic current		56 - 63 mA
Emitter bias		-200 V
Probe radius	r_p	0.025 mm
Probe length	l_p	15 mm

TABLE 4.1 – Discharge parameters in the plasma bulk as well as available experimental parameters. $T_{e,c}$, $n_{e,c}$, n_i, and $n_{e,h}$ were measured by the Langmuir probe, and T_i has been assumed following similar experiments [287, 290]. $\lambda_{i,e}$ refers loosely to characteristic collisional mean free paths for ions and electrons determined from the literature [273] or by experiment in Section 4.8.

A cylindrical Langmuir probe with protruding tungsten tip of radius $r_p = 25$ μm and length $l_p = 15$ mm was aligned with its axis parallel to the plane of the floating plate. The probe axis was vertically aligned such that it pointed towards the bottom of the vacuum chamber and filament with the midpoint of the probe aligned to the centre of the plate. The position of the floating plate relative to the thermionic filament, depicted in the inset of Figure 4.8, interrupted the direct line of sight between the filament and the probe when within 5 mm of the plate surface.

The probe was mounted on a stepper motor with 1 mm stepping increments, enabling measurements normal to the plate surface. The Langmuir probe was swept between -120 to 120 V for approximately 1 second. This slow sweep minimised reactive currents in the circuit. The additional constant parasitic resistive current in the Langmuir probe circuit was removed by subtracting the average background $i - V$ curve taken for the same probe bias sweep without a discharge and in vacuum before and after each experiment from data sets. For a more complete description of the Langmuir probe driver see Carr [371]. The probe data used for analysis was for a maximum probe voltage of 25 V above ground to avoid the the $i - V$ region of a probe tip generated discharge at 50 V. The full sweep to 120 V was used to heat and clean the tip

surface throughout an experiment. Probe current signal was calibrated against a known resistor before and after each experiment. The Langmuir probe driver, stepper motor, data acquisition and power bank were computer controlled. It was found that the floating potential on the plate could not be measured without significant perturbation of the discharge. This was likely due to high resistance voltage probes still drawing a significant fraction of the very small build-up of charge on the plate at the floating potential due to it's low capacitance with the chamber walls. Experimental settings and determined discharge values are presented in Table 4.1.

4.4.1   Probe cleaning and preliminary $i - V$ curve analysis

Each set of discharge conditions was operated for 1 hour before taking measurements. The Langmuir probe was cleaned by performing 10 voltage sweeps at the start of each experiment followed by a further sweep before each recorded measurement. This method was not reliable for pressures lower than 5 mTorr, below which the discharge current was insufficient to clean the probe during a voltage sweep. Sets of five $i - V$ curves were measured at positions between $2 - 22$ mm due to experimental configuration constraints and to minimise the duration of the experiment. This process was performed 3 times in succession per experiment, such that a total of 15 measurements were made at each location. The resulting $i - V$ curves where averaged together to obtain the final $i - V$ curve.

The voltage sweep applied to the probe involved a full wavelength of a triangular voltage pulse starting from and ending at 0 V. This allowed the cleanliness of the probe tip to be checked for each experiment by using both a visual inspection as well as checking the level of hysteresis in the upward and downward voltage sweep. Hysteresis describes differences in the $i - V$ curve between when the voltage sweeps upwards and when it sweeps downward [343]; a greater magnitude of difference between the two $i - V$ curves generated in this manner indicates a likely greater probe contamination. In the following analysis, if the point-wise difference between the upward and downward sweep $i - V$ curves was on average greater than 5 %, the $i - V$ curve was discarded before the averaging procedure. A highly contaminated probe tip can also manifest in an $i - V$ curve as a discontinuous change in collected current for a given applied voltage or by an unrealistically high density of positive ions needed to replicate the collected ion current for the experimental conditions. These effects can be detected by visual inspection and are attributable to the significant change in the secondary electron emission coefficient of a material as it transitions from clean to 'dirty' [73]. A negatively biased dirty probe collecting ion current will also emit secondary electrons by ion impact bombardment (see Chapter 1.1.8) which registers identically as further collected ion current due to their opposite charge. All individual $i - V$ curves measured at a single location were overlaid and inspected for such discontinuities. An example is provided in Figure 4.9 taken from early experimentation before the probe cleaning
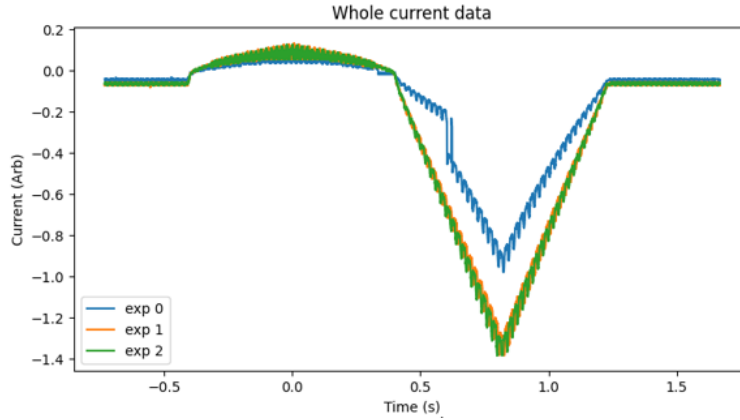
FIGURE 4.9 – Overlayed $i - V$ curves from an early experiment with 1 mTorr of argon gas taken and without the magnetic dipole arrangement. The x axis has not been converted from time (the duration of the voltage sweep), and electronic current registers as negative. The blue data set shows multiple discontinuities in the current indicative of a dirty probe tip. The significant influence of the slight AC ripple voltage remaining in the thermionic filaments on the discharge conditions is also visible when at low discharge pressures without the magnetic dipole.

procedure was fully developed. At this point only three $i - V$ curves were collected at each location without cleaning of the probe performed between each recorded measurement. Any $i - V$ curves showing likely signs of contamination were then removed. Although it is difficult to ensure that a Langmuir probe tip is truly clean, these methods can help to determine when surface contaminants have significantly affected the measured $i - V$ curve.

High frequency noise in each final $i - V$ curve at a location was removed using a rolling six point average. This was used alone since Savitzky-Golay (SG) filters [372] of polynomial order $n \geq 2$ and sufficient window length to noticeably smooth the data were found to significantly distort the transition region and increase the maximum slope of each $i - V$ curve. Preliminary testing was performed by scanning through a variety of SG filter window lengths and polynomial order followed by visual inspection; all combinations that noticeably smoothed the data resulted in too significant a distortion from the original $i - V$ curve, as shown in Figure 4.10. The distortion is likely due to the high frequency change between the two low-frequency energetic and bulk electron currents that results from their significant difference in population temperature when considering the $i - V$ curve in a frequency domain. This high frequency change cannot be captured without insufficiently removing high frequency noise present within the data that invalidated the $i - V$ curve analyses procedures via differentiation, such as Druyvesteyn's method [98] discussed in Section 4.3.1. Second order polynomial SG filters were used to calculate derivatives of the $i - V$ curve or for minor smoothing when necessary for the regression fitting method described in Section 4.5.

A set of example $i - V$ curves at 7.5 mTorr, discharge voltage and current of -200 V and 63 mA respectively, are given in Figure 4.11a). Note the electron saturation current that decreases with

decreasing distance to the plate, indicating a decrease in bulk electron density. However, the increase in collected electron current in the repulsion region (shown in the inset) indicates the presence of a hot electron population. The repulsion region of the corresponding $i^2 - V$ curves that have been offset to have zero current at $V_{\mathrm{p}} = -114\,\mathrm{V}$ are also given in Figure 4.11b), approximately demonstrating the linear behaviour predicted by Equations 4.15 and 4.16 at very negative probe biases. The solid black line in this figure was determined using a least squares regression on the averaged $i^2 - V$ curve data for $V_{\mathrm{p}} \leq -80\,\mathrm{V}$ and subsequent extrapolation, and is intended to be illustrative only. Eventual departure from linear behaviour with increasing probe bias is expected as the secondary electron current to the probe begins to equal the magnitude of the ionic current.

4.5 Analysis routines

There is disagreement in the literature about best practice of Langmuir probe analysis. Therefore, we have used multiple analytical methods to determine the plasma parameters from the $i - V$ curve. We have defined bounds on measurement uncertainty when rigorous statistical methods where not available.

4.5.1 The plasma potential, V_{p}

The plasma potential at each position was found using two common analysis methods [99, 343]. First, from the zero crossing of the second derivative of the $i - V$ curve, $\mathrm{d}^2 i / \mathrm{d} V_{\mathrm{B}}^2$. The $i - V$ curve could be reliably differentiated using the SG method to determine values from the saturation
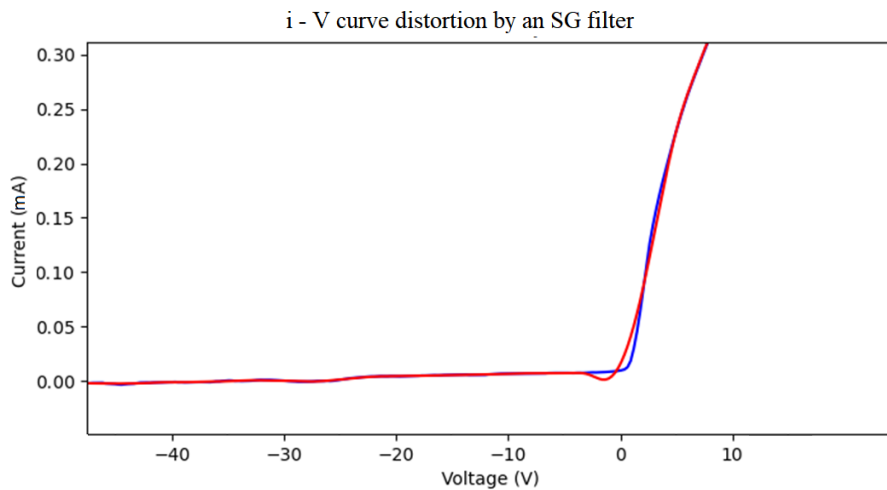
FIGURE 4.10 – The typical distortion of an averaged experimental $i - V$ curve at a location with a rolling window filter (blue) by a Savitzky-Golay filter [372] of polynomial order 2 and window length 31 (red).
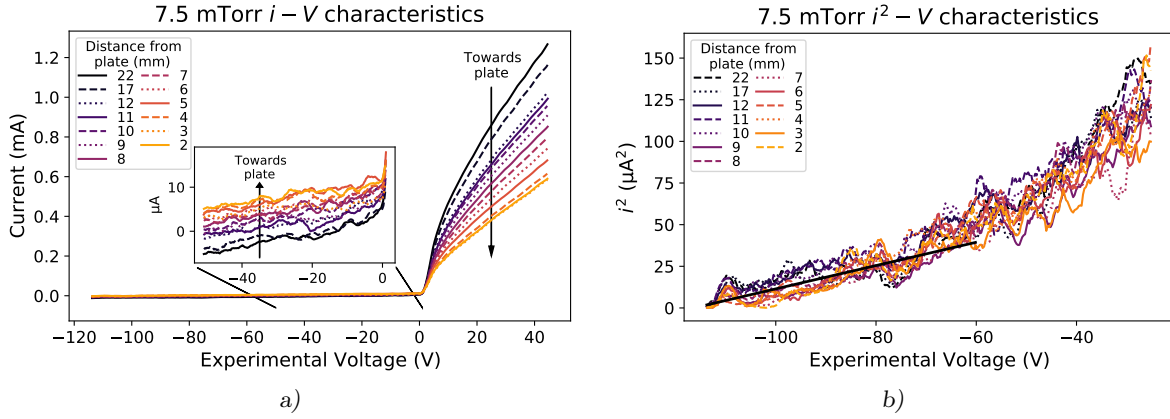
FIGURE 4.11 – *a)* An overlay of averaged experimental $i-V$ curves taken at each measurement location with minimal digital smoothing. The repulsion region of the $i-V$ curves has been expanded within the inset image. *b)* The repulsion region of the corresponding i^2-V curves offset to zero current at $V_{\mathrm{p}} = -114\,\mathrm{V}$, qualitatively demonstrating the linear behaviour (solid black line) predicted by Equation 4.16 at low probe potentials.

region alone due to the total current drawn by the probe being dominated by the bulk electron population alone. Second, using the 'intersecting slope' method on the total probe current, where the exponential and saturation regions of the $\ln(i)-V$ curve are linearly extrapolated to their intersection point. The latter can account for the rounding of the knee of the $i-V$ curve by noise [99], which tends to push the inflection point the of $i-V$ curve to more negative values. Thus, the intersecting slope method consistently returned a plasma potential that was higher than that given by the double derivative approach. Each method was used as a natural upper and lower bound respectively for each value since the literature is divided between their efficacy [341, 344, 368]. Small changes in line fits following the intersecting slopes method were found to vary the value of the plasma potential by a maximum of 0.1 V. The method was applied five times for each $i-V$ curve and the average value taken.

4.5.2 The cold electron temperature, $T_{\mathrm{e,c}}$

The cold (bulk) electron temperature, $T_{\mathrm{e,c}}$, was found from the fitted gradient in the exponential region of the $i-V$ curve within the intersecting slopes method. The mean value and standard deviation of five repeated applications was taken for each position. The regression fitting method, also described below, was significantly more varied in determining $T_{\mathrm{e,c}}$ due to its dependence on the simultaneous fit for V_{p} and $n_{\mathrm{e,c}}$ and was not used, but consistently resulted in similar mean values.

4.5.3 The cold electron density $n_{\mathrm{e,c}}$ and remaining parameter estimation

An ideal characteristic formed by ion, bulk electron, and hot electron currents following Equations 4.16, 4.5 using a non-drifting Maxwellian distribution function, and 4.10 using a drifting Maxwellian distribution function respectively has seven free parameters for fitting to an measured $i - V$ curve: The plasma potential V_{p}, the cold electron density $n_{\mathrm{e,c}}$ and temperature $T_{\mathrm{e,c}}$, ion density n_{i}, and the hot electron density $n_{\mathrm{e,h}}$, temperature $T_{\mathrm{e,h}}$, and drift velocity u_{D}. Bounds for each parameter were therefore required before the Bayesian model fitting technique could be implemented. A non-linear least squares regression method was used to fit simultaneously the sum from all population currents to the numerically smoothed $i - V$ curves. The regression method included a basic weighting function that equalised all values in an $i - V$ curve so that the fitting algorithm spanned the repulsion and saturation regions equally. The regression algorithm was not stable in the repulsion region of the $i - V$ curve when fitting for the hot electron population. The final estimates of bulk electron and ion densities were improved using an iterative scheme similar to Hopkins *et al.* [344] where a fit was made to each population that dominates a region of the $i - V$ curve and removed iteratively for more accurate fits of the remaining populations. The bulk electron density was relatively unchanged by other populations, and was consistent to within $10\,\%$ across separate analyses of the same $i - V$ in which the ion and hot electron parameters were allowed to vary. The mean value and uncertainty found in this way were used to determine $n_{\mathrm{e,c}}$. The initial fit of the $i - V$ curve to the ion population was made for values below -80 V to compromise between sufficient data values and minimal hot electron current collection. Only an initial estimate of the ion density was possible since a hot electron population can have sufficient energy to contribute to the probe current at all applied potentials. The final ion density will be calculated in the proceeding analysis by simultaneously fitting the predicted ion, cold and hot electron currents to all of the experimental $i - V$ curve in which $V_{\mathrm{B}} \leq 0$. The purpose of the Bayesian estimation routine was then to resolve the resulting over-fitting of the data that occurs when using this method.

The effect of secondary electron emission by ion bombardment on the current collected by the Langmuir probe at negative biases was ignored. This may have caused a further inaccuracy of a maximum $10\,\%$ in ion density estimates due to the secondary electron yield $\gamma_{\mathrm{e,i}}$ for argon ions bombarding clean tungsten at energies up to 200 eV is roughly constant at 0.1. [318].

4.6 Bayesian parameter estimation algorithm

Having determined $n_{\mathrm{e,c}}$, $T_{\mathrm{e,c}}$, and V_{p}, the set of free variables $\mathbf{Z} = \{n_{\mathrm{i}}, n_{\mathrm{e,h}}, T_{\mathrm{e,h}}, u_{\mathrm{D}}\}$ were then used in models of currents for the ion and hot electron populations. A selected $i - V$ model

was computed and fitted to the repulsion region ($V_B \leq 0$) of a data set. A Bayesian likelihood calculation method was developed to solve the resulting over-fitting issue. Specifically, the free parameters for an experimental $i - V$ curve were systematically varied and compared with computed ideal curves formed by the choice of analytical models and each set of values $\mathbf{Z}$. The likelihood of a model fit producing the experimental characteristic, considering noise in the data set, then gives a quantitative estimate of the relative goodness of fit of each model type.

For each experiment, one can select a particular value combination of variables $\mathbf{Z}_k = \{n_{i,k}, n_{e,h,k}, T_{e,h,k}, u_{D,k}\}$ which, along with the known parameters, $n_{e,c}$, $T_{e,c}$, and V_p, can be used in Equations 4.6, 4.9, and 4.16 and integrated using Equations 4.5 and 4.10 to compute the ideal $i - V$ curve

$$i_{id,k}\left(\mathbf{Z}_k\right) \tag{4.17}$$

that can be compared to the experimental curve $i_{exp}\left(V_B\right)$. By quantifying the form of the noise in the experimental curve, we estimated the likelihood of obtaining i_{exp} given that our posterior $i_{id,k}$ was correct. The relative likelihood values between different choices of posteriori correspond to a relative measure of the quality of our assumed models and choices of $\mathbf{Z}_k$. Comparison was performed between the non-drifting and drifting Maxwellian forms for the hot electrons by allowing $u_D = 0$ in Equation 4.9, which reduces it to the non-drifting Maxwellian form (Equation 4.6).

Each choice of posterior and parameters $\mathbf{Z}_k$ gave a predicted current value $\mu_j(\mathbf{Z}_k)$ at each voltage V_{B_j} within a voltage sweep. We assume the noise to be of Gaussian form by the central limit theorem and calculated its global variance σ^2 by fitting a horizontal line to the experimental data taken when the probe voltage was kept constant and near V_p before each voltage sweep. The σ^2 value used was then kept constant across all $\mathbf{Z}_k$. For any predicted value $\mu_j(\mathbf{Z}_k)$, the likelihood $\mathcal{L}_{j,k}\left(y_j|\mu_j(\mathbf{Z}_k)\right)$ of making a measurement y_j at voltage V_{B_j} is given by

$$\mathcal{L}_{j,k}\left(y_j|\mu_j(\mathbf{Z}_k)\right) = \frac{1}{\sqrt{2\pi}\sigma} \exp\left[\frac{-\left(y_j - \mu_j(\mathbf{Z}_k)\right)^2}{2\sigma^2}\right], \tag{4.18}$$

where the pre-factor $1/\left(\sqrt{2\pi}\sigma\right)$ can be manipulated to reduce underflow errors so long as the final choice of pre-factor is maintained across all choices of $\mathbf{Z}_k$. The total likelihood of measuring an entire $i - V$ characteristic is therefore given by the product of the individual likelihoods given in Equation 4.18 over all voltage points V_{B_j};

$$\mathcal{L}_k\left(i_{exp}|i_{id,k}\left(\mathbf{Z}_k\right)\right) = \prod_j \mathcal{L}_{j,k}\left(y_j|\mu_j(\mathbf{Z}_k)\right), \tag{4.19}$$

where voltages were restricted to $V_B \leq 0$ so that the likelihood calculation over $\mathbf{Z}$ values was not dominated by noise from the previously determined cold electron population in the saturation

region. This calculation was repeated for each choice of variables $\mathbf{Z}_k$, followed by normalisation of the $\mathcal{L}_k$ likelihoods such that a probability density space is formed across all choices of free parameters.

This algorithm requires an appropriate choice of range for each parameter in $\mathbf{Z}$, to include all realistically possible values that could have produced the measured current, i_{exp}. This was achieved by using the previously determined values for n_{i}, $n_{\mathrm{e,c}}$, $T_{\mathrm{e,c}}$, and V_{p} and manually selecting values of $\mathbf{Z}$ until $i_{\mathrm{id},k}\left(\mathbf{Z}_k\right)$ and i_{exp} overlapped by visual inspection followed by a least-squares minimisation. A parameter space for each variable was then chosen around each estimate such that each selected value was contained within bounds that extended beyond all realistic choices for that value. For example, $0.1 \leq n_{\mathrm{i}}/n_{\mathrm{e,c}} \leq 10$ in the plasma bulk and parameter values did not vary between adjacent locations within the pre-sheath by more than a factor of 10.

Example heat maps, indicating a slice of the probability distribution for $T_{\mathrm{e,h}}$ and $u_{\mathrm{D_{eV}}}$ (the drift velocity u_{D} expressed as an equivalent energy in eV), are given in Figure 4.12. It is seen that the most likely values for each experiment were found to be localised around a single region of high probability density rather than being sparsely spread across the entire parameter space. This indicates accuracy in the determined parameters; an incorrect input model may lead to a sparse probability density since the model fit to the data would be poor. However, this result does not preclude the possibility that a more correct model exists that we did not compare against to since the proposed algorithm is only a relative likelihood calculation. The final, 'best-fit' variable set, $\mathbf{Z}_{\mathrm{fit}}$, was then determined as the mean of each trial $\mathbf{Z}_k$, where each set was weighted by its corresponding likelihood. The computation was carried out in order of decreasing likelihood until the total summed likelihood exceeded 95%,

$$\mathbf{Z}_{\mathrm{fit}} = \sum_{k}^{95\,\%} \left(\mathcal{L}_k \cdot \mathbf{Z}_k\right)_{\mathrm{max.}} \tag{4.20}$$

The uncertainty bounds for each $\mathbf{Z}_{\mathrm{fit}}$ set, given in the results section, were determined using this same 95% confidence interval. By quantifying the effect of noise, each $i_{\mathrm{id},k}\left(\mathbf{Z}_k\right)$ was compared to a measured $i-V$ curve with minimal digital smoothing, thus avoiding possible distortion by such processes. An example of the numerical implementation of the Bayesian routine is given in Appendix A.

The algorithm given above was validated against synthetic data sets in which the parameters of ideal $i-v$ curves with arbitrary levels of Gaussian noise were determined. For example, an ideal $i-V$ curve was formed by including the theoretical currents created by various Laframboise ion, non-drifting Maxwellian cold electron, and drifting Maxwellian hot electron populations as described in the formation of Equation 4.17. Artificial Gaussian noise with an arbitrary standard deviation, σ_{art}, was then added to the ideal curve, and the Bayesian routine implemented to determine the original parameter values. This process has been outlined in Figure 4.13. It was
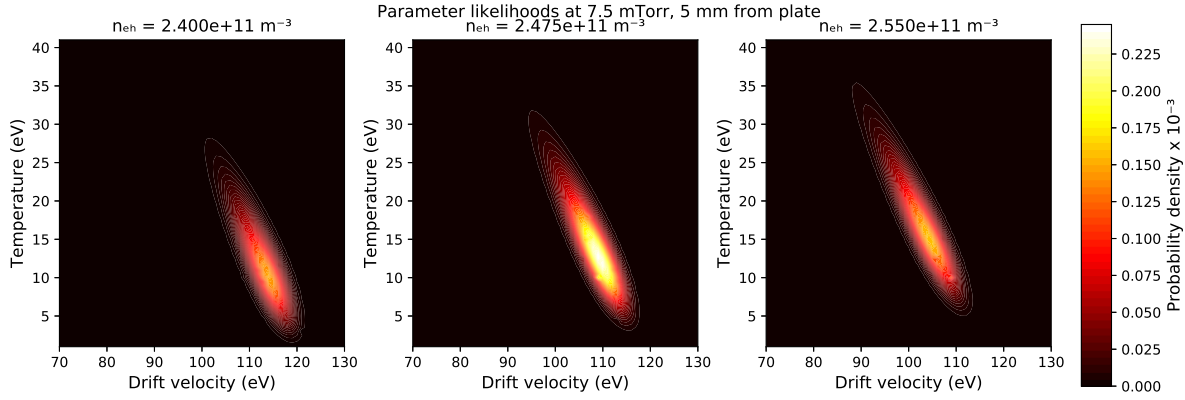
FIGURE 4.12 – Slices of the probability density space formed by all $\mathcal{L}_k$ (Equation 4.19) centered around the most likely discharge value set $\mathbf{Z}_k = \{n_{i,k}, n_{e,h,k}, T_{e,h,k}, u_{D,k}\}$ 5 mm from the plate at 7.5 mTorr. Each plot shows a scan in $T_{e,h}$ and u_D (expressed in equivalent energy) per $n_{e,h}$ with $n_i = 2.2 \times 10^{15}$ m^{-3}.

found that the Bayesian algorithm was robust to Gaussian noise, with error bar values that increased with the magnitude of σ_{art}. However, the current implementation of the algorithm fails if σ_{art} is too large relative to the variation of the ideal $i - V$ curve or if too many artificial outliers are added to the data. This is since the product of likelihoods calculation for each experimental voltage given in Equation 4.19 results in an underflow error given that each outlier results in a very small individual likelihood value $\mathcal{L}_{j,k}$. This is not well rectified by significantly increasing the global variance σ^2 used in the Bayesian routine since this reduces the difference in the likelihood values $\mathcal{L}_{j,k}$ for a given V_{B_j} for non-outliers. In other words, increasing the global variance σ^2 by too much pushes the likelihood of each parameter set $\mathbf{Z}_k$ for a voltage V_{B_j} that is not an outlier towards 1, such that they are irrelevant to the calculation. The most likely results are then a reflection of which input parameters best fit the most extreme outliers. It is possible to rectify this issue by excluding outliers from the calculation, but this requires that an arbitrary choice be made concerning which data to exclude.

4.7 Results

It was found that a non-drifting bi-Maxwellian electron population could not be fitted to any measured $i - V$ characteristic. The Baysian fitting algorithm consistently demonstrated that only a hot drifting Maxwellian population, described by Equation 4.9, accurately represented the data with probability density values centered around a locus of values in n_i, $n_{e,h}$, $T_{e,h}$, and u_D. An example of this is given for the 7.5 mTorr experiment, at a distance of 5 mm from the floating plate, in Figure 4.12. Slices of the parameter space along $T_{e,c}$ and u_D are shown for different values of $n_{e,h}$, and the region of highest likelihood is seen to be well defined and centered about the most likely values. This grouping of values indicates that the determined values for n_i, $n_{e,h}$,
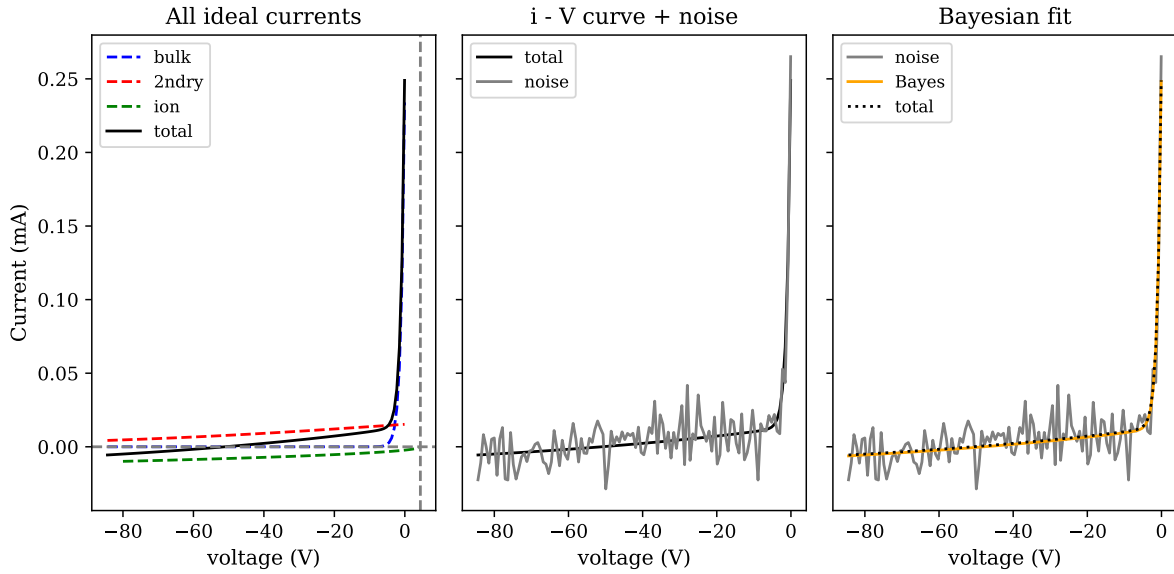
FIGURE 4.13 – A typical validation of the Bayesian routine against synthetic data. *Left*: An ideal $i - V$ curve (total) formed using $n_i = n_{ec} = 4 \times 10^{15}$ m^{-3}, $T_{ec} = 1$ eV, $n_{ec} = 4 \times 10^{11}$ m^{-3}, $T_{eh} = 25$ eV, and $u_D = 50$ eV. Each individual population current is shown as a dashed line. *Middle:* Arbitrary Gaussian noise is added to the $i-V$ curve. *Right:* The Bayesian scan returns values of $n_i = (4.25 \pm 1.50) \times 10^{15}$ m^{-3}, $n_{eh} = (3.75 \pm 1.00) \times 10^{14}$ m^{-3}, $T_{eh} = 25.0 \pm 5.0$ eV, $u_D = 52.5 \pm 10$ eV. The $i - V$ curve formed using the most likely values Z_k (orange line) against the original $i - V$ curve (dotted black line).

$T_{e,h}$ and u_D accurately represent the discharge parameters and are not artefacts of over-fitting to the repulsion region of a single $i - V$ curve.

The results from two experiments, using 5 mTorr and 7.5 mTorr of background argon gas pressure, with an electron extraction bias of -200 V applied to the filaments, are given in Figure 4.14. Figures 4.14 *a)* and *d)* demonstrate the argon ion and non-drifting Maxwellian cold electron densities (left axis) modelled using Equation 4.16 and 4.6 respectively as well as the hot electron density (right axis) modelled using Equation 4.9. Figures 4.14 *b)* and *e)* show the cold electron temperature (left axis) and plasma potential (right axis). Figures 4.14 *c)* and *f)* show the hot electron drift velocity u_D expressed as an equivalent energy in units of eV, $u_{D_{eV}}$ (left axis) and their temperature $T_{e,h}$ (right axis), along with the total average energy of a particle in a drifting Maxwellian population, $E_{tot} = 3/2 k_B T_{e,h} + u_{D_{eV}} + E_{pot}$, where E_{pot} is the electron potential energy relative to the plasma potential in the bulk plasma.

Experiments attempted at lower pressures and discharge voltages had insufficient discharge currents to successfully maintain a clean Langmuir probe tip. This was visible as a sudden and significant increase in the ion current and departure from Equation 4.16 over repeat measurements at the same location. Experiments performed below 5 mTorr with higher extraction voltages became too distorted for meaningful analysis of the hot electron population by the slight AC signal remaining within the rectified DC current that heated the filaments. The bulk electron
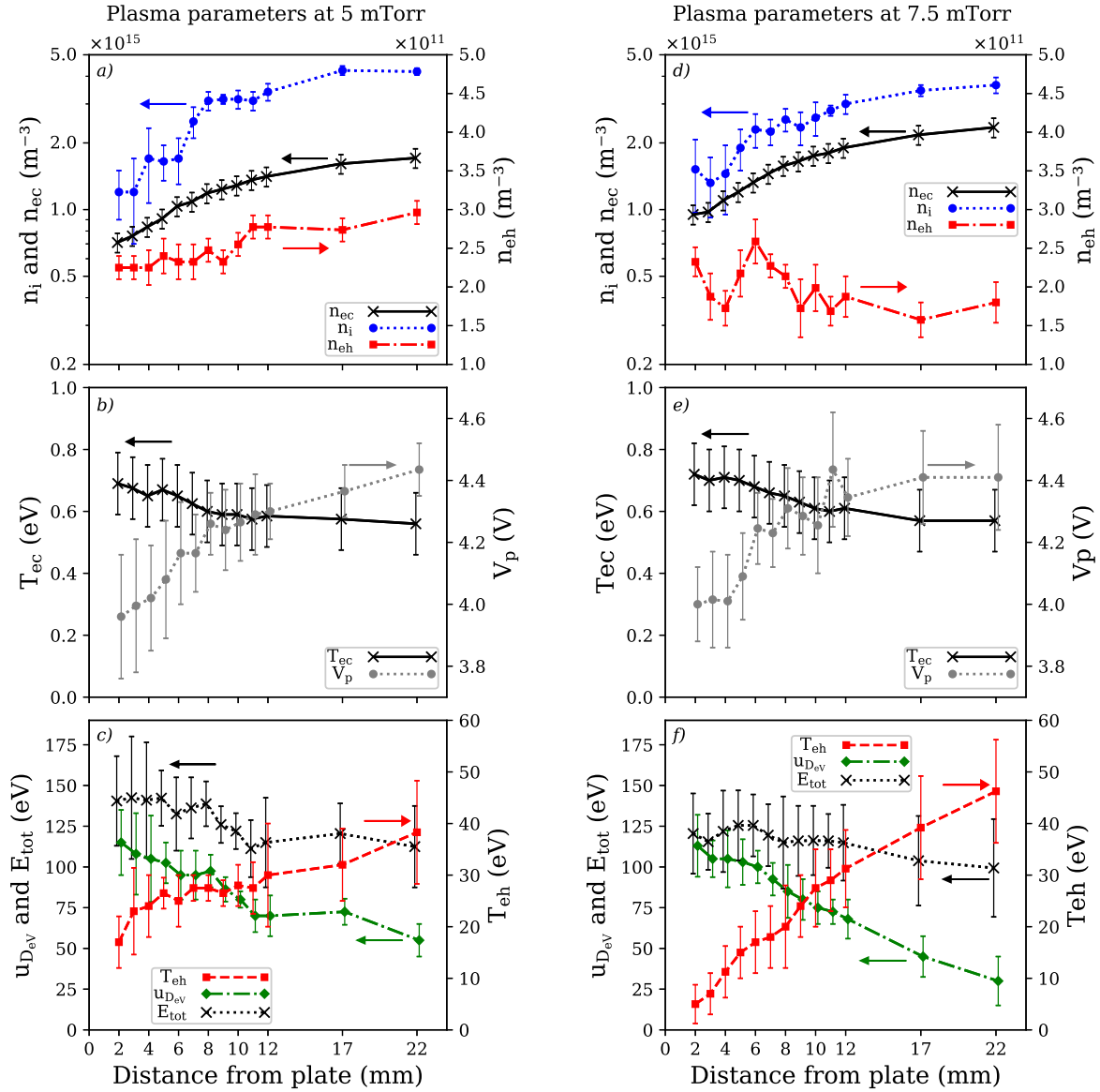
FIGURE 4.14 – Plasma parameters measured along the pre-sheath of a floating plate, using a cylindrical Langmuir probe, for DC discharges in argon. A filament bias of -200 V was used, with discharge currents of 58 mA at 5 mTorr (left column) and 63 mA at 7.5 mTorr (right column). Vertically aligned figures share a horizontal axis. Arrows indicate the vertical axis used. *a)* and *d)*: the argon ion, cold electron, and secondary electron densities (n_i, $n_{e,c}$, and $n_{e,h}$ respectively). *b)* and *e)*: The cold electron temperature and plasma potential, $T_{e,c}$ and V_p. *c)* and *f)*: The secondary electron drift velocity u_D expressed in equivalent energy and their temperature, $u_{D_{eV}}$ and $T_{e,h}$. The total average energy per particle E_{tot} is also shown.

and ion populations followed the same trends in such experiments as those shown in Figures 4.14 *a)* and *d)*.

4.8   Discussion

The decreasing plasma potential towards the floating plate shown in Figures 4.14 *b)* and *e)* correlates with the expected density evolution of the cold electron and ion populations within a cathodic pre-sheath, shown in Figures 4.14 *a)* and *d)*. The cold electron density decays from a peak value $n_{e,0}$ in the plasma bulk according to Boltzmann's factor $n_{ec} = n_{e,0} \exp\left(q_e\phi/k_B T_{ec}\right)$ within the experimental uncertainty. Moreover, the cold ion population density decreases with ion acceleration along this potential drop due to conservation of flux. The discrepancy between the ion density and the cold electron density towards the bulk plasma at 22 mm from the plate fall within reported levels from the literature (see Section 4.3.1). The cold electron temperature increases with decreasing distance from the plate, which may imply a heating mechanism, but no strong claim about this can be made once the experimental uncertainties are taken into account.

The origin of the detected hot electron population can not be conclusively resolved given multiple possible sources of high energy electrons within an experiment. It is possible, for example, that an electron population with a high total energy as evidenced in Figures 4.14 *c)* and *f)* could have arisen as primary electrons emitted from the thermionic filament. It is the opinion of the authors, however, that the results for the hot electron populations shown in Figure 4.14 provide evidence that they originate as secondary electrons, emitted from the plate floating at a negative potential with respect to the plasma potential. Otherwise, it is difficult to hypothesise an electron source that could create a population with enough energy to cause the probe to detect a significant electron current when biased at -80 V within 5 mm of the floating plate. A current analysis will be given first to demonstrate that primary electrons are unlikely to be the source of the energetic electrons even in the most favourable case. We then provide arguments that support the secondary electron hypothesis.

Let us assume that the entire 63 mA of current drawn from the filaments in the 7.5 mTorr experiment consisted of primary electrons emitted upwards and into the discharge chamber without collisions or losses. This discounts the effects of the magnetic dipole array as well as the region of grounded chamber wall below the filament. We consider the distance between the filaments and the probe to be 20 cm (see the inset of Figure 4.8) and ignore shadowing by the plate. Furthermore, we assume a sufficiently negative potential of the plate that can deflect primary electrons travelling vertically upwards toward the probe, such that its entire surface area of $2.4 \times 10^{-6}\,\mathrm{m}^2$ can collect electrons. We also assume the primary electron current travels upwards as a uniform beam with a divergence angle of $25°$, such that the beam has a radius of 10 cm with a current density of $2\,\mathrm{A/m}^2$ at the height of the probe. The probe would then collect $4.8\,\mu\mathrm{A}$ of current when biased at the plasma potential, while the detected electronic current increased from 6-$11\,\mu\mathrm{A}$ when approaching the plate. The maximum collected current in this highly idealised case is insufficient to explain the departure from the expected shape of the $i - V$ curve due to an ion and cold electron population alone. This is not changed if an ion temperature of a few eV

is included in the analysis. The primary current that could be collected by the planar probe tip that faced the filament in the situation proposed above is limited to 4 nA, providing a lower bound. Shadowing by the floating plate, electron deflection by the magnetic dipole arrangement, and losses to the ground chamber walls will all serve to reduce the maximum primary current collected by the probe. We therefore propose that the filament was an unlikely source for the detected energetic electron current.

We now consider the arguments in favour of the secondary electron hypothesis. First, the hot electron parameters can be validated against the ion population by considering a secondary electron emission flux balance analysis from and to the plate. The production of secondary electrons from a cold cathode discharge in argon by all possible discharge processes can be characterised by the bombardment of singly ionised argon alone [73]. In this case, we assume as in Section 4.3.3 that the ions gain a flux $\Gamma_i = n_i u_{D,i}$ through their inertia dominated free-fall across the pre-sheath to create a secondary electron flux $\Gamma_e = n_e v_{D,e} = \gamma_e \Gamma_i$, where γ_e is the effective secondary electron emission coefficient. The values taken 2 mm from the floating plate imply $\gamma_{e,5} = 0.8$ at 5 mTorr and $\gamma_{e,7.5} = 0.7$ at 7.5 mTorr. This order of magnitude for γ_e has been observed [373] and analytically predicted [73] for both unclean and clean steel surfaces respectively in reduced electric fields in the order of $10^4 - 10^6$ Td likely to have occurred directly in front of the floating plate.

Second, electrons emitted in a Maxwellian distribution from a negatively biased surface would gain a uniform drift velocity that would reach a maximum at the edge of the cathodic sheath if $\lambda_D \ll \lambda_e$. These secondary electrons would then experience collisional deceleration over the pre-sheath, as well as a proportional thermalisation determined by $\lambda_e \propto 1/p$ as shown by Brewer and Westhaver [374]. Thermalisation is indicated in Figures 4.14 *c)* and *f)* by the loss of hot electron drift kinetic energy matched by an equivalent gain in thermal energy. Thermalisation occurs faster than is perhaps expected given that $\lambda_e \approx 2 - 11$ cm for momentum transfer [273] and $\lambda_e \approx 13 - 20$ cm for inelastic collisions [313–317] as described below, seeming to exhibit Langmuir's paradox [365]. This may be explained by the instability-enhanced collective plasma model of Baalrud *et al.* [334] that posits a possible 100 fold increase in the thermalisation of electron populations within the pre-sheath of absorbing boundaries in low pressure discharges, which later received some experimental verification [260]. Without significant ionisation or excitation collisions, or other loss mechanisms, the total energy of the electrons would be expected to remain approximately constant. The mean value for E_{tot} given in Figures 4.14 *c)* and *e)* decreases by 28 eV at 5 mTorr and 21 eV at 7.5 mTorr, indicating that inelastic collisional processes are likely affecting the electron population. However, the loss of total energy is less than the range of the experimental uncertainty across the measurement domain, such that no firm conclusion can be drawn. A drift velocity of the given magnitudes could not have arisen from collisional processes given the discharge parameters. The arguments outlined in Section 4.3.2 indicate that

a population with a directional drift is unlikely to arise from other boundaries in the discharge chamber that surround the probe.

The expected density evolution of a drifting Maxwellian secondary electron population along the pre-sheath is confounded by multiple factors. In an imperfectly planar system, a secondary electron population would diverge somewhat as it travelled away from its source into the surrounding volume of the vacuum chamber, decreasing its density. Further decrease could be caused by collisional losses as electrons are scattered away from the collection region of the probe or lose energy to become part of the bulk population. Few electrons created by ionisation processes within the pre-sheath would have the required drift velocity to be captured by the drifting Maxwellian model. From these arguments, one would expect that a secondary electron population density should decrease with increasing distance from the floating plate.

In competition with the above processes is the increase in density caused as the population decelerates. A basic estimate of the density evolution of the proposed secondary electrons, excluding beam divergence, can be performed using the steady state, planar, collisional continuity equation and simplifying inelastic collision processes as a loss of density, given by [35]

$$\nabla_x \left(n_{\mathrm{e,h}} v_{\mathrm{D}} \right) + S_{\mathrm{loss}} = 0, \tag{4.21}$$

where S_{loss} includes the collisional reaction rate $k_{\mathrm{inel}} = \langle \sigma_i \left(g \right) g \rangle$ and is given by

$$S_{\mathrm{loss}} = n_{\mathrm{e,h}} n_{\mathrm{Ar}} \sum_i \left[\int \int \sigma_i \left(g \right) g f_{\mathrm{Ar}} \left(\tilde{\boldsymbol{v}}_1 \right) f_{\mathrm{eh}} \left(\tilde{\boldsymbol{v}}_2 \right) d\tilde{\boldsymbol{v}}_1 d\tilde{\boldsymbol{v}}_2 \right] \tag{4.22}$$

where σ_i represents the electron impact ionisation and excitation cross sections of neutral argon σ_{ion} and σ_{exc}, respectively. Here, n_{Ar} is the argon gas number density and $g = |\tilde{\boldsymbol{v}}_1 - \tilde{\boldsymbol{v}}_2|$ is the modulus of the relative velocity between the neutral argon and hot electron velocity distribution functions $f_{\mathrm{Ar}} \left(\tilde{\boldsymbol{v}}_1 \right)$ and $f_{\mathrm{eh}} \left(\tilde{\boldsymbol{v}}_2 \right)$. Equation 4.21 gives an upper bound on the effects of the conservation of flux as well as collisional loss. As such, this simplified analysis is only illustrative in support of the hypothesis that the detected energetic electron population originated by secondary electron emission from the floating plate. Modelling the apparent rate of thermalisation of the population would require an extensive collisional rate analysis beyond the scope of this chapter. Equation 4.22 can be significantly simplified by using a Cartesian velocity co-ordinate basis moving with the electron drift velocity $\tilde{\boldsymbol{u}}_{\mathrm{D}} = \hat{\boldsymbol{x}} \sqrt{2 u_{\mathrm{D,eV}}/m_{\mathrm{e}}}$. This reduces f_{Ar} to the Dirac delta function centered about $\tilde{\boldsymbol{u}}_{\mathrm{D}}$ and f_{eh} to a non-drifting Maxwellian, such that

$$S_{\mathrm{loss}} = n_{\mathrm{e,h}} n_{\mathrm{Ar}} \sum_i \left[\int \sigma_i \left(|\tilde{\boldsymbol{v}}_2 - \tilde{\boldsymbol{u}}_{\mathrm{D}}| \right) |\tilde{\boldsymbol{v}}_2 - \tilde{\boldsymbol{u}}_{\mathrm{D}}| \left(\frac{m_{\mathrm{e}}}{2\pi k_{\mathrm{B}} T_{\mathrm{e,h}}} \right)^{3/2} \exp \left\{ -\frac{m_{\mathrm{e}}}{2 k_{\mathrm{B}} T_{\mathrm{e,h}}} \left(|\tilde{\boldsymbol{v}}_2| \right)^2 \right\} d\tilde{\boldsymbol{v}}_2 \right]. \tag{4.23}$$

σ_{ion} and σ_{exc} have been taken as the average of experimental values within the literature [313–317]. The resulting density evolution with increasing distance from the floating plate is shown in Figure 4.15 starting at a distance of 2 mm. The increasing uncertainty with distance is the

result of the compounded experimental uncertainties included in the computation. One would expect that the uncertainty in Equation 4.21, arising from the simplification of collisional loss processes, would increase with increasing experimental pressure. Otherwise, deviation between predicted and measured densities could be due to the spatial divergence of a secondary electron population travelling away from the plate.
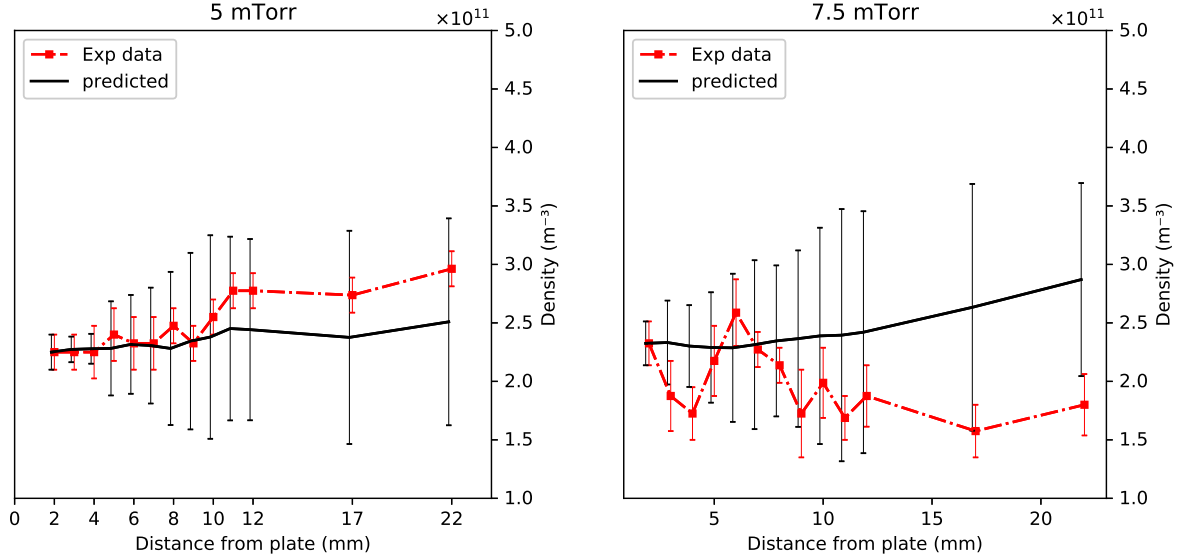
FIGURE 4.15 – The hot electron density $n_{e,h}$ from Figures 4.14 *a)* and *d)* (red line) with the predicted density (black line) for a secondary electron population following the continuity equation with inelastic collisions (Equation 4.21) from the measurement at 2 mm from the floating plate.

The effect of energetic electrons on bulk discharge parameters can be seen in the deviations from their expected values. For example, the floating potential of surfaces within a discharge consisting solely of singly ionised argon and a Maxwellian bulk electron population is approximated by [343]

$$V_f = V_p - 5.3 \frac{k_B T_{e,c}}{q_e}. \tag{4.24}$$

Floating potentials measured by the Langmuir probe were significantly more negative relative to the plasma potential than that predicted by Equation 4.24, approaching a value $V_f \approx u_{D_{eV}}/q_e$ measured at 2 mm from the plate. The probe's original $i - V$ curves demonstrated multiple possible floating potentials without an inhibitive level of digital smoothing. Instead, the probe's floating potential at each measurement is best estimated by setting the currents from the ion, cold and secondary electron populations to be equal and using the data in Figure 4.14.

The floating potential of the plate is indicated by the hot electron drift velocity to be approximately 100 eV if indeed the population is arising from secondary electron emission. This value is surprisingly high considering that electrons released from the plate would decrease the magnitude of the negative floating potential. Floating potentials can decrease dramatically in a low

pressure discharges that have a primary electron population of significant density, approaching a limiting value of the peak energy of the population as its density increases relative to the cold electron density [259, 260, 290, 324, 325]. We have argued above, however, that the primary electron population is unlikely to be the cause of the observed hot electron current to the probe, which may seem to present an inconsistency. The orientation of the Langmuir probe relative to the filaments compared to the geometry of the floating plate could be responsible for this discrepancy. Equal currents of primary and secondary electrons in the vicinity of the probe would be unlikely to be collected equally by it given that the planar probe tip was directed toward the filament. This is very likely to be the case for measurements within 5 mm of the floating plate that were shadowed from the filament, as depicted in Figure 4.8. The plate may receive a higher fraction of its total current as primary electrons than the probe in the same distribution due its horizontal plane above the filament. It could not be determined by analysis of the experimental $i - V$ curves if any energetic populations, other than the secondary electrons, were present in sufficient densities to decrease the floating potential. For the reasons listed above, however, we remain of the opinion that the most likely source of the hot electron population was by secondary electron emission from the floating plate.

One may expect the relatively high flux ratio between the secondary electron and bulk particle populations shown in Figures 4.14 to distort cathodic pre-sheath theories, discussed in the introduction. The prediction that $l \propto \lambda_i$ by Riemann (see Equation 4.14), for example, has so far been corroborated in similar discharge conditions by Oksuz *et al.* [282, 320] as well as in N$_2$ and CF$_4$ discharges in etching devices [375]. The ion-neutral collisional mean free path λ_i for ions at room temperature with less than 1 eV of drift energy will be the result of momentum transfer and charge exchange collisions. λ_i values given below were calculated using an extrapolation of charge exchange cross-sections below their original energy limit of 0.5 eV [34] to the minimum reported energy for momentum transfer cross-sections [338] of 0.1 eV. Denoting mean free paths with a subscript of their experimental pressure, in milli-torr, cross section data [338] collated by Phelps [34] give $\lambda_{i,5} \approx 2.5$ mm and $\lambda_{i,7.5} \approx 1.8$ mm. Wobschall *et al.* report collision frequency data at the same pressures, corresponding to $\lambda_{i,5} \approx 4.6$ mm and $\lambda_{i,7.5} \approx 3.5$ mm, respectively [376], while other experiments collated by McDaniel give values lying between these limits [229]. Calculations following the method of Oksuz *et al.* give $\lambda_{i,5} \approx 6.7$ mm and $\lambda_{i,7.5} \approx 4.5$ mm. Using Equation 4.12, Figures 4.14 *b)* and *e)* indicate a pre-sheath characteristic length of $l \approx 10 - 20$ mm. Using Riemann's model to compute l from Figures 4.14 *b)* and *e)* is obfuscated by the large uncertainties in V_p relative to the total potential drop $\phi(x)$. Equation 4.14 is better suited to the current analysis if adapted slightly into

$$\phi(x) = V_p - \frac{T_{ec}}{q_e} \left(\sqrt{1 - \frac{x - x_0}{l}} \right). \tag{4.25}$$
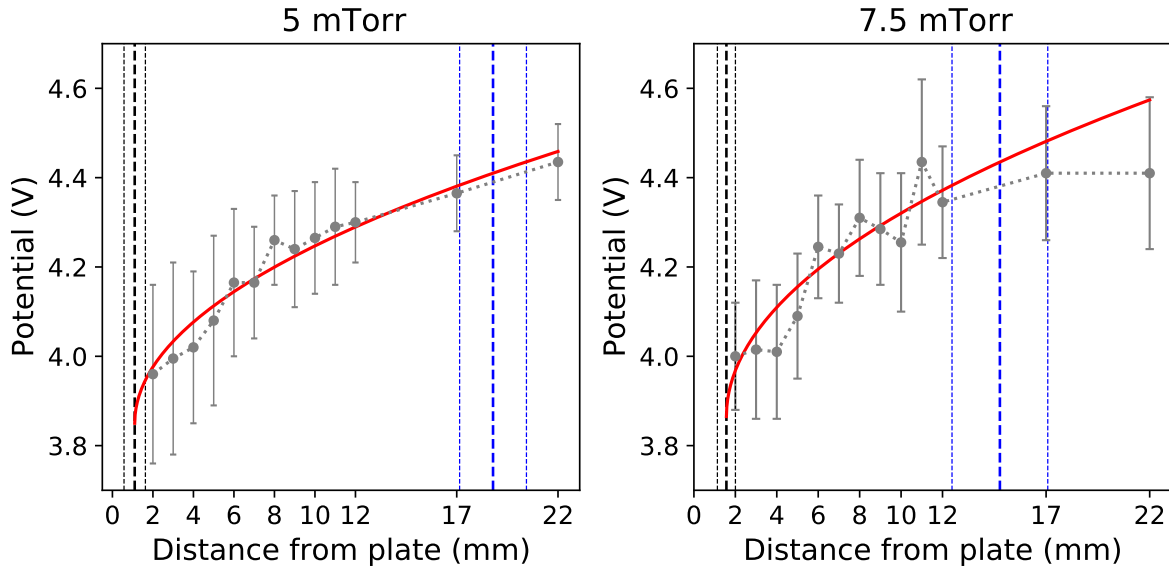
FIGURE 4.16 – Experimental values for the plasma potential from Figure 4.14 (grey circles with dashed line) with the least-squares regression fit (red solid line) of Equation 4.25 having free parameters x_0 and l (black and blue vertical dashed lines respectively). The standard deviation within x_0 and l is indicated by the surrounding dashed vertical lines. The model fit is only valid for positions $x_0 \leq x \leq x_0 + l$. *Left*: 5 mTorr, $x_0 = 1.1 \pm 0.5$ mm, $l = 17.7 \pm 1.1$ mm, $\phi(x_0 + l) - \phi(x_0) = 0.56\,V$. *right*: 7.5 mTorr, $x_0 = 1.6 \pm 0.4$ mm, $l = 13 \pm 2$ mm, $\phi(x_0 + l) - \phi(x_0) = 0.57\,V$.

Presented in Figure 4.16 are the results of fitting Equation 4.25 to plasma potential measurements using a least-squares regression method to predict values for x_0 and l that included the experimental uncertainty. The fit was performed using data from $x \leq 12$ mm for the 7.5 mTorr experiment as Riemann's model is only valid up to $x - x_0 = l$. The plasma potential measurements strongly correlate with Riemann's model. The total potential drop across the pre-sheath at $\phi(x_0)$ given in Figure 4.16 is within the experimental uncertainty of $k_B T_{ec}/2$ as predicted by Bohm's original theory, but is likely slightly larger. This perhaps indicates the effect of a significant energetic electron current on pre-sheath theories as in Equation 4.13. Including values beyond $x = 12$ mm did not affect predicted values for x_0 and l by more than the given uncertainty. The proposition that $l \approx \lambda_i$ is supported by the observation that $l_5/l_{7.5} = p_{7.5}/p_5$ within the experimental uncertainty. The discrepancy between values for $\lambda_{i,5}$ and $\lambda_{i,7.5}$ from the literature and those found using this method could have arisen from multiple causes. Possible candidates range from incorrect measurements of experimental pressure to unidentified changes in the pre-sheath caused by the presence of a significant secondary electron population.

4.9   Conclusion

In this chapter we have presented the ion, bulk and secondary electron parameters at multiple locations across the pre-sheath of a floating, stainless steel plate in a low pressure DC discharge

in argon. Parameters were determined using a translatable cylindrical Langmuir probe and likely population distribution functions analysed using probe theory in the collisionless sheath regime. The merit of various analytical techniques were presented, compared, and used where possible to set uncertainty bounds on values derived from $i - V$ curves. A Bayesian estimation method was then presented to address the over-fitting issue that results from deriving three currents due to three different charges species from a single $i - V$ curve. This method was applied to $i - V$ curves with minimal digital smoothing and enabled quantitative validation of distribution function models fitted to an $i - V$ curve as well as giving relative uncertainties on the discharge parameters used for each fit.

These analytical methods were shown to confirm the use of Laframboise's radial ion model for the ion population, and the use of non-drifting and drifting Maxwellian distribution functions and OML theory for the bulk and hot electron populations, respectively. The ion and bulk electron populations were found to decrease in density along the pre-sheath towards the floating plate as expected for decreasing plasma potential. The second, higher mean energy electron population present in the pre-sheath was confirmed, by the Bayesian method, to have a drifting Maxwellian form that lost drift energy and thermalised travelling away from the floating plate at a rate proportional to the discharge pressure. The origin of the hot electron population was shown to be unlikely to have arisen from the thermionic filament or other sources while evidence was provided in favour of secondary electron emission from the floating plate. The plasma potential within the pre-sheath was found to follow Riemann's model that $\phi\left(x\right) \propto T_{\text{ec}}\sqrt{\left(x_0 - x\right)/l}$. It was found that indeed $l \propto 1/p$, however using $l \propto \lambda_{\text{i}}$ as suggested by Riemann and Oksuz *et al.* gave values for λ_{i} between two to five times greater than those suggested by the literature.

The spatial development of the ion, bulk and hot electron populations along with the potential drop in the pre-sheath presented above has not been previously published within a single experiment, to the best of our knowledge. Such information could provide significant insight into the validity of competing pre-sheath theories.

This analysis was intended to replicate the experimental conditions that resulted in the planar anomalous metastable density increase shown in Figure 3.3 for the purpose of solving a collisional rate equation. With these discharge parameters in hand, it is possible to solve a planar collisional rate equation for the ArII 3d′ ^{2}G$_{9/2}$ metastable with foundations set by experimental measurements. The Langmuir probe analysis could not detect a primary electron population although a mono-energetic isotropic population was detected in the multipole discharge used to create Figure 3.3. Determining the influence of a secondary electron population on the ArII 3d′ ^{2}G$_{9/2}$ population relative to the total ArII density distribution given in Figures 4.14 *a)* and *b)* may still be enough to assess the validity of assuming a representative $r_{m/g}$ as discussed in Chapter 3.2. All that is required is to show that an energetic electron population that varies

rapidly over space could change the IVDF of metastable argon ions relative to the ground state. The drifting Maxwellian secondary electron population with a rapidly decreasing kinetic energy determined in the chapter above is also a likely candidate to reproduce the anomalous density phenomenon. In the following chapter we present a review of the literature in order to determine the relevant collisional rate processes involved in the calculation of the spatial distribution of the ArII 3d' ^{2}G$_{9/2}$ population. This shall be followed by a computational solution of the resulting collisional rate equation for a proposed set of secondary electron populations based on the drifting Maxwellian population given in Figure 4.14.

Chapter 5

The collisional rate equation

A collisional rate equation determines the distribution functions of the particles within a discharge through their mutual interaction with each other as well as electromagnetic fields and boundaries. Solving particle transport for each individual population involves calculating their drift and diffusion throughout the discharge [377]. Then, the individual rate equations for each population must be coupled together via the creation and loss processes that link them to all other populations in the discharge. This means that an extensive system of rate equations must be written for each of the many particle species, often to the extent of considering an individual $L - S$ state as a separate population. Solving a collisional rate equation is hence a notorious process that requires the painstaking consideration of the hundreds of available interaction pathways that can affect a state. As an example, the collisional-radiative equation proposed by Bogaerts *et al.* [304, 305] to determine the relative concentrations of ArI metastables and sputtered cathode atoms in a DC glow discharge involved the further consideration of all of the transitions between the ArI and ArII $L-S$ states, not just to and from metastable states. Such a task is frequently inhibitive even if data for all of the relevant interaction pathways exists, which is not always the case. Instead, the researcher must reduce the complexity of the problem by discarding pathways or terms that can be argued negligible to the solution. This is either done using existing literature or otherwise one must rely upon a theoretical or numerical calculation to determining each term's influence.

In this chapter we shall develop a collisional rate equation to determine the spatial distribution of ArII $3d'\,^2G_{9/2}$ metastable ions in front of the floating plate discharge in 5 mTorr of argon given in Chapter 4.2. Specifically, we shall use the data from Figures 4.14 *a)*, *c)*, and *e)*, and compare the solution to the experiment by Claire *et al.* [290] that resulted in the anomalous density increase given in Figure 3.3. The reasoning is that knowing the spatial distribution of many of the other species that contributes to the ArII $3d'\,^2G_{9/2}$ state drastically reduces the number of coupled

equations to solve. Indeed, we shall be able to reduce the calculation to the single equation for the ArII $3d'\,^2G_{9/2}$ state. This can be done since the ion, electron, and neutral argon populations as well as the local electric fields have been set by experimental measurement, such that the ArII $3d'\,^2G_{9/2}$ state is the only relevant unknown. We need not calculate the electric field in the pre-sheath arbitrarily, for example, requiring that a model based on a set of assumptions that affect the final solution be chosen to determine it. Some assumptive calculations will be required nonetheless, particularly in regions of the calculation domain not measured by the probe such as the cathode sheath. This issue can be reduced by treating such regions as solely an improved form of boundary condition since knowledge of the ArII $3d'\,^2G_{9/2}$ distribution within them is not necessary for the discussion of $r_{m/g}$. Once formed, the rate equation will be solved numerically using a relaxation method. The results should indicate which discharge factors could contribute to the anomalous density phenomenon in the pre-sheath of a floating plate that has been given again in Figure 5.4.

It shall be found in the formation of the ArII $3d'\,^2G_{9/2}$ rate equation that not all of the contributing pathways are well characterised or known. We shall follow the style of Bogaerts *et al.* [304, 305] for ArI metastables and particularly a previous work by Goeckner *et al.* [287] to form an ArII $3d'\,^2G_{9/2}$ rate equation. Both used a one-dimensional rate analysis in front of a planar cathode or floating plate, and Reference [287] specifically was performed in a similar multipole system as that used in Chapter 3.3. In these works, each contributing pathway was collated from the literature and listed relative to the dominant production or loss rate process, as shall be done below. In some cases experimental data is lacking such that assumptions must be made. In these cases we shall rely on the above references for precedent. Note, however, that this process forces the following analysis to be an approximation at best, and does not have completely rigorous foundations. It shall be shown that the important rate processes determined for the ArII $3d'\,^2G_{9/2}$ state pertain to all of the ArII metastable states that were listed in Table 3.1. This is a necessary condition of the calculation as many of the methods for determining the cross-sections of interaction pathways related to a metastable state cannot distinguish between individual metastable states within a level, term, or even in general.

We stress that this technique may yet be valid since we are only attempting to determine whether it is *possible* that collisional processes could affect the ArII $3d'\,^2G_{9/2}$ VDF relative to the IVDF in general. We do not intend to make claims about the exact form of interactions nor quantitative densities, which may not be possible given the lack of available data. The Langmuir probe data, for example, contains no information on a primary electron population that we saw was very likely to affect ArII $3d'\,^2G_{9/2}$ creation shown in Figure 3.8 and argued in Chapter 3.5. In the multipole experiment, however, the density, spatial profile, or even existence of a secondary electron population was not determined. We chose to model the experiment including the secondary electron population since many more of the parameters were experimentally determined.

Attempting to include a primary electron population in the calculation of the Langmuir probe discharge would require drastic assumptions about what sort of distribution it may have had and remove the solution from an experimental foundation. Instead, we argue to preclude a primary population from the calculation considering that it was not strictly necessary to form the anomalous density phenomenon as indicated by the self-sustaining discharge given in Figure 3.8c). Furthermore, a one-dimensional analysis of the discharge in front of the floating plate is expected to lose accuracy with distance since the discharge system was not truly planar. This work is not definitive in regards to the relationship between ground state and metastable ion distribution functions $r_{m,g}$ discussed in Chapter 3.2. By forming this equation we merely hope to provide a qualitative argument that clarifies the use of historical assumptions that relate the ArII 3d′ ^{2}G$_{9/2}$ metastable state as an indicator of the ArII population in general.

5.1 Defining the rate equation

The one-dimensional collisional rate equation for the density distribution of the ArII 3d′ ^{2}G$_{9/2}$ state, $n_G^+(x)$, in the presence of electric fields is given by [113]

$$\frac{\delta n_G^+(x)}{\delta t} + \nabla \cdot \tilde{\mathbf{\Gamma}}_G = \sum_k \left[r_{p,k}(x) - r_{l,k}(x) \right], \tag{5.1}$$

where $\tilde{\mathbf{\Gamma}}_G = n_G^+ \tilde{\boldsymbol{v}}_G$ is the metastable ion flux given a velocity $\tilde{\boldsymbol{v}}_G$ and $r_{p,k}$, $r_{l,k}$ refer to all possible reaction rates for the production and loss of the ArII 3d′ ^{2}G$_{9/2}$ ion respectively. Equation 5.1 can be expanded into parameters dependent on the non-uniform electric field $\tilde{\boldsymbol{E}}$ in front of the floating plate using Fick's law [36],

$$\frac{\delta n_G^+(x)}{\delta t} + \frac{\delta}{\delta x} \left[\mu(x) n_G^+(x) \tilde{\boldsymbol{E}}(x) \right] - \frac{\delta}{\delta x} \left[D(x) \frac{\delta n_G^+(x)}{\delta x} \right] = \sum_k \left[r_{p,k}(x) - r_{l,k}(x) \right], \tag{5.2}$$

where $\mu(x)$ and $D(x)$ are the spatially dependent ion mobility and diffusion coefficients parallel to $\tilde{\boldsymbol{E}}$. The spatial dependence of each parameter within the second and third terms of the left hand side of Equation 5.2 will require that each parameter be smooth over the calculation domain.

Approximating μ and D as independent of the local electric fields strength in a cathodic sheath and pre-sheath can lead to significant error in determining particle transport [42], as discussed in Chapter 1.1.3. We use the average of values from the literature for the reduced mobility of argon ions in argon as a function of E/n that demonstrate excellent agreement [55–57, 338, 378–380]. Longitudinal diffusion coefficients were determined using the characteristic energy relationship relative to the reduced mobility values following Petrovic *et al.* [73, 381] and Dashdorj *et al.*

[57]. This uses the Einstein relation [43]

$$\frac{D_{\text{Ar}^+}}{\mu_{\text{Ar}^+}} = \frac{k_{\text{B}} T_{\text{e}}}{q_{\text{e}}} \quad \text{as} \quad \frac{E}{n} \to 0. \tag{5.3}$$

This approach has been argued valid for low and intermediate E/n [382] where thermalisation of the population holds, and will only become invalid once drift processes dominate diffusion processes in the calculation near to the cathodic sheath region. The inaccuracy in using Equation 5.3 to determine D within these regions may be reduced somewhat by the population rethermalisation phenomena discussed in Chapter 3.5.2. We must use this technique given the lack of alternatives that are based on experimental data in the literature, to the best knowledge of the authors. Furthermore, in the cathode sheath we can assume that diffusion processes become negligible relative to ion acceleration by the cathode potential drop.

Solving Equation 5.2 requires the specification of all possible production and loss mechanisms that could contribute to a change in $n_{\text{G}}^+(x)$ at a location x. The result will then be simplified by discarding terms that contribute negligibly using arguments collected from the literature as it stands. Each reaction rate r_k based on a binary collision between two species of density n_1 and n_2 can be calculated following [35]

$$r_k(x) = n_1(x) n_2(x) K_k(x) = n_1(x) n_2(x) \int \int |\tilde{\boldsymbol{g}}| \sigma_k(|\tilde{\boldsymbol{g}}|) f_1(\tilde{\boldsymbol{v}}_1) f_2(\tilde{\boldsymbol{v}}_2) d\tilde{\boldsymbol{v}}_1 d\tilde{\boldsymbol{v}}_2, \tag{5.4}$$

where $\tilde{\boldsymbol{g}} = \tilde{\boldsymbol{v}}_2 - \tilde{\boldsymbol{v}}_1$ is the relative velocity of the collision, f_1 and f_2 are the velocity distribution functions such that $\int f(\tilde{\boldsymbol{v}}) d\tilde{\boldsymbol{v}} = 1$, and σ_k and K_k are the cross section and reaction rate coefficient respectively for process k. The reaction rates of all possible contributing mechanisms relevant to this discussion shall be discussed below and are listed in Table 5.1. The production and loss processes shall be given in terms of their maximum contribution to the ArII 3d′ ^{2}G$_{9/2}$ population relative to what we shall argue are the most dominant rate processes $r_{p,1}$ and $r_{l,1}$ respectively. Relevant variables have been labelled with a subscript of p or l for production and loss respectively along with a numeral indicating the specific process the variable relates to.

5.1.1 Production processes

Although the literature agrees that electronic collisions are mainly responsible for the creation of the ArII 3d′ ^{2}G$_{9/2}$ state, there is some debate over whether this is a single or double step process. We shall show that the dominant contribution to the ArII 3d′ ^{2}G$_{9/2}$ metastable state in a typical low pressure glow discharge is through the single step electron impact ionisation and excitation of neutral argon atoms in the ground state. We then consider all other terms that may contribute

Symb.	Production processes	Mechanism	Species	Rel. rate
$r_{p,1}$	$\mathrm{Ar} + \mathrm{e}^- \rightarrow \mathrm{Ar}_\mathrm{G}^+ + 2\mathrm{e}^-$	e^- impact ionisation/excitation	n_Ar, n_e	1
$r_{p,2}$	$\mathrm{Ar}^\mathrm{m} + \mathrm{e}^- \rightarrow \mathrm{Ar}_\mathrm{G}^+ + 2\mathrm{e}^-$	$r_{p,1}$ of metastable argon	n_Ar^m, n_e	$< 10^{-2}$
$r_{p,3}$	$\mathrm{Ar}^{+(\mathrm{m})} + \mathrm{e}^- \rightarrow \mathrm{Ar}_\mathrm{G}^+ + \mathrm{e}^-$	e^- impact excitation	n_Ar^+, n_e	$< 10^{-4}$
$r_{p,4}$	$\mathrm{Ar}^* + h\nu \rightarrow \mathrm{Ar}_\mathrm{G}^+ + \mathrm{e}^-$	Photo-ionisation	n_Ar^*, I_ν	$< 10^{-4}$
$r_{p,5}$	$\mathrm{Ar}^{+,*} \rightarrow \mathrm{Ar}_\mathrm{G}^+ + h\nu$	Cascade	$n_\mathrm{Ar}^{+,*} > \epsilon_\mathrm{G}$	0
$r_{p,6}$	$\mathrm{Ar}^{2+} + \mathrm{e}^- \rightarrow \mathrm{Ar}_\mathrm{G}^+ + h\nu$	Recombination	n_Ar^{2+}, n_e	0
$r_{p,7}$	$\mathrm{Ar}_2^{2+} + \mathrm{e}^- \rightarrow \mathrm{Ar} + \mathrm{Ar}_\mathrm{G}^+ + h\nu$	Dissociative recombination	$n_{\mathrm{Ar}_2}^{2+}$, n_e	0
$r_{p,8}$	$\mathrm{Ar}^* + \mathrm{Ar}^+ \rightarrow \mathrm{Ar}^{(+)} + \mathrm{Ar}_\mathrm{G}^+$	Atom/ion - ion excitation	$n_\mathrm{Ar}^{(+)}$, n_Ar^+	0
$r_{p,9}$	$\mathrm{Ar}^* + \mathrm{Ar} \rightarrow \mathrm{Ar}_\mathrm{G}^+ + \mathrm{Ar}^*$	Atomic ionisation/excitation	n_Ar^*, n_Ar	0

Symb.	Loss processes	Mechanism	Species	Rel. Rate
$r_{l,1}$	$\mathrm{Ar}_\mathrm{G}^+ + \mathrm{Ar} \rightarrow \mathrm{Ar}^{+(*)} + \mathrm{Ar}$	Gas quenching	n_G^+, n_Ar	1
$r_{l,2}$	$\mathrm{Ar}_\mathrm{G}^+ + \mathrm{e}^- \rightarrow \mathrm{Ar}^{+(*)} + \mathrm{e}^-$	e^- quenching	n_G^+, n_e	$\approx 10^{-5}$
$r_{l,3}$	$\mathrm{Ar}_\mathrm{G}^+ + \mathrm{e}^- \rightarrow \mathrm{Ar}^{(+)}$	Recombination	n_G^+, n_e	$\approx 10^{-10}$
$r_{l,4}$	$\mathrm{Ar}_\mathrm{G}^+ + h\nu \rightarrow \mathrm{Ar}^{+,*}/\mathrm{Ar}^{2+}$	Photon absorption	n_G^+, I_ν	0

TABLE 5.1 – * refers to a particle in any state (ground, excited, metastable, ionised, or a combination). All loss processes except for photon absorption may also emit a photon that has been omitted for brevity. Rates were calculated using experimental values measured 5 mm from the plate in the 5 mTorr experiment from Chapter 4.2 relative to $r_{p,1}$ and $r_{l,1}$.

to the creation of ArII $3\mathrm{d}'\,^2\mathrm{G}_{9/2}$ metastables and argue that they are negligible. We shall refer to the energetic electron population with a drifting Maxwellian distribution function determined by the Langmuir probe analysis given in Chapter 4.2 as the 'secondary electron population' for clarity.

5.1.1.1 Single step ionisation of ArI by electron impact $(r_{p,1})$.

This process describes the direct creation of argon ion metastables from neutral argon by single step electron impact, as is indicated by the arrow in Figure 5.1b). The cross-section, $\sigma_{p,1,\mathrm{tot}}$, that was previously given in Figure 3.1b), has been experimentally determined using secondary electron coefficients [254, 274] or by the metastable 'neutralisation method' [309]. Both methods are unable to distinguish the cross-section of an individual ArII metastable state listed in Table 3.1, $\sigma_{p,1,m}$, from the combined cross-section of all possible metastable states of the ion. $\sigma_{p,1,\mathrm{tot}}$ was the cross-section given in Figure 3.1b). $\sigma_{p,1,\mathrm{tot}}$ has also been given in Figure 5.1a) as a ratio of the relatively constant cross-section for the general ionisation of ArII by electron impact, σ_ion, in order to highlight their differences.

The various $\sigma_{p,1,m}$, and indeed the cross-section for the single step creation of many ArII excited states by electron impact, are known [383] to follow the characteristic shape given in Figure 5.1a); a steep, near linear rise from a threshold energy ϵ_0 to a narrow peak at roughly $1.5\epsilon_0$, followed by an asymptotic decline. Rosner *et al* [384] determined a similar curve analogous to Figure 3.1b) for the 3d′ ^{2}G doublet states alone relative to $\sigma_{p,1,\text{tot}}$ using LIF on an electron bombardment source. Goeckner *et al.* [287] corroborated this evidence using LIF in a low pressure multipole system that found $n_\text{G}^+ \propto n_{\text{e,c}}$. This implies that the dominant electron impact creation mechanism must be a single step process, since the ionisation and subsequent excitation of argon is a two step process that should manifest as $n_\text{G}^+ \propto n_\text{e}^2$. The references given above all demonstrated that the total density of metastable states in the discharge is proportional to the electron current. This has also been shown to be the case for many of the upper laser levels of ArII, including other metastable states [385–390]. The single step production of excited argon ions by electron impact has also been argued to be the main production process by actinometric analysis in reactive and etching plasmas [391, 392].

Goeckner *et al.* [287] proposed that the ArII 3d′ ^{2}G$_{9/2}$ state cross-section $\sigma_{p,1}$ will be within 10 % of $A\sigma_{p,1,\text{tot}}$ where $0 < A < 1$ is an unknown proportion coefficient. As a rough estimate, we have chosen that $A = g_{\text{G}_{9/2}}/\Sigma_m g_m = 10/62$, where g represents the statistical weight of the ArII metastable states listed in Table 3.1, based on the observation of the relative occupation of excited states for ArI metastables [305]. This means we have used $\sigma_{p,1} = (10/62)\sigma_{p,1,\text{tot}}$.

Calculating $r_{p,1}(x)$ at a location x technically requires knowledge of all of the local electron populations. However, the direct electron impact ionisation and excitation to the ArII 3d′ ^{2}G$_{9/2}$ metastable state has a threshold energy of $\epsilon_0 = 34.88$ eV and has a peak value for a relative collision energy of $\epsilon_{\text{pk}} \approx 52$ eV. A classical glow discharge cold electron population with a temperature $T_{\text{e,c}} \lesssim 3$ eV will contribute negligibly to $r_{p,1}$ if energetic (or 'hot') electron populations are present at a density ratio following $n_{\text{e,c}}/n_{\text{e,h}} \leq 10^5$. Indeed, it has been suggested that heavy dependence of the creation of ArII metastables on $r_{p,1}$ means that they will not be created without an energetic electron population [287, 389]. $r_{p,1}$ due to the presence of the drifting Maxwellian secondary electron population with density $n_{\text{e,s}}$, temperature $T_{\text{e,s}}$, and drift velocity $\tilde{\boldsymbol{u}}_{\text{e,D}}$ can be calculated analogously to Equation 4.23 considering the ArI population with density n_{Ar} as stationary using

$$r_{p,1}(x) =$$
$$n_{\text{Ar}}n_{\text{e,s}}(x)\int \sigma_{p,1}\left(|\tilde{\boldsymbol{v}}_2 - \tilde{\boldsymbol{u}}_{\text{e,D}}|\right)|\tilde{\boldsymbol{v}}_2 - \tilde{\boldsymbol{u}}_{\text{e,D}}|\left(\frac{m_\text{e}}{2\pi k_\text{B}T_{\text{e,s}}}\right)^{\frac{3}{2}}\exp\left[-\frac{m_\text{e}}{2k_\text{B}T_{\text{e,s}}}\left(|\tilde{\boldsymbol{v}}_2|\right)^2\right]d\tilde{\boldsymbol{v}}_2. \quad (5.5)$$

Using the values taken 5 mTorr from the floating plate in Figure 4.14, we can calculate that $r_{p,1} \approx 10^{16}$ m^{-3}s^{-1}. This value will be used to set the relative production rates of processes $r_{p,2-9}$ in Table 5.1.
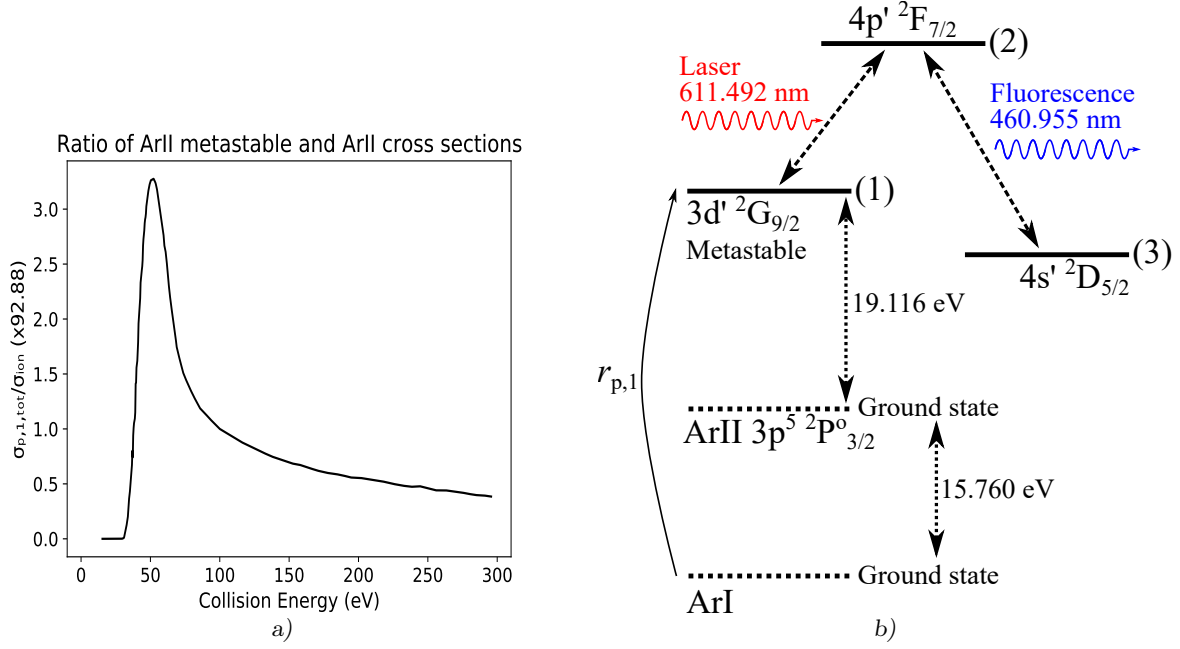
FIGURE 5.1 – *a)*: The ratio of cross sections for the main creation mechanisms of the all metastable ions ($\sigma_{p,1,tot}$) to all ionic states (σ_{ion}) by electron impact, normalised to the value at 100 eV. σ_{exc} is the mean cross section for the simultaneous ionisation and excitation of ArI to ArII metastable states by electron impact [306, 309, 384]. σ_{ion} is the average of values taken from the literature [313–317] The data extends to the threshold energy for ionisation, 15.7596 eV. *b)* The levels involved in the single step ionisation and excitation of the ArI ground state to the ArII $3d'\,^2G_{9/2}$ level are connected by the arrow.

Finally, Willems *et al.* have shown [390] that $n_G^+/n_e \approx 10^{-5}$ in a very high current discharge. This value shall be used as an order of magnitude target for n_G^+ that shall be numerically calculated.

5.1.1.2 Single step ionisation of metastable ArI by electron impact $(r_{p,2})$

It has been shown that the maximum density of metastable ArI atoms, n_{Ar}^m, relative to that of the ground state, n_{Ar}, follows $n_{Ar}^m/n_{Ar} \leq 1\,\%$ and is usually much lower than this [305, 316, 393, 394]. The cross-section peak value for the electron impact ionisation from excited states of neutral argon to any state of the argon ion [395] are of the same order of magnitude as the equivalent process from the ground state [313–317], albeit with reduced threshold energies of $\epsilon_0 \gtrsim 23$ eV. The contribution to the ArII $3d'\,^2G_{9/2}$ population from $r_{p,2}$ due to cold electrons will still be negligible in the present analysis given that $T_{e,c} < 1$ eV at all measurement locations given in Figure 4.14. Given the ratio $n_{Ar}^m/n_{Ar} \leq 10^{-2}$, we estimate that the relative contribution to the production of the ArII $3d'\,^2G_{9/2}$ state is at most 1 %, and likely much lower. The contribution from metastable ArI populations will therefore be implicitly included in the calculation of $r_{p,1}$ as neutral metastables contribute to the total pressure measurement. However, the uneven distribution of neutral metastables that has been indicated by Bogaerts *et al.* [304, 305] was not

included explicitly. Given the arguments above, we estimate that this omission will create an error in the calculation of at most 1 %.

5.1.1.3   Electron impact excitation of ionised argon $(r_{p,3})$

This process, as well as the excitation from lower excited states of the argon ion, was first proposed to be a significant contribution to the ArII 3d′ ^{2}G$_{9/2}$ density by Gordon *et al.* [396]. Later, the excitation cross-section from lower excited states of the argon ion was experimentally determined [397] to have maximum values in the order of $10^{-18} - 10^{-17}$ cm^2. The experimental method for this technique has since been questioned by Jolly [389]. Mcgarrah and Brake [398] have given numerical calculations for the cross sections of at most similar magnitudes to $\sigma_{p,1}$ for the electron impact excitation of ArII to various excited states. However, their work, published in 1990, has so far received no external citations, and the given cross-sections could not be replicated by the author using their formulation. Using the most generous values given above to calculate $r_{p,3}$ analogously to Equation 5.5 for a stationary ion population gives $r_{p,3} \lesssim 10^{12}$ m^{-3}s^{-1}, such that $r_{p,3}/r_{p,1} \lesssim 10^{-4}$. We therefore discount $r_{p,3}$ from the numerical calculation, particularly given the discussion that $n_G^+ \propto n_e$ in Section 5.1.2.1.

5.1.1.4   Photo-ionisation and excitation $(r_{p,4})$

Goeckner *et al.* [287] argued that the contribution from this process relative to $r_{p,1}$ is less than 10^{-4} based off of the low magnitude cross sections given by Silfvast *et al.* [399] for the photo-ionisation of neutral argon into excited states of ArII. The cross-section for optically allowed processes usually exhibit maxima at roughly 3-4 times the threshold energy of the interaction that are not followed by a steep decline (see [400], for example). The shape of the cross-sections for the creation of ArII metastables determined in experiments therefore indicates that the production mechanism is optically forbidden [306]. Bogaerts *et al.* showed [304, 305] that a typical argon discharge plasma is too optically thin to observe an appreciable level of photonic excitation or ionisation from the metastable states of ArI in a glow discharge. This will also be the case for all states of ArII given that it exists in equivalent or even lower densities than those predicted for ArI metastables states. Therefore, we also consign the relative rate of production from this process to be negligible, and exclude it from the calculation.

5.1.1.5   Cascades from higher states (including recombination) $(r_{p,5/6/7})$

Of the extensive list of optically allowed transitions between the excited states of singly ionised argon collated by Hibbert and Hansen [327], only two are given that end in the ArII 3d′ ^{2}G$_{9/2}$ state. The 4p ^{4}D$_{7/2}$ → 3d′ ^{2}G$_{9/2}$ transition has negligible oscillator strength, while the 4p ^{2}F$_{7/2}$ →

3d′ ^{2}G$_{9/2}$ transition represents 10 % of all possible transitions from the upper state. Given the arguments outlined in Section 5.1.1.3 for the low density of excited states of argon ions, and that this fraction is considerably reduced for any individual excited state, this process is proposed to contribute negligibly to the total production of the ArII 3d′ ^{2}G$_{9/2}$ metastable. We therefore discount the direct cascade from higher ArII excited states, $r_{p,5}$, from the calculation.

Any doubly ionised argon atom or molecule that recombines with an electron must also follow the unlikely cascade route to the ArII 3d′ ^{2}G$_{9/2}$ state in order to contribute to it. The cross-section for the electron impact double ionisation of argon has a low magnitude and high threshold energy [401] relative to single ionisation. The density of doubly ionised or even high order ionised argon will likely be much lower than its singly ionised counterpart. Furthermore, the recombination of positive ions in discharges that could lead to a cascade has been observed to mostly occur through dissociative recombination processes [402]. These cannot involve the ArII 3d′ ^{2}G$_{9/2}$ state which is peculiar to singly ionised atomic argon since the formation of a molecule necessary changes the electronic configuration of each particle within it. This allows us to discount $r_{p,7}$. Collisional radiative recombination rates of ArIII that may contribute to the ArII 3d′ ^{2}G$_{9/2}$ state have been observed to be somewhat insensitive to the species of ion involved [403]. These rates are on the order of $\alpha \approx 10^{-19} \, \mathrm{m^3 s^{-1}}$ given a bulk electron population of density $n_{\mathrm{e,c}} \approx 10^{15} \, \mathrm{m^{-3}}$ and temperatures $T_{\mathrm{e,c}} \approx 1 - 2 \, \mathrm{eV}$. We therefore expect low to negligible densities of doubly ionised atomic and molecular argon and correspondingly a negligible $r_{p,8}$ by cascade after they recombine with an electron.

5.1.1.6 Argon collisional excitation and/or ionisation $(r_{p,8/9})$

These processes can be discounted within the pre-sheath and plasma due to the observed temperature limits of 0.1 eV for the ArI and ArII populations in the bulk plasma, as discussed in Chapter 3.5. It was also discussed there that the ArII 3d′ ^{2}G$_{9/2}$ temperature in the plasma bulk was at most 0.1 eV in the hollow cathode experiments. Combined with a maximum ion drift velocity of 0.56 eV within the pre-sheath as given by Equation 4.14, the fraction of the ion or neutral population able to ionise or even excite to the ArII 3d′ ^{2}G$_{9/2}$ level will be negligible.

5.1.2 Loss processes

The purely radiative lifetime τ_{G} of the ArII 3d′ ^{2}G$_{9/2}$ metastable state has been categorised as $\tau_{\mathrm{G}} > 10 \, \mu\mathrm{s}$ [254, 309, 310]. However this lower limit was experimentally set by the time of flight of ions through an evacuated chamber, such that the true radiative lifetime is likely much longer than this. The destruction processes are therefore any collisional or excitation processes that cause a change out of the ArII 3d′ ^{2}G$_{9/2}$ state, including transitions to the ArII 3d′ ^{2}G$_{7/2}$ doublet state that is nearly degenerate to it. These processes are hard to measure for a particular
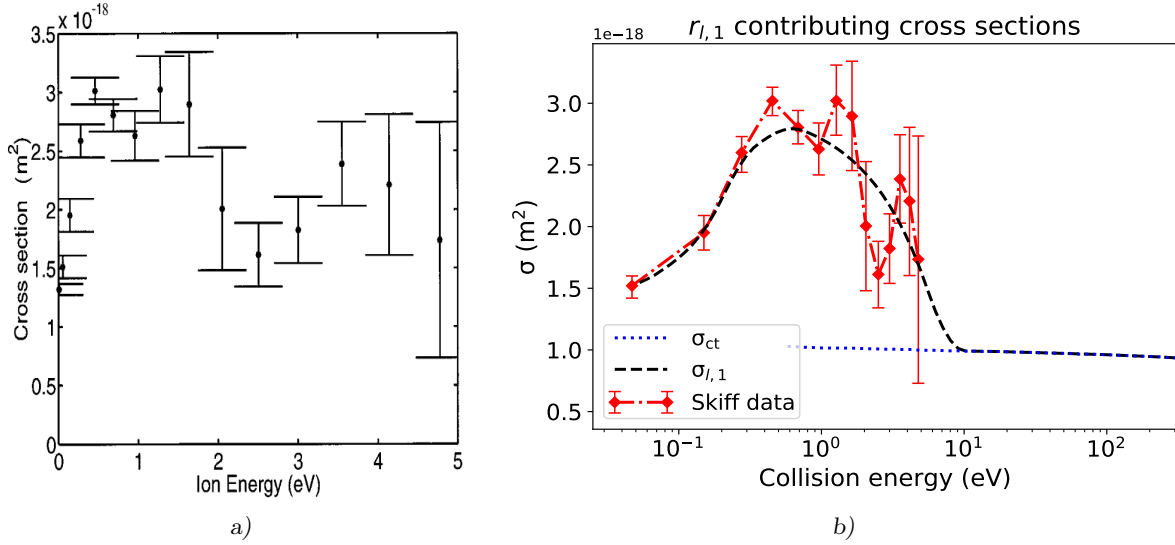
FIGURE 5.2 – *a)*: The quenching of the ArII 3d′ ^{2}G$_{9/2}$ state by collisions with ArI atoms, taken from Skiff *et al.* [280]. *b)*: (••••••) The cross-section for charge transfer between ArII and ArI taken from the literature. (•—•—•) The data from Figure 5.2a). (•—•—•) The values used for $\sigma_{l,1}$ in the calculation.

ionic metastable since collisional quenching mechanisms become available to it that may not change the ionic ground state in an experimentally discernible way. The clearest example of this process is that of symmetric charge exchange (or charge transfer) [229], where the transfer of charge between particles is unlikely to result in the final ion maintaining the original ion's exact electronic configuration. We give a summary of the literature relating to the quenching of the ArII 3d′ ^{2}G$_{9/2}$ metastable that strongly suggests that gas-collisional quenching is the dominant loss mechanism for the discharge conditions given in Table 4.1. Relative rates will be compared using the reaction rate coefficients K_l multiplied by the interacting species since the reaction rate depends on n_G^+ which is yet to be calculated.

5.1.2.1 Gas collisional quenching $(r_{l,1})$

Only one direct cross-section for the collisional quenching of ArII 3d′ ^{2}G$_{9/2}$ metastable ions with any form of background argon gas could be found [280] by the author, and has been given in Figure 5.2a). Measurements were only given up to 5 eV of collision energy, yet this should be adequate to capture the vast majority of the ArII 3d′ ^{2}G$_{9/2}$ population outside of the cathode sheath. No other literature for this interaction seems to exist as stated by Goeckner *et al.* [287] except for the specific case of a collisional interaction energy of 30 eV measured by Kadota *et al.* [309]. Goeckner *et al.* use the data of Kadota *et al.* to argue that the mean free path $\lambda_{l,1}$ for $r_{l,1}$ can be approximated by the mean free path for symmetric charge transfer λ_{ct} ($\lambda_{l,1}/\lambda_{ct} \approx 0.1 - 3.4$). The average value of σ_{ct} given in the literature [229, 338] as collated by Phelps [34] that exist down to 0.56 eV of interaction energy have been given in Figure 5.2b).

Given few other options, we have approximated the cross section for this loss mechanism, $\sigma_{l,1}$, as the black dashed line given in Figure 5.2b), which uses a combination of the data from Skiff *et al.* [280] and for σ_{ct}. The reaction rate coefficient for this process $K_{l,1}$ was then calculated analogously to Equation 5.5, and was on the order of $K_{l,1} \approx 2.5 \times 10^{-15}\,\mathrm{m^3 s^{-1}}$. Therefore, we use $n_{Ar}K_{l,1} \approx 4.4 \times 10^6\,\mathrm{s^{-1}}$ for a discharge at 5 mTorr as a benchmark value for the relative reaction rates. Here, the ion population was modelled as a drifting Maxwellian population at room temperature and the neutral population was considered stationary, as will be discussed in Section 5.5. The ion drift velocity at a location x was approximated against the potential difference from the bulk discharge to that at x.

As a final note, gas-collisional quenching of ArI metastables in neutral argon has been suggested to be irrelevant at pressures below 0.1 Torr [404]. This has only been shown to be true for the ArII 3d′ $^2\mathrm{G}_{9/2}$ population for current to pressure ratios much higher than those used in regular glow discharges [390, 405]. We therefore use the $\sigma_{l,1}$ value shown in Figure 5.2b) to calculate $r_{l,1}$ alone.

5.1.2.2 Electron collisional quenching and recombination ($r_{l,2/3}$)

Electron quenching and recombination processes have been shown to be independent of the relative velocity of the collision due to the possibility of de-excitation or recombination [390, 405]. This process will therefore be dominated by the higher density cold electron population. The reaction rate coefficient $K_{l,2}$ given in these references was measured in high current to pressure ratio discharges as $K_{l,2} = (2.5 \pm 1.0) \times 10^{-14}\,\mathrm{m^3 s^{-1}}$. Therefore, $n_{e,c}K_{l,2} \approx 2.5\,\mathrm{s^{-1}}$ using the $n_{e,c}$ values 5 mm from the plate given in Figure 4.14 *a)*, such that $r_{l,2}/r_{l,1} \approx 10^{-5}$. Similarly, the radiative recombination coefficient α_{G} for the ArII 3d′ $^2\mathrm{G}_{9/2}$ metastable state has been measured to be in the order of $\alpha_{G} \approx 10^{-19}\,\mathrm{m^3 s^{-1}}$ [403] for the discharge parameters measured by the Langmuir probe and given in Table 4.1. We need not consider dissociative recombination rates as the ArII 3d′ $^2\mathrm{G}_{9/2}$ state does not exist in molecular argon. The value for $r_{l,3}/r_{l,1}$ was calculated analogously as for $r_{l,2}$ and is given in Table 5.1. $r_{l,2}$ and $r_{l,3}$ were included in the calculation, however, due to the simplicity of their inclusion.

5.1.2.3 Photon absorption to higher states ($r_{l,4}$)

The rate of this process could not be reliably determined for the experimental conditions given in Table 4.1. The arguments made in Section 5.1.1.6 in that the plasma is optically thin for the excitation into the ArII 3d′ $^2\mathrm{G}_{9/2}$ state also applies here. We therefore do not include $r_{l,5}$ in the calculation.

5.2 Computational solution of the rate equation

Solving a collisional rate equation in 1-D for a single species requires that all of the remaining parameters that contribute to the final form of Equation 5.1 are known. The remaining rate process to consider after elimination using the arguments above are given by

$$\sum_k [r_{p,k} - r_{l,k}] = r_{p,1} - r_{l,1} - r_{l,2} - r_{l,3}. \tag{5.6}$$

Consultation of Table 5.1 reveals we are in need of the background gas density n_{Ar}, the ion density and velocity n_{i} and u_{i}, the cold electron density and temperature $n_{\mathrm{e,c}}$ and $T_{\mathrm{e,c}}$, the potential distribution ϕ, and the secondary electron density $n_{\mathrm{e,s}}$, temperature $T_{\mathrm{e,s}}$, and drift velocity u_{D} throughout the entire calculation domain in front of the floating plate. All of these values for 13 discrete locations within the cathodic pre-sheath have been given in the results for the Langmuir probe experiment in 5 mTorr of argon gas in Figures 4.14 *a)*, *c)*, and *e)*. The experimental values for ϕ have been reproduced as solid black points in Figure 5.3, and those for $n_{\mathrm{e,s}}$, $T_{\mathrm{e,s}}$, and $u_{\mathrm{D_{eV}}}$ (u_{D} expressed in eV) are given as solid grey points in the various subfigures of Figures 5.6 and 5.7. The Figures are not given here as they are more relevant to the future discussion.

We use the mean value of each population ignoring their experimental uncertainty in the following analysis, with temperatures given in units of eV. Equation 5.1 can then be solved using a Gauss-Siedel Successive Over-Relaxation (GSSOR) computational method (see Chapters 1.2 and 2.7) given an appropriate domain, discretisation, boundary conditions, and interpolation or projection of the datasets. These will be elucidated below. The use of a least squares regression algorithm to fit a model to a dataset will be referred to as having been 'fitted' from this point onwards.

5.2.1 Defining the solution domain

The experimental data is only available between 2 and 22 mm in front of the central perpendicular to the plane of the floating plate, a region corresponding to the majority of the cathodic pre-sheath. The numerical solution of Equation 5.6 will require that a computational domain be set with appropriate boundary conditions. The most appropriate computational domain will be one that allows the model to capture the change in reaction rates and metastable ion behaviour as the secondary electron population travels into the bulk plasma region. These changes will be most dramatic when the mean energy of secondary electrons transitions from above to below the energy corresponding to the peak value of $\sigma_{p,1}$ at $\epsilon_{\mathrm{pk}} \approx 52$ eV. However, the mean energy of the secondary electron population, E_{tot}, given in Figure 4.14 *e)* remains well above ϵ_{pk} within

the pre-sheath domain set by $x_0 \leq x \leq x_0 + l$. This will mean that we are less likely to observe unusual behaviour in the metastable ion population given that $\sigma_{p,1}$ is relatively stable for these E_{tot} values. Such a high secondary electron mean energy will not have occurred in the experiment by Claire *et al.* given in Figure 5.4 that had a floating potential of only -50 V on the plate. Essentially, we would like to be able to solve the rate equation for multiple different assumed secondary electron populations that transition through ϵ_{pk} within the pre-sheath, or we would like to extend the computation domain until this would naturally occur due to collisional energy losses. Both cases will require assumptions that may not be able to be based on existing literature, however.

For this reason, we have separated the calculation of Equation 5.1 into two parts:

1. A solution domain consisting of the cathodic sheath ($x < x_0$) and the domain containing the data ($x_0 \leq x \leq 22$ mm) alone. This will only involve the calculation based directly on the experimental data as well as assumed secondary electron distributions with reduced total energies. This shall be called Calculation 1.

2. A solution domain that has been extended into the bulk plasma up to 80 mm from the plate, such that a quasi-neutral region exists between $x_0 + l < x \leq 80$ mm. This will involve the reduced energy secondary electron distributions as well as further assumptions concerning how each population may have been projected into the plasma. This shall be called Calculation 2.

The results for $x \leq 22$ mm in Calculation 2 should be identical to the results for Calculation 1, however, Calculation 1 was still performed separately to compare if the connection at $x = 22$ mm was valid. The calculation domains consist of three possible regions:

a) $x < x_0$, corresponding to the cathodic sheath, included in both calculations,

b) $x_0 \leq x \leq 22$, the domain containing the experimental data and the cathodic pre-sheath (up to $x = x_0 + l$), included in both calculations,

c) $x > 22$ mm, the bulk plasma region, only included in Calculation 2,

with an appropriate discretisation of the domain using a step size of $\Delta x = 0.05$ mm. The calculation domains have been given in Figure 5.3, with the position of $x = 22$ mm and $x = 80$ mm corresponding to the RHS boundary of Calculation 1 and Calculation 2 respectively given by the two black vertical dotted lines.

The setting of realistic boundary conditions will also require that assumptions be made as to how a floating plate would interact with the discharge used in the Langmuir probe experiments

of Chapter 4.2. We shall begin by outlining the definition of the boundary conditions, and then proceed to a description of the assumptions made in Calculation 1 followed by those for Calculation 2. In the aim of merely demonstrating that it is *possible* that $r_{m/g}$ is not representative, the modelling given below will not be based on more rigorous and complicated discharge models to try and capture the true behaviour of multiple charged species. Such a model like that of Bogearts *et al.* [304, 305] but for the ArII 3d′ ^{2}G$_{9/2}$ state would be an excellent extension of the work performed in this thesis. However, it has been well noted in the literature and discussed in Chapter 1.2 that numerical discharge modelling has not proven reliable even when using well developed models. Given that fact it was not considered necessary within the scope of this work to refine the simple model that we shall use.

5.2.2   Calculation boundary conditions

The connection between the calculation domain and the quasineutral plasma is well captured by a Neumann boundary condition. Setting the location of the floating plate at $x = 0$ as the left hand side of the domain, the Neumann boundary will be defined on the right hand boundaries as

$$\frac{dn_{\mathrm{G}}^+}{dx}\bigg|_{x=22\,mm} = 0 \quad \text{or} \quad \frac{dn_{\mathrm{G}}^+}{dx}\bigg|_{x=80\,mm} = 0, \tag{5.7}$$

where the first and second conditions are for Calculation 1 and Calculation 2 respectively. The best boundary condition to realistically capture the metastable ion diffusion and mobility through the pre-sheath as well as their absorption at the floating plate should involve a cathodic sheath. In either of the calculations, however, we are mainly interested in the metastable behaviour in the pre-sheath. All that is required of the cathodic sheath, then, is that the metastable ion population is rapidly accelerated towards the floating plate by the potential drop within it. We first set a Dirichlet boundary condition corresponding to the absorption of metastable ions at the cathode, given by $n_{\mathrm{G}}^+(0) = 0$. We must then use a sheath model to describe the potential drop.

5.2.2.1   Evaluating the potential distribution

The electric field and its derivative can be determined using a centered difference approximation of the potential distribution if it is known. The potential distribution across the entire pre-sheath was fitted using Riemann's model adapted to the Langmuir probe experimental arrangement given in Equation 4.25. This places the floating plate at $x = 0$ on the left boundary of the domain, with the potential increasing to the right. The fitting procedure, given in Figure 4.16, returns mean values of $x_0 = 1.1$ mm and $l = 17.7$ mm, outlined as the grey vertical dashed lines in Figures 5.3, 5.5, 5.6, and 5.7. The exponential decay of the pre-sheath potential beyond

$x = x_0 + l$ into the plasma was captured by fitting an exponential asymptote following

$$\phi(x) = A\left[1 - \exp\left(-Bx\right)\right] + C \tag{5.8}$$

to the last 3 mm of the pre-sheath data and extrapolating it up to each RHS boundary, where A, B, and C are free variables in the regression fitting algorithm. A rolling window filter of window length 20 was then used for points within 2 mm of $x = x_0 + l$ to smooth the transition over the pre-sheath boundary and avoid discontinuities in derivatives. This process creates a smooth potential distribution that matches the measured potential profile well.

The potential profile in the sheath could be solved directly at a location x_j by using a centered difference approximation for the collisionless infinite plane cathode sheath solution of Poisson's equation analogous to the method used in Chapter 2.7. The charge density within the cathode sheath was modelled as due to a cold electron population following the Boltzmann criterion and an inertial ion population described by the Bohm criterion [36],

$$\phi(x_j) = \tag{5.9}$$
$$2\phi(x_j + \Delta x) - \phi(x_j + 2\Delta x) + \frac{\Delta x^2 q_e n_{c,p}}{\epsilon_0}\left[\exp\left(\frac{q_e \phi(x_j + \Delta x)}{k_B T_{c,p}}\right) - \left(1 - \frac{2q_e \phi(x_j + \Delta x)}{m_i u_0^2}\right)^{-1/2}\right],$$

where $n_{c,p}$ and $T_{c,p}$ are the density and temperature of the cold electron population at $x = 22$ mm (corresponding to the best value for the bulk plasma), and u_0 is the drift velocity of ions at x_0 given by Riemann's pre-sheath model (Equation 4.25). This uses two potential values to the right to iteratively calculate the next sheath potential one discrete spatial step to the left starting from the first two pre-sheath potential values.

We note that Equation 5.9 indicates a floating potential on the plate of -24 V less than V_p. This magnitude of floating potential is far too low to have caused the observed $u_{D_{ev}} = 117.5$ eV measured at 2 mm from the floating plate given in Figure 4.14 *e)*. This is likely due to the fact that Equation 5.9 does not include collisional effects nor the effects of other electron populations in the discharge. It was discussed in Chapter 4.8 that it may be possible that a primary electron population could reduce the floating potential of the plate without being able to be detected by the Lanmguir probe due to the experimental arrangement. This is evidenced by the fact that $V_f = V_p - 24$V is also a much greater magnitude than $V_f = V_p - 3.1$ V that is predicted by Equation 4.24 [43] for a Maxwellian cold electron and singly ionised argon discharge. This implies that the pre-sheath potential used as the initial boundary values in setting Equation 5.9 indicated a much greater magnitude of potential on the floating plate than by these two populations alone. The true floating potential of the plate would lie somewhere between these bounds set by $u_{D_{ev}}$ and Equation 4.24. The potential solution $\phi(x)$, however, was merely intended to provide a more accurate boundary for the removal of metastable ions near $x = x_0$. A completely accurate
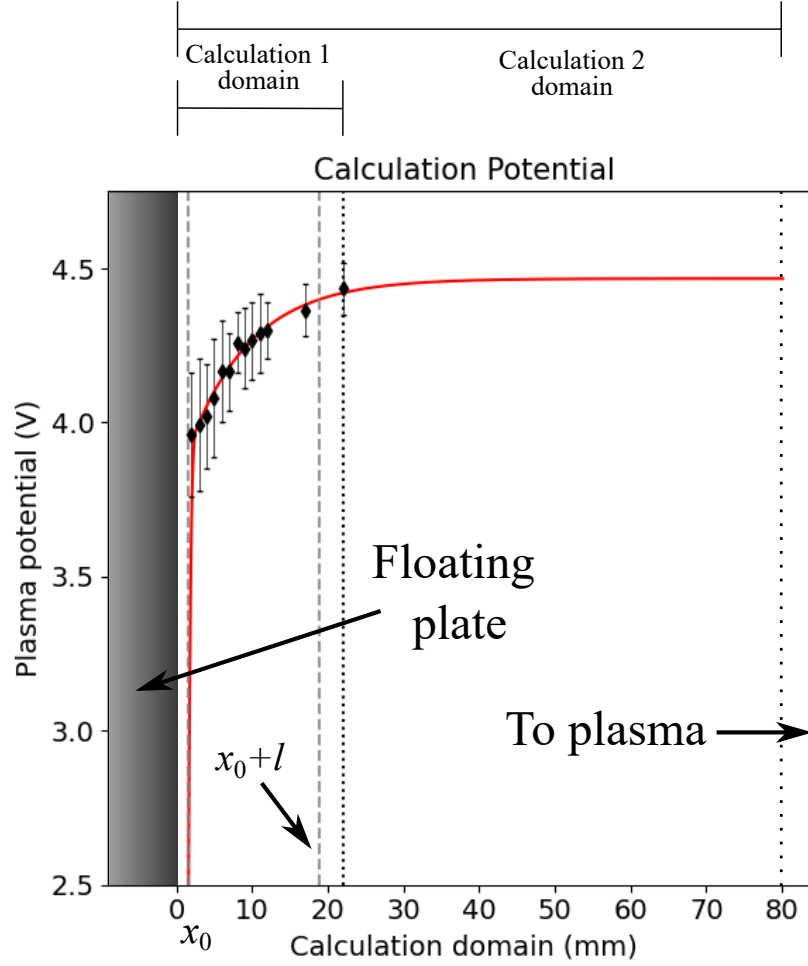
FIGURE 5.3 – An illustration of the computational domain including the calculated potential distribution (red line) and the plasma potential measurements (black diamonds). The separate discharge regions are indicated by the vertical dashed lines.

replication of the true sheath potential profile would likely not provide a significant improvement of the final result. A diagram of the solution space including the potential distribution and the experimental plasma potential data is given in Figure 5.3. Values for $\tilde{E}$, $D\left(\tilde{E}\right)$, and $\mu\left(\tilde{E}\right)$ as well as their spatial derivatives were calculated using this potential distribution for all of the proceeding computations.

The velocity limit for the integration of reaction rate processes was set at 2000 eV for the secondary electrons and 100 eV for ions in each velocity dimension. These high integration limits were to accommodate convergence issues that arise in the numerical computation of rate processes involving a large Maxwellian temperature spread about a drift velocity such as in Equation 5.5.

5.2.3 Determining collisional data sets

The values used for $\sigma_{p,1}$, $\sigma_{l,1}$, $D\left(\tilde{\boldsymbol{E}}\right)$, and $\mu\left(\tilde{\boldsymbol{E}}\right)$ from the literature have been described in Section 5.1. These can be defined anywhere within the computational domain once the potential profile has been determined. $\sigma_{p,1}$ was only defined up to 300 eV of relative interaction kinetic energy in the literature [306, 309, 384], which is enough to include the vast majority of the secondary electron VDF $f_{e,s}$ but not enough to cover the extremes of the integration limits. $\sigma_{p,1}$ was extrapolated beyond 300 eV by fitting

$$\sigma_{p,1}\left(\varepsilon\right) = A\varepsilon^n + B, \quad n \,\epsilon\, \mathbb{R} \tag{5.10}$$

to the high energy tail of the data set, where A, B, and n are free parameters. This ensured an extrapolation that captured the asymptotic decay of the high energy tail, and has negligible effect on the final result of the computation.

5.3 Determining discharge parameters for Calculation 1

Calculating $r_{p,1}$ within the cathodic sheath would require that we set the secondary electron distribution function there. However, the rate of density loss due to ion acceleration by the sheath potential represented by the second term in Equation 5.1 that contains $\tilde{\boldsymbol{E}}$ dominates over the other terms that contribute to n_{G}^{+} within the cathode sheath. This argument is used to neglect production processes in the sheath for both Calculation 1 and Calculation 2. All that remains in order to solve the collisional rate equation for the experimentally determined discharge parameters given in Figure 4.14 is to interpolate the data-sets so that calculations can be made everywhere within the domain. The experimental values for $n_e\left(x\right)$ were fitted and interpolated using Equation 5.8.

Otherwise, we would like to specify secondary electron populations with reduced total energies given by

$$\varepsilon_{\mathrm{r,tot}}\left(x\right) = u_{\mathrm{r,D_{eV}}}\left(x\right) + T_{\mathrm{r,e,s}}\left(x\right) + \left(V_{\mathrm{p}} - \phi\left(x\right)\right), \tag{5.11}$$

where the additional subscript r refers to a secondary electron population that has been reduced in average energy. This creates the issue in that we do not know how the other discharge parameters would have been changed in order to produce a secondary electron population with different $\varepsilon_{\mathrm{r,tot}}$. It was discussed in Chapter 4.8, however, that the magnitude of the floating potential on the plate was likely increased by its peculiar L-shaped geometry that likely allowed it to efficiently collect primary electrons from the filament. In this case, it would be possible that different plate geometries may have reduced the magnitude of the floating potential without otherwise affecting the discharge parameters significantly. We therefore propose that maintaining

all discharge parameters apart from the secondary electron energy values would be an appropriate level of approximation for this qualitative numerical model. This means that the electric potential and cold electron parameters $n_{e,c}$ and $T_{e,c}$ were kept as the original experimental data for all of the calculations given below. Furthermore, the secondary electron density $n_{e,s}$ does not seem to follow a definitive trend relative to the experimental uncertainty. This was linearly fitted for Calculation 1 and used for all reduced secondary electron parameters, as shown by the solid black line in Figure 5.6 *d)*. A mechanism for predicting the change in secondary electron density when projected into the bulk plasma for each reduced population corresponding to a value of $\varepsilon_{r,tot}$ will be given for Calculation 2. The possible development of a more comprehensive model including Langmuir probe experiments that could better isolate the contribution from different electron populations will be discussed in Chapter 6.

5.3.1 The reduced secondary electron parameters

The reduced electron populations were formed from the experimental secondary electron drift velocity $u_{D_{ev}}$ and temperature $T_{e,s}$ by using arbitrary energy multiplier ε_r, where $0 \leq \varepsilon_r < 1$. One could simply determine the reduced data-sets $u_{r,D_{ev}}$ and $T_{r,e,s}$ by multiplying the experimental data-sets by ε_r. However, this would not capture the likely reduction in the collisional thermalisation of a drifting Maxwellian population that was created with a reduced drift velocity. The procedure was slightly adapted in an attempt to better capture such behaviour. First, the reduced temperature $T_{r,e,s}$ was formed by multiplying the maximum $T_{e,s}$ value, $T_{s,max}$, by $1 - \varepsilon_r$ and subtracting this from the entire data-set, such that

$$T_{r,e,s} = T_{e,s} \left[1 - T_{s,max} \left(1 - \varepsilon_r \right) \right]. \tag{5.12}$$

Then, a minimum secondary electron temperature had to be set. Thermalised secondary electron populations are regularly observed in glow discharges with temperatures approximately a few times greater than the cold electron temperature, as discussed in Chapter 1.1.8. However, the exact value for the minimum threshold of $T_{r,e,s}$ will not matter significantly so long as it is less than the full width at half maximum of the peak of $\sigma_{p,1}$ given in Figures 3.1b) and 5.1a). This was likely to be the case given an experimental value of $T_{e,c} = 0.7$ eV measured 22 mm from the plate. We therefore set an arbitrary minimum value of $\min(T_{r,e,s}) = 2 \cdot T_{e,c} = 1.5$ eV.

The subtraction procedure given in Equation 5.12 meant that the $T_{r,e,s}$ population which used $\varepsilon_r < 0.5$ had initial values less than the defined minimum. These $T_{r,e,s}$ data-sets were shifted by $\Delta\varepsilon$ such that their initial value was equal to 1.5 eV and then multiplied by $(T_{max} - \Delta\varepsilon)/T_{max}$ to capture a less energetic population typified by this difference. Each manipulated $T_{r,e,s}$ data set was then fitted using Equation 5.8 and interpolated across the calculation domain, and are

shown in Figure 5.6 *f)*.

Each $u_{r,D_{eV}}$ was found by subtracting $u_{D,max}(1-\varepsilon_r)$ from u_{D-eV}. These data-sets were then fitted considering that drift velocity is lost collisionally using

$$u_{r,D_{eV}}(x) = A\exp\left[-(x-x_0)/\lambda_{u_{r,D}}\right], \tag{5.13}$$

where A is a free fitting parameter and $\lambda_{u_{r,D}}$ is the inferred mean free path for the collisional loss of drift velocity. These have been given in Figure 5.6 *e)*. The reduced total energies $\varepsilon_{r,tot}$ were then calculated according to Equation 5.11, and are given in Figure 5.6 *c)*. The results for Calculation 1 including the various sets of secondary electron parameters corresponding to a value of ε_r have been given in Figure 5.6 *a)*. The upper and lower horizontal dotted lines in Figures 5.6 *c)* and *e)* represents ϵ_{pk} and ϵ_0 for $\sigma_{p,1}$ respectively.

These results will be discussed after the method used for Calculation 2 has been described.

5.4 Parameter projections for Calculation 2

The secondary electron parameters could be simply projected by extrapolating the fits used for each $\varepsilon_{r,tot}$ given in Section 5.3. This was done for $u_{D_{eV}}$ considering that the fitting procedure used for each $u_{r,D_{eV}}$ given by Equation 5.13 had calculated $\lambda_{u_{r,D}}$. Using this procedure for $T_{r,e,s}$, however, would create temperature projections that tend towards a horizontal asymptotic limit without declining. This does not well describe the fact that the gain in secondary electron temperature comes from the collisional loss of their drift velocity. We therefore expect each $T_{r,e,s}$ to stop increasing once the corresponding $u_{r,D_{eV}}$ has dropped below a given critical value and even to eventually decrease through collisions with the background gas at room temperature. We also cannot calculate the rate of gain of thermal energy with distance from the plate as merely the corresponding loss rate of kinetic energy given that the total secondary electron energy E_{tot} was not conserved, as discussed in Chapter 4.8. The secondary electron kinetic energy was likely also being lost through inelastic collisions with the background gas.

It may be possible to better infer the rate of inelastic kinetic energy loss for each reduced population at locations beyond $x = 22\,\text{mm}$ from the difference in the rate of change of $\varepsilon_{r,tot}$ from the loss rate of $u_{r,D_{eV}}$ and the gain rate of $T_{r,e,s}$. The effect of this extra rate of energy loss can then be included in the projection of each $T_{r,e,s}$. This was achieved by iteratively adding the rate of loss of $u_{r,D_{eV}}$ and subtracting that of $\varepsilon_{r,tot}$ following

$$T_{r,e,s}(x+\Delta x) = T_{r,e,s}(x) + \frac{du_{r,D_{eV}}}{dx}(x+\Delta x) - \frac{d\varepsilon_{r,tot}}{dx}(x+\Delta x) \tag{5.14}$$

The data set is then smoothed at the connection point at $x = 22\,\text{mm}$ as described for the potential distribution in Section 5.2.2.1. The results of this calculation are shown in Figure 5.7 *f)*. A new $\varepsilon_{\text{r,tot}}$ was then calculated using the updated $T_{\text{r,e,s}}$ values, and is shown in Figure 5.7 *c)*. The upper horizontal dotted line in Figures 5.7 *c)* and *e)* represents the energy corresponding to the peak of $\sigma_{p,1}$.

The experimental values for $n_{\text{e,s}}$ do not sufficiently increase with distance from the plate to match the conservation of flux alone. An approximate steady state, planar continuity calculation to determine the expected evolution of $n_{\text{e,s}}$ was proposed in Chapter 4.8 in which all electron-neutral inelastic collision processes are interpreted as a loss of density. The linear fit to the experimental data was extrapolated to create a set of $n_{\text{r,e,s}}$ data-sets using this same calculation for the different secondary electron energy parameters determined above. The results are shown
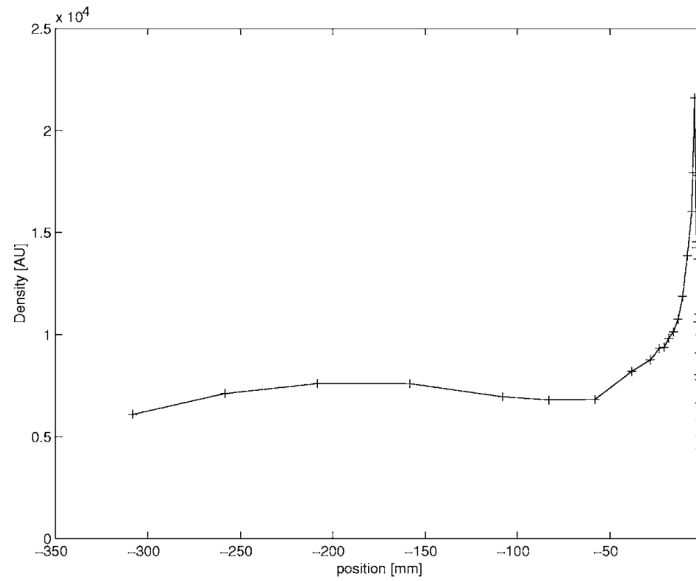
FIGURE 5.4 – The LIF observation of the anomalous ArII 3d′ ^{2}G$_{9/2}$ density distribution in front of a floating plate in a multipole discharge with 3.6 mTorr of argon and -50 V applied to the thermionic filaments, reproduced with permission from Claire *et al.* [103]

in Figure 5.7 *d)*. The lower energy projections become largely unaffected by inelastic collisions as the drift velocity drops below the threshold energy for the excitation of neutral argon. It should be noted that the increase in density with distance from the plate will correspondingly increase $r_{p,1}$ with distance from the plate. Therefore, an increase in n_{G}^+ towards the plate will occur in spite of this inaccurate density projection.
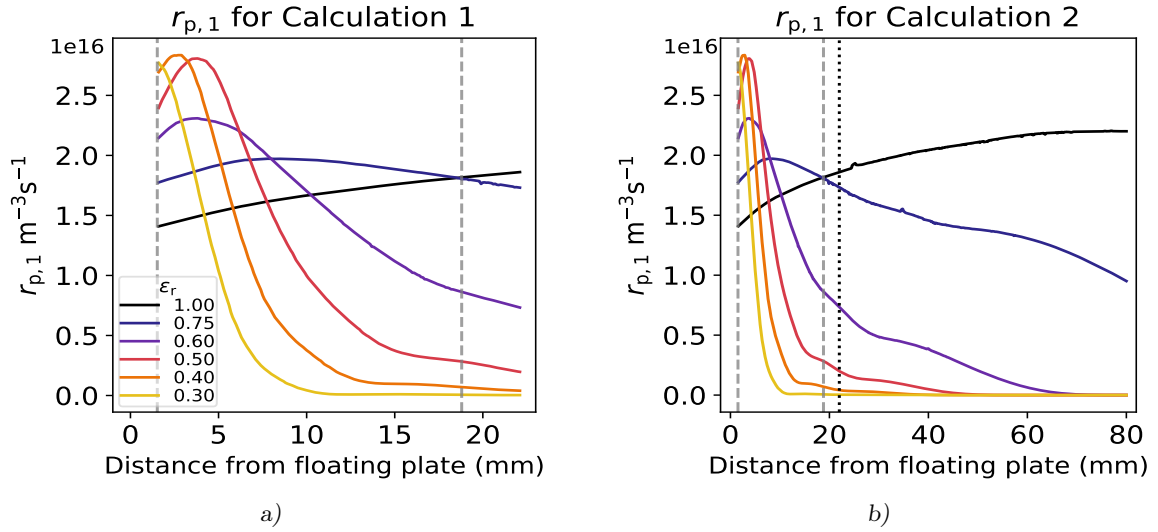
FIGURE 5.5 – *a)*: $r_{p,1}$ for Calculation 1. The vertical dashed lines correspond to $x = x_0$ and $x = x_0 + l$ *b)*: $r_{p,1}$ for Calculation 2, using the legend from *a)*. The additional vertical dotted line indicates $x = 22$ mm.

5.5   Calculating rate coefficients

$r_{p,1}$ was then calculated for all $x \geq x_0$ in Calculation 1 and Calculation 2 using Equation 5.5. The spatial distribution of $r_{p,1}$ for the various secondary electron energy projections is given in Figure 5.5a) for Calculation 1 and Figure 5.5b) for Calculation 2. The integral was performed by dividing the domain in each velocity dimension into 21 logarithmic sub-intervals in order to more accurately capture the sharp peak of the drifting Maxwellian distribution function. The metastable ion population was given a drifting Maxwellian form with the background gas temperature (see the discussion in Chapter 4.3.3). The ion drift velocity was approximated as corresponding to the potential difference from the plasma at 80 mm to the location in question. This was used to calculate $r_{l,1}$ against a stationary background gas population using the formula given in Equation 5.5. Including the thermal temperature of the neutral argon gas would require a six-dimensional integral too computationally expensive for the gain in accuracy it would provide.

Equation 5.1 was then discretised for each Calculation and solved using a centered difference approximation for the projected parameter values under a GS-SOR scheme with a tolerance of 10^{-6} % between updates. The results for the absolute n_G^+ distribution for Calculation 1 and Calculation 2 are given in Figures 5.6 and 5.7 *a)* respectively. Each of these results has been given normalised to their maximum value within the computational domain in Figures 5.6 and 5.7 *b)*.
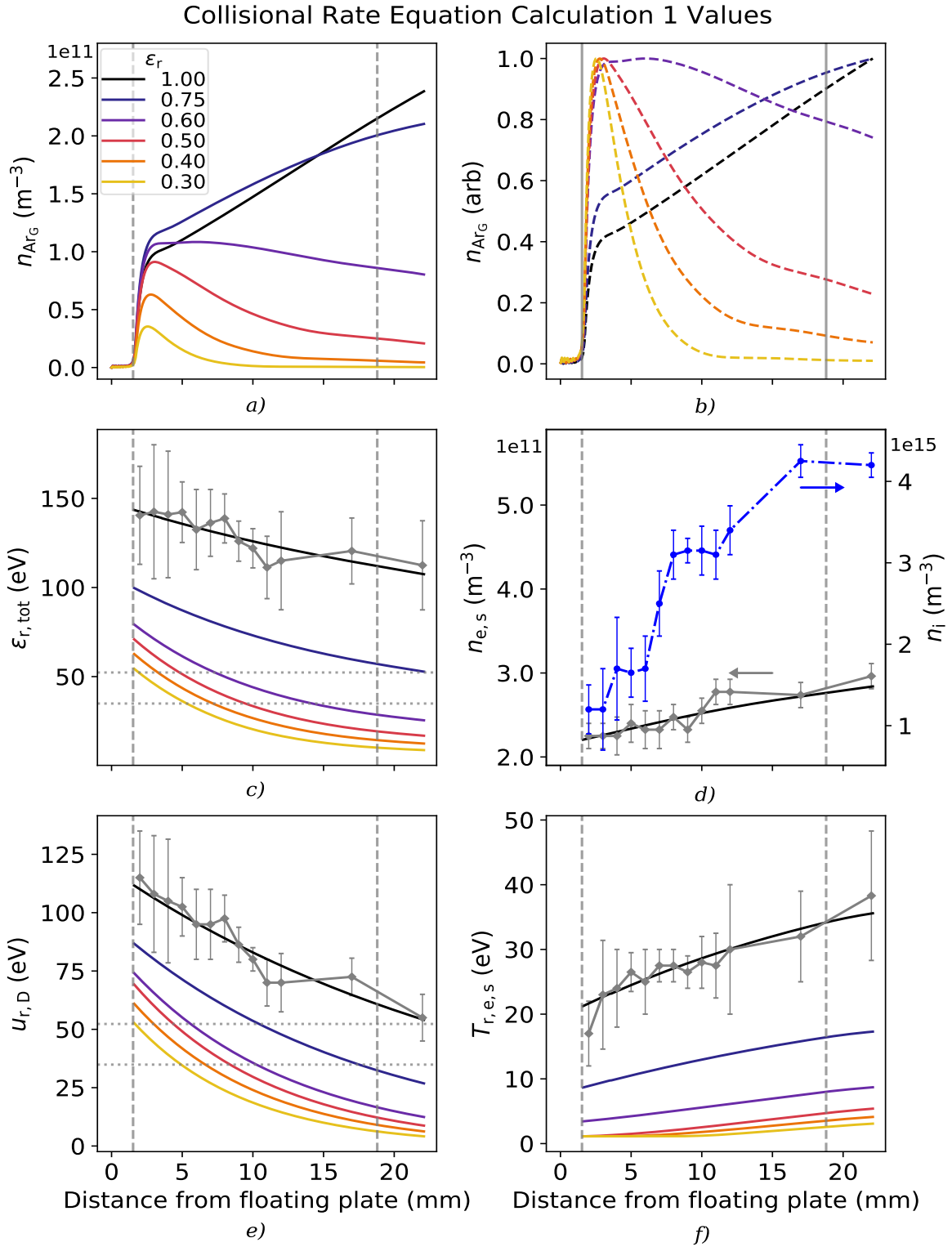
FIGURE 5.6 – *a)*: The total ArII $3d'\,^2G_{9/2}$ density distribution by Calculation 1. *b)*: a) normalised to the maximum n_G^+ value. *c),e),f)*: Secondary electron parameters used in Calculation 1. *d)*: The experimental ion density (right axis) and secondary electron density (left axis). The legend in *a)* is common to all sub-figures except *d)*. Vertical dashed lines indicate $x = x_0$ (left) and $x = x_0 + l$ (right). Horizontal dashed lines indicate ϵ_0 (below) and ϵ_{pk} (above).
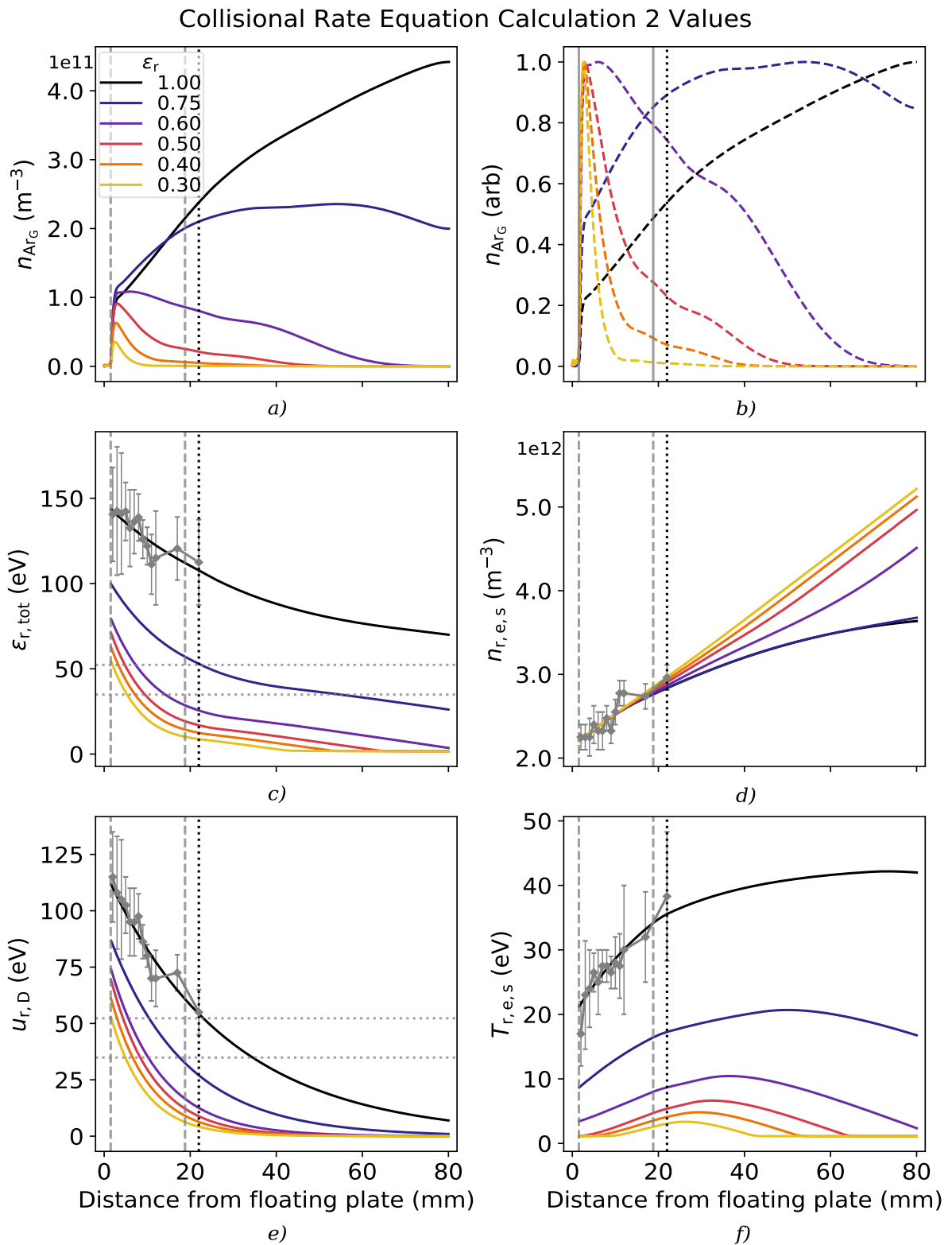
FIGURE 5.7 – The same as in Figure 5.6 but for Calculation 2. *d)* The secondary electron density projections $n_{\mathrm{r,e,s}}$ used in Calculation 2. The additional dashed vertical line indicates $x = 22$ mm.

5.6   Discussion of computational results

First, we note that the results for $x \leq 22 \, \text{mm}$ in Calculation 2 given in Figures 5.7 and 5.5b) are nearly identical to those for Calculation 1 given in Figures 5.6 and 5.5a). We can therefore discuss the results for both Calculations simultaneously while noting that fewer assumptions were required for Calculation 1. The calculated ratio $n_{\text{G}}^{+}/n_{\text{e,c}}$ using the $\varepsilon_{\text{r}} = 1$ data at $22 \, \text{mm}$ from the plate in Figures 5.7 and 4.14 *a)* is between 10^{-5} and 10^{-4}, corresponding to the target value discussed in Section 5.1.1.1. We note that $\varepsilon_{\text{r}} = 1$ corresponds to no manipulation of the secondary electron parameters after fitting to the experimental data. The spatial density distribution results shown in Figures 5.7 *a)* and *b)* contain a viable explanation of the anomalous ArII 3d′ ^{2}G$_{9/2}$ metastable density observations shown in Figure 5.4, and likely also for the hollow cathode results shown in Figure 3.9a). Furthermore, the range of possible secondary electron energies indicates how this metastable density increase can occur while the majority of the ArII population decreases according to pre-sheath theory. This shall be discussed below. In doing so, the use of the VDF of an ArII metastable ion as a representative of that of the ground state ion is thrown into doubt, particularly in the vicinity of emitting surfaces. The implication of this statement on the validity of the conclusions concerning the diverging ion hypothesis given in Chapter 2.3 will need to be revisited.

The energy corresponding to the threshold and peak value of $\sigma_{p,1}$ in Figure 5.1a), $\epsilon_0 = 34.88 \, \text{eV}$ and $\epsilon_{\text{pk}} \approx 52 \, \text{eV}$ respectively, have been indicated in Figures 5.6 and 5.7 *c)* and *e)* as the lower and upper horizontal dotted lines. The spatial variation in $r_{p,1}$ given in Figure 5.5 is low when the secondary electron average energy per particle given in Figures 5.6 and 5.7 *c)* is above ϵ_{pk} or if the population temperature given in Figures 5.6 and 5.7 *f)* is large relative to the width of the peak of $\sigma_{p,1}$. This is due to the slow variation of $\sigma_{p,1}$ for energies above $80 \, \text{eV}$ or, in the case of large temperatures, since the IVDF is spread over a large energy range such that a change in $\langle \tilde{\boldsymbol{v}} \rangle$ is relatively inconsequential to the final reaction rate. This effect can be seen for the secondary electron populations corresponding to $\varepsilon_{\text{r}} = \{1, 0.75\}$, where the corresponding reaction rates given in Figure 5.5 do not demonstrate a sharp peak anywhere within the domain. In these cases, the effects of diffusion or of acceleration by the electric field in the pre-sheath will dominate the metastable ion density distribution, as is expected by most pre-sheath theory [19]. The metastable ion population in Figures 5.6 and 5.7 *a)* and *b)* for $\varepsilon_{\text{r}} = \{1, 0.75\}$ behave similarly to how ground state ions are expected to behave; a maximum density occurring in the bulk plasma that decays across the pre-sheath as the ions are accelerated. This was observed in the Langmuir probe experiment of Chapter 4 for the ground state ion population density n_{i}, which has been reproduced as the blue dash-dotted line in Figure 5.6 *d)*. This type of density distribution will likely also occur in front of non-emitting surfaces at negative bias relative to

the plasma potential in which ion or metastable ion creation occurs predominantly in the bulk plasma.

When $\varepsilon_{\mathrm{r,tot}}$ passes through $\varepsilon_{\mathrm{pk}}$, and particularly when $T_{\mathrm{r,e,s}}$ is low, $r_{p,1}$ can be seen to change rapidly with position and form a sharp peak within the pre-sheath. This occurs for the population projections with $\varepsilon_{\mathrm{r}} \lesssim 0.6$ in Figure 5.5. The highly localised distribution of $r_{p,1}$ throughout space begins to dominate over ion drift and diffusion processes to the extent that the relative density distributions given in Figures 5.6 and 5.7 *b)* begins to replicate their form. The total density of ArII 3d′ $^{2}\mathrm{G}_{9/2}$ ions given in Figures 5.6 and 5.7 *a)* decreases with decreasing ε_{r} since an increasing fraction of each artificial secondary electron population no longer has sufficient energy to create ArII 3d′ $^{2}\mathrm{G}_{9/2}$ ions by a single step impact process. $u_{\mathrm{r,D_{eV}}}$ passes below ϵ_0 within the pre-sheath while $T_{\mathrm{r,e,s}}$ decreases, causing the sharp peak in each $r_{p,1}$ there. When these criteria are met, the solution of Equation 5.1 closely replicates the experimental anomalously increasing metastable ion density approaching a floating plate [103] given in Figure 5.4. The -50 V plate floating potential that occurred in Figure 5.4 could create a secondary electron population with $\varepsilon_{\mathrm{r,tot}} \lesssim 50\,\mathrm{eV}$. It is quite likely that the secondary electron population in that experiment would have had a different distribution function from the approximate ones proposed in Figures 5.6 and 5.7. However, so long as the population transitions past ϵ_0, it is likely to increase the rate of creation of ArII 3d′ $^{2}\mathrm{G}_{9/2}$ metastables in the pre-sheath relative to the bulk plasma.

The multipole system used by Claire *et al.* [290] to produce Figure 5.4 measured an isotropic mono-energetic primary electron population of mean energy 50 eV and density $2 \times 10^{12}\,\mathrm{m}^{-3}$ emitted from thermionic filaments in 0.14 mTorr of argon gas. This population would manifest as the addition of a constant value of $r_{p,1}$ everywhere within the discharge volume excluding the cathodic sheath, as discussed in Chapter 3.5. However, we can see for $\varepsilon_{\mathrm{r}} = \{1, 0.75\}$ in Figure 5.5 that a relatively constant $r_{p,1}$ does not lead to the anomalous density phenomenon. We can also evaluate the possible prevalence of secondary electrons in front of the plate relative to the primary electrons using a flux balance as was done in Chapter 4.8. Populations from the experiment by Claire *et al.* [103] will be clarified with a subscript Cl.

The primary electron and ion densities were given as $n_{\mathrm{e,p,Cl}} = 2 \times 10^{11}\,\mathrm{m}^{-3}$ and $n_{\mathrm{i,\,Cl}} = 5.5 \times 10^{15}\,\mathrm{m}^{-3}$ respectively as determined by a Langmuir probe analysis [103], so that $n_{\mathrm{p,Cl}}/n_{\mathrm{i,\,Cl}} = 3.6 \times 10^{-5}$. We assume that the ion population enters the cathode sheath with a drift velocity of $u_{\mathrm{i,D,Cl}} = 2.5\,\mathrm{eV} = 3.48\,\mathrm{km/s}$ according to Riemann's pre-sheath theory given by Equation 4.14 and since $T_{e,c,Cl} = 2.5\,\mathrm{eV}$ [103]. This gives an ion flux $\Gamma_{\mathrm{i,Cl}} = 1.92 \times 10^{19}\,\mathrm{m}^{-2}\mathrm{s}^{-1}$. A secondary electron population with density $n_{\mathrm{e,s,Cl}}$ will have a drift velocity of $u_{\mathrm{e,D,Cl}} \approx 50\mathrm{eV} = 4.2 \times 10^{6}\,\mathrm{m/s}$ at the sheath/pre-sheath edge due to the -50 V plate potential, such that $u_{\mathrm{i,D,Cl}}/u_{\mathrm{e,D,Cl}} = 8.3 \times 10^{-4}$. This can be used to determine what value of secondary electron emission coefficient

$\gamma_{e,i}$ would be necessary such that $n_{e,s,Cl}/n_{e,p,Cl} = 1$;

$$\frac{n_{e,s,Cl}}{n_{e,p,Cl}} = \frac{n_{e,D,Cl}}{n_{i,Cl}} \frac{n_{i,Cl}}{n_{e,p,Cl}} = \gamma_{e,i} \frac{u_{i,D,Cl}}{u_{e,D,Cl}} \frac{n_{i,Cl}}{n_{e,p,Cl}} \quad \Rightarrow \quad n_{e,s,Cl} = 23\gamma_{e,i}n_{e,p,Cl}. \tag{5.15}$$

Therefore, it would be possible to have a secondary electron population emitted from the floating plate of equal density to the primary electron population emitted from the filaments if $\gamma_{e,i} = 0.043$. The primary and secondary electron populations would also both have a similar flux given that they both would have a mean energy near to 50 eV. The floating plate in Figure 5.4 was covered in a photon absorbing layer of unspecified material, such that $\gamma_{e,i}$ was not known. However, $\gamma_{e,i} \approx 0.01$ is regularly observed for various cathode materials in glow discharges with a similar value of electric field [73].

We therefore have a plausible explanation of how the anomalous metastable ion density phenomenon may arise while the ground state ion population simultaneously follows classical pre-sheath theory. If metastable ions are predominantly created by an energetic electron population that varies in energy over space, this electron population can dictate the metastable ion density distribution. This can cause the maximum metastable ion density in a discharge to occur near to the sheath/pre-sheath boundary in a planar system if the electron population arises from secondary electron emission. This may also occur in non-planar systems at higher cathode voltages in which the secondary electron population quickly diverges into the discharge volume, as was possibly the case for the self-sustaining hollow cathode experiment biased at -1000 V given in Figure 3.8c). The drift velocity of the secondary electron beam in this experiment with 38 mTorr of background gas pressure may well have remained above 100 eV in the measurements taken up to 59 mm. Considering this alone, we would expect the ArII $3d'\,^2G_{9/2}$ density to decrease as it is accelerated toward the cathode. However, the secondary electron beam may have diverged into space such that it rapidly lost density with distance from the cathode, correspondingly reducing the creation of metastables. Furthermore, the possible convergence of metastable ions that are not collisionally quenched into the laser path would push the location of the density peak closer to the sheath boundary. This same effect as well as transition of the secondary electron drift velocity below ϵ_0 may also have contributed to the anomalous ArII $3d'\,^2G_{9/2}$ densities observed in the filament mediated hollow cathode discharges at -200 V given in Figure 3.8.

The results in Figures 5.7 *a)* and *b)* indicate how it is possible to observe an anomalous ArII $3d'\,^2G_{9/2}$ density increase while the total density of all combined ArII states decreases. It was argued in Section 5.1.1 that cold electrons and ions with mean energies below 1 eV will not contribute to the production of further ions in any form relative to energetic electron populations. Consider the ratio of the cross sections for the main creation mechanism (by electron impact) of ground state and metastable ions throughout the solution domain, given in Figure 5.1a). The reaction rates for the production of metastable ions to ground state ions by a single step electron impact collision have the same prefactors such that the ratio between them is given

by the ratio of the cross-sections for each process, given in Figure 5.1a). The total calculated density of metastable ions in the discharge of the Langmuir probe experiment (which can be found by multiplying the densities given in Figures 5.6 and 5.7 *a)* by the inverse of A=10/62, see Section 5.1.1.1) is at most less than 1 % of the total ion density detected by the Langmuir probe. The behaviour of ground state ions will therefore dominate the total ion density behaviour detected in experiments that cannot distinguish between excited states of the ion. The cross-section for the electron impact ionisation of argon has a threshold energy of 15.76 eV which is followed by a rapid increase to a approximately constant value that is maintained up to 300 eV of interaction energy [313–317]. The reaction rate for this process will vary slowly for a far greater range of energetic electron populations likely to exist in a glow discharge, filament mediated or otherwise. Furthermore, the lower threshold energy can increase the relative rate of creation of ionised argon by the cold electron population to dominant levels in the bulk plasma for discharges in which $T_{e,c} \gtrsim 2$ eV such as in Figure 5.4. Therefore, for the secondary electron parameters at which $\varepsilon_r = 0.5$ shown in Figures 5.6 and 5.7 *b)* for example, the ArII ground state population density will be created evenly across the calculation domain. This means that the ground state ion density will decrease approaching the cathodic sheath as the population is dominated by drift and diffusion processes in the pre-sheath. Simultaneously, the metastable ion population experiences a sharply peaked $r_{p,1}$ within the pre-sheath since the same value of $\varepsilon_{r,tot}$ transitions through ϵ_{pk} and ϵ_0. Thus, it is possible for the metastable ion population to increase approaching an emissive surface while the total ion population simultaneously decreases. Although based somewhat on conjecture, this argument shows that it is possible in glow discharges that the IVDF of metastable argon is *not* representative of the IVDF in general.

The calculated peak metastable ion density relative to the density in the bulk plasma shown in Figure 5.7 *b)* is in some cases greater than was observed in experiment (Figures 3.8 and 5.4). It is important to reiterate that the isotropic mono-energetic primary electron population that classifies the multipole discharge system was not included in the calculation since any form of primary electron population could not be detected in the Langmuir probe experiments given in Figure 4.14. One could expect that the metastable ion density may still peak within the cathodic pre-sheath in the presence of a primary electron population if its density is smaller than that of the secondary electron population density in the vicinity of the floating plate. The magnitude of the metastable density peak relative to the its value in the bulk plasma would then likely be dependent on the ratio of the reaction rates due to the primary and secondary electron populations. Comparing the rate products for $\varepsilon_r = 0.75$ and $\varepsilon_r = 0.60$ in Figure 5.5 to the resulting density profiles in Figure 5.7 *b)* one can see that $r_{p,1}$ must be appreciably larger in the pre-sheath than in the bulk to observe the anomalous density effect at all.

5.7 Conclusion

This analysis has demonstrated that the relative density of an ArII metastable state's IVDF at different locations throughout a discharge is not always a reliable indicator of the ground state density distribution. This will be true for any ionic metastable state in which the cross-section of its main creation mechanism relative to that of the equivalent ground state is qualitatively different. All of the ArII metastables listed in Table 3.1 will therefore exhibit the same density phenomena as the ArII $3d'\,^2G_{9/2}$ state under the analysis given above, for example. We have shown that the ArII metastable population will be affected differently than that of the ground state in any case in which the mean energy of an electron population transitions near to ϵ_{pk}. $r_{m/g}$ is therefore unlikely to remain representative throughout velocity space near to biased emissive surfaces or in any case in which the distribution function of the primary electron population varies rapidly in space. It may be possible to make inferences of the spatial distribution of the ArII ground state distribution function far from surfaces if one is certain that only Maxwellian or otherwise stable electron populations exist in the discharge. Even in this case, however, the uncertainty in the comparison will be difficult if not impossible to quantify. Furthermore, stable electron distributions are unlikely to be observed in systems that exhibit interesting ion transport phenomena.

More concerning for the use of the LIF diagnostic is whether $r_{m/g}$ will remain proportional throughout velocity space even if the distribution functions of the majority energetic electron populations are isotropic in phase space, particularly in higher pressure systems. This is due to the fact that charge transfer collisions that form the majority of the ion-neutral collisional cross-section [34] serve to decelerate ground state ions and often quench metastable ions. The LIF diagnostic may therefore observe a smaller fraction of metastable ions that have undergone charge transfer than will be the case for the ArII ground state population. This may cause the metastable IVDF to have a different mean velocity than the ground state IVDF, and not accurately represent the collisional deceleration of an ion group, as was discussed by Skiff *et al.* [280]. Simultaneously, where metastable ions are predominantly created within the changing electric field of the pre-sheath will differ from ground state ions. This effect will not necessary be alleviated at lower discharge pressures if $l \propto \lambda_{\mathrm{i}}$, as discussed for Equation 4.14.

For these reasons, we propose that direct comparisons between the IVDFs of the ground state and metastable states of singly ionised argon must be performed with extreme caution. This is particularly the case in the presence of electric fields, emissive surfaces, or charge density gradients in the discharge. Researchers must explicitly state the assumed relationship between the measured IVDF and the ground state IVDF if one exists, and give supporting evidence for why such a relationship may be inferred. Any publication that uses the relative density between

measurement locations of an ArII metastable to make inferences of the relative density of the ground state is significantly weakened by the observations made in this chapter.

5.7.1   Implications for the diverging ion model

The unrepresentative nature of $r_{m/g}$ for the ArII 3d$'$ ^{2}G$_{9/2}$ metastable state reduces the strengths of the conclusion made in the first publication by the author [193] given in Chapter 2.3. The potential difference between the hybrid hollow cathode surface and its central axis according to the computational model as shown in Figure 2.11 would indicate that secondary electrons emitted from its surface would be accelerated to above 100 eV within the virtual anode. The assumed presence of such a secondary electron population was argued as the fundamental cause of the divergent ion hypothesis as the two-ring cathode was likened to a hollow cathode discharge. If present, this secondary electron population would certainly affect $r_{m/g}$ albeit to an unknown extent. The question remains as to whether a changing $r_{m/g}$ could result in a diverging metastable ion density up to 25 times larger than the converging density as shown in Figure 2.10 while the ground state ion population displays the opposite effect, particularly in a filament mediated multipole discharge. In fact, the relatively low density of converging metastable ions is further evidence for the prevalence of a dominant secondary electron population in the discharge. ArII 3d$'$ ^{2}G$_{9/2}$ ions are created efficiently by the primary electron population emitted from the filaments, particularly for a mean primary population energy of 50 eV that is near to ϵ_{pk}. The background gas pressure of 0.2 mTorr would mean that many of these ions created in the much larger volume of bulk plasma and cathodic pre-sheath could be accelerated to the cathode centre without being collisionally quenched. The relatively low density of observed converging ArII 3d$'$ ^{2}G$_{9/2}$ ions therefore indicates that the secondary electron population inside of the two-ring cathode contributes to $r_{p,1}$ at a much higher rate overall, especially when considering that converging ions would be collected from a larger volume than the cathode interior. Given this, it is therefore likely that ionisation to any of the ArII states by electron impact was predominantly localised to the cathode centre, which would still result in a majority of diverging ions.

However, the shape of the ground state ion distribution function cannot be reliably inferred from the data given in Figures 2.9 and 2.10. It could be possible that the electron beam along the axis of the two ring cathode (evidenced by the microchannel) reaches the most efficient energy for the $r_{p,1}$ process after their acceleration out of the cathode centre. This could have resulted in the highest density of metastable ions observed to the left of the rings at $z \leq 22$ cm in Figures 2.10 and 2.9. The ground state ionisation density is more likely to follow the density distribution of secondary electrons within the two-ring cathode given the relatively constant cross-section σ_{ion} for electron energies above 40 eV [313–317] shown in Figure 3.1a).

Chapter 6

Conclusion and further work

In this thesis we have attempted to address multiple phenomena concerning charge transport in low pressure hollow cathode discharge systems that were sometimes unexpected in or even contradictory to the literature. The ion divergence hypothesis that counteracts the originally proposed convergent ion dynamics of discharge IEC devices was studied as an aspect of the hollow cathode effect. This effort revealed a possible flaw in the precedent of conclusions that can be drawn from the use of the LIF diagnostic. The remainder of the thesis was concerned with uncovering the cause of this flaw such that its effects on the analysis of discharge IEC devices could be addressed. In having built on existing evidence, we propose that discharge IEC devices be reclassified as only 'electrostatic' nuclear fusion systems that exhibit ion divergence due to the hollow cathode effect. We have provided a new method of analysing Langmuir probe data such that multiple electronic species can be more reliably determined from a single $i - V$ curve, which was done for the first time throughout a cathodic pre-sheath. Finally, we have shown that the distribution function of the metastable states of ArII are highly dependent on energetic electron populations in a fundamentally different way to the ArII ground state. This means that a relationship between them can not always be reliably drawn when using the LIF diagnostic, as has been done historically.

In Chapter 2 an LIF analysis was given along the central axis of the two-ring hybrid IEC/hollow cathode. A majority density of ions diverging from its center was found rather than converging to it as proposed in the literature. This was hypothesised to be due to the pendular trapping of secondary electrons emitted from the cathode surface resulting in efficient ionisation within its volume, or in other words, due to the hollow cathode effect. The virtual anode that accelerates ions outward was found to be replicable using only a zeroth order cathode sheath numerical model and without the need for ambipolar effects that were previously indicated. This may have been due to the particular geometry of the two-ring cathode. This led to the LIF experimentation

of a cylindrical hollow cathode with solid walls in Chapter 3 that was intended to better linked the hollow cathode effect to a spherically gridded IEC cathode. It was not possible to observe the interior of the solid cathode, and diverging ions were not observed exterior to it, possibly as a result of its long axial aspect ratio. This was insufficient evidence to discount either the relationship between IEC cathodes and the hollow cathode effect or the contribution of ambipolar effects to the diverging ion phenomenon. However, the ArII 3d′ ^{2}G$_{9/2}$ metastable ion population that was observed by the LIF diagnostic and is often related to the ArII ground state in the literature showed an apparently anomalous increasing density approaching the hollow cathode for all discharge types tested. The results suggested the influence of an energetic secondary electron population on the density distribution of the ArII 3d′ ^{2}G$_{9/2}$ state. The remainder of the thesis turned to resolving the cause of this anomalous phenomenon that had also been previously observed in planar discharges.

A Langmuir probe analysis of a low pressure planar discharge was proposed in order to experimentally determine the spatial distribution of secondary electrons in a cathodic pre-sheath for the first time. In Chapter 4, a cylindrical Langmuir probe was used in the OML discharge regime to measure $i - V$ curves at 13 locations in front of a floating plate in filament mediated low pressure discharges. A Bayesian estimation routine was proposed and implemented to improve the determination of experimental uncertainties and resolve the over-fitting issue that arises from the collection of multiple electronic currents in a single $i - V$ curve. This method allowed for the more robust determination of the parameters of a cold ion, non-drifting Maxwellian cold and drifting Maxwellian hot electron distribution functions as well as the plasma potential throughout the pre-sheath. The drifting Maxwellian hot electron population was found to thermalise with distance travelled into the plasma and was argued to have arisen from secondary electron emission from the floating plate.

These experimentally determined discharge parameters were then used to solve a collisional rate equation collated from the literature for the density distribution of ArII metastables in a planar DC discharge in Chapter 5. It was determined that the dominant source of ArII metastables was the single step ionisation and excitation of ArI by electron impact, and that the dominant sink was from ion-neutral collisions. The numerical solution could replicate the anomalous density phenomenon while the ArII ground state behaved as expected due to the difference in their creation mechanisms, given certain proposed secondary electron distributions. This therefore revealed that the VDF of an ArII metastable population can not be simply related to that of the ArII ground state in the presence of inhomogeneous energetic electron populations or even near to changing electric fields. Indeed, this was argued to be true for any system of quantum states in which the cross-sections for the main creation and loss reaction rates are qualitatively different. Caution was suggested for future use of the LIF diagnostic for which it has sometimes been assumed that a representative relationship exists between the two states. This was argued

to weaken the knowledge of the exact distribution function of the ArII population inferred from the LIF analysis in Chapter 2, but not to counteract the evidence that the two-ring cathode exhibited the hollow cathode effect and therefore a likely majority ion divergence.

In conclusion, we have given further evidence that discharge IEC systems do not exhibit the inertial oscillation of ions that converge to a highly confined fusion core. Instead, we suggest that such devices be reclassified as 'electrostatic' nuclear fusion devices based on their behaviour as a DC abnormal hollow cathode discharge. We have failed to clarify between the physical mechanisms of the cathode sheath and ambipolar flow that likely govern diverging ion transport in low pressure or abnormal hollow cathode discharges. In doing so, however, we have provided important knowledge pertaining to the diagnostic methods that can be used to analyse them. More work is needed to reveal the full array of possible uses of the low pressure hollow cathode discharge, some of which will be outlined below. But, by studying their relevance to improving the efficiency of portable neutron generation systems, we have hopefully shown one of the many ways in which the low pressure hollow cathode discharge has been under-utilised.

6.1 Further work

The most obvious outstanding issue from this thesis is that the interior of a solid hollow cathode that is exhibiting the ion divergence phenomena in discharge conditions similar to those used in an IEC device was never directly observed. This could be rectified in two easier modifications of the experiments attempted in Chapter 3, or by the proposal of an entirely new experimental method. First, an optical system could be developed using lenses with different focal lengths such that the hollow cathode interior could be viewed in the multipole system without negative magnification effects. This will always remain difficult if S_1 is large, as was forced by the multipole chamber and hollow cathode support systems. Otherwise, keeping the current system identical, more amenable cathode geometries could be tested. It was for this reason that two cathodes have been designed, manufactured, and sent to Dr. Nicolas Claire at Aix-Marseille université where the LIF diagnostic is accessible. This included: a spherical gridded cathode arranged such that the laser beam could pass unobstructed through the cathode interior and be viewed with the radial optical arrangement, given in Figure 6.1a); and a 'square' cylindrical hollow cathode of an equal inner diameter and length of 2 cm, given in Figure 6.1b). The gridded cathode interior could be observed directly at cathode biases of $V_c \leq -1$ kV to observe if the metastable ion population predominantly diverges. The square hollow cathode will be in turn more likely to exhibit ion divergence that could be observed using the radial optical array if divergence indeed occurs. This may be the case given the lesser distance that ions would have to travel along the central axis of the cathode before reaching a position that could be viewed
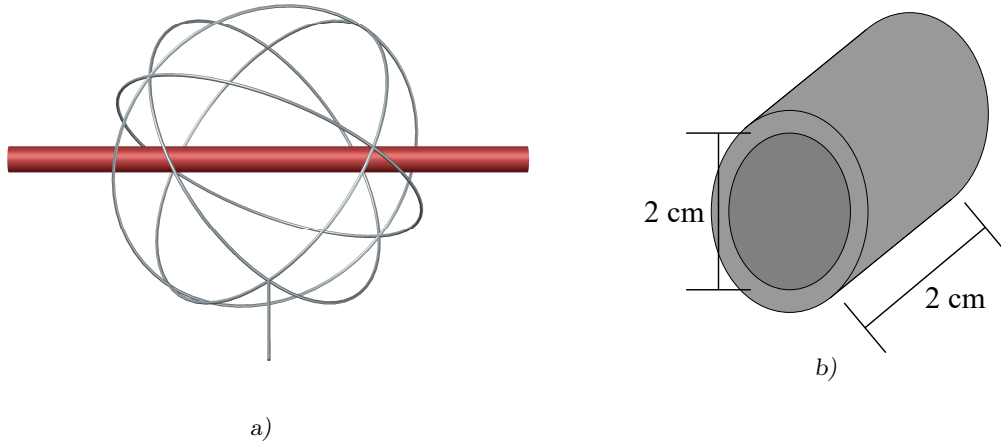
FIGURE 6.1 – *a)*: The spherical grid cathode as would be viewed by the optical array given in Figure 3.4 in the same system as used in Chapter 3. The path of the red laser beam used to pump the ArII 3d′ ^{2}G$_{9/2}$ state has been shown. *b)*: The square hollow cathode.

radially. However, it was discussed in Chapter 3.5.1 that it may not be possible to observe distinct IVDFs in regions of very high electric field due to the spreading of the fluorescence signal over a large range of ion velocities. This would make the proposed experiments less likely to succeed. Preliminary testing by Dr Claire (a supervisor of the author's candidature) has indeed shown that it is difficult to register an IVDF signal with appreciable signal-to-noise at all in the spherical gridded cathode. Furthermore, whatever observations that can be made of the ArII 3d′ ^{2}G$_{9/2}$ state near to or within a hollow cathode will have an unknown relationship to the ionic ground state. A tune-able UV laser would resolve this issue by being able to pump the ArII ground state directly, but is not currently feasible given the resources available to the author's research groups.

It is difficult to conceptualise other non-perturbative diagnostic methods offering high spatial resolution that could distinguish the relative densities of converging and diverging ion populations inside of a hollow cathode. It may be enlightening to perform a spectroscopic analysis of a high voltage hollow cathode discharge in a continuously pumped ultra high vacuum in which argon gas is inlet into the cathode interior alone. This is similar to the electrostatic charge-exchange satellite thruster system [6], which makes use of a diverging ion population that undergoes charge exchange with the background gas to emit diverging neutrals from a hollow cathode to provide thrust. In this way, it might be possible to isolate the internal discharge mechanics of the hollow cathode even for line of sight integrated spectroscopic methods. Otherwise, the possible influence of ambipolar diffusion and/or drift as well as a cathodic sheath on the creation of a virtual anode in a low pressure hollow cathode might best be addressed analytically. It may be possible to form a well-posed partial differential equation of the fluid aspects of a hollow cathode discharge in cylindrical co-ordinates that captures ambipolar flow. One would need to add

the ambipolar drift and diffusion terms included in Equation 1.15 with Poisson's and Maxwell's equations given in Equations 1.25 to 1.31 to couple the equations for electrons and ions given by a reduced form of Boltzmann's equation 1.26. If a unique solution to this problem could be found, it may better reveal whether a virtual anode could be a natural consequence of ambipolar dynamics that arise as a result of the hollow cathode effect. This could be used to predict the most efficient hollow cathode geometries for creating a maximum magnitude of virtual anode and therefore the nuclear fusion efficiency of a device.

Otherwise, further development into a hybrid fluid/MC computational code that solves a rate equation for all discharge species simultaneously analogous to that developed by Bogaerts *et al.* [153] may be better able to resolve the outstanding issues from Chapters 2, 3, and 5. First, the combination of a fluid treatment able to capture local discharge effects like the development of space charge with the kinetic treatment of ionisation by non-local pendular electrons may be able to reproduce the development of a virtual anode in various hollow cathode geometries. Second, such a model could include the effects of both having a non-planar system geometry as well as a primary electron population on the collisional rate equation for the ArII 3d′ ^{2}G$_{9/2}$ state that was solved in Chapter 5. This could be developed in tandem with an experiment analogous to that performed in Chapter 3 in conjunction with a Langmuir probe analysis such that greater detail of the discharge parameters are known to guide the computation. Experiments could be performed with various cathode geometries as well as with materials with varying $\lambda_{e,i}$ in order to isolate the relevance of a secondary electron population in a filament mediated multipole discharge.

Furthermore, the analysis of the $r_{m/g}$ relationship could be significantly improved if the VDF of the ArII 3d′ ^{2}G$_{9/2}$ state could be computationally determined rather than assumed or neglected, as was the case in Chapter 5. This might resolve the influence of quenching mechanisms on the proportionality of $r_{m/g}$ throughout velocity space for a single measurement location. A Monte-Carlo differential scattering analysis of the collisional rate equation with the aim of resolving the development of an ionisation and bulk peak of the IVDF (see Chapter 3.5) within the pre-sheath was begun but not completed by the time of thesis submission. The initial results from this analysis indicated that this would be a viable method for reproducing the anomalous ion density phenomenon, however, the results were not robust enough to be included here.

Finally, the Langmuir probe experiments given in Chapter 4 included a hot electron population with a surprisingly high drift velocity. It could not be conclusively determined that the drifting Maxwellian hot electron population arose by secondary electron emission from the plate, and

primary electrons emitted from the filaments presented a possible obfuscating issue. The Langmuir probe experiments could therefore be improved in a number of ways, some of which were also suggested by a referee of Reference [339]:

- A shielded planar Langmuir probe could possibly be used to isolate the true direction of the drift velocity of a given population. This would increase the confidence that the source of drifting Maxwellian electrons originates from the floating plate.

- Floating plates of different $\gamma_{e,i}$ could be compared in otherwise identical discharge conditions. If the energetic electron density $n_{e,h}$ was then observed to correspond to $\gamma_{e,i}$, this would be further evidence that they arose by secondary electron emission.

- Control experiments without the floating plate could be performed to determine the influence of the primary electron population emitted from the filaments. This would be much easier to isolate if present without the influence of a secondary electron population.

- The same experiment could be performed in a multipole system at 0.1 mTorr with -50 V applied to the thermionic filaments since an isotropic mono-energetic electron population may be relatively easy to isolate from a drifting Maxwellian population in an $i - V$ curve using the Bayesian method. This is in comparison to having a possible primary electron population of unknown distribution present in the experimental $i - V$ curves.

Option 3 was attempted in the Langmuir probe analysis of Chapter 4 but unfortunately before a rigorous Langmuir probe cleaning routine was implemented. As such, almost all of the measured $i - V$ curves exhibited a discontinuity characteristic of a dirty Langmuir probe. The experimental system had begun to be adapted for another researcher's use before this issue was noticed.

Finally, the full benefit of the improved nuclear fusion rate by using hollow cathodes of various geometries instead of gridded cathodes discussed in Chapter 2 was never fully investigated. It may be possible that the correct choice of cathode geometry and material would be able to push the nuclear fusion reaction rate to useful levels for neutron activation analysis. Such a device could be of extremely high value to both modern research and in industry. Given a dramatic increase in both time and monetary investment, the author would investigate the use of liquid-cooled hollow cathode geometries operated at as high discharge powers as possible using deuterium fuel. This would necessarily require expensive power supply systems as well as the secure shielding of the experimental laboratory to protect the surroundings from the intense neutron and electromagnetic radiation likely to be generated. The success of this type of investigation would also incidentally be the most convincing form of evidence for the IEC community of the ion divergence and hollow cathode hypotheses presented in this thesis.

Appendix A

Bayesian Analysis code

This code is a short summary of the key features of the total analysis routine used in Chapter 4, including the Bayesian algorithm. Many of the smaller steps of the code are not included since these only involved the simple application of mathematics, digital smoothing algorithms, data cleaning, and rectification that could likely be done better and more efficiently by a professional coder. Combined together, all of the protocols used to analyse and test the data totalled to more than 5000 lines of code, which are available upon request from the author (also at neranson@gmail.com). An ellipses ($\cdots$) indicates further, repetitive code similar to that which proceeded the ellipses.

```
1  ############################################################################
2  # DECLARING IMPORTANT VARIABLES
3  ############################################################################
4
5  #IMPORTANT CONSTANTS
6  m_Ar = 6.6335e-26 #Argon ion mass, kg
7
8  #EXPERIMENTAL VALUES
9  dwell_time = 1 #Time per voltage step, ms
10 exp_max_voltage = 120 #Maximum probe voltage, V
11 exp_min_voltage = -120 #Minimum probe voltage, V
12 resistor_val = 100.7e3 #Used to calibrate probe currnt, Ohm
13 extractor_voltage = -200 #Electron gun voltage, V
14 probe_radius = 25.0e-6 #m
15 probe_length = 15.0e-3 #m
16
17 #PROBE DRIVER INTERNAL RESISTANCe VALUES
18 current_per_volt = 1.0e-3 #A
19 voltage_per_volt = 100.0 #V
20
21 #DIGITAL SMOOTHING PARAMETERS
22 polynomial_order = 2 #For SG filter. must be less than window length
```

```
23 window_length = 31 #For SG filter, must be odd.
24 notch_Q_factor = 10.0 #Notch filter quality factor. Data distorted too
       significantly.
25
26 ##############################################################################
27 # CHECKING BACKGROUND DATASETS, HYSTERESIS, VISUAL INSPECTION OF DATA,
       CALIBRATION.
28 ##############################################################################
29
30 # CHECK EXPERIMENTS IN SAME LOCATION FOR LEVEL OF SIMILARITY, THEN AVERAGE
       TOGETHER
31 time_data, ... =
       compare_experiments_in_same_location_and_average_together_4_channels(
32 experiment_path,...)
33
34 # SUBTRACTING AVERAGED BACKGROUND CHARACTERISTIC AFTER ENSURING CONSISTENCY.
35 background_time, background_current =
       produce_background_characteristic_4_channels(experiment_path, 'plot',
       smooth_background='all filters', window_size=100, window_length=101,
         polynomial_order=2, notch_freq=50, quality_factor=100.0, check_overlap='n'
       )
36
37 whole_current, ... = subtract_background_characteristic(background_time, ...)
38
39 #CHECK FOR HYSTERESIS
40 check_for_hysteresis(time_data, ..., 'auto', tol_percent_of_maximum=0.1)
41
42 # ADJUST VOLTAGE STAIRCASE DATA TO TRUE EXPERIMENTAL VOLTAGE AND FIT STRAIGHT
       LINE TO IT.
43 time_data,... = correct_voltage_data_and_remove_staircase_aspect_4_channels(
       time_data, ...)
44
45 # ADJUST CURRENT DATA TO THE TRUE VALUE USING VOLTAGE SWEEP ACROSS KNOWN
       RESISTOR.
46 whole_current, ... = calibrate_current(... resistor_val, current_per_volt,
       voltage_per_volt)
47
48 #SUBTACTING SPURIOUS BASELINE CURRENT FROM OSCILLOSCOPE DATA
49 zero_whole_current, ... = set_baseline_to_zero_4_channels(time_data, ...)
50
51 ##############################################################################
52 # DETERMINING PLASMA POTENTIAL, BULK ELECTRON PARAMETERS
53 ##############################################################################
54
55 #INITIAL MOVING WINDOW FILTER AS SIMPLE AVERAGING METHOD.
56 s_time_data,... = moving_window_cleaner(
57     time_data, ..., window_size=6, mode='same', clip_ends='y')
58
```

```
59  #USING SG FILTER TO CALCULATE 2ND DERIVATIVE AND DETERMINE PLASMA POTENTIAL.
60  SG_current = savgol_filter(zero_whole_current_ramp, window_length=window_length,
        polyorder=polynomial_order, deriv=0, mode='interp')
61  SG_current_1st = ...
62
63  #USING INTERSECTING SLOPES METHOD TO GET PLASMA POTENTIAL, BULK ELECTRON TEMP.
        DONE AGAINST LOGARITHMIG DATA.
64  T_e_eV_slopes, V_p_slopes, ... = intersecting_line_method_for_V_p_4_channels(
        whole_current_ramp, ... line_fits='user_select_points', ...)
65
66  ############################################################################
67  # INITIAL ESTIMATION OF ION, HOT ELECTRON PROPERTIES BY REGRESSION METHODS.
68  ############################################################################
69
70  #SELECT REGION TO ANALYSE FOR ION CURRENT.
71  ion_voltage, = choose_ion_current_analysis_region(..., selection_method='
        user_select')
72
73  #FIT LAFRAMBOISE'S MODEL WITH CHOSEN PARAMETERS TO SELECTED ION CURRENT.
74  ion_current, ... = fit_to_ion_current(ion_current, ... model_type='laframboise
        sqrt', current_offset='y', T_e_bounds=[0.1,4], n_i_bounds=[1e14,1e16],
        use_p0='n')
75  #EXAMPLE OF FITTING FUNCTION USED
76  [def laframboise_radial_ion_theory(x, A, D):
77      return A * D * np.sqrt(x) ]
78
79  #SUBTRACTING ION CURRENT TO ESTIMATE ELECTRON CURRENTS, BEGINNING ITERATIVE
        SCHEME.
80  electron_current, values_dic = subtract_ion_current(ion_current, ...)
81
82  #FITTING ELECTRON DATA USING REGRESSION METHOD. BULK ELECTRON DENSITY DETERMINED
         THIS WAY. CAN FIT SECONDARY ELECTRON CURRENT SIMULTANEOUSLY.
83  values_dic = fit_electron_data_11_2021(electron_current, ..., T_e_bounds
        =[0.25,5], T_e_0=values_dic['T_e_eV_slopes'], T_eh_0 = 40, n_ec_bounds=[1e14
        ,1e16], T_eh_bounds = [3,100], n_eh_bounds= [1e10, 1e13], V_p_0=0, n_eh_0=1
        e11, V_p_bounds=[-10, 10], fit_secondary_current='y')
84  #EXAMPLE OF SOME OF FITTING PROCEDURE WITHIN ELECTRON CURRENT FITTING FUNCTION
85      fit_bounds_c, fit_p0_c = electron_fit_bounds_11_2021(...) #BULK ELECTRON
        FITTING PARAMETERS
86      fit_bounds_h, fit_p0_h = electron_fit_bounds_11_2021(...) #HOT ELECTRON
        FITTING PARAMETERS
87      #AN EXAMPLE OF ATTEMPTING TO FIT A DOUBLE MAXWELLIAN CURRENT TO THE ELECTRON
         DATA.
88          e_fit_params, variances = curve_fit(
        curve_fit_langmuir_double_maxwellian_integral, voltage, electron_current,
        bounds=fit_bounds, p0=fit_p0, maxfev=int(1e9))
89
```

```
 90          #EXAMPLE OF DOUBLE MAXWELLIAN FITTING FUNCTIONS USING THE INTEG.QUAD
        METHOD.
 91          def curve_fit_langmuir_double_maxwellian_integral(V, A_1, B_1, A_2, B_2,
         V_p):
 92              return [integ.quad(langmuir_maxwellian_integral, np.sqrt(abs(2 *
        const.e * (x - V_p) / const.m_e)) if x <= V_p else 0,
 93              1e8, args=(A_1, B_1, x, V_p))[0] + Integ.quad(
        langmuir_maxwellian_integral,
 94              np.sqrt(abs(2 * const.e * (x - V_p) / const.m_e)) if x <= V_p else
        0, 1e8, args=(A_2, B_2, x, V_p))[0] for x in V]
 95          def drifting_maxwellian_integral(theta, U, T_e, n_e, u_0, r_p, l_p, V):
 96              A = 2 * r_p * l_p * n_e * const.e
 97              A_exp = const.m_e / (2*const.k * T_e)
 98              return A * U * np.sqrt(U**2 + 2 * const.e * V / const.m_e) * (A_exp/
        np.pi) * np.exp(-A_exp*(U**2 + u_0**2 + 2*u_0*U*np.cos(theta)))
 99
100 #OPTION OF SUBTRACTING BULK ELECTRON CURRENT FROM INDIVIDUAL FIT TO FIND HOT
        ELECTRON CURRENT, AND CONTINUE ITERATIVE PROCEDURE
101 secondary_current = subtract_bulk_electron_current(..., compare_2ndry_to_fitted=
        'y')
102
103 #OVERLAYING THE IDEAL CHARACTERISTIC FORMED BY THE DETERMINED ELECTRON
        PARAMETERS AGAINST THE DATA FOR VISUAL INSPECTION.
104 values_dic = compare_characteristic_to_ideal(...)
105
106 repeat_analysis = user_check('\nWould you like to re-analyse the value fitting
        procedures? y/n: ')
107 while repeat_analysis == 'y':
108     ...
109
110 ##########################################################################
111 # BAYESIAN SCANNING ROUTINE.
112 ##########################################################################
113
114 #DETERMINING THE MEAN AND GLOBAL VARIANCE OF THE BACKGROUND DATA.
115 Bayes_mean, Bayes_std, Bayes_variance = mean_std_var_from_start_of_dataset(
        zero_whole_current)
116
117 #THE BAYESIAN SCANNING ROUTINE, WITH OPTIONS TO UPDATE THE SCAN PARAMETERS ON
        THE SAME INITIAL DATA.
118 values_dic = bayesian_scan_over_ideal_characterstic_inputs_faster_method(...,
        likelihood_threshold=0.95, use_log_probs = 'n', exclude_outliers='n')
119
120 def bayesian_scan_over_ideal_characterstic_inputs_faster_method(...,
        likelihood_threshold = 0.95, use_log_probs = 'n', exclude_outliers = 'n',
        scale_prob_value = 'y', compare_beyond_V_p = 'n'):
121     while True:
```

```
122        print('\nInput the variables that you would like to scan over. Type
      names in full with spaces between.')
123        while True: #INPUT PARAMETER SET TO SCAN
124            variables_to_scan = input('select from \n(n_eh | n_i | T_eh | u_D |
      V_p | all): ')
125            ...
126        # SET SCANNING PARAMETER BOUNDS AND NUMBER OF STEPS
127        if 'n_eh' in variables_to_scan or 'all' in variables_to_scan:
128            n_eh_lb = input_loop_until_correct_value_given(input_message='Input
      the n_eh scanning range lower bound: ')
129            n_eh_ub = input_loop_until_correct_value_given(input_message='Input
      the n_eh scanning range upper bound: ')
130            n_eh_steps = input_loop_until_correct_value_given(variable_type=int,
       input_message='Input the number of scanning steps for n_eh:')
131        if 'n_i' in variables_to_scan or 'all' in variables_to_scan:
132            ...
133
134        n_eh_vals = np.linspace(n_eh_lb, n_eh_ub, n_eh_steps) if 'n_eh' in
      variables_to_scan or 'all' in variables_to_scan else [values_dic['n_eh']]
135        n_i_vals = ...
136
137        V_p_cutoff = find_nearest_index_in_array(raw_voltage, values_dic['V_p'])
       #STOPPING CALCULATION AT PLASMA POTENTIAL
138        scan_voltage = raw_voltage[:V_p_cutoff] if compare_beyond_V_p == 'n'
      else raw_voltage
139        scan_current = raw_current[:V_p_cutoff] if compare_beyond_V_p == 'n'
      else raw_current
140        n, p, total_scan_array_length, n_eh_dic = 0, 0, len(n_eh_vals) * len(
      n_i_vals) * len(T_eh_ev_vals) * len(u_D_ev_vals), {}
141        for n_eh_val in n_eh_vals:
142            print('Calculating values for n_eh = {:.2e}'.format(n_eh_val))
143            T_eh_ev_dic, n_eh_start_timer, t = {}, timeit.default_timer(), 0
144            for T_eh_ev_val in T_eh_ev_vals:
145                u_D_ev_dic, T_eh_start_timer = {}, timeit.default_timer()
146                for u_D_ev_val in u_D_ev_vals:
147                    n_i_dic = {}
148                    for n_i_val in n_i_vals:
149                        if n_i_round == 0: #CREATE IDEAL CHARACTERISTIC FROM SET
       OF INPUT PARAMETERS AND CHOSEN MODEL
150                            ideal_current, ... =
      create_ideal_characteristic_drifting_secondary(
151                                ...)
152                        else: ...
153                        #CALCULATE THE PROBABILITY PRODUCT FROM DIFFERENCE
      BETWEEN PREDICTED AND EXPERIMENTAL CURRENT AT ALLL VOLTAGES.
154                        total_probability_density =
      total_combined_probability_density(scan_current, ...)
155                            ...
```

```
156        #AT ITS HEART, THE PROBABILITY DENSITY CALCULATION INVOLVES THE
      FOLLOWING FUNCTION
157        def probability_density_of_result(value, standard_dev, mean,
      scale_prob_value='n', return_log='n'):
158            front_value = 1.0 / (np.sqrt(2 * np.pi) * standard_dev) if
      scale_prob_value == 'n' else 1.0
159            if return_log == 'y':
160                return np.log10(front_value) + -(1.0 / (2.0 * standard_dev ** 2)
      ) * (value - mean) ** 2
161            else:
162                return front_value * np.exp(-(1.0 / (2.0 * standard_dev ** 2)) *
       (value - mean) ** 2)
163
164        #NORMALISE THE PROBABILITY DENSITIES FOR ALL POSSIBLE PARAMETER
      COMBINATIONS
165        final_dic = divide_dic_entries_by_val(final_dic, sum_of_entries=True)
166
167        #ACCUMULATE PROBABILITY VALUES STARTING FROM MOST LIKELY AND
      CONTINUINING UNTIL THRESHOLD MET (95 %)
168        likelihood_dic, total_probability_range =
      sum_max_values_in_dic_until_threshold_reached(final_dic, val=
      likelihood_threshold, return_sum=True)
169        ...
170    return values_dic, likelihood_dic
```

LISTING A.1 – Analysis code for Chapter 4

Bibliography

[1]   F. Paschen. "Bohrs Heliumlinien". In: *Annalen der Physik* 355.16 (1916), pp. 901–940. DOI: 10.1002/andp.19163551603.

[2]   A. Walsh. "The application of atomic absorption spectra to chemical analysis". In: *Spectrochimica Acta* 7 (1955), pp. 108–117. DOI: 10.1016/0371-1951(55)80013-6.

[3]   R. R. Arslanbekov, A. A. Kudryavtsev, and R. C. Tobin. "On the hollow-cathode effect: conventional and modified geometry". In: *Plasma Sources Science and Technology* 7.3 (1998), pp. 310–322. DOI: 10.1088/0963-0252/7/3/009.

[4]   V. I. Kolobov and A. S. Metel. "Glow discharges with electrostatic confinement of fast electrons". In: *Journal of Physics D: Applied Physics* 48.23 (2015), p. 233001. DOI: 10.1088/0022-3727/48/23/233001.

[5]   S. Mazouffre. "Electric propulsion for satellites and spacecraft: established technologies and novel approaches". In: *Plasma Sources Science and Technology* 25.3 (2016), p. 033002. DOI: 10.1088/0963-0252/25/3/033002.

[6]   L. Blackhall and J. Khachan. "A simple electric thruster based on ion charge exchange". In: *Journal of Physics D: Applied Physics* 40.8 (2007), pp. 2491–2494. DOI: 10.1088/0022-3727/40/8/011.

[7]   G. H. Miley. *Inertial electrostatic confinement (IEC) fusion : fundamentals and applications*. eng. EBL. Dordrecht: Springer, 2013.

[8]   O. A. Lavrent'ev. In: *Ukrainskii Fizicheskii Zhurnal* 8 (1963), p. 440.

[9]   P.T. Farnsworth. "Electric discharge device for producing interactions between nuclei". In: (1966). US Patent 3,258,402. URL: http://www.google.com/patents/US3258402.

[10] G. H. Miley, J. Javedani, Y. Yamamoto, R. Nebel, J. Nadler, Y. Gu, A. Satsangi, and P/ Heck. "Inertial-Electrostatic Confinement Neutron-Proton Source". In: *Dense Z-Pinches: Third International Conference*. Ed. by M. Haines and A. Knight. AIP Conference Proceedings 299. 1994, pp. 675–689.

[11] F. F. Chen. *Introduction to Plasma Physics and Controlled Fusion*. 2nd. Vol. 1. New York: Plenum Press, 1984.

[12] Y. P. Razier. *Gas discharge physics*. 1st. Vol. 1. Berlin, Heidelberg: Springer-Verlag, 1991.

[13] E. W. McDaniel. *Collision phenomena in ionized gases*. 1st. Vol. 1. New York: John Wiley & sons Inc., 1964.

[14]   J. Huba. "NRL: Plasma Formulary". In: (2004), p. 73.

[15]   F. F. Chen. "Introduction to Plasma Physics and Controlled Fusion". In: 2nd. Vol. 1. New York: Plenum Press, 1984. Chap. 2,3.

[16]   I. H Hutchinson. "Principles of plasma diagnostics". In: 2nd. Cambridge: Cambridge University Press, 2002. Chap. 20.

[17]   Y. P. Razier. "Gas discharge physics". In: 1st. Vol. 1. Berlin, Heidelberg: Springer-Verlag, 1991. Chap. 3,8.

[18]   P. F. Little and A. Von Engel. "The hollow-cathode effect and the theory of glow discharges". In: *Proceedings of the Royal Society of London. A. Mathematical and Physical Sciences* 224.1157 (1954), pp. 209–227. DOI: 10.1098/rspa.1954.0152.

[19]   K. U. Riemann. "The Bohm criterion and sheath formation". In: *Journal of Physics D: Applied Physics* 24.4 (1991), pp. 493–518. DOI: 10.1088/0022-3727/24/4/001.

[20]   A. V. Phelps. "Abnormal glow discharges in Ar: experiments and models". In: *Plasma Sources Science and Technology* 10.2 (2001), pp. 329–343. DOI: 10.1088/0963-0252/10/2/323.

[21]   A Bogaerts, E Neyts, R Gijbels, and J van der Mullen. "Gas discharge plasmas and their applications". In: *Spectrochimica Acta Part B - ATomic Spectroscopy* 57.4 (2002), pp. 609–658. DOI: 10.1016/S0584-8547(01)00406-2.

[22]   A. L. Yerokhin, X. Nie, A. Leyland, A. Matthews, and S. J. Dowey. "Plasma electrolysis for surface engineering". In: *Surface & Coatings Technology* 122.2-3 (1999), pp. 73–93. DOI: 10.1016/S0257-8972(99)00441-7.

[23]   A.J. Demaria. "Review of CW high-power CO2lasers". In: *Proceedings of the IEEE* 61.6 (1973), pp. 731–748. DOI: 10.1109/proc.1973.9153.

[24]   K. L. Choy. "Chemical vapour deposition of coatings". In: *Progress in Materials Science* 48.2 (2003), pp. 57–170. DOI: 10.1016/S0079-6425(01)00009-3.

[25]   M. A. Lieberman and A. J. Lichtenberg. "Principles of Plasma Discharges and Materials Processing, 2nd Edition". In: 2005, pp. 1–757.

[26]   P. K. Chu, S. Qin, C. Chan, N. W. Cheung, and L. A. Larson. "Plasma immersion ion implantation - A fledgling technique for semiconductor processing". In: *Materials Science & Engineering R-Reports* 17.6-7 (1996), pp. 207–280. DOI: 10.1016/S0927-796X(96)00194-5.

[27]   U. Kogelschatz. "Dielectric-barrier discharges: their history, discharge physics, and industrial applications". In: *Plasma Chemistry and Plasma Processing* 23.1 (2003), pp. 1–46. DOI: 10.1023/a:1022470901385.

[28]   G. Fridman, G. Friedman, A. Gutsol, A. B. Shekhter, V. N. Vasilets, and A. Fridman. "Applied Plasma Medicine". In: *Plasma Processes and Polymers* 5.6 (2008), pp. 503–533. DOI: 10.1002/ppap.200700154.

[29]   M. G. Kong, G. Kroesen, G. Morfill, T. Nosenko, T. Shimizu, J. van Dijk, and J. L. Zimmermann. "Plasma medicine: an introductory review". In: *New Journal of Physics* 11 (2009). DOI: 10.1088/1367-2630/11/11/115012.

[30]   E. W. McDaniel. "Collision phenomena in ionized gases". In: 1st. Vol. 1. New York: John Wiley & sons Inc., 1964. Chap. 1,2.

[31]   J. R. Taylor. *Scattering Theory: The quantum theory of nonrelatavistic collisions*. 1st ed. Vol. 1. John Wiley & sons, Inc., 1972.

[32]   US Department of Commerce. *National Institute of Standards and Technology*. May 2023. URL: https://www.nist.gov/.

[33]   A. V. Phelps. "Cross Sections and Swarm Coefficients for H+, H2+, H3+, H, H2, and H- in H2 for Energies from 0.1 eV to 10 keV". In: *Journal of Physical and Chemical Reference Data* 19.3 (1990), pp. 653–675. DOI: 10.1063/1.555858.

[34]   A. V. Phelps. "Cross Sections and Swarm Coefficients for Nitrogen Ions and Neutrals in N2 and Argon Ions and Neutrals in Ar for Energies from 0.1 eV to 10 keV". In: *Journal of Physical and Chemical Reference Data* 20.3 (1991), pp. 557–573. DOI: 10.1063/1.555889.

[35]   J.L. Delcroix. *Plasma Physics: Weakly Ionized Gases*. Vol. 2. John Wiley & Sons LTD., 1968, pp. 10–13.

[36]   F. F. Chen. "Introduction to Plasma Physics and Controlled Fusion". In: 2nd. Vol. 1. New York: Plenum Press, 1984. Chap. 5-7.

[37]   Z. Lj. Petrovic et al. "Measurement and interpretation of swarm parameters and their application in plasma modelling". In: *Journal of Physics D - Applied Physics* 42.19 (2009). DOI: 10.1088/0022-3727/42/19/194002.

[38]   S. Dujko, R. D. White, K. F. Ness, Z. Lj. Petrović, and R. E. Robson. "Non-conservative electron transport in CF4in electric and magnetic fields crossed at arbitrary angles". In: *Journal of Physics D: Applied Physics* 39.22 (2006), pp. 4788–4798. DOI: 10.1088/0022-3727/39/22/009.

[39]   Y. Fu and J. P. Verboncoeur. "On the Similarities of Low-Temperature Plasma Discharges". In: *IEEE Transactions on Plasma Science* 47.5 (2019), pp. 1994–2003. DOI: 10.1109/tps.2018.2886444.

[40]   A. L. Ward. "Calculations of Cathode-Fall Characteristics". In: *Journal of Applied Physics* 33.9 (1962), pp. 2789–2794. DOI: 10.1063/1.1702550.

[41]   J. H. Parker and J. J. Lowke. "Theory of Electron Diffusion Parallel to Electric Fields .1. Theory". In: *Physical Review* 181.1 (1969), pp. 290–&. DOI: 10.1103/PhysRev.181.290.

[42]   J. J. Lowke and J. H. Parker. "Theory of Electron Diffusion Parallel to Electric Fields .2. Application to Real Gases". In: *Physical Review* 181.1 (1969), p. 302. DOI: 10.1103/PhysRev.181.302.

[43]   Y. P. Raĭzer. "Gas discharge physics". eng. In: Berlin: Springer-Verlag, 1991. Chap. 2.

[44]   A.V. Phelps. "The diffusion of charged particles in collisional plasmas: Free and ambipolar diffusion at low and moderate pressures". In: *Journal of Research of the National Institute of Standards and Technology* 95.4 (1990), p. 407. DOI: 10.6028/jres.095.035.

[45]   H. Bethe, W. Heitler, and P. A. M. Dirac. "On the stopping of fast particles and on the creation of positive electrons". In: *Proceedings of the Royal Society of London. Series A, Containing Papers of a Mathematical and Physical Character* 146.856 (1934), pp. 83–112. DOI: 10.1098/rspa.1934.0140.

[46]   Y. P. Raĭzer. "Gas discharge physics". eng. In: Berlin: Springer-Verlag, 1991. Chap. 9.

[47]   E. W. McDaniel. "Collision phenomena in ionized gases". In: 1st. Vol. 1. New York: John Wiley & sons Inc., 1964. Chap. 11.

[48] R. W. Crompton and R. L. Jory. "On the Swarm Method for Determining the Ratio of Electron Drift Velocity to Diffusion Coefficient". In: *Australian Journal of Physics* 15.4 (1962), p. 451. DOI: 10.1071/ph620451.

[49] L. J. Varnerin and S. C. Brown. "Microwave Determinations of Average Electron Energies and the 1st Townsend Coefficient in Hydrogen". In: *Physical Review* 79.6 (1950), pp. 946–951. DOI: 10.1103/PhysRev.79.946.

[50] G. S. Hurst, J. A. Stockdale, L. B. Okelly, and E. B. Wagner. "Time-of-flight Investigations of Electron Transport in Gases". In: *Journal of Chemical Physics* 39.5 (1963), pp. 1341–&. DOI: 10.1063/1.1734438.

[51] J. S. Townsend and V. A. Bailey. "XCVII. The motion of electrons in gases". In: *The London, Edinburgh, and Dublin Philosophical Magazine and Journal of Science* 42.252 (1921), pp. 873–891. DOI: 10.1080/14786442108633831.

[52] L.G.H. Huxley and R.W. Crompton. "The Motions of Slow Electrons in Gases". In: *Pure and Applied Physics*. Vol. 13. 1962. Chap. 10, pp. 335–373.

[53] E. W. McDaniel. "Collision phenomena in ionized gases". In: 1st. Vol. 1. New York: John Wiley & sons Inc., 1964. Chap. 9.

[54] J. A. Hornbeck. "The Drift Velocities of Molecular and Atomic Ions in Helium, Neon, and Argon". In: *Physical Review* 84.4 (1951), pp. 615–620. DOI: 10.1103/physrev.84.615.

[55] E. Basurto, J. De Urquijo, I. Alvarez, and C. Cisneros. "Mobility of He^+, Ne^+, Ar^+, N_2^+, O_2^+, and CO_2^+ in their parent gas". In: *Physical Review E* 61.3 (2000), pp. 3053–3057. DOI: 10.1103/physreve.61.3053.

[56] M. V. V. S. Rao, R. J. Van Brunt, and J. K. Olthoff. "Resonant charge exchange and the transport of ions at high electric-field to gas-density ratios (E/N) in argon, neon, and helium". In: *Physical Review E* 54.5 (1996), pp. 5641–5656. DOI: 10.1103/physreve.54.5641.

[57] J. Dashdorj, W. C. Pfalzgraff, A. Trout, D. Fingerlow, M. Cordier, and L. A. Viehland. "Determination of mobility and diffusion coefficients of Ar^+ and Ar^{2+} ions in argon gas". In: *International Journal for Ion Mobility Spectrometry* 23.2 (2020), pp. 143–151. DOI: 10.1007/s12127-020-00258-z.

[58] M.. F. Hoyaux. "Some Remarks Concerning the Phenomenon of Ambipolar Diffusion in Gaseous Discharges". In: *American Journal of Physics* 35.3 (1967), pp. 232–242. DOI: 10.1119/1.1974015.

[59] N. Hershkowitz, F. Ze, and H. Kozima. "Negative plasma potentials produced by supplemental electron emission". In: *Physics of Fluids* 22.2 (1979), p. 338. DOI: 10.1063/1.862585.

[60] L. Oksuz and N. Hershkowitz. "Negative plasma potential in unmagnetized DC electropositive plasma with conducting walls". In: *Physics Letters A* 375.22 (2011), pp. 2162–2165. DOI: https://doi.org/10.1016/j.physleta.2011.04.036.

[61] R. N. Franklin. "The plasma-wall boundary region in negative-ion-dominated plasmas at low pressures". In: *Plasma Sources Science and Technology* 9.2 (2000), p. 191. DOI: 10.1088/0963-0252/9/2/312.

[62] A. M. Soroka and G. I. Shapiro. "The stimulated ambipolar diffusion under high frequency electric field". In: *Pisma V Zhurnal Tekhnicheskoi Fiziki* 5.3 (1979), pp. 129–132.

[63] V. I. Kolobov and L. D. Tsendin. "Analytic model of the cathode region of a short glow discharge in light gases". In: *Physical Review A* 46.12 (1992), pp. 7837–7852. DOI: 10.1103/physreva.46.7837.

[64] G. L. Rogoff. "Ambipolar diffusion coefficients for discharges in attaching gases". In: *Journal of Physics D: Applied Physics* 18.8 (1985), p. 1533. DOI: 10.1088/0022-3727/18/8/018.

[65] J. B. Thompson. "Negative Ions in the Positive Column of the Oxygen Discharge". In: *Proceedings of the Physical Society* 73.5 (1959), pp. 818–821. DOI: 10.1088/0370-1328/73/5/416.

[66] R. A. Gottscho, A. Mitchell, G. R. Scheller, Y-Y. Chan, and D. B. Graves. "Electric field reversals in dc negative glow discharges". In: *Physical Review A* 40.11 (1989), pp. 6407–6414. DOI: 10.1103/physreva.40.6407.

[67] G. Hairapetian and R. L. Stenzel. "Particle dynamics and current-free double layers in an expanding, collisionless, two-electron-population plasma". In: *Physics of Fluids B: Plasma Physics* 3.4 (1991), pp. 899–914. DOI: 10.1063/1.859847.

[68] V. A. Godyak and B. M. Alexandrovich. "Comparative analyses of plasma probe diagnostics techniques". In: *Journal of Applied Physics* 118.23 (2015), p. 233302. DOI: 10.1063/1.4937446.

[69] D. Xiao. "Fundamental Theory of Townsend Discharge". In: Energy and Environment Research in China, 2016, pp. 47–88. DOI: 10.1007/978-3-662-48041-0_3.

[70] H. Bruining. *Physics and applications of secondary electron emission.* eng. Pergamon science series. Electronics and waves. London: Pergamon Press, 1954.

[71] K. L Jensen. *Introduction to the physics of electron emission.* eng. 1st ed. Chichester, England: Wiley, 2017.

[72] E. W. McDaniel. "Collision phenomena in ionized gases". In: 1st. Vol. 1. New York: John Wiley & sons Inc., 1964. Chap. 13.

[73] A. V. Phelps and Z. Lj. Petrovic. "Cold-cathode discharges and breakdown in argon: surface and gas phase production of secondary electrons". In: *Plasma Sources Science and Technology* 8.3 (1999), R21–R44. DOI: 10.1088/0963-0252/8/3/201.

[74] E. M. Baroody. "A Theory of Secondary Electron Emission from Metals". In: *Physical Review* 78.6 (1950), pp. 780–787. DOI: 10.1103/physrev.78.780.

[75] W. D. Davis and T. A. Vanderslice. "Ion Energies at the Cathode of a Glow Discharge". In: *Physical Review* 131.1 (1963), pp. 219–228. DOI: 10.1103/physrev.131.219.

[76] A. V. Bondarenko. "Mass-Energy Ion Analysis in a Near-Cathode Region of Anomalous Glow Discharge". In: *Zhurnal Tekhnicheskoi Fiziki* 43.4 (1973), pp. 821–828.

[77] A. V. Bondarenko. "Mass-Energy Ion Analysis in a Near-Cathode Region of Anomalous Glow Discharge .3. Normal Discharge". In: *Zhurnal Tekhnicheskoi Fiziki* 45.2 (1975), pp. 308–313.

[78] H. D. Hagstrum. "Theory of Auger Ejection of Electrons from Metals by Ions". In: *Physical Review* 96.2 (1954), pp. 336–365. DOI: 10.1103/physrev.96.336.

[79] H. D. Hagstrum. "Effect of Monolayer Adsorption on the Ejection of Electrons from Metals by Ions". In: *Physical Review* 104.6 (1956), pp. 1516–1527. DOI: 10.1103/physrev.104.1516.

[80] A. L. Ward. "Effect of Space Charge in Cold-Cathode Gas Discharges". In: *Physical Review* 112.6 (1958), pp. 1852–1857. DOI: 10.1103/physrev.112.1852.

[81] I. Langmuir. "The Effect of Space Charge and Residual Gases on Thermionic Currents in High Vacuum". In: *Physical Review* 2.6 (1913), pp. 450–486. DOI: 10.1103/physrev.2.450.

[82] A. Von Engel. *Elektrische gasentladungen, ihre physik und technik*. ger. Vol. 2. Berlin: J. Springer, 1934.

[83] A. Von Engel. *Ionized gases*. eng. 2d ed. Oxford: Clarendon Press, 1965.

[84] F. Paschen. "Ueber die zum Funkenübergang in Luft, Wasserstoff und Kohlensäure bei verschiedenen Drucken erforderliche Potentialdifferenz". In: *Annalen der Physik* 273.5 (1889), pp. 69–96. DOI: 10.1002/andp.18892730505.

[85] M. J. Druyvesteyn and F. M. Penning. "The Mechanism of Electrical Discharges in Gases of Low Pressure". In: *Reviews of Modern Physics* 12.2 (1940), pp. 87–174. DOI: 10.1103/revmodphys.12.87.

[86] G. A. Mesyats. "Similarity laws for pulsed gas discharges". In: *Physics-Uspekhi* 49.10 (2006), pp. 1045–1065. DOI: 10.1070/PU2006v049n10ABEH006118.

[87] C. D. Child. "Discharge From Hot Cao". In: *Physical Review (Series I)* 32.5 (1911), pp. 492–511. DOI: 10.1103/physrevseriesi.32.492.

[88] A. Von-Engel and M. Steenbeck. *Elektrische Gasentladungen: Ihre Physik und Technik*. Springer Berlin, Heidelberg, 1932. DOI: https://doi.org/10.1007/978-3-662-25701-2.

[89] I. Langmuir. "The Interaction of Electron and Positive Ion Space Charges in Cathode Sheaths". In: *Physical Review* 33.6 (1929), pp. 954–989. DOI: 10.1103/physrev.33.954.

[90] V. A. Lisovskiy and S. D. Yakovin. "Experimental study of a low-pressure glow discharge in air in large-diameter discharge tubes: I. conditions for the normal regime of a glow discharge". In: *Plasma Physics Reports* 26.12 (2000), pp. 1066–1075. DOI: 10.1134/1.1331142.

[91] M.E. Pillow. "A critical review of spectral and related physical properties of the hollow cathode discharge". In: *Spectrochimica Acta Part B: Atomic Spectroscopy* 36.8 (1981), pp. 821–843. DOI: 10.1016/0584-8547(81)80064-x.

[92] M. S. Benilov. "The Child–Langmuir law and analytical theory of collisionless to collision-dominated sheaths". In: *Plasma Sources Science and Technology* 18.1 (2009), p. 014005. DOI: 10.1088/0963-0252/18/1/014005.

[93] V. A. Lisovskiy, V. A. Derevianko, and V. D. Yegorenkov. "The Child-Langmuir collision laws for the cathode sheath of glow discharge in nitrogen". In: *Vacuum* 103 (2014), pp. 49–56. DOI: 10.1016/j.vacuum.2013.12.008.

[94] V Orlinov and G. Mladenov. "Dependence of Cathode Sputtering Rate on Current in a glow discharge". In: *International Journal of Electronics* 27.1 (1969), pp. 65–&. DOI: 10.1080/00207216908900006.

[95] J.E. Allen. "The plasma–sheath boundary: its history and Langmuir's definition of the sheath edge". In: *Plasma Sources Science and Technology* 18.1 (2008), p. 014004. DOI: 10.1088/0963-0252/18/1/014004.

[96] R. J. Roth. "Industrial Plasma Engineering : Volume 2 - Applications to Nonthermal Plasma Processing". eng. In: *Industrial Plasma Engineering : Volume 2 - Applications to Nonthermal Plasma Processing*. First edition. London: Taylor and Francis, 2017. Chap. 3.

[97]   Y. Fu, J. P. Verboncoeur, A. J. Christlieb, and X. Wang. "Transition characteristics of low-pressure discharges in a hollow cathode". In: *Physics of Plasmas* 24.8 (2017), p. 083516. DOI: 10.1063/1.4997764.

[98]   M. J. Druyvesteyn. "Der Niedervoltbogen". In: *The European Physical Journal A* 64.11-12 (1930), pp. 781–798. DOI: 10.1007/bf01773007.

[99]   N. Hershkowitz. "How Langmuir Probes Work". In: *Plasma Diagnostics*. Ed. by O. Auciello and D. L. Flamm. 1st ed. Vol. 1. Academic Press, 1989. Chap. 3, pp. 113–184.

[100]   Z. Sternovsky and S. Robertson. "Langmuir probe interpretation for plasmas with secondary electrons from the wall". In: *Physics of Plasmas* 11.7 (2004), pp. 3610–3615. DOI: 10.1063/1.1760090.

[101]   M. Surendra, D. B. Graves, and G. M. Jellum. "Self-consistent model of a direct-current glow discharge: Treatment of fast electrons". In: *Physical Review A* 41.2 (1990), pp. 1112–1125. DOI: 10.1103/physreva.41.1112.

[102]   M. J. Goeckner, J. Goree, and T. E. Sheridan. "Measurements of ion velocity and density in the plasma sheath". In: *Physics of Fluids B: Plasma Physics* 4.6 (1992), pp. 1663–1670. DOI: 10.1063/1.860074.

[103]   N. Claire, S. Mazouffre, C. Rebont, and F. Doveil. "Examination of argon metastable atom velocity distribution function close to a conducting wall". In: *Physics of Plasmas* 19.3 (2012), p. 032108. DOI: 10.1063/1.3692729.

[104]   E. W. McDaniel. "Collision Phenomena In Ionized Gases". In: 1st. John Wiley and Sons, 1964. Chap. 5, p. 189.

[105]   J. M. Anderson. "Ultimate and secondary electron energies in the negatie glow of a cold-cathode discharge in helium". In: *Journal of Applied Physics* 31.3 (1960), pp. 511–515. DOI: 10.1063/1.1735620.

[106]   Kurt F. Schoenberg and Wulf B. Kunkel. "General plasma characteristics of a Berkeley multifil-ament ion source". In: *Journal of Applied Physics* 50.7 (1979), pp. 4685–4691. DOI: 10.1063/1.326578.

[107]   N. D. Twiddy. "Electron energy distributions in plasmas V. A search for evidence of a high anomalous rate of energy exchange between the electrons of a low-pressure discharge". In: *Proceedings of the Royal Society of London. A. Mathematical and Physical Sciences* 275.1362 (1963), pp. 338–356. DOI: 10.1098/rspa.1963.0174.

[108]   B. N. Chapman. "Glow Discharge Processes; Sputtering and Plasma Etching". In: 1st ed. John Wiley & Sons, Inc., 1980. Chap. 4, pp. 84–90.

[109]   P. Gill and C. E. Webb. "Electron energy distributions in the negative glow and their relevance to hollow cathode lasers". In: *Journal of Physics D: Applied Physics* 10.3 (1977), pp. 299–301. DOI: 10.1088/0022-3727/10/3/010.

[110]   G. S. Evtushenko, A. G. Gridnev, and I. I. Muravev. "Distribution of Electrokinetic Parameters of Negative Glow-Discharge Plasma". In: *Izvestia Vysshikh Uchebnykh Zavedenii.* 9 (1975), pp. 80–87.

[111] G. G. Lister. "Low-pressure gas discharge modelling". In: *Journal of Physics D: Applied Physics* 25.12 (1992), pp. 1649–1680. DOI: 10.1088/0022-3727/25/12/001.

[112] Z. Donkó, P. Hartmann, and K. Kutasi. "On the reliability of low-pressure dc glow discharge modelling". In: *Plasma Sources Science and Technology* 15.2 (2006), pp. 178–186. DOI: 10.1088/0963-0252/15/2/002.

[113] J. A. Bittencourt. "Fundamentals of Plasma Physics". In: 3rd ed. Vol. 1. New York: Springer Science+Business Media, 2004. Chap. 5-9, pp. 122–238.

[114] L. D. Tsendin. "Electron kinetics in glows - from Langmuir to the present". In: *Plasma Sources Science and Technology* 18.1 (2009), pp. 014020–014038. DOI: 10.1088/0963-0252/18/1/014020.

[115] V. Kolobov and R. Arslanbekov. "Deterministic Boltzmann solver for electron kinetics in plasma reactors for microelectronics applications". In: *Microelectronic Engineering* 69.2-4 (2003), pp. 606–615.

[116] T. Zhou, N. Xiang, C. Gan, X. Wang, G. Jia, J. Chen, X. Zhai, and Y. Huang. "Particle-in-cell simulations on parametric instability of the lower hybrid wave". In: *Physics of Plasmas* 29.10 (2022), p. 102302. DOI: 10.1063/5.0104505.

[117] P. L. Bhatnagar, E. P. Gross, and M. Krook. "A Model for Collision Processes in Gases. I. Small Amplitude Processes in Charged and Neutral One-Component Systems". In: *Physical Review* 94.3 (1954), pp. 511–525. DOI: 10.1103/physrev.94.511.

[118] M Moatamedi. *Finite Element Analysis*. eng. First edition. Boca Raton, F. L.: CRC Press, 2019.

[119] J. Crank and P. Nicolson. "A practical method for numerical evaluation of solutions of partial differential equations of the heat-conduction type". In: *Mathematical Proceedings of the Cambridge Philosophical Society* 43.1 (1947), pp. 50–67. DOI: 10.1017/s0305004100023197.

[120] J. C Butcher. *The numerical analysis of ordinary differential equations: Runge-Kutta and general linear methods*. eng. New York: Wiley, J., 1987.

[121] D Bohm. "The characteristics of electrical discharges in magnetic fields". eng. In: 1st ed. National nuclear energy series. Manhattan Project technical section. Division I, v. 5. New York: McGraw-Hill, 1949. Chap. 3.

[122] S. Longo. "Monte Carlo simulation of charged species kinetics in weakly ionized gases". In: *Plasma Sources Science and Technology* 15.4 (2006), S181. DOI: 10.1088/0963-0252/15/4/S04.

[123] J. P. Boeuf and E. Marode. "A Monte Carlo analysis of an electron swarm in a nonuniform field: the cathode region of a glow discharge in helium". In: *Journal of Physics D: Applied Physics* 15.11 (1982), p. 2169. DOI: 10.1088/0022-3727/15/11/012.

[124] J. U. Brackbill. "On energy and momentum conservation in particle-in-cell plasma simulation". In: *Journal of Computational Physics* 317 (2016), pp. 405–427. DOI: 10.1016/j.jcp.2016.04.050.

[125] M. Fitzgerald. "Discharge Physics and Plasma Transport in Inertial Electrostatic Confinement Devices". PhD thesis. The university of Sydney, 2009.

[126] W. Stephenson. "XLVIII.On the effect of the shape of the cathode on the glow discharge". In: *The London, Edinburgh, and Dublin Philosophical Magazine and Journal of Science* 2.9 (1926), pp. 556–577. DOI: 10.1080/14786442608564085.

[127] G. Stockhausen and M. Kock. "Proof and analysis of the pendulum motion of beam electrons in a hollow cathode discharge". In: *Journal of Physics D: Applied Physics* 34.11 (2001), pp. 1683–1689. DOI: 10.1088/0022-3727/34/11/320.

[128] A. D. White. "New Hollow Cathode Glow Discharge". In: *Journal of Applied Physics* 30.5 (1959), pp. 711–719. DOI: 10.1063/1.1735220.

[129] Y. Fu, J. P. Verboncoeur, and A. J. Christlieb. "Pressure effect on a tandem hollow cathode discharge in argon". In: *Physics of Plasmas* 24.10 (2017), p. 103514. DOI: 10.1063/1.5004681.

[130] W. Grimm. "New Glow Discharge Lamp for Optical Emission Spectral Analysis". In: *Spectrochimica Acta Part B - Atomic Spectroscopy* B 23.7 (1968), pp. 443–&. DOI: 10.1016/0584-8547(68)80023-0.

[131] A. Metel and Y. Melnik. "Distinctive features of the high-current glow discharge with the hollow cathode at low gas pressures". In: *Journal of Applied Physics* 124.21 (2018), p. 213302. DOI: 10.1063/1.5055280.

[132] A. V. Bondarenko. "Mass-Energy Ion Analysis in a Near-Cathode Region of Anomalous Glow Discharge .4. Discharge with Hollow Cathode". In: *Zhurnal Tekhnicheskoi Fiziki* 46.12 (1976), pp. 2535–2540.

[133] H. Helm. "Experimental Evidence of Existence of Pendel Effect 1 In a Low-Pressure Hollow Cathode Discharge in Argon". In: *Zeitschrift Fur Naturforschung Section A-A Journal of Physical Sciences* A 27.12 (1972), pp. 1812–1820.

[134] "Die behinderte Glimmentladung. II". In: *The European Physical Journal A* 61.9-10 (1930), pp. 581–586. DOI: 10.1007/bf01341163.

[135] W. Krug. "Eine neue Glimmentladungserscheinung und ihre Anwendungsmöglichkeit für Braunsche Röhren mit niedrigen Kathodenspannungen". In: *Archiv für Elektrotechnik* 30.3 (1936), pp. 157–183. DOI: 10.1007/bf01657311.

[136] M. E. Hines. "Equivalent Temperature of an Electron Beam". In: *Journal of Applied Physics* 22.11 (1951), pp. 1385–1386. DOI: 10.1063/1.1699871.

[137] D. Ciobotaru. "On the Hollow Cathode Effect†". In: *Journal of Electronics and Control* 17.5 (1964), pp. 529–540. DOI: 10.1080/00207216408937726.

[138] E. A. Den Hartog, D. A. Doughty, and J. E. Lawler. "Laser optogalvanic and fluorescence studies of the cathode region of a glow discharge". In: *Physical Review A* 38.5 (1988), pp. 2471–2491. DOI: 10.1103/physreva.38.2471.

[139] G. J. M. Hagelaar, D. B. Mihailova, and J. Van Dijk. "Analytical model of a longitudinal hollow cathode discharge". In: *Journal of Physics D: Applied Physics* 43.46 (2010), p. 465204. DOI: 10.1088/0022-3727/43/46/465204.

[140] A. Lompe, R. Seeliger, and E. Wolter. "Untersuchungen an Hohlkathoden". eng. In: *Annalen der Physik* 428.1 (1939), pp. 9–37.

[141] T. Musha. "Cathode Sputtering in Hollow Cathode Discharges". In: *Journal of the Physical Society of Japan* 17.9 (1962), pp. 1440–&. DOI: 10.1143/JPSJ.17.1440.

[142] T. Musha. "Theory of Negative Resistance in Hollow Cathode Discharges". In: *Journal of the Physical Society of Japan* 17.9 (1962), pp. 1447–&. DOI: 10.1143/JPSJ.17.1447.

[143] F. Howorka and M. Pähl. "Experimentelle Bestimmung innerer und äußerer Parameter des negativen Glimmlichtplasmas einer zylindrischen Hohlkathodenentladung in Argon / Plasma Diagnostic Measurements in the Negative Glow of a Cylindrical Hollow Cathode Discharge". In: *Zeitschrift für Naturforschung A* 27.10 (1972), pp. 1425–1433. DOI: `10.1515/zna-1972-1008`.

[144] V. S. Borodin, Y. M. Kagan, and R. I. Lyagushc. "Investigation of a Hollow-Cathode Discharge .2." In: *Soviet Physics Technical Physics-USSR* 11.7 (1967), pp. 887–&.

[145] V. M. Tkachenko and V. B. Tyutyunnik. "Plasma Parameters in a Discharge with Cylindrical Hollow-Cathode in Helium". In: *Zhurnal Tekhnicheskoi Fiziki* 46.7 (1976), pp. 1449–1458.

[146] V. S. Borodin and Y. M Kagan. "Investigation of Hollow-Cathode Discharge .I. Comparison of Electrical Characteristics of a Hollow Cathode and a Positive Column". In: *Soviet Physics Technical Physics-USSR* 11.1 (1966), pp. 131–&.

[147] J. A. Piper and P. Gill. "Output characteristics of the He-Zn laser". In: *Journal of Physics D: Applied Physics* 8.2 (1975), p. 127. DOI: `10.1088/0022-3727/8/2/005`.

[148] S. Muhl, J. Cruz, I. Camps, and A. Garzon-Fontecha. "Deposition of metal thin films using a hollow cathode hydrogen discharge". In: *Surface and Coatings Technology* 442 (2022), p. 128404. DOI: `https://doi.org/10.1016/j.surfcoat.2022.128404`.

[149] A. G. Zhiglinskii, G. G. Kund, and A O Morozov. "Holographic method for determining the spatial coherence of radiation from light sources of low brightness". rus. In: *Optika i Spektroskopiia* 42 (1977), pp. 1158–1161.

[150] O. Shrier, J. Khachan, S. Bosi, M. Fitzgerald, and N. Evans. "Diverging ion motion in an inertial electrostatic confinement discharge". In: *Physics of Plasmas* 13.1 (2006), p. 012703. DOI: `10.1063/1.2167584`.

[151] J. Kipritidis, J. Khachan, M. Fitzgerald, and O. Shrier. "Absolute densities of energetic hydrogen ion species in an abnormal hollow cathode discharge". In: *Physical Review E* 77.6 (2008). DOI: `10.1103/physreve.77.066405`.

[152] I. D. Boyd and M. W. Crofton. "Modeling the plasma plume of a hollow cathode". In: *Journal of Applied Physics* 95.7 (2004), pp. 3285–3296. DOI: `10.1063/1.1651333`.

[153] A. Bogaerts, R. Gijbels, and W. J. Goedheer. "Hybrid Monte Carlo-fluid model of a direct current glow discharge". In: *Journal of Applied Physics* 78.4 (1995), pp. 2233–2241. DOI: `10.1063/1.360139`.

[154] N. Baguer, A. Bogaerts, and R. Gijbels. "Hybrid model for a cylindrical hollow cathode glow discharge and comparison with experiments". In: *Spectrochimica Acta Part B: Atomic Spectroscopy* 57.2 (2002), pp. 311–326. DOI: `10.1016/s0584-8547(01)00385-8`.

[155] N. Baguer. "Numerical modeling of a hollow cathode discharge". PhD thesis. Universiteit Antwerpen, 2005.

[156] C. Hardy. *Atomic rise and fall : the Australian Atomic Energy Commission, 1953-1987*. eng. Peakhurst, N.S.W: Glen Haven Publishing, 1999.

[157] S. M. Qaim. *Medical Radionuclide Production: Science and Technology*. eng. Berlin/Boston: Walter de Gruyter GmbH, 2019.

[158] J. P. Freidberg. *Plasma physics and fusion energy.* eng. Cambridge: Cambridge University Press, 2007.

[159] *ITER organization Annual Report 2021.* Tech. rep. St. Paul-lez-Durance Cedex, France: ITER organization, 2021. URL: www.iter.org/news/publicationcentre/annual-reports.

[160] N. Mitchell et al. "Superconductors for fusion: a roadmap". In: *Superconductor Science and Technology* 34.10 (2021), p. 103001. DOI: 10.1088/1361-6668/ac0992.

[161] T. Filburn and S. Bullard. *Three Mile Island, Chernobyl and Fukushima: Curse of the Nuclear Genie.* Springer International Publishing AG, 2016.

[162] *Maintenance, Testing, Surveillance and Inspection in Nuclear Power Plants.* Specific Safety Guides SSG-74. Vienna: International Atomic Energy Agency, 2022. URL: https://www.iaea.org/publications/14905/maintenance-testing-surveillance-and-inspection-in-nuclear-power-plants.

[163] W. M. Nevins and R. Swain. "The thermonuclear fusion rate coefficient for p-B-11 reactions". In: *Nuclear Fusion* 40.4 (2000), pp. 865–872. DOI: 10.1088/0029-5515/40/4/310.

[164] D. D. Clayton. "Principles of stellar evolution and nucleosynthesis : with a new preface". eng. In: *Principles of stellar evolution and nucleosynthesis : with a new preface.* University of Chicago Press ed. Chicago: University of Chicago Press, 1968. Chap. 6.

[165] S. Kaufman and W. F. Libby. "The Natural Distribution of Tritium". In: *Physical Review* 93.6 (1954), pp. 1337–1344. DOI: 10.1103/physrev.93.1337.

[166] G.A. Emmert et al. "Possibilities for breakeven and ignition of D-3He fusion fuel in a near term tokamak". In: *Nuclear Fusion* 29.9 (1989), pp. 1427–1448. DOI: 10.1088/0029-5515/29/9/001.

[167] J. D. Lawson. *Some Criteria for a Useful Thermonuclear Reactor.* Tech. rep. 1. Harwell, Berkshire, U. K.: Atomic Energy Research Establishment, 1955.

[168] S. E. Wurzel and S. C. Hsu. "Progress toward fusion energy breakeven and gain as measured against the Lawson criterion". In: *Physics of Plasmas* 29.6 (2022), p. 062103. DOI: 10.1063/5.0083990.

[169] P. S. Sarkar, Y. S. Kashyap, and Dinesh. K. Aswal. *Neutron imaging : basics, techniques and applications.* eng. Gateway East, Singapore: Springer, 2022.

[170] G. H. Miley, L. Wu, and H. J. Kim. "Nuclear Techniques in National Security Studies on Contraband Detection". In: *Journal of Radioanalytical and Nuclear Chemistry* 263.1 (2005), pp. 159–164. DOI: 10.1007/s10967-005-0031-3.

[171] K. Bernard. *The Atomic Fingerprint: Neutron Activation Analysis.* Project Gutenberg, 2015.

[172] Critical Technologies Policy Coordination Office. *List of critical technologies in the national interest.* Tech. rep. Canberra, ACT, Australia: Australian Government Department of the Prime Minister and Cabinet, 2021. URL: https://www.pmc.gov.au/resource-centre/domestic-policy/list-critical-technologies-national-interest.

[173] D. Kramer. *National Ignition Facility surpasses long-awaited fusion milestone.* 2022. DOI: 10.1063/PT.6.2.20221213a.

[174] D Clery. *With historic explosion, a long sort fusion breakthrough.* 2022. DOI: 10.1126/science.adg2803.

[175] J. Ongena, R. Koch, R. Wolf, and H. Zohm. "Magnetic-confinement fusion". In: *Nature Physics* 12.5 (2016), pp. 398–410. DOI: 10.1038/nphys3745.

[176] A.L. Gardner. *Studies of charged-particle distributions in an electrostatic confinement system. Progress report, August 1, 1972–March 31, 1974*. 1974. DOI: 10.2172/4298965.

[177] J. H. Nadler, G. H. Miley, Y. Gu, and T. Hochberg. "Characterization of an Inertial-Electrostatic Confinement Glow Discharge (IECGD) Neutron Generator". In: *Fusion Technology* 21.3P2A (1992), pp. 1639–1643. DOI: 10.13182/fst92-a29955.

[178] G. H. Miley and J. Sved. "The IEC—A plasma-target-based neutron source". In: *Applied Radiation and Isotopes* 48.10 (1997), pp. 1557–1561. DOI: https://doi.org/10.1016/S0969-8043(97)00257-1.

[179] W. C. Elmore, James L. Tuck, and Kenneth M. Watson. "On the Inertial-Electrostatic Confinement of a Plasma". In: *Physics of Fluids* 2.3 (1959), p. 239. DOI: 10.1063/1.1705917.

[180] T. J. Dolan, J. T. Verdeyen, D. J. Meeker, and B. E. Cherrington. "Electrostatic-Inertial Plasma Confinement". In: *Journal of Applied Physics* 43.4 (1972), pp. 1590–1600. DOI: 10.1063/1.1661367.

[181] R. L. Hirsch. "Inertial-Electrostatic Confinement of Ionized Fusion Gases". In: *Journal of Applied Physics* 38.11 (1967), pp. 4522–4534. DOI: 10.1063/1.1709162.

[182] D. A. Swanson, B.E. Cherrington, and J. T. Verdeyen. "Theory of the negative electrostatic potential well in spherical geometry". In: *Physics of Fluids* 17.6 (1974), p. 1269. DOI: 10.1063/1.1694877.

[183] O. A. Lavrent'ev. In: *Annals of the New York Academy of Sciences* (1975), pp. 152–178.

[184] G. H. Miley and J. Sved. "The IEC—A plasma-target-based neutron source". In: *Applied Radiation and Isotopes* 48.10 (1997), pp. 1557–1561. DOI: https://doi.org/10.1016/S0969-8043(97)00257-1.

[185] G. H. Miley and J. Sved. "The IEC star-mode fusion neutron source for NAA - status and next-step designs". In: *Applied Radiation and Isotopes* 53.4-5 (2000), pp. 779–783. DOI: 10.1016/S0969-8043(00)00215-3.

[186] M. Bakr, K. Masuda, and M. Yoshida. "Improvement of the Neutron Production Rate of IEC Fusion Device by the Fusion Reaction on the Inner Surface of the IEC Chamber". In: *Fusion Science and Technology* 75.6 (2019), pp. 479–486. DOI: 10.1080/15361055.2019.1609821.

[187] T.A Thorson, R.D Durst, R.J Fonck, and A.C Sontag. "Fusion reactivity characterization of a spherically convergent ion focus". In: *Nuclear Fusion* 38.4 (1998), pp. 495–507. DOI: 10.1088/0029-5515/38/4/302.

[188] Y. B. Gu and G. H. Miley. "Experimental study of potential structure in a spherical IEC fusion device". In: *IEEE Transactions on Plasma Science* 28.1 (2000), pp. 331–346. DOI: 10.1109/27.842929.

[189] J. Khachan and S. Collis. "Measurements of ion energy distributions by Doppler shift spectroscopy in an inertial-electrostatic confinement device". In: *Physics of Plasmas* 8.4 (2001), p. 1299. DOI: 10.1063/1.1349875.

[190]   J. Khachan, D. Moore, and S. Bosi. "Spatial distribution of ion energies in an inertial electrostatic confinement device". In: *Physics of Plasmas* 10.3 (2003), pp. 596–599. DOI: 10.1063/1.1544665.

[191]   J. Khachan and A. Samarian. "Dust diagnostics on an inertial electrostatic confinement discharge". In: *Physics Letters A* 363.4 (2007), pp. 297–301. DOI: 10.1016/j.physleta.2006.11.015.

[192]   J. Hermens, R. Jaspers, and J. Khachan. "Measurements of diverging ion motion in an inertial electrostatic confinement device using Doppler spectroscopy". In: *Physics of Plasmas* 26.10 (2019), p. 102703. DOI: 10.1063/1.5119285.

[193]   N. Ranson, V. Pigeon, N. Claire, and J. Khachan. "Measurements and modeling of ion divergence from a gridded inertial electrostatic confinement device using laser induced fluorescence". In: *Physics of Plasmas* 27.10 (2020), p. 103501. DOI: 10.1063/5.0002916.

[194]   A. S. Bolukdemir, Y. Akgun, and A. Alacakir. "Preliminary Results of Experimental Studies from Low Pressure Inertial Electrostatic Confinement Device". In: *Journal of Fusion Energy* 32.5 (2013), pp. 561–565. DOI: 10.1007/s10894-013-9607-z.

[195]   J-P. Wulfkuehler and M. Tajmar. "Novel Inertial Electrostatic Confinement Fusion with Buckyball-Shaped Multi-Grids". In: *52nd AIAA/SAE/ASEE Joint Propulsion Conference*. 2016. DOI: 10.2514/6.2016-4777.

[196]   M. Yousefi, V. Damideh, and H. Ghomi. "Low-Energy Electron Beam Extraction From Spherical Discharge". In: *IEEE Transactions on Plasma Science* 39.11 (2011), pp. 2554–2555. DOI: 10.1109/tps.2011.2159130.

[197]   V. Damideh, A. Sadighzadeh, A. Koohi, A. Aslezaeem, A. Heidarnia, N. Abdollahi, F. Abbasi Davani, and R. Damideh. "Experimental Study of the Iranian Inertial Electrostatic Confinement Fusion Device as a Continuous Neutron Generator". In: *Journal of Fusion Energy* 31.2 (2012), pp. 109–111. DOI: 10.1007/s10894-011-9438-8.

[198]   E. H. Ebrahimi, R. Amrollahi, A. Sadighzadeh, M. Torabi, M. Sedaghat, R. Sabri, B. Pourshahab, and V. Damideh. "The Influence of Cathode Voltage and Discharge Current on Neutron Production Rate of Inertial Electrostatic Confinement Fusion (IR-IECF)". In: *Journal of Fusion Energy* 32.1 (2013), pp. 62–65. DOI: 10.1007/s10894-012-9524-6.

[199]   T. Takamatsu, K. Masuda, T. Kyunai, H. Toku, and K. Yoshikawa. "Inertial electrostatic confinement fusion device with an ion source using a magnetron discharge". In: *Nuclear Fusion* 46.1 (2005), p. 142. DOI: 10.1088/0029-5515/46/1/016.

[200]   K. Noborio, Y. Yamamoto, and S. Konishi. "Neutron production rate of inertial electrostatic confinement fusion device with fusion reaction on surface of electrodes". In: *Fusion Science and Technology* 52.4 (2007), pp. 1105–1109. DOI: 10.13182/FST07-A1645.

[201]   K. Masuda, T. Fujimoto, T. Nakagawa, H. Zen, T. Kajiwara, K. Nagasaki, and K. Yoshikawa. "Diagnostic System Development for D-D and D-He-3 Reaction Distributions in an Intertial-Electrostatic Confinement Device by Collimated Proton Measurements". In: *Fusion Science and Technology* 56.1 (2009), pp. 528–532. DOI: 10.13182/FST09-A8957.

[202]   K. Noborio, S. Konishi, T. Maegawa, and Y. Yamamoto. "Numerical Calculation of Reactions on Electrode Surfaces and in a Volume of a Discharge Type Fusion Neutron Source By developing a one dimensional particle-in-cell Monte Carlo code". In: *2011 IEEE/NPSS 24th Symposium on Fusion Engineering (SOFE)*. IEEE; NPSS. 2011.

[203]   B. B. Cipiti. "The fusion of advanced fuels to produce medical isotopes using inertial electrostatic confinement". PhD thesis. University of Wisconsin, 2004.

[204]   D. R. Boris. "Novel diagnostic approaches to characterising the performance of the wisconsin inertial electrostatic confinement plasma". PhD thesis. University of Wisconsin, 2009.

[205]   S. K. Murali, G. A. Emmert, J. F. Santarius, and G. L. Kulcinski. "Effects of chamber pressure variation on the grid temperature in an inertial electrostatic confinement device". In: *Physics of Plasmas* 17.10 (2010). DOI: 10.1063/1.3484224.

[206]   E. C. Alderson. "Experimental and theoretical characterisation of deuterium ion distributions in a gridded inertial electrostatic confinement device". PhD thesis. University of Wisconsin, 2012.

[207]   D. C. Donovan, D. R. Boris, G. L. Kulcinski, J. F. Santarius, and G. R. Piefer. "Measuring time of flight of fusion products in an inertial electrostatic confinement fusion device for spatial profiling of fusion reactions". In: *Review of Scientific Instruments* 84.3 (2013). DOI: 10.1063/1.4793771.

[208]   P.T. Farnsworth. "Method and apparatus for producing nuclear-fusion reactions". In: (1968). US Patent 3,386,883. URL: https://www.google.com.au/patents/US3386883.

[209]   R.L. Hirsch. "Apparatus for generating fusion reactions". In: (1970). US Patent 3530036A. URL: https://patents.google.com/patent/US3530036.

[210]   R.L. Hirsch and Meeks G.A. "Apparatus for generating fusion reactions". In: (1970). US Patent 3530497A. URL: https://patents.google.com/patent/US3530497.

[211]   I. Langmuir and K. B. Blodgett. "Currents Limited by Space Charge between Concentric Spheres". In: *Physical Review* 24.1 (1924), pp. 49–59. DOI: 10.1103/physrev.24.49.

[212]   R. L. Hirsch. "Experimental Studies of a Deep, Negative, Electrostatic Potential Well in Spherical Geometry". In: *Physics of Fluids* 11.11 (1968), p. 2486. DOI: 10.1063/1.1691842.

[213]   J. Park, R. A. Nebel, S. Stange, and S. Krupakar Murali. "Periodically oscillating plasma sphere". In: *Physics of Plasmas* 12.5 (2005), p. 056315. DOI: 10.1063/1.1888822.

[214]   J. Park, R. Nebel, S. Stange, and S. Murali. "Experimental Observation of a Periodically Oscillating Plasma Sphere in a Gridded Inertial Electrostatic Confinement Device". In: *Physical Review Letters* 95.1 (2005). DOI: 10.1103/physrevlett.95.015003.

[215]   R. Bandara and J. Khachan. "Spherical ion oscillations in a positive polarity gridded inertial-electrostatic confinement device". In: *Physics of Plasmas* 20.7 (2013), p. 072705. DOI: 10.1063/1.4813801.

[216]   D. A. Swanson. "Potential well structure in an inertial electrostatic plasma confinement device". In: *Physics of Fluids* 16.11 (1973), p. 1939. DOI: 10.1063/1.1694238.

[217]   D. A. Swanson, B. E. Cherrington, and J. T. Verdeyen. "Multiple potential-well structure created by electron injection in spherical geometry". In: *Applied Physics Letters* 23.3 (1973), pp. 125–126. DOI: 10.1063/1.1654829.

[218] T. H. Rider. "A general critique of inertial-electrostatic confinement fusion systems". In: *Physics of Plasmas* 2.6 (1995), pp. 1853–1872. DOI: 10.1063/1.871273.

[219] T. H. Rider. "Fundamental limitations on plasma fusion systems not in thermodynamic equilibrium". In: *Physics of Plasmas* 4.4 (1997), pp. 1039–1046. DOI: 10.1063/1.872556.

[220] L. Chacón, G. H. Miley, D. C. Barnes, and D. A. Knoll. "Energy gain calculations in Penning fusion systems using a bounce-averaged Fokker–Planck model". In: *Physics of Plasmas* 7.11 (2000), pp. 4547–4560. DOI: 10.1063/1.1310199.

[221] L. Gardner A, M. Hatch D, I. Y. Chan A, and P. Evans R. "Measurements on a Spherical Electrostatic Confinement System Employing Six Ion Guns". In: *Annals of the New York Academy of Sciences* 251.1 (1975), pp. 179–189. DOI: 10.1111/j.1749-6632.1975.tb00090.x.

[222] R. W. Bussard. "Method and Apparatus for Controlling Charged Particles". In: (1985). US4826646A. URL: https://patents.google.com/patent/US4826646A/en.

[223] J. Rasmussen, T. Jensen, S. B. Korsholm, N. E. Kihm, F. K. Ohms, M. Gockenbach, B. S. Schmidt, and E. Goss. "Characterization of fusion plasmas in the cylindrical DTU inertial electrostatic confinement device". In: *Physics of Plasmas* 27.8 (2020), p. 083515. DOI: 10.1063/5.0013013.

[224] G.H. Miley, Y. Gu, J.M. Demora, R.A. Stubbers, T.A. Hochberg, J.H. Nadler, and R.A. Anderl. "Discharge characteristics of the spherical inertial electrostatic confinement (IEC) device". In: *IEEE Transactions on Plasma Science* 25.4 (1997), pp. 733–739. DOI: 10.1109/27.640696.

[225] H. Momota and G. H. Miley. "Virtual Cathode in a Stationary Spherical Inertial Electrostatic Confinement". In: *Fusion Science and Technology* 40.1 (2001), pp. 56–65. DOI: 10.13182/fst01-a180.

[226] K. Masuda, T. Mizutani, K. Yoshikawa, K. Nagasaki, K. Takiyama, F. Toku, I. Hashimoto, and A. Nagafuchi. "Measurement of the energy distribution of fast excited atoms by Doppler shift spectroscopy in an inertial-electro static confinement fusion device". In: *19TH IEEE/NPSS Symposium on Fusion Enginerring, Proceedings*. 2002, pp. 434–437.

[227] R. Bowden-Reid, Joe K., J-P. Wulfkühler, and M. Tajmar. "Evidence for surface fusion in inertial electrostatic confinement devices". In: *Physics of Plasmas* 25.11 (2018), p. 112702. DOI: 10.1063/1.5053616.

[228] R. Bowden-Reid and J. Khachan. "An inertial electrostatic confinement fusion system based on graphite". In: *Physics of Plasmas* 28.4 (2021), p. 042703. DOI: 10.1063/5.0038766.

[229] E. W. McDaniel. "Collision Phenomena In Ionized Gases". In: 1st. John Wiley and Sons, 1964. Chap. 6, p. 189.

[230] G. A. Emmert and J. F. Santarius. "Atomic and molecular effects on spherically convergent ion flow. II. Multiple molecular species". In: *Physics of Plasmas* 17.1 (2010). DOI: 10.1063/1.3290801.

[231] K. Masuda, R. Kashima, and M. A. Bakr. "Potential Profile Measurements Inside a Gridded Cathode at High Potential in a Spherical Inertial Electrostatic Confinement Device". In: *Fusion Science and Technology* 75.7 (2019), pp. 608–613. DOI: 10.1080/15361055.2019.1610292.

[232] A. S. Metel and Y. A. Melnik. "Sustaining of a Glow Discharge with Electrostatic Confinement of Electrons for Plasma Emitter Production in Small Sized Beam Sources of Fast Neutral Molecules". In: 2006.

[233]   S. N. Grigoriev, Yu. A. Melnik, A. S. Metel, and M. A. Volosova. "Focused beams of fast neutral atoms in glow discharge plasma". In: *Journal of Applied Physics* 121.22 (2017), p. 223302. DOI: 10.1063/1.4985249.

[234]   J. D. Builth-Williams. "Geometrically and Reflectively Enhanced Embedded Fusion". PhD thesis. University of Sydney, 2020. URL: https://hdl.handle.net/2123/23256.

[235]   R. W. Solarz. *Laser Spectroscopy and its Applications*. eng. First edition. Boca Raton, FL: CRC Press, 2017.

[236]   D. N. Hill, S. Fornaca, and M. G. Wickham. "Single frequency scanning laser as a plasma diagnostic". In: *Review of Scientific Instruments* 54.3 (1983), pp. 309–314. DOI: 10.1063/1.1137389.

[237]   F. P. Schäfer and K. H. Drexhage. *Dye lasers*. eng. 3rd enl. and rev. ed. Topics in applied physics ; v. 1. Berlin: Springer-Verlag, 1990.

[238]   A. Pérot and C. Fabry. "On the application of interference phenomena to the solution of various problems of spectroscopy and metrology". In: *Astrophysical Journal* 9 (1899), pp. 87–115. DOI: 10.1086/140557.

[239]   W. C. Michels and N. L. Curtis. "A Pentode Lock-In Amplifier of High Frequency Selectivity". In: *Review of Scientific Instruments* 12.9 (1941), pp. 444–447. DOI: 10.1063/1.1769919.

[240]   J. H. Scofield. "Frequency-domain description of a lock-in amplifier". In: *American Journal of Physics* 62.2 (1994), pp. 129–133. DOI: 10.1119/1.17629.

[241]   A. C. Eckbreth. eng. In: *Laser diagnostics for combustion temperature and species*. First edition. Combustion science and technology book series ; v. 3. CRC Press, 2022. Chap. 7.

[242]   J. Goree and M. J. Goeckner. "Laser-Induced Fluorescence Measurements of Ion Distribution Functions". In: *Plasma-Surface Interactions and Processing of Materials*. Ed. by O. Auciello, A. Gras-Marti, J. A. Valles-Abarca, and D. L. Flamm. Dordrecht: Springer Netherlands, 1990, pp. 163–165. DOI: 10.1007/978-94-009-1946-4_10.

[243]   R Altkorn and R N Zare. "Effects of Saturation on Laser-Induced Fluorescence Measurements of Population and Polarization". In: *Annual Review of Physical Chemistry* 35.1 (1984), pp. 265–289. DOI: 10.1146/annurev.pc.35.100184.001405.

[244]   M. J. Goeckner, J. Goree, and T. E. Sheridan. "Saturation broadening of laser-induced fluorescence from plasma ions". In: *Review of Scientific Instruments* 64.4 (1993), pp. 996–1000. DOI: 10.1063/1.1144103.

[245]   V. Pigeon, N. Claire, C. Arnas, and F. Doveil. "Laser-induced fluorescence saturation effects on ion velocity distribution functions in the vicinity of reflecting surfaces". In: *Physics of Plasmas* 26.2 (2019), p. 023508. DOI: 10.1063/1.5077047.

[246]   K. Kohse-Höinghaus. "Laser techniques for the quantitative detection of reactive intermediates in combustion systems". In: *Progress in Energy and Combustion Science* 20.3 (1994), pp. 203–279. DOI: 10.1016/0360-1285(94)90015-9.

[247]   R. Forster, M. Frost, D. Fulle, H. F. Hamann, H. Hippler, A. Schlepegrell, and J. Troe. "High pressure range of the addition of HO to HO, NO, NO2, and CO. I. Saturated laser induced fluorescence measurements at 298 K". In: *The Journal of Chemical Physics* 103.8 (1995), pp. 2949–2958. DOI: 10.1063/1.470482.

[248] D. A. Edrich, R. Mcwilliams, and N. S. Wolf. "Single beam laser induced fluorescence technique for plasma transport measurements". In: *Review of Scientific Instruments* 67.8 (1996), pp. 2812–2817. DOI: 10.1063/1.1147111.

[249] A. P. Baronavski and J. R. McDonald. "Application of saturation spectroscopy to the measurement of C2, 3Πu concentrations in oxy-acetylene flames". In: *Applied Optics* 16.7 (1977), pp. 1897–1901. DOI: 10.1364/AO.16.001897.

[250] M. Mrkvi, P. Dvorak, M. Svoboda, J. Kratzer, J. Vorac, and J. Dedina. "Dealing with saturation of the laser-induced fluorescence signal: An application to lead atoms". In: *Combustion and Flame* 241 (2022). DOI: 10.1016/j.combustflame.2022.112100.

[251] J. Vorac, P. Dvorak, V. Prochazka, T. Moravek, and J. Rahel. "Dependence of laser-induced fluorescence on exciting-laser power: partial saturation and laser - plasma interaction". In: *European Physical Journal - Applied Physics* 71.2 (2015). DOI: 10.1051/epjap/2015150022.

[252] E. L. Foley and F. M. Levinton. "Progress on the motional Stark effect with laser-induced fluorescence diagnostic (invited)". In: *Review of Scientific Instruments* 77.10 (2006), 10F311. DOI: 10.1063/1.2219432.

[253] E. J. Yadlowsky and R. C. Hazelton. "Laser-induced fluorescent measurements of magnetic field contours in a low-pressure discharge". In: *IEEE Transactions on Plasma Science* 20.1 (1992), pp. 24–29. DOI: 10.1109/27.120190.

[254] H. D. Hagstrum. "Metastable Ions of the Noble Gases". In: *Physical Review* 104.2 (1956), pp. 309–316. DOI: 10.1103/physrev.104.309.

[255] R. Limpaecher and K. R. Mackenzie. "Magnetic Multipole Containment of Large Uniform Collisionless Quiescent Plasmas". In: *Review of Scientific Instruments* 44.6 (1973), pp. 726–731. DOI: 10.1063/1.1686231.

[256] K. N. Leung, N. Hershkowitz, and K. R. Mackenzie. "Plasma confinement by localized cusps". In: *Physics of Fluids* 19.7 (1976), p. 1045. DOI: 10.1063/1.861575.

[257] M. Carrère, L. Chérigier, C. Arnas-Capeau, G. Bachet, and F. Doveil. "Steady state behavior of a multipolar plasma device". In: *Review of Scientific Instruments* 67.12 (1996), pp. 4124–4129. DOI: 10.1063/1.1147558.

[258] K. N. Leung, R. E. Kribel, and G. R. Taylor. "Measurement of the effective mean free paths of primary electrons in a multidipole device". In: *Journal of Applied Physics* 47.12 (1976), pp. 5245–5247. DOI: 10.1063/1.322599.

[259] N. Hershkowitz, J. R. Dekock, P. Coakley, and S. L. Cartier. "Surface trapping of primary electrons by multidipole magnetic fields". In: *Review of Scientific Instruments* 51.1 (1980), pp. 64–69. DOI: 10.1063/1.1136020.

[260] C. S. Yip, N. Hershkowitz, and G. Severn. "Verifying effects of instability enhanced ion–ion Coulomb collisions on ion velocity distribution functions near the sheath edge in low temperature plasmas". In: *Plasma Sources Science and Technology* 24.1 (2014), p. 015018. DOI: 10.1088/0963-0252/24/1/015018.

[261] M-H. Cho, N. Hershkowitz, and T. Intrator. "Particle and power balances of hot-filament discharge plasmas in a multidipole device". In: *Journal of Applied Physics* 67.7 (1990), pp. 3254–3259. DOI: 10.1063/1.345358.

[262] G. Bachet, L. Chérigier, and F. Doveil. "Ion velocity distribution function observations in a multipolar argon discharge". In: *Physics of Plasmas* 2.5 (1995), pp. 1782–1788. DOI: 10.1063/1.871328.

[263] O. Shrier, J. Khachan, and S. Bosi. "A Markov chain approach to modelling charge exchange processes of an ion beam in monotonically increasing or decreasing potentials". In: *Journal of Physics A-Mathematical and General* 39.35 (2006), pp. 11119–11128. DOI: 10.1088/0305-4470/39/35/012.

[264] N. Buzarbaruah, N. J. Dutta, D. Borgohain, S. R. Mohanty, and H. Bailung. "Study on discharge plasma in a cylindrical inertial electrostatic confinement fusion device". In: *Physics Letters A* 381.30 (2017), pp. 2391–2396. DOI: 10.1016/j.physleta.2017.05.029.

[265] T. Motoyasu, S. Namba, and K. Takiyama. "Measurements of localized potential profiles by LIF polarization spectroscopy in an inertial-electrostatic confinement discharge". In: *Journal of the Korean Physical Society* 65.8, SI (2014), pp. 1205–1208. DOI: 10.3938/jkps.65.1205.

[266] D. J.. Spasojevic, S. Mijin, N. M. Sisovic, and N. Konjevic. "Spectroscopic application of an iterative kinetic cathode sheath model to high voltage hollow cathode glow discharge in hydrogen". In: *Journal of Applied Physics* 119.5 (2016). DOI: 10.1063/1.4941267.

[267] F. F. Chen. "Introduction to Plasma Physics And Controlled Fusion, 2nd Edition". In: ed. by C. M. Savage and M. Das. Springer, 1984. Chap. 8.

[268] B. J. Nicholas and F. C. Witteborn. *Measurements of Resonant Charge Exchange Cross Sections In Nitrogen and Argon Between 0.5 and 17 EV*. Tech. rep. NASA, 1966.

[269] C. R. Kitchin. "Optical Astronomical Spectroscopy". In: Bristol and Philadelphia: IoP Publishing, 1995. Chap. 3.

[270] H. N. Russell and F. A. Saunders. "New regularities in the spectra of the alkaline earths". In: *Astrophysical Journal* 61.1 (1925), pp. 38–69. DOI: 10.1086/142872.

[271] G. G. Raju. *Gaseous electronics : theory and practice*. eng. Electrical and computer engineering ; 128. Boca Raton: Taylor & Francis, 2006.

[272] R. B. Leighton. "Principles of modern physics." eng. In: International series in pure and applied physics. New York: McGraw-Hill, 1959. Chap. 8.

[273] G. G. Raju. "Electron-atom collision cross sections in argon: an analysis and comments". In: *IEEE Transactions on Dielectrics and Electrical Insulation* 11.4 (2004), pp. 649–673. DOI: 10.1109/tdei.2004.1324355.

[274] P. Varga and H. Winter. "Determination of metastable fractions in noble-gas-ion beams". In: *Physical Review A* 18.6 (1978), pp. 2453–2458. DOI: 10.1103/physreva.18.2453.

[275] G. Racah. "On a new type of vector coupling in complex spectra". In: *Physical Review* 61.7/8 (1942), p. 537. DOI: 10.1103/PhysRev.61.537.

[276] R. M. Measures. "Selective Excitation Spectroscopy and Some Possible Applications". In: *Journal of Applied Physics* 39.11 (1968), pp. 5232–5245. DOI: 10.1063/1.1655946.

[277] R. A. Stern and J. A. Johnson. "Plasma Ion Diagnostics Using Resonant Fluorescence". In: *Physical Review Letters* 34.25 (1975), pp. 1548–1551. DOI: 10.1103/physrevlett.34.1548.

[278]   R.A. Stern, D.N. Hill, and N. Rynn. "Direct ion-transport measurement by optical tagging". In: *Physics Letters A* 93.3 (1983), pp. 127–130. DOI: https://doi.org/10.1016/0375-9601(83)90073-7.

[279]   F. Anderegg, X.-P. Huang, E. Sarid, and C. F. Driscoll. "A new pure ion plasma device with laser induced fluorescence diagnostic". In: *Review of Scientific Instruments* 68.6 (1997), pp. 2367–2377. DOI: 10.1063/1.1148119.

[280]   F. Skiff, G. Bachet, and F. Doveil. "Ion dynamics in nonlinear electrostatic structures". In: *Physics of Plasmas* 8.7 (2001), pp. 3139–3142. DOI: 10.1063/1.1379044.

[281]   L. Oksuz, M. A. Khedr, and N. Hershkowitz. "Laser induced fluorescence of argon ions in a plasma presheath". In: *Physics of Plasmas* 8.5 (2001), pp. 1729–1733. DOI: 10.1063/1.1358312.

[282]   L. Oksuz and N. Hershkowitz. "Plasma, presheath, collisional sheath and collisionless sheath potential profiles in weakly ionized, weakly collisional plasma". In: *Plasma Sources Science and Technology* 14.1 (2005), pp. 201–208. DOI: 10.1088/0963-0252/14/1/022.

[283]   G. D. Severn, X. Wang, E. Ko, and N. Hershkowitz. "Experimental Studies of the Bohm Criterion in a Two-Ion-Species Plasma Using Laser-Induced Fluorescence". In: *Physical Review Letters* 90.14 (2003). DOI: 10.1103/physrevlett.90.145001.

[284]   R. N. Zare and P. J. Dagdigian. "Tunable Laser Fluorescence Method for Product State Analysis". In: *Science* 185.4153 (1974), pp. 739–747. DOI: 10.1126/science.185.4153.739.

[285]   J L Kinsey. "Laser-Induced Fluorescence". In: *Annual Review of Physical Chemistry* 28.1 (1977), pp. 349–372. DOI: 10.1146/annurev.pc.28.100177.002025.

[286]   E. E. Scime, P. A. Keiter, M. W. Zintl, M. M. Balkey, J. L. Kline, and M. E. Koepke. "Control of ion temperature anisotropy in a helicon plasma". In: *Plasma Sources Science and Technology* 7.2 (1998), pp. 186–191. DOI: 10.1088/0963-0252/7/2/013.

[287]   M. J. Goeckner, J. Goree, and T. E. Sheridan. "Laser-induced fluorescence characterization of a multidipole filament plasma". In: *Physics of Fluids B: Plasma Physics* 3.10 (1991), pp. 2913–2921. DOI: 10.1063/1.859924.

[288]   J. L. Kline, E. E. Scime, P. A. Keiter, M. M. Balkey, and R. F. Boivin. "Ion heating in the HELIX helicon plasma source". In: *Physics of Plasmas* 6.12 (1999), pp. 4767–4772. DOI: 10.1063/1.873764.

[289]   N. Claire, M. Dindelegan, G. Bachet, and F. Skiff. "Nonlinear optical tagging diagnostic for the measurement of Fokker-Planck diffusion and electric fields". In: *Review of Scientific Instruments* 72.12 (2001), pp. 4372–4376. DOI: 10.1063/1.1419221.

[290]   N. Claire, G. Bachet, U. Stroth, and F. Doveil. "Laser-induced-fluorescence observation of ion velocity distribution functions in a plasma sheath". In: *Physics of Plasmas* 13.6 (2006), p. 062103. DOI: 10.1063/1.2206786.

[291]   F. Anderegg, R. A. Stern, F. Skiff, B. A. Hammel, M. Q. Tran, P. J. Paris, and P. Kohler. "Ion Heating Due to Rotation and Collision in Magnetized Plasma". In: *Physical Review Letters* 57.3 (1986), pp. 329–332. DOI: 10.1103/physrevlett.57.329.

[292]   W. A. Noonan, T. G. Jones, and P. F. Ottinger. "Laser induced fluorescence diagnostic for measuring small magnetic fields". In: *Review of Scientific Instruments* 68.1 (1997), pp. 1032–1035. DOI: 10.1063/1.1147780.

[293] S. Mazouffre. "Laser-induced fluorescence diagnostics of the cross-field discharge of Hall thrusters". In: *Plasma Sources Science & Technology* 22.1 (2013). DOI: 10.1088/0963-0252/22/1/013001.

[294] J. C. Camparo. "The diode laser in atomic physics". In: *Contemporary Physics* 26.5 (1985), pp. 443–477. DOI: 10.1080/00107518508210984.

[295] Carl E. Wieman and Leo Hollberg. "Using diode lasers for atomic physics". In: *Review of Scientific Instruments* 62.1 (1991), pp. 1–20. DOI: 10.1063/1.1142305.

[296] Roger Mcwilliams and Daniel Sheehan. "Experimental Measurements of Phase Space". In: *Physical Review Letters* 56.23 (1986), pp. 2485–2488. DOI: 10.1103/physrevlett.56.2485.

[297] J. M. Mcchesney, R. A. Stern, and P. M. Bellan. "Observation of fast stochastic ion heating by drift waves". In: *Physical Review Letters* 59.13 (1987), pp. 1436–1439. DOI: 10.1103/physrevlett.59.1436.

[298] R. F. Boivin and E. E. Scime. "Laser induced fluorescence in Ar and He plasmas with a tunable diode laser". In: *Review of Scientific Instruments* 74.10 (2003), pp. 4352–4360. DOI: 10.1063/1.1606095.

[299] A. Stark, W. Fox, J. Egedal, O. Grulke, and T. Klinger. "Laser-Induced Fluorescence Measurement of the Ion-Energy-Distribution Function in a Collisionless Reconnection Experiment". In: *Physical Review Letters* 95.23 (2005). DOI: 10.1103/physrevlett.95.235005.

[300] I. Romadanov, Y. Raitses, A. Diallo, K. Hara, I. D. Kaganovich, and A. Smolyakov. "On limitations of laser-induced fluorescence diagnostics for xenon ion velocity distribution function measurements in Hall thrusters". In: *Physics of Plasmas* 25.3 (2018), p. 033501. DOI: 10.1063/1.5020749.

[301] E. Ban and E. J. Song. "Recent developments and applications of capillary electrophoresis with laser-induced fluorescence detection in biological samples". In: *Journal of Chromatography B* 929 (2013), pp. 180–186. DOI: https://doi.org/10.1016/j.jchromb.2013.04.028.

[302] C. M. Ferreira and A. Ricard. "Modelling of the low-pressure argon positive column". In: *Journal of Applied Physics* 54.5 (1983), pp. 2261–2271. DOI: 10.1063/1.332380.

[303] N. I. Uzelac and F. Leis. "Measurement of gas temperatures and metastable state densities in a microwave boosted glow-discharge using a diode-laser". In: *Spectrochimica Acta Part B - Atomic Spectroscopy* 47.7 (1992), pp. 877–887. DOI: 10.1016/0584-8547(92)80082-R.

[304] A. Bogaerts and R. Gijbels. "Modeling of metastable argon atoms in a direct-current glow discharge". In: *Physical Review A* 52.5 (1995), pp. 3743–3751. DOI: 10.1103/physreva.52.3743.

[305] Annemie Bogaerts, Renaat Gijbels, and Jaroslav Vlcek. "Collisional-radiative model for an argon glow discharge". In: *Journal of Applied Physics* 84.1 (1998), pp. 121–136. DOI: 10.1063/1.368009.

[306] P Varga, W Hofer, and H Winter. "Apparent cross sections for metastable ion production by electron impact". In: *Journal of Physics B: Atomic and Molecular Physics* 14.8 (1981), pp. 1341–1351. DOI: 10.1088/0022-3700/14/8/019.

[307] R. A. Gottscho and T. A. Miller. "Optical techniques in plasma diagnostics". In: *Pure and Applied Chemistry* 56.2 (1984), pp. 189–208. DOI: 10.1351/pac198456020189.

[308] E. Apaydin and M. Celik. "Investigation of the plasma parameters of a laboratory argon plasma source using a collisional radiative model with the comparison of experimental and simulated spectra". In: *Spectrochimica Acta Part B: Atomic Spectroscopy* 160 (2019), p. 105673. DOI: https://doi.org/10.1016/j.sab.2019.105673.

[309] Kiyoshi Kadota and Yozaburo Kaneko. "Neutralization Method for Detection of Metastable Ions and Its Application to the Production of Metastable Rare Gas Ions by Electron Impact". In: *Journal of the Physical Society of Japan* 38.2 (1975), pp. 524–531. DOI: 10.1143/jpsj.38.524.

[310] B.F.J. Luyken. "Transition probabilities and radiative lifetimes for Ar II". In: *Physica* 60.2 (1972), pp. 432–458. DOI: 10.1016/0031-8914(72)90114-0.

[311] M. J. Goeckner, J. Goree, and T. E. Sheridan. "Laser-induced fluorescence characterization of ions in a magnetron plasma". In: *Journal of Vacuum Science & Technology A* 8.6 (1990), pp. 3920–3924. DOI: 10.1116/1.576421.

[312] G. D. Severn, D. A. Edrich, and R. Mcwilliams. "Argon ion laser-induced fluorescence with diode lasers". In: *Review of Scientific Instruments* 69.1 (1998), pp. 10–15. DOI: 10.1063/1.1148472.

[313] D. Rapp and P. Englander-Golden. "Total Cross Sections for Ionization and Attachment in Gases by Electron Impact. I. Positive Ionization". In: *The Journal of Chemical Physics* 43.5 (1965), pp. 1464–1479. DOI: 10.1063/1.1696957.

[314] J. Bretagne, J. Godart, and V. Puech. "Low-energy electron distribution in an electron-beam-generated argon plasma". In: *Journal of Physics D: Applied Physics* 15.11 (1982), pp. 2205–2225. DOI: 10.1088/0022-3727/15/11/014.

[315] J. Bretagne, G. Callede, M. Legentil, and V. Puech. "Relativistic electron-beam-produced plasmas. I. Collision cross sections and loss function in argon". In: *Journal of Physics D: Applied Physics* 19.5 (1986), pp. 761–777. DOI: 10.1088/0022-3727/19/5/010.

[316] J. Vlcek. "A collisional - radiative model applicable to argon discharges over a wide range of conditions. 1. Formulation and basic data". In: *Journal of physics D: Applied Physics* 22.5 (1989), pp. 623–631. DOI: 10.1088/0022-3727/22/5/009.

[317] Á. Yanguas-Gil, J. Cotrino, and L. L Alves. "An update of argon inelastic cross sections for plasma discharges". In: *Journal of Physics D: Applied Physics* 38.10 (2005), pp. 1588–1598. DOI: 10.1088/0022-3727/38/10/014.

[318] H. D. Hagstrum. "Auger ejection of electrons from tungsten by noble gas ions". In: *Physical Review* 96.2 (1954), pp. 325–335. DOI: 10.1103/PhysRev.96.325.

[319] K.-U. Riemann. "The influence of collisions on the plasma sheath transition". In: *Physics of Plasmas* 4.11 (1997), pp. 4158–4166. DOI: 10.1063/1.872536.

[320] L. Oksuz and N. Hershkowitz. "First Experimental Measurements of the Plasma Potential throughout the Presheath and Sheath at a Boundary in a Weakly Collisional Plasma". In: *Physical Review Letters* 89.14 (2002). DOI: 10.1103/physrevlett.89.145001.

[321] M. A. Lieberman and A. J. Lichtenberg. "Direct Current (DC) Sheaths". In: *Principles of Plasma Discharges and Materials Processing*. John Wiley & Sons, Ltd, 2005. Chap. 6, pp. 165–206. DOI: https://doi.org/10.1002/0471724254.ch6.

[322]   V. Lisovskiy, E. Kravchenko, E. Skubenko, N. Kharchenko, and V. Yegorenkov. "Obstructed DC Glow Discharge in Low-Pressure Nitrogen". In: *Problems of Atomic Science and Technology* 6 (2010), pp. 156–158.

[323]   N. Hershkowitz, R. L. Goettsch, C. Chan, K. Hendricks, and R. T. Carpenter. "Detection of secondary electrons in a multidipole plasma". In: *Journal of Applied Physics* 53.7 (1982), pp. 5330–5332. DOI: 10.1063/1.329880.

[324]   David Coulette and Giovanni Manfredi. "Collisionless "thermalization" in the sheath of an argon discharge". In: *Physics of Plasmas* 22.4 (2015). DOI: 10.1063/1.4917239.

[325]   I V Schweigert, S. J. Langendorf, M. L. R. Walker, and M. Keidar. "Sheath structure transition controlled by secondary electron emission". In: *Plasma Sources Science and Technology* 24.2 (2015), p. 025012. DOI: 10.1088/0963-0252/24/2/025012.

[326]   G. García and J. Campos. "Lifetimes and transition probabilities of Ar(II)". In: *Journal of Quantitative Spectroscopy and Radiative Transfer* 34.1 (1985), pp. 85–94. DOI: https://doi.org/10.1016/0022-4073(85)90175-X.

[327]   A. Hibbert and J. E. Hansen. "Transitions in Ar II". In: *Journal of Physics B: Atomic, Molecular and Optical Physics* 27.15 (1994), pp. 3325–3347. DOI: 10.1088/0953-4075/27/15/012.

[328]   T. E. Sheridan. "Solution of the plasma-sheath equation with a cool Maxwellian ion source". In: *Physics of Plasmas* 8.9 (2001), pp. 4240–4245. DOI: 10.1063/1.1391448.

[329]   N. Grumman. "Basic Optics and Optical Instruments". eng. In: vol. 1. SPIE, 1963, pp. 1–160.

[330]   I. Hubeny and D. Mihalas. *Theory of stellar atmospheres: An introduction to astrophysical non-equilibrium quantitative spectroscopic analysis*. Princeton series in astrophysics. Princeton: Princeton University Press, 2014.

[331]   G. A. Hebner. "Spatially resolved, excited state densities and neutral and ion temperatures in inductively coupled argon plasmas". In: *Journal of Applied Physics* 80.5 (1996), pp. 2624–2636. DOI: 10.1063/1.363178.

[332]   S. A. Cohen, N. S. Siefert, S. Stange, R. F. Boivin, E. E. Scime, and F. M. Levinton. "Ion acceleration in plasmas emerging from a helicon-heated magnetic-mirror device". In: *Physics of Plasmas* 10.6 (2003), pp. 2593–2598. DOI: 10.1063/1.1568342.

[333]   G. A. Emmert, R. M. Wieland, A. T. Mense, and J. N. Davidson. "Electric sheath and presheath in a collisionless, finite ion temperature plasma". In: *Physics of Fluids* 23.4 (1980), p. 803. DOI: 10.1063/1.863062.

[334]   S. D. Baalrud, J. D. Callen, and C. C. Hegna. "Instability-Enhanced Collisional Effects and Langmuir's Paradox". In: *Physical Review Letters* 102.24 (2009). DOI: 10.1103/PhysRevLett.102.245005.

[335]   S. D. Baalrud and C. C. Hegna. "Kinetic theory of the presheath and the Bohm criterion". In: *Plasma Sources Science and Technology* 20.2 (2011), p. 025013. DOI: 10.1088/0963-0252/20/2/025013.

[336]   Toshiki Nakano, Nader Sadeghi, and Richard A. Gottscho. "Ion and neutral temperatures in electron cyclotron resonance plasma reactors". In: *Applied Physics Letters* 58.5 (1991), pp. 458–460. DOI: 10.1063/1.104606.

[337] K. N. Leung, R. D. Collier, L. B. Marshall, T. N. Gallaher, W. H. Ingham, R. E. Kribel, and G. R. Taylor. "Characteristics of a multidipole ion source". In: *Review of Scientific Instruments* 49.3 (1978), pp. 321–325. DOI: 10.1063/1.1135392.

[338] R. Hegerberg, M. T. Elford, and H. R. Skullerud. "The cross section for symmetric charge exchange of Ne+in Ne and Ar+in Ar at low energies". In: *Journal of Physics B: Atomic and Molecular Physics* 15.5 (1982), pp. 797–811. DOI: 10.1088/0022-3700/15/5/022.

[339] N. Ranson, R. Bowden-Reid, J. Khachan, and N. Claire. "Langmuir probe measurements of the secondary electron population across the cathodic pre-sheath of a DC argon discharge". In: *Physics of Plasmas* 30.4 (2023), p. 043502. DOI: 10.1063/5.0130291.

[340] P. M. Chung, L. Talbot, and K. J. Touryan. *Electric Probes in Stationary and Flowing Plasmas: Theory and Application*. eng. Vol. 11. Applied Physics and Engineering, An International Series. Berlin, Heidelberg: Springer Berlin / Heidelberg, 1975.

[341] F. F. Chen. "Electric probes". eng. In: *Plasma diagnostic Techniques*. Ed. by R. H. Huddlestone and S. L. Leonard. 111 Fifth Avenue, New York, New York, 10003, 1965. Chap. 4.

[342] B. E. Cherrington. "The use of electrostatic probes for plasma diagnostics?A review". In: *Plasma Chemistry and Plasma Processing* 2.2 (1982), pp. 113–140. DOI: 10.1007/bf00633129.

[343] Y. P. Raĭzer. "Gas discharge physics". eng. In: *Gas discharge physics*. Berlin ; Springer-Verlag, 1991. Chap. 6.

[344] M. B. Hopkins and W. G. Graham. "Langmuir probe technique for plasma parameter measurement in a medium density discharge". In: *Review of Scientific Instruments* 57.9 (1986), pp. 2210–2217. DOI: 10.1063/1.1138684.

[345] J. F. Waymouth. "Perturbation of a Plasma by a Probe". In: *Physics of Fluids* 7.11 (1964), p. 1843. DOI: 10.1063/1.2746785.

[346] H. M. Mott-Smith and I. Langmuir. "The Theory of Collectors in Gaseous Discharges". In: *Physical Review* 28.4 (1926), pp. 727–763. DOI: 10.1103/physrev.28.727.

[347] R. Bowden-Reid. "An Experimental Study of Gridded and Virtual Cathode Inertial Electrostatic Confinement Fusion Systems". PhD thesis. School of Physics, 2019.

[348] Sheridan T. E. and J. Goree. "Langmuir-probe characteristic in the presence of drifting electrons". In: *Physical Review E* 50.4 (1994), pp. 2991–2996. DOI: 10.1103/PhysRevE.50.2991.

[349] W. R. Hoegy and L. H. Brace. "Use of Langmuir probes in non-Maxwellian space plasmas". In: *Review of Scientific Instruments* 70.7 (1999), pp. 3015–3024. DOI: 10.1063/1.1149862. URL: https://dx.doi.org/10.1063/1.1149862.

[350] M. Nachman and P. C. Thanh. "Thickness of the ion sheath around a cylindrical electrode in a plasma". In: *IEEE Transactions on Plasma Science* 19.2 (1991), pp. 423–427. DOI: 10.1109/27.106841.

[351] F. F. Chen. "Langmuir probes in RF plasma: surprising validity of OML theory". In: *Plasma Sources Science & Technology* 18.3 (2009). DOI: 10.1088/0963-0252/18/3/035012.

[352] L. J. Mahoney, A. E. Wendt, E. Barrios, C. J. Richards, and J. L. Shohet. "Electron-density and energy distributions in a planar inductively coupled discharge". In: *Journal of Applied Physics* 76.4 (1994), pp. 2041–2047. DOI: 10.1063/1.357672.

[353] U. Kortshagen, A. Shivarova, E. Tatarova, and D. Zamfirov. "Electron energy distribution function in a microwave discharge created by propagating surface waves". In: *Journal of Physics D: Applied Physics* 27.2 (1994), p. 301. DOI: 10.1088/0022-3727/27/2/019.

[354] V. A. Godyak, R. B. Piejak, and B. M. Alexandrovich. "Electron energy distribution function measurements and plasma parameters in inductively coupled argon plasma". In: *Plasma Sources Science and Technology* 11.4 (2002), p. 525. DOI: 10.1088/0963-0252/11/4/320.

[355] W. Lu et al. "Improved Double-Probe Technique for Spatially Resolved Diagnosis of Dual-Frequency Capacitive Plasmas". In: *Plasma Science and Technology* 15.6 (2013), p. 511. DOI: 10.1088/1009-0630/15/6/05.

[356] C. Küllig, Th. Wegner, and J. Meichsner. "Spatially resolved Langmuir probe diagnostics in a capacitively coupled radio frequency argon and oxygen plasma". In: *Plasma Sources Science and Technology* 24.1 (2015), p. 015027. DOI: 10.1088/0963-0252/24/1/015027.

[357] P. Zhang, Á. Valfells, L. K. Ang, J. W. Luginsland, and Y. Y. Lau. "100 years of the physics of diodes". In: *Applied Physics Reviews* 4.1 (2017), p. 011304. DOI: 10.1063/1.4978231.

[358] S. Langendorf and M. Walker. "Effect of secondary electron emission on the plasma sheath". In: *Physics of Plasmas* 22.3 (2015), p. 033515. DOI: 10.1063/1.4914854.

[359] B. L. Henke, J. A. Smith, and D. T. Attwood. "0.1–10-keV x-ray-induced electron emissions from solids—Models and secondary electron measurements". In: *Journal of Applied Physics* 48.5 (1977), pp. 1852–1866. DOI: 10.1063/1.323938.

[360] V. Pigeon, N. Claire, C. Arnas, K. Terasaka, and S. Inagaki. "Plasma sheath material induced dependence due to secondary electron emission". In: *Physics of Plasmas* 27.4 (2020), p. 043505. DOI: 10.1063/1.5141348.

[361] S. B. Song, C. S. Chang, and Duk-In Choi. "Effect of two-temperature electron distribution on the Bohm sheath criterion". In: *Physical Review E* 55.1 (1997), pp. 1213–1216. DOI: 10.1103/physreve.55.1213.

[362] K-L. Persson. "Inertia-Controlled Ambipolar Diffusion". In: *Physics of Fluids* 5.12 (1962), p. 1625. DOI: 10.1063/1.1706574.

[363] L. S. Pilling and D. A. Carnegie. "Validating experimental and theoretical Langmuir probe analyses". In: *Plasma Sources Science & Technology* 16.3 (2007), pp. 570–580. DOI: 10.1088/0963-0252/16/3/016.

[364] E. Ahedo. "Presheath/sheath model with secondary electron emission from two parallel walls". In: *Physics of Plasmas* 9.10 (2002), pp. 4340–4347. DOI: 10.1063/1.1503798.

[365] Irving Langmuir. "Scattering of Electrons in Ionized Gases". In: *Physical Review* 26.5 (1925), pp. 585–613. DOI: 10.1103/physrev.26.585.

[366] S. Knappmiller, S. Robertson, and Z. Sternovsky. "Method to find the electron distribution function from cylindrical probe data". In: *Physical Review E* 73.6 (2006). DOI: 10.1103/PhysRevE.066402.

[367] X. Hou, Y. Fu, H. Wang, X. Zou, H. Luo, and X. Wang. "Determination of the cathode layer thickness in the normal glow discharge". In: *Physics of Plasmas* 24.8 (2017), p. 083506. DOI: 10.1063/1.4995266.

[368] L. Schott. "Electrical Probes". In: *Plasma Diagnostics*. Ed. by W. Lochte-Holtgreven. 1st ed. Vol. 1. North-Holland Publishing Company - Amsterdam, 1968. Chap. 11, pp. 668–725.

[369] J. G. Laframboise. *Theory of spherical and cyolindrical langmuir probes in a collisionless, maxwellian plasma at rest.* report 100. University of Toronto Institute for Aerospace Studies, 1966.

[370] C. Steinbruchel. "A new method for analyzing Langmuir probe data and the determination of ion densities and etch yields in an etching plasma". In: *Journal of Vacuum Science & Technology A - Vacuum Surfaces and Films* 8.3 (1990), pp. 1663–1667. DOI: 10.1116/1.576782.

[371] M. Carr. "Electrostatic potential measurements and point cusp theories applied to a low beta Polywell fusion device". PhD thesis. School of Physics, 2013.

[372] A. Savitzky and M. J. E. Golay. "Smoothing and Differentiation of Data by Simplified Least Squares Procedures." In: *Analytical Chemistry* 36.8 (1964), pp. 1627–1639. DOI: 10.1021/ac60214a047.

[373] Guseva L. G. "On discharge striking in polyatomic Gases at pd<(pd)min". eng;rus. In: *Investigations into electrical discharges in gases.* Ed. by Klyarfel'd. Oxford, ; Pergamon Press; [distributed in the Western Hemisphere by Macmillan pursuant to a special arrangement with Pergamon Press], 1964.

[374] A. K. Brewer and J. W. Westhaver. "The Cathode Region in the Glow Discharge". In: *Journal of Applied Physics* 8.11 (1937), pp. 779–782. DOI: 10.1063/1.1710254.

[375] J. A. Meyer, G.-H. Kim, M. J. Goeckner, and N. Hershkowitz. "Measurements of the presheath in an electron cyclotron resonance etching device". In: *Plasma Sources Science and Technology* 1.3 (1992), pp. 147–150. DOI: 10.1088/0963-0252/1/3/001.

[376] D. Wobschall, J. R. Graham, and D. P. Malone. "Ion cyclotron resonance and determination of collision cross sections". In: *Physical Review* 131.4 (1963), pp. 1565–&. DOI: 10.1103/PhysRev.131.1565.

[377] F. L. Hinton. "Collisional transport in plasma". In: *Basic Plasma Physics: Selected Chapters, Handbook of Plasma Physics, Volume 1*. 1984, p. 147.

[378] Lorne M. Chanin and Manfred A. Biondi. "Temperature Dependence of Ion Mobilities in Helium, Neon, and Argon". In: *Physical Review* 106.3 (1957), pp. 473–479. DOI: 10.1103/physrev.106.473.

[379] K. B. Mcafee, D. Sipler, and D. Edelson. "Mobilities and Reactions of Ions in Argon". In: *Physical Review* 160.1 (1967), pp. 130–135. DOI: 10.1103/physrev.160.130.

[380] A Hennad, O Eichwald, M Yousfi, and O Lamrous. "Effect of the ion-atom collision anisotropy on the ion transport from Monte-Carlo simulation". In: *Journal De Physique III* 7.9 (1997), pp. 1877–1892.

[381] Z. Lj. Petrović, M. Šuvakov, Ž. Nikitović, S. Dujko, O. Šašić, J. Jovanović, G. Malović, and V. Stojanović. "Kinetic phenomena in charged particle transport in gases, swarm parameters and cross section data". In: *Plasma Sources Science and Technology* 16.1 (2007), S1–S12. DOI: 10.1088/0963-0252/16/1/s01.

[382] T. H. Lovaas, H. R. Skullerud, O. H. Kristensen, and D. Linhjell. "Drift and longitudinal diffusion of lithium ions in helium". In: *Journal of Physics D- Applied Physics* 20.11 (1987), pp. 1465–1471. DOI: 10.1088/0022-3727/20/11/016.

[383] L. J. Kieffer and G. H. Dunn. "Electron Impact Ionization Cross-Section Data for Atoms, Atomic Ions, and Diatomic Molecules: I. Experimental Data". In: *Reviews of Modern Physics* 38.1 (1966), pp. 1–35. DOI: `10.1103/revmodphys.38.1`.

[384] S. D. Rosner, T. D. Gaily, and R. A. Holt. "Laser fluorescence measurement of relative electron impact cross sections for metastable states of Ar+and Xe+". In: *Journal of Physics B: Atomic and Molecular Physics* 9.16 (1976), pp. L489–L491. DOI: `10.1088/0022-3700/9/16/006`.

[385] W. R. Bennett, J. W. Knutson, G. N. Mercer, and J. L. Detch. "Super-radiance, excitation mechanisms, and quasi-CW oscillation in the visible Ar+ Laser 1". In: *Applied Physics Letters* 4.10 (1964), pp. 180–182. DOI: `10.1063/1.1753927`.

[386] J. M. Hammer and C. P. Wen. "Measurements of Electron Impact Excitation Cross Sections of Laser States of Argon(II)". In: *The Journal of Chemical Physics* 46.4 (1967), pp. 1225–1230. DOI: `10.1063/1.1840839`.

[387] P. N. Clout and D. W. O. Heddle. "Electron impact excitation of argon II lines". In: *Journal of Physics B: Atomic and Molecular Physics* 4.4 (1971), p. 483. DOI: `10.1088/0022-3700/4/4/010`.

[388] J. N. Ross. "The populations of some excited states of singly ionized argon in an argon laser discharge". In: *Journal of Physics D: Applied Physics* 7.10 (1974), pp. 1426–1433. DOI: `10.1088/0022-3727/7/10/316`.

[389] J. Jolly. "Determination of the rate coefficients for the collisional excitation and de-excitation of the upper laser levels of Ar". In: *Journal of Quantitative Spectroscopy and Radiative Transfer* 20.5 (1978), pp. 503–518. DOI: `10.1016/0022-4073(78)90055-9`.

[390] H. M. J. Willems, K. Yuasa, B. Vandersijde, D. C. Schram, and J. A. M. Vandermullen. "Laser fluorescence experiments with a pulsed dye-laser in an argon plasma". In: *Journal of Quantitative Spectroscopy & Radiative Transfer* 41.4 (1989), pp. 251–258. DOI: `10.1016/0022-4073(89)90121-0`.

[391] J. W. Coburn and M. Chen. "Optical emission spectroscopy of reactive plasmas: A method for correlating emission intensities to reactive particle density". In: *Journal of Applied Physics* 51.6 (1980), pp. 3134–3136. DOI: `10.1063/1.328060`.

[392] R. D'Agostino, F. Cramarossa, S. De Benedictis, and G. Ferraro. "Spectroscopic diagnostics of CF4-O2 plasmas during Si and SiO2 etching processes". In: *Journal of Applied Physics* 52.3 (1981), pp. 1259–1265. DOI: `10.1063/1.329748`.

[393] S. H. Koozekanani. "An excitation mechanism for the A+ laser". In: *Applied Physics Letters* 11.3 (1967), pp. 107–108. DOI: `10.1063/1.1755038`.

[394] J. Jolly. "Étude d'un plasma d'argon fortement ionisé à basse pression produit par une décharge pulsée". In: *Revue de Physique Appliquée* 12.4 (1977), pp. 553–558. DOI: `10.1051/rphysap:01977001204055300`.

[395] H. A. Hyman. "Electron-impact ionization cross sections for excited states of the rare gases (Ne, Ar, Kr, Xe), cadmium, and mercury". In: *Physical Review A* 20.3 (1979), pp. 855–859. DOI: `10.1103/physreva.20.855`.

[396] E. I. Gordon, E. F. Labuda, and W. B. Bridges. "Continuous visible laser action in singly ionized argon, krypton, and xenon". In: *Applied Physics Letters* 4.10 (1964), pp. 178–180. DOI: `10.1063/1.1753926`.

[397] I. P. Zapesochnyĭ, A. I. Imre, A. I. Daschenko, V. S. Vukstich, F. F. Danch, and V. A. Kel'man. "Experimental investigation of the excitation of Ar II and Kr II in electron-ion collisions". In: *Soviet Physics JETP - USSR* 26.6 (1972), pp. 1056–1060.

[398] D. B. Mcgarrah and M. L. Brake. "Argon ion excitation by relativistic electrons: I. Collision cross sections and deposition efficiencies". In: *Laser and Particle Beams* 8.3 (1990), pp. 493–506. DOI: 10.1017/s0263034600008739.

[399] W. T. Silfvast, D. Y. Al-Salameh, and O. R. Wood Ii. "Multielectron photoionization to the3p4". In: *Physical Review A* 34.6 (1986), pp. 5164–5167. DOI: 10.1103/physreva.34.5164.

[400] K-H. Tan and J. W. Mcconkey. "Simultaneous ionization and excitation of Ar by electrons with particular attention to configuration-interaction effects". In: *Physical Review A* 10.4 (1974), pp. 1212–1222. DOI: 10.1103/physreva.10.1212.

[401] W. Bleakney. "Ionization Potentials and Probabilities for the Formation of Multiply Charged Ions in Helium, Neon and Argon". In: *Physical Review* 36.8 (1930), pp. 1303–1308. DOI: 10.1103/physrev.36.1303.

[402] L. Frommhold and M. A. Biondi. "Interferometric Study of Dissociative Recombination Radiation in Neon and Argon Afterglows". In: 185.1 (1969), pp. 244–252. DOI: 10.1103/physrev.185.244.

[403] D. R. Bates, A. E. Kingston, and R. W. P. Mcwhirter. "Recombination between electrons and atomic ions, I. Optically thin plasmas". In: *Proceedings of the Royal Society of London. A. Mathematical and Physical Sciences* 267.1330 (1962), pp. 297–312. DOI: 10.1098/rspa.1962.0101.

[404] A. V. Phelps and J. P. Molnar. "Lifetimes of Metastable States of Noble Gases". In: *Physical Review* 89.6 (1953), pp. 1202–1208. DOI: 10.1103/physrev.89.1202.

[405] S. A. Babin, S. I. Kablukov, and S. M. Kobstev. "Parameters of metastable ArII ions in a gas-discharge plasma". In: *Optics and Spectroscopy* 84.6 (1998), pp. 828–833.